UNIVERSITÄT ZU KÖLN

Fakultät für Mathematik und Naturwissenschaften

Institut für Theoretische Physik

UNIVERSITÀ DEGLI STUDI DI PADOVA

Dipartimento di Fisica e Astronomia “Galileo Galilei”

QUANTUM OPTIMAL CONTROL OF SPIN SYSTEMS AND TRAPPED ATOMS

by

Phila K. M. Rembold

born in Frankfurt am Main

This dissertation is submitted for the degree of

Doctor rerum naturalium & *Dottore di Ricerca in Physics*

February 2022

Supervisors:	Prof. Dr. Simone Montangero Prof. Dr. Tommaso Calarco
External reviewers:	Prof. Dr. Christiane Koch Dr. Nicole Fabbri
Main funding:	QuSCo (Marie Skłodowska-Curie ITN No 765267)
Date of the defence:	29 April 2022

Abstract

Quantum technology is advancing from the lab into the commercial world. However, this path from scientific discovery to revolutionising technology cannot be built without the precise control of quantum systems. Quantum optimal control describes a family of techniques that improve quantum operations by systematically shaping the control fields applied to the system. The bespoke control strategies that optimisations can offer push quantum hardware to realise its full potential. In this thesis, we apply optimal control to spin systems, namely nitrogen-vacancy centres in diamond and pentacene-doped naphthalene, as well as to trapped atoms, specifically Rydberg atoms, and ultracold atomic condensates. Generally, a well-modelled system with a clear objective corresponds to a well-defined control problem approachable via open-loop optimisation, i.e. by using a model. However, when unknown experimental or environmental factors have a strong influence, the complexity of the control problem increases. Once any viable model diverges from reality, closed-loop, i.e. feedback-based, control offers a solution. From the collection of quantum optimal control methods, we focus on the dressed chopped random basis algorithm combined with a gradient-free search. This pairing enables us to apply bandwidth restrictions and limit the number of optimisation parameters, simplifying closed-loop applications. We introduce several techniques and modifications, such as a novel basis approach, that allow efficient closed-loop control using the "RedCRAB" software package. As a result, we optimise for the following very distinct goals each on a different platform: sensitivity, hyperpolarisation, number squeezing, and entangled state preparation. All four objectives directly or indirectly improve sensing methods. Enhancing the sensitivity of shallow nitrogen-vacancy centres presents an opportunity for improving diamond-based scanning probe magnetometers. Hyperpolarisation of materials such as naphthalene crystals promises to enable more precise cancer cell imaging. Atom interferometry is used to detect minimal changes in the gravitational field. The number-squeezed states whose creation we explore could increase that sensitivity further. Lastly, large entangled states are the key to exceeding the classical sensitivity limit. We create a record-breaking 20-qubit entangled state via optimisation. Ultimately, these results show how quantum optimal control interconnects and boosts the rise of quantum technology across the platforms.

Kurzfassung

Die Quantentechnologie ist auf dem Weg aus dem Labor in die kommerzielle Welt. Allerdings führt dieser nicht an der präzisen Kontrolle der Quantensysteme in ihrem Herzen vorbei. Die optimale Quantenkontrolle besteht aus einer Familie von Algorithmen, die Kontrollfelder systematisch verformen, um einen Quantenprozess zu verbessern. Die maßgeschneiderten Kontrollstrategien, die mit Hilfe der optimalen Quantenkontrolle produziert werden, ermöglichen es, das volle Potential der Quantenhardware auszuschöpfen. In dieser Dissertation wenden wir optimale Kontrolle auf Spinsysteme und gefangenen Atome an. Im Allgemeinen entspricht ein gutmodeliertes System mit einem klaren Ziel einem wohldefinierten Kontrollproblem. Dieses kann durch eine modellbasierte Optimierung angegangen werden. Wenn das Experiment oder die Umgebung allerdings unbekannte Faktoren mit einem starken Einfluss aufweisen, erhöht sich die Komplexität des Kontrollproblems. Sobald das Modell an seine Grenzen stößt und sich zu weit von der Realität entfernt, bietet sich eine experimentbasierte Optimierung an. Wir fokussieren uns auf den sogenannten dCRAB-Algorithmus kombiniert mit einer ableitungsfreien Suche. Diese Auswahl erlaubt es uns, Bandbreitenbegrenzungen zu implementieren und die Anzahl der Optimierungsparameter einzuschränken, was die experimentbasierte Optimierung erleichtert. Wir führen verschiedene Techniken und Modifikationen ein, darunter einen neuen Basisansatz. Diese Erweiterungen ermöglichen effizientere experimentbasierte Quantenkontrolle über das Softwarepaket “RedCRAB”. Im Ergebnis optimieren wir Kontrollprobleme mit den folgenden äußerst unterschiedlichen Zielstellungen: Das Verbessern der Sensitivität von flachen Stickstoff-Fehlstellen-Zentren eröffnet die Möglichkeit diamantbasierte Rastersondenmagnetometer zu verbessern. Die Hyperpolarisierung von Stoffen, wie Naphthalenkristall, verspricht eine präzisere Krebszellenerkennung zu ermöglichen. Atominterferometrie wird verwendet um kleinste Veränderungen im Gravitationsfeld zu messen. Wir nehmen die Erzeugung gequetschter Quantenzustände unter die Lupe, um die Sensitivität von atombasierten Interferometern zu verbessern. Schließlich erschaffen wir durch Optimierung mit 20 Rydbergatomen einen rekordbrechenden, verschränkten Schrödinger-Katzen-Zustand. Zusammenfassend zeigen unsere Ergebnisse wie die optimale Quantenkontrolle auf verschiedenen Plattformen basierende Quantentechnologien verbindet und verbessert.

Research Output

Parts of this thesis are based on or have been taken from material first published in the following peer-reviewed journals or as preprint (arXiv) versions. The author contributions are listed at the relevant passages.

[1] ***Generation and Manipulation of Schrödinger Cat States in Rydberg Atom Arrays***
A. Omran†, H. Levine†, A. Keesling, G. Semeghini, T. T. Wang, S. Ebadi, H. Bernien, A. S. Zibrov, H. Pichler, S. Choi, J. Cui, M. Rossignolo, P. Rembold, S. Montangero, T. Calarco, M. Endres, M. Greiner, V. Vuletić, M. D. Lukin
Science, 365 (6453), 570–574 (2019)

[2] ***Introduction to Quantum Optimal Control for Quantum Sensing with Nitrogen-Vacancy Centers in Diamond***
P. Rembold†, N. Oshnik†, M. M. Müller, T. Calarco, S. Montangero, and E. Neu
AVS Quantum Science 2, 024701 (2020)

[3] ***Robust Magnetometry with Single NV Centers via Two-Step Optimization***
N. Oshnik, P. Rembold, T. Calarco, S. Montangero, and E. Neu, M. M. Müller
in preparation for publication: arXiv:2111.12684 [quant-ph]

[4] ***Macroscopic Hyperpolarization Enhanced with Quantum Optimal Control***
A. Marshall†, T. Reisser†, P. Rembold†, C. Müller, J. Scheuer, M. Gierse, T. Eichhorn, J. M. Steiner, P. Hautle, T. Calarco, F. Jelezko, M. B. Plenio, S. Montangero, I. Schwartz, M. M. Müller, and P. Neumann
in preparation for publication: arXiv:2112.15021 [quant-ph]

The work in this thesis has led to contributions to the following software packages:

RedCRAB: Remote Implementation of the dCRAB Algorithm
J. Zoller, F. Höb, M. Rossignolo, P. Rembold, T. Reisser, S. Montangero, and T. Calarco
not publicly available but described in references [5, 6]

†These authors contributed equally to this work.

[7] ***UNIQORN: Universal Neural Network Interface for Quantum Observable Readout from N-body Wavefunctions***
A. U. J. Lode, P. Molignini, R. Lin, M. Büttner, P. Rembold, C. Lévêque, M. C. Tsatsos, and L. Papariello
`https://gitlab.com/auj.lode/UNIQORN.git` (2020).

[8] ***QuOCS: Quantum Optimal Control Suite***
M. Rossignolo, A. Marshall, T. Reisser, P. Rembold, A. Pagano, P. Vetter, R. S. Said, M. M. Müller, T. Calarco, S. Montangero, and F. Jelezko
`https://github.com/Quantum-OCS/QuOCS` (2021).

The outreach component of the doctoral programme (Marie Skłodowska-Curie ITN – QuSCo) is reflected in the following content:

[9] ***A Tale of Claw Machines and Quantum Mechanics*** (blog post)
P. Rembold
`https://qusco-itn.eu/2019/10/08/phila/` (2019).

[10] ***Diamond and boxing gloves: an introduction to quantum sensing and quantum control*** (video)
Directed by Aviv Kosloff, featuring P. Rembold, C. Koch, A. Marshall, and M. Garsi, published by QuSCo.
`https://www.youtube.com/watch?v=dl4nyCXhOr4` (2021).

Table of contents

Introduction

The largest companies and countries worldwide are racing to build the first scalable, fault-tolerant quantum computer [11]. However, while quantum computation certainly forms the centre of public attention, other quantum technologies are already close to revolutionising technology. Quantum sensors, for example, might support self-driving cars by making them independent from GPS [12], while quantum cryptography will herald a new age of cyber security [13]. What gives quantum systems the advantage is that they follow different rules than classical objects. Generally, anything small enough, provided it is effectively isolated from the environment, is a quantum object and inherits the properties that distinguish the quantum from the classical. Three features define quantum systems and consequently play crucial roles in many applications: Superposition, the uncertainty principle, and entanglement.

Combining these properties leads to a wide selection of potential applications summarised by the big four: Quantum simulation, quantum computing, quantum communication, and quantum sensing. All of them include use cases that have already been commercialised. The quantum sensor is a focus of this thesis and natural application as, by definition, quantum systems are tiny and commonly evolve on fast time scales. Not only are quantum systems able to break classical sensitivity limits, but their size also allows for nanoscale resolution. Using their quantum properties enhances their ability to detect minor differences in, for example, temperature [14], magnetic fields [15], and gravity [16]. However, this strong reaction to their surroundings also hampers their controllability [17]. If the controllability is insufficient, it is impossible to execute the delicate protocols that form the basis for any advanced (sensing) operation. State-of-the-art quantum technology combats unwanted influences through improvements in manufacturing and calibration. Nevertheless, to reveal the hardware's full potential, those approaches need to be complemented by control methods that shape the fields guiding the quantum state's evolution. These control fields commonly form the bridge between the conceived concept of the quantum operation, like executing a gate sequence or qubit preparation, and the actual implementation.

Quantum optimal control (QOC) describes a family of strategies designed to find the most

effective shape of the control fields in pursuit of a specified goal [18]. Commonly, in quantum mechanics, the controls are resonant magnetic fields [19], laser pulses [20], or trap configurations [21] that are adjusted dynamically, i.e. as a function of time. The synergy of QOC and an experiment or accurate model thereof allows for the development of advanced manipulation protocols tailored to a specific system. The most common representatives of QOC algorithms use iterative methods that allow a search outside of the obvious analytical solution space. Here, the effectiveness, called the figure of merit, of the dynamical pulses is assessed either in a simulation (open-loop) or directly on the experiment (closed-loop). An updating algorithm picks new pulses in each iteration depending on the previous figure of merit or its gradient/Hessian with respect to the control parameters. Different strategies are available to translate dynamical pulses into control parameters, such as splitting the pulse into time slices [22] or using a set of time-dependent basis functions like Fourier components [23, 24]. In this thesis, we focus on methods tightly connected to experimental hardware and broadening their scope.
Any quantum system presents a potential target for QOC and a multitude of them has already been successfully improved: Nitrogen-vacancy (NV) centres in diamond, for example, are a promising spin system that can be operated at room temperature and manipulated with microwave pulses. QOC has enhanced NV-based protocols for different quantum operations [25–27]. Technology based on superconducting qubits is also manipulated with microwave signals and has benefited from QOC in many ways [28–30]. Other applications include nuclear magnetic resonance techniques [31], the manipulation of Rydberg atoms [1], operations with trapped ions [32], gates with quantum dots [33], the creation of Bose Einstein condensates and generally the manipulation of ultracold atoms [34, 21, 6].
This manuscript comprises a description of different modelling techniques, the theoretical background of QOC, and a range of applications that summarise the work carried out at the Universities of Padua and Cologne, as well as the Jülich Research Centre. The manuscript is structured as follows:

- Chapter 1 is devoted to a range of models representing the quantum systems and processes that are optimised in Chapter 3. The fundamental dynamical equations are introduced first, before going into a more detailed analysis. The first part is focused on electron spins, such as NV centres, and pentacene molecules in naphthalene crystals. Ultimately, it introduces a method used to model ultracold atoms, namely the multi-configurational time-dependent Hartree approach for bosons.

- Chapter 2 describes the theoretical background of QOC. These concepts are the basis for later applications. It starts with an introduction to QOC, followed by an overview

of some of the most common algorithms. It concludes with the introduction of a new basis approach developed by the doctoral candidate.

- Finally, Chapter 3 summarises the original work from the candidate's doctoral studies on the optimisation of a range of quantum systems. QOC is applied to electron spin systems to enable the enhanced polarisation of a naphthalene crystal despite experimental challenges, and to increase the sensing capability of NV centres close to the diamond surface. Furthermore, spin squeezing is investigated considering a realistic experimental model using ultracold atoms. Finally, we outline the role of QOC in the creation of a record-breaking, maximally entangled superposition state with twenty Rydberg atoms.

Chapter 1

Modelling Quantum Systems

In this chapter, we will introduce several concepts for modelling quantum systems. They are split up into "Few Spin Systems" (Section 1.1), where we give a more general introduction, and "Atomic Condensates" (Section 1.2), which is focused on condensates of ultracold atoms. The first section contains examples focused on nitrogen-vacancy (NV) centres. Still, the described methods can be applied to a wide range of quantum systems. The second part is centred around a particular simulation method that found its application in one of the projects described in Chapter 3.

1.1 Few Spin Systems

> Before the year 1928, every physicist knew what we meant by an elementary particle. [...] But then the discovery of [...] the electron spin changed this picture considerably [...] and emphasized that perhaps such particles have more than one property, and that they are not simple, not so elementary as we had thought before.
>
> *Werner Heisenberg* [35]

Many interesting spin systems are being investigated in the field of quantum technologies. In this chapter we focus on one of them: The negatively charged NV centre [36, 37] is a point defect in diamond, specifically a place where two carbon atoms are replaced with one nitrogen atom and an adjacent vacancy. When this system traps an additional electron, it becomes simple to initialise and read out with a laser. It is furthermore manipulable with microwaves, sensitive to magnetic fields, and bio-compatible. These features make it a promising quantum sensor and candidate for a whole range of quantum applications. This section introduces the basic concepts of modelling quantum systems with a focus on few

spin systems like the NV centre. A thorough introduction and examples for the application of quantum optimal control (QOC) to NV centres can be found in the review by Rembold et al. [2].

1.1.1 Dynamical Equations

1.1.1.1 Schrödinger Equation

The Schrödinger equation (SE) governs the dynamics of any pure quantum system [38]. In its most basic time-dependent form it reads

$$i\hbar\frac{\partial}{\partial t}|\phi\rangle = H|\phi\rangle. \tag{1.1}$$

The Hamiltonian operator (or just Hamiltonian) H is a Hermitian operator, which represents the energy and dynamics of the system [39]. The wavefunction $|\phi\rangle$ is a mathematical description of that quantum system's state. It is a complex vector of probability amplitudes, normalised such that $\langle\phi|\phi\rangle = 1$. The eigenvectors $|\phi_i\rangle$ of the Hamiltonian are time-independent states.
Another form of the SE is the von Neumann equation

$$i\hbar\frac{\partial}{\partial t}\rho = [H,\rho], \tag{1.2}$$

where $\rho = |\phi\rangle\langle\phi|$ is the density function of the pure state $|\phi\rangle$. Density matrices can also describe statistical mixtures of pure states, called mixed states, taking a form like

$$\rho = \sum_i p_i |\phi_i\rangle\langle\phi_i| \tag{1.3}$$

with probabilities p_i to be in the state $|\phi_i\rangle$. On the Bloch sphere pure states lie at the surface while mixed states lie inside the sphere.
The time evolution of a system is described by the propagator $U(t)$

$$\begin{aligned} |\phi(t)\rangle &= U(t)\,|\phi(0)\rangle, \\ \rho(t) &= U(t)\rho(0)\,U^\dagger(t). \end{aligned} \tag{1.4}$$

The propagator is unitary and its relationship to the Hamiltonian is defined by

$$i\hbar\frac{\partial}{\partial t}U(t) = H(t)U(t). \tag{1.5}$$

If the Hamiltonian is time-independent the solution is

$$U(t) = e^{-iHt/\hbar}, \text{ for } U(0) = \mathbb{I}. \tag{1.6}$$

Please note that in this thesis, we omit the hat on a symbol when it is clearly defined as an operator. This applies, for example, to Hamiltonians, propagators, and density functions.

Example: NV Centre Coupled to N_n Nuclear Spins The ground state of the NV centre is a triplet, i.e. a spin one system. Let us consider the most basic Hamiltonian H_{nv} for an NV centre coupled to N_n surrounding nuclei (also introduced in reference [2] and explained in further detail in Section 1.1.2). It covers a Hilbert space of dimension 3×2^{N_n}. This example shows one of the most common approximations made with regard to NV centres – the two-level approximation – which reduces the dimension to 2×2^{N_n}. Together with the resonant frequency and gyromagnetic ratio of the NV centre, the two-level approximation is responsible for the familiar electron spin representation.

$$H_{\text{nv}}/\hbar = D_g\left[\hat{S}_z^2 - \frac{2}{3}\mathbb{I}\right] + E_g\left(\hat{S}_x^2 - \hat{S}_y^2\right) + \gamma_{\text{nv}}\vec{B}\cdot\hat{\vec{S}} + \sum_{i=1}^{N_n}\left(\hat{\vec{S}}\mathcal{A}^i\hat{\vec{I}}^i + \gamma_i\vec{B}\cdot\hat{\vec{I}}^i + \hat{\vec{I}}^i Q^i \hat{\vec{I}}^i\right). \tag{1.7}$$

The spin operators $\hat{\vec{S}} = \left(\hat{S}_x, \hat{S}_y, \hat{S}_z\right)^\intercal$ correspond to the NV centre. The nuclear spins are distinguished by the index i, each with spin operators $\hat{\vec{I}}^i = \left(\hat{I}_x^i, \hat{I}_y^i, \hat{I}_z^i\right)^\intercal$. At room temperature $D_g \approx 2.87\,\text{GHz}$ represents the axial, and $E_g \approx 0$ the non-axial zero field parameter [40]. The magnetic field is given by $\vec{B} = (B_\perp(t), 0, B_\parallel)^\intercal$, where the z-component, $B_\parallel$, is static and the x-component, $B_\perp(t)$, is commonly applied with a microwave (MW) frequency that is resonant with one of the NV spin transitions. γ_{nv} and γ_i are the gyromagnetic ratios of the NV centre and the i^{th} nuclear spin, respectively. The hyperfine coupling tensor is given by $\mathcal{A}^i$ and the quadrupolar interaction by $Q^i \approx 0$, thus we will neglect it hereafter.
As the NV spin state rapidly rotates around the z-axis (the frequency is dependent on D_g and $B_\parallel$), we can assume that any perpendicular hyperfine coupling averages out $\hat{\vec{S}}\mathcal{A}^i\hat{\vec{I}}^i \approx \hat{S}_z\vec{A}^i\hat{\vec{I}}^i$. This is called the secular approximation [41]. By applying it, we disregard the transverse components of the hyperfine tensor. In the following Hamiltonian, identity terms are also neglected as they corresponds to constant energy shifts. Thus,

$$H_{\text{nv}}/\hbar \approx D_g\hat{S}_z^2 + \gamma_{\text{nv}}\left(B_\parallel\hat{S}_z + B_\perp(t)\hat{S}_x\right) + \sum_{i=1}^{N_n}\left(\hat{S}_z\vec{A}^i\hat{\vec{I}}^i + \gamma_i\vec{B}\cdot\hat{\vec{I}}^i\right). \tag{1.8}$$

Writing the NV spin components out as matrices, it becomes clear how to go from a three to a two level system.

$$H_{\mathrm{nv}}/\hbar \approx D_g \left[\frac{1}{2}\begin{pmatrix} 1 & 0 & 0 \\ 0 & -1 & 0 \\ 0 & 0 & 1 \end{pmatrix} + \frac{\mathbb{I}}{2}\right] + \gamma_{\mathrm{nv}} B_{\parallel} \left[\frac{1}{2}\begin{pmatrix} 1 & 0 & 0 \\ 0 & -1 & 0 \\ 0 & 0 & -3 \end{pmatrix} + \frac{\mathbb{I}}{2}\right] + \frac{\gamma_{\mathrm{nv}} B_{\perp}(t)}{\sqrt{2}} \begin{pmatrix} 0 & 1 & 0 \\ 1 & 0 & 1 \\ 0 & 1 & 0 \end{pmatrix} + \sum_{i=1}^{N_n} \begin{pmatrix} 1 & 0 & 0 \\ 0 & 0 & 0 \\ 0 & 0 & -1 \end{pmatrix} \vec{A}^i \hat{\vec{I}}^i + \mathbb{I}\gamma_i \vec{B} \cdot \hat{\vec{I}}^i. \tag{1.9}$$

The term multiplied by $B_{\parallel}$ lifts the degeneracy between the $m_s = \pm 1$ states inducing the so-called Zeeman splitting. If the Zeeman splitting is large the $+1 \leftrightarrow 0$ -transition is far detuned from the $-1 \leftrightarrow 0$ -transition. Hence, each of them can be addressed independently. As the NV is initialised in $m_s = 0$ no population is expected to leak into the ± 1 -states in a decoherence-free model unless it is specifically addressed by the drive field $B_{\perp}$.
Let us consider the case, where the $B_{\perp}$-field is resonant with the $+1 \leftrightarrow 0$ -transition and the Zeeman splitting is sufficiently large. Now, the Hamiltonian can be simplified by abandoning all constant terms and only keeping the $m_s = 0$ and $m_s = +1$ levels.

$$H_{\mathrm{nv}}/\hbar \approx \left(D_g + \gamma_{\mathrm{nv}} B_{\parallel}\right) \frac{1}{2}\begin{pmatrix} 1 & 0 \\ 0 & -1 \end{pmatrix} + \gamma_{\mathrm{nv}} B_{\perp}(t) \frac{1}{\sqrt{2}} \begin{pmatrix} 0 & 1 \\ 1 & 0 \end{pmatrix} + \sum_{i=1}^{N_n} \begin{pmatrix} 1 & 0 \\ 0 & 0 \end{pmatrix} \vec{A}^i \hat{\vec{I}}^i + \mathbb{I}\gamma_i \vec{B} \cdot \hat{\vec{I}}^i. \tag{1.10}$$

Replacing the matrices by Pauli spin operators leads to the full Hamiltonian for the two level system of $m_s = 0$ and $m_s = +1$:

$$\begin{aligned} H_+/\hbar &= \frac{D_g + \gamma_{\mathrm{nv}} B_{\parallel}}{2} \hat{\sigma}_z + \frac{\gamma_{\mathrm{nv}} B_{\perp}(t)}{\sqrt{2}} \hat{\sigma}_x + \sum_{i=1}^{N_n} \left(\hat{\sigma}_{\uparrow} \vec{A}^i \hat{\vec{I}}^i + \gamma_i B_{\parallel} \hat{I}_z^i + \gamma_i B_{\perp}(t) \hat{I}_x^i \right), \\ &\text{with } \hat{\sigma}_{\uparrow} = \begin{pmatrix} 1 & 0 \\ 0 & 0 \end{pmatrix}, \end{aligned} \tag{1.11}$$

where $\hat{\vec{\sigma}}$ are the Pauli matrices [39].

A similar approximation can be made for $m_s = -1$, where the Hamiltonian equivalently reads

$$\begin{aligned} H_-/\hbar &= \frac{D_g - \gamma_{\mathrm{nv}} B_\parallel}{2}\hat{\sigma}_z + \frac{\gamma_{\mathrm{nv}} B_\perp(t)}{\sqrt{2}}\hat{\sigma}_x + \sum_{i=1}^{N_n}\left(\hat{\sigma}_\downarrow \vec{A}^i \hat{\vec{I}}^i + \gamma_i B_\parallel \hat{I}_z^i + \gamma_i B_\perp(t)\hat{I}_x^i\right), \\ \text{with } \hat{\sigma}_\downarrow &= \begin{pmatrix} 0 & 0 \\ 0 & 1 \end{pmatrix}. \end{aligned} \tag{1.12}$$

1.1.1.2 Unitary frame transformations

Sometimes the description of a system is simplified by transforming to a different frame of reference, e.g. the rotating frame, defined by the unitary operator V. If a qubit is spinning around the z-axis with a frequency ω, the frame in which it stands still is defined by $V = \exp(i\omega\hat{\sigma}_z t/2)$.
In general, we consider the transformed wavefunction $\left|\tilde{\phi}\right\rangle = V|\phi\rangle$. To derive the correct transformation for the Hamiltonian, we multiply the SE (Eq. (1.1)) with V.

$$\begin{aligned} V\left|\dot{\phi}\right\rangle &= -\frac{i}{\hbar}VH|\phi\rangle \\ &= -\frac{i}{\hbar}VHV^\dagger V|\phi\rangle \\ &= -\frac{i}{\hbar}\tilde{H}_0\left|\tilde{\phi}\right\rangle, \end{aligned} \tag{1.13}$$

where $\tilde{H}_0$ is the partially transformed Hamiltonian. To get the full expression, we have to compute the derivative of the transformed wavefunction using the chain rule:

$$\begin{aligned} \left|\dot{\tilde{\phi}}\right\rangle &= \dot{V}|\phi\rangle + V\left|\dot{\phi}\right\rangle \\ &= \dot{V}V^\dagger V|\phi\rangle - \frac{i}{\hbar}\tilde{H}_0\left|\tilde{\phi}\right\rangle \\ &= \left(\dot{V}V^\dagger - \frac{i}{\hbar}\tilde{H}_0\right)\left|\tilde{\phi}\right\rangle. \end{aligned} \tag{1.14}$$

The fully transformed Hamiltonian in the new frame is thus defined as

$$\begin{aligned} \tilde{H} &= VHV^\dagger + i\hbar\dot{V}V^\dagger \\ &= VHV^\dagger - i\hbar V\dot{V}^\dagger, \end{aligned} \tag{1.15}$$

where the equivalence of the second line can be shown by doing the same derivation starting from the Hermitian conjugate of the SE.

1.1.1.3 Imaginary Hamiltonian

The energy E of a quantum state $|\phi\rangle$ is given by

$$E|\phi\rangle = H|\phi\rangle. \tag{1.16}$$

As long as H is Hermitian, the Hamiltonian's eigenvalues and hence the energy will always be real. This property also means that a time-dependent wavefunction stays normalised when it evolves according to the SE (Eq. (1.1)).
Let us consider what happens to the quantum state if a constant imaginary Hamiltonian $H_i = -i\hbar\frac{\Gamma}{2}\mathbb{I}$ is applied according to Eq. (1.6).

$$\begin{aligned} |\phi(t)\rangle &= e^{-\frac{\Gamma}{2}t}|\phi(0)\rangle, \\ \langle\phi(t)|\phi(t)\rangle &= e^{-\Gamma t} < 1. \end{aligned} \tag{1.17}$$

This clearly describes a decay process with a lifetime of $\frac{1}{\Gamma}$. Yet, the loss of normalisation [42] makes this model unphysical. A better description of decay is the Lindblad master equation (Section 1.1.1.4). It makes use of the density function (Eq. (1.3)), which allows the representation of mixed states. However, it is also computationally more expensive. Considering a system as in Eq. (1.11) with one NV and N_n nuclear spins, the number of entries in the density matrix scales as $\upsilon_\rho = \upsilon_{|\phi\rangle}^2 = 2^{2(N_n+1)}$, i.e. more steeply than the number of entries in a state vector $\upsilon_{|\phi\rangle}$. As a result, a system with $N_n = 4$ nuclei, would need a density matrix with $\upsilon_\rho = 1024$ entries to describe it, or a state vector with $\upsilon_{|\phi\rangle} = 32$ entries. It becomes clear that, for larger systems, the imaginary Hamiltonian method is significantly less costly. We tested both for the project presented in Section 3.2.3. Ultimately, we chose the Lindblad master equation, as we resorted to a smaller system ($N_n = 3$).

1.1.1.4 Lindblad Master Equation

The most common decay channels for spin systems are dephasing and depolarisation [43]. Depolarisation describes the general loss of coherence along all axes. For a quantum system, this means that the state tends toward being completely mixed. In a Bloch sphere representation (see Fig. 1.1) the state vector, initially with unit length, ends up in a single point at the origin after the full decay. In solid state physics, this phenomenon is called spin-lattice relaxation, as it describes how the state returns to its natural orientation. The decay time is usually denoted as T_1.
Dephasing describes a process in which the coherence is lost along the x- and y-axis, but the z-axis component stays stable. The dynamics correspond to an ensemble of spins rotating

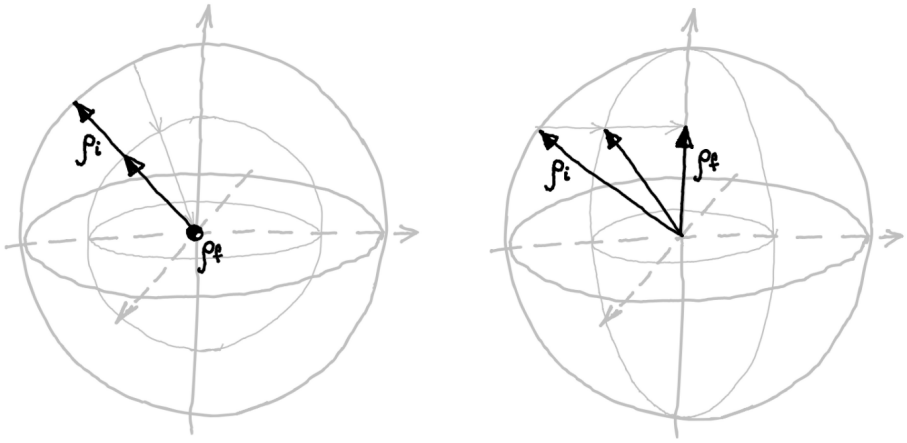

Fig. 1.1 Decay processes on the Bloch sphere from initial state ρ_i to final state ρ_f; (*left*) depolarisation, (*right*) dephasing.

around the z-axis, all with slightly different frequencies. In the rotating frame, the spins spread out over time. Consequently, the average state vector decreases further and further along x and y but stays stable along z as shown in Fig. 1.1. Dephasing is also called spin-spin relaxation when it is caused by surrounding spins influencing the local magnetic field along the z-axis. A spatially inhomogeneous magnetic field that is applied to an ensemble along z leads to a similar effect. The decay rate characterising the overall dephasing is denoted by T_2^*.
Dephasing and depolarisation, as well as other types of noise can be described using the Lindblad master equation [39]:

$$\dot{\rho} = -\frac{i}{\hbar}[H,\rho] + \sum_i \frac{\Gamma_i}{2}\left(2L_i\rho L_i^\dagger - L_i^\dagger L_i\rho - \rho L_i^\dagger L_i\right). \tag{1.18}$$

The first term resembles the von Neumann equation (Eq. (1.2)). The second term which includes the Lindblad operators L_i and decay rates Γ_i describes the decay of the system.
For a two-level system, the Lindblad operator for the dephasing is $L_\varphi = \frac{\hat{\sigma}_z}{2}$ with the corresponding rate $\Gamma_\varphi = \frac{1}{T_2^*}$ [43]. In general, $T_2^* \leq 2T_1$, as depolarisation inherently includes a dephasing component. For the depolarisation, one needs to take into account two Lindblad operators $L_\pm = \frac{\hat{\sigma}_\pm}{2} = (\hat{\sigma}_x \pm i\hat{\sigma}_y)/4$, with equal decay rates $\Gamma_\pm = \frac{1}{T_1}$. An in depth calculation for NV centres is given in reference [44]. Similarly, the exponential relaxation from one state $|\phi_1\rangle$ into another $|\phi_0\rangle$ (f.e. the ground state, or due to thermal excitations) is expressed through the Lindbladian $L_s = |\phi_0\rangle\langle\phi_1|$ [43]. This method is applied in the work presented in Section 3.2.3.

1.1.1.5 Rate Equations

One way to simplify the master equation is through rate equations. Here, off-diagonal elements of the density matrix are ignored and we only consider the probabilities of being in a specific state. Those correspond to the diagonal entries of the density function [45, 46].
As an example, we will go through the decay of a qubit from state $|e\rangle$ to state $|g\rangle$. The corresponding Lindbladian is denoted by $L = |g\rangle\langle e|$ with decay rate Γ_s. The master equation can be written as

$$\dot{\rho} = -\frac{i}{\hbar}[H,\rho] + \mathbb{L}(L,\Gamma_s). \tag{1.19}$$

We will write the density matrix in the following way.

$$\rho = \begin{pmatrix} p_g & \rho_{eg} \\ \rho_{ge} & p_e \end{pmatrix}, \tag{1.20}$$

where the diagonal elements p_g and p_e give the probability of being in the respective state. Now let us look at the effect of the Lindblad term of the master equation.

$$\begin{aligned}
\mathbb{L}(L,\Gamma_s) &= \frac{\Gamma_s}{2}\left(2|g\rangle\langle e|\rho|e\rangle\langle g| - |e\rangle\langle g|g\rangle\langle e|\rho - \rho|e\rangle\langle g|g\rangle\langle e|\right) \\
&= \frac{\Gamma_s}{2}\left(2p_e|g\rangle\langle g| - |e\rangle\langle e|e\rangle\rho_{eg}\langle g| - |e\rangle\langle e|e\rangle p_e\langle e| - |g\rangle\rho_{ge}\langle e|e\rangle\langle e| - |e\rangle p_e\langle e|e\rangle\langle e|\right) \\
&= \frac{\Gamma_s}{2}\left(2p_e|g\rangle\langle g| - \rho_{eg}|e\rangle\langle g| - \rho_{ge}|g\rangle\langle e| - 2p_e|e\rangle\langle e|\right) \\
&= \begin{pmatrix} \Gamma_s p_e & -\frac{\Gamma_s}{2}\rho_{eg} \\ -\frac{\Gamma_s}{2}\rho_{ge} & -\Gamma_s p_e \end{pmatrix}.
\end{aligned} \tag{1.21}$$

The evolution of the probabilities can now be written as rate equations

$$\begin{aligned}
\dot{p}_g &= \Gamma_s p_e, \\
\dot{p}_e &= -\Gamma_s p_e
\end{aligned} \tag{1.22}$$

or more concisely as

$$\frac{d\mathbf{p}}{dt} = \mathbf{\Gamma}\cdot\mathbf{p}, \tag{1.23}$$

with

$$\mathbf{p} = \begin{pmatrix} p_g \\ p_e \end{pmatrix}, \qquad \mathbf{\Gamma} = \begin{pmatrix} 0 & \Gamma_s \\ 0 & -\Gamma_s \end{pmatrix}. \tag{1.24}$$

As this approximation only includes state populations, it completely disregards the coherence of the system. Whether the system was in a pure or mixed state cannot be reconstructed. As opposed to the Lindblad master equation, the rate equations do not preserve the phase of the state. Hence, they cannot include the effects of dephasing: Dephasing does not change the state population, it only destroys their coherence. We used this technique for preliminary calculations in the project described in Section 3.1.3. A very similar model is presented in the example below.
Rate equations can also be used to approximate the evolution of expectation values starting from the Heisenberg picture [47, 48], where the evolution of an operator $\hat{O}$ is described by

$$\frac{d\hat{O}}{dt} = \frac{i}{\hbar}[H, \hat{O}] + \frac{\partial \hat{O}}{\partial t}. \tag{1.25}$$

Applying this approach to a quantum system coupled to a resonant field, eventually leads to the quantum-Langevin equation [49]. It models the system's macroscopic properties including the evolution of the field amplitude, i.e. the expectation value of the field's creation operator. The quantum-Langevin equation finds its application in Section 1.1.2.

Example: Optical Manipulation of NV centres Let us consider an NV centre, with seven energy levels depicted in Fig. 1.2 [50]. The ground state triplet $|g, 0/\pm 1\rangle$ and the excited state triplet $|e, 0/\pm 1\rangle$ each contain states with spin quantum numbers $m_s = 0/\pm 1$. The intermediate state singlet $|m\rangle$ has zero spin $m_s = 0$. When left to evolve freely the NV centre will decay into a mixture of its ground states. This is described through the transition rates Γ_{nm} from state n to state m and depolarisation with decay rate $1/T_1$. A laser is applied with an amplitude $A(t)$ and coupling k. Using the rate equations, we can find the occupation of the different levels dependent on the time and strength of the laser. In the experiment such laser pulses are used to initialise the population in the $|g, 0\rangle$-state.
The corresponding rate equation reads [51]

$$\frac{d\mathbf{p}}{dt} = \mathbf{\Gamma} \cdot \mathbf{p}, \tag{1.26}$$

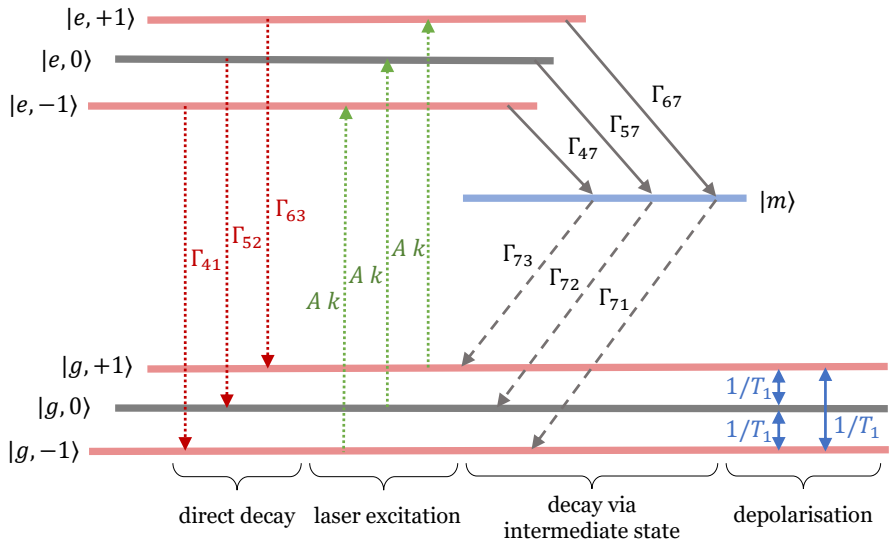

Fig. 1.2 Decay channels in the NV centre energy level diagram. The energy levels labelled $|g,0/\pm1\rangle$ represent the ground state triplet, $|e,0/\pm1\rangle$ the excited state triplet, and $|m\rangle$ the intermediate spin state singlet.

with

$$\mathbf{p} = \left(p_{g,-1},\ p_{g,0},\ p_{g,+1},\ p_{e,-1},\ p_{e,0},\ p_{e,+1},\ p_m\right)^{\mathsf{T}},$$

$$\mathbf{\Gamma} = \begin{pmatrix} -A(t)k - \frac{1}{T_1} & \frac{1}{2T_1} & \frac{1}{2T_1} & \Gamma_{41} & 0 & 0 & \Gamma_{71} \\ \frac{1}{2T_1} & -A(t)k - \frac{1}{T_1} & \frac{1}{2T_1} & 0 & \Gamma_{52} & 0 & \Gamma_{72} \\ \frac{1}{2T_1} & \frac{1}{2T_1} & -A(t)k - \frac{1}{T_1} & 0 & 0 & \Gamma_{53} & \Gamma_{73} \\ A(t)k & 0 & 0 & -\Gamma_{41} - \Gamma_{47} & 0 & 0 & 0 \\ 0 & A(t)k & 0 & 0 & -\Gamma_{52} - \Gamma_{57} & 0 & 0 \\ 0 & 0 & A(t)k & 0 & 0 & -\Gamma_{63} - \Gamma_{67} & 0 \\ 0 & 0 & 0 & \Gamma_{47} & \Gamma_{57} & \Gamma_{67} & -\Gamma_{71} - \Gamma_{72} - \Gamma_{73} \end{pmatrix}. \tag{1.27}$$

Similar expressions have been used in reference [52] to determine the best laser pulse shapes to initialise NV centres.

To also model the dynamics in the ground state triplet caused by the application of magnetic fields, we can use $\mathbf{p}$ to create an initial state and continue the propagation with the von Neumann equation (Eq. (1.2)). An appropriate Hamiltonian for this system would consist of

a ground state Hamiltonian H_g and an excited state Hamiltonian H_e:

$$\begin{aligned} H_g &= \hbar D_g \left(\hat{S}_z^2 - \frac{2}{3}\mathbb{I} \right) + \hbar \gamma_{\mathrm{nv}} \vec{B} \cdot \hat{\vec{S}}, \\ H_e &= \hbar \Delta_e \mathbb{I} + \hbar D_e \left(\hat{S}_z^2 - \frac{2}{3}\mathbb{I} \right) + \hbar \gamma_{\mathrm{nv}} \vec{B} \cdot \hat{\vec{S}}, \\ \vec{B} &= \begin{pmatrix} B_\perp(t) \\ 0 \\ B_\parallel \end{pmatrix}, \end{aligned} \tag{1.28}$$

where $\hat{\vec{S}} = \left(\hat{S}_x, \hat{S}_y, \hat{S}_z \right)^\mathsf{T}$. $D_g = 2.87\,\mathrm{GHz}$ and $D_e = 1.42\,\mathrm{GHz}$ represent the ground and excited state zero-field splittings respectively [40]. $\Delta_{e/m}$ is the energy difference between the ground state triplet and the excited state triplet/intermediate state. The static magnetic field $B_\parallel$ is accompanied by an oscillating magnetic field $B_\perp(t) = 2A_B \cos(\omega_{\mathrm{mw}} t + \phi_B)$, with an amplitude A_B, phase ϕ_B, and frequency ω_{mw}, usually at resonance with one of the ground state transitions from 0 to ±1. The two Hamiltonians can then be combined into H_{full}:

$$H_{\mathrm{full}} = \begin{pmatrix} & & & 0 & 0 & 0 & 0 \\ & H_g & & 0 & 0 & 0 & 0 \\ & & & 0 & 0 & 0 & 0 \\ 0 & 0 & 0 & & & & 0 \\ 0 & 0 & 0 & & H_e & & 0 \\ 0 & 0 & 0 & & & & 0 \\ 0 & 0 & 0 & 0 & 0 & 0 & \hbar\Delta_m \end{pmatrix}. \tag{1.29}$$

For simplicity, one may only consider H_g or drop the dependence of the excited states on the magnetic field, as those dynamics are not expected to play a role in the readout. Other approaches to represent ODMR measurements using rate equations have been introduced in references [53, 54].

1.1.1.6 Kraus Operators

Different techniques have been discussed to model a range of physical effects on the evolution of quantum states. Kraus operators represent a mathematically rigorous way to describe any quantum operation. They can be used to derive the Lindblad master equation but also represent processes that go beyond what has been described so far in this thesis, such as measurements [43].

We only give a brief introduction to Kraus operators with a definition and an example. Still,

Kraus operators are covered because they present a suitable alternative for modelling instant polarisation without loss of normalisation. For their broader field of application and more details please refer to references [43, 55, 56].
The evolution of the density matrix $\rho \to \rho'$ is given by

$$\rho' = \sum_j K_j \rho K_j^\dagger, \tag{1.30}$$

where K_j is a set of Kraus operators which is normalised such that $\sum_j K_j^\dagger K_j = \mathbb{I}$. Unitary time evolution given in Eq. (1.2) according to the propagator $U(t)$ is easily represented by the single Kraus operator $K = U(t)$. As a more elaborate example, let us consider the operators for the polarisation of a single qubit.

Example: Qubit Polarisation The initial density matrix of the qubit is defined as

$$\rho = \begin{pmatrix} \rho_g & \rho_{eg} \\ \rho_{ge} & \rho_e \end{pmatrix}. \tag{1.31}$$

During the polarisation process, all the population is transferred into the ground state. Hence, we expect the density matrix to evolve into ρ'.

$$\rho' = \begin{pmatrix} \rho_g + \rho_e & 0 \\ 0 & 0 \end{pmatrix}. \tag{1.32}$$

To achieve this we define the operators

$$\begin{aligned} K_1 &= \begin{pmatrix} 1 & 0 \\ 0 & 0 \end{pmatrix}, \\ K_2 &= \begin{pmatrix} 0 & 1 \\ 0 & 0 \end{pmatrix}, \\ K_1^\dagger K_1 + K_2^\dagger K_2 &= \begin{pmatrix} 1 & 0 \\ 0 & 0 \end{pmatrix} + \begin{pmatrix} 0 & 0 \\ 0 & 1 \end{pmatrix} = \begin{pmatrix} 1 & 0 \\ 0 & 1 \end{pmatrix}, \end{aligned} \tag{1.33}$$

which satisfy the normalisation condition and lead to the expected result:

$$\begin{aligned}\rho' &= K_1\rho K_1^\dagger + K_2\rho K_2^\dagger \\ &= \begin{pmatrix} \rho_g & 0 \\ 0 & 0 \end{pmatrix} + \begin{pmatrix} \rho_e & 0 \\ 0 & 0 \end{pmatrix}.\end{aligned} \tag{1.34}$$

These operators can be extended to describe the polarisation of one qubit in an (N_n+1)-qubit system such that $K_j^{N_n} = K_j \otimes \mathbb{I}_2^{N_n}$, while maintaining the coherence of the other N_n qubits. Hence, these operators can be used to describe the initialisation of an NV centre in a quantum register of nuclear spins used, for example, in quantum error correction protocols [57].

1.1.2 Electron Spin Inside a Cavity

The following model is used to describe the experiment in Section 3.2. It represents an electron spin inside a MW cavity coupled to a number of nuclear spins. The derivation starts by taking into account the quantum properties of the MW field. Similar models have been used to described quantum electrodynamic systems [58], but also NV centres [59], and electron spin resonance setups [60]. A schematic of the system is provided in Fig. 1.3.

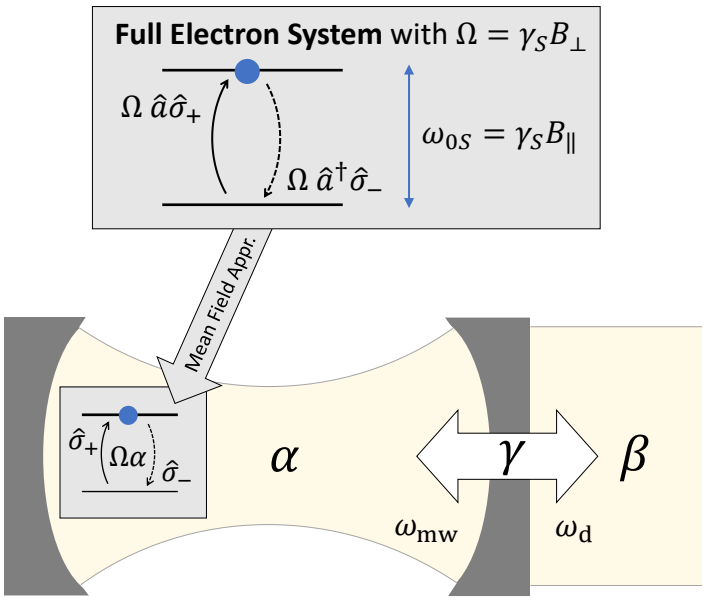

Fig. 1.3 The setup consisting of an electron qubit inside a cavity and an external drive. We start with the full electron system which is simplified later using a mean field approximation. The symbols are introduced throughout the section.

1.1.2.1 The Jaynes-Cummings Model

We start by considering a single electron spin in a magnetic field. The electron spin has a magnetic moment that can be described through the operators $\hat{\vec{M}}$.

$$\hat{\vec{M}} = -\frac{\hbar}{2}\gamma_S \hat{\vec{\sigma}}, \tag{1.35}$$

where $\hat{\vec{\sigma}} = (\hat{\sigma}_x, \hat{\sigma}_y, \hat{\sigma}_z)^\intercal$ is the vector of Pauli matrices and γ_S the electron's gyromagnetic ratio.
The magnetic field is composed of two parts: The static component $B_\parallel$ points along z and a microwave field with amplitude $B_\perp \ll B_\parallel$ oscillating along x. The microwave field has a frequency ω_{mw} and is quantised through the creation and annihilation operators $\hat{a}^\dagger$ and $\hat{a}$.[1] The full magnetic field is given by

$$\hat{\vec{B}} = \begin{pmatrix} B_\perp(\hat{a}+\hat{a}^\dagger) \\ 0 \\ B_\parallel \end{pmatrix}. \tag{1.36}$$

The Hamiltonian of the microwave field H_{MW} accounts for its energy and is given by

$$H_{MW}/\hbar = \omega_{\mathrm{mw}} \hat{a}^\dagger \hat{a}. \tag{1.37}$$

The interaction of the field with the electron spin is described by a second component of the Hamiltonian H_{e-B}:

$$\begin{aligned} H_{e-B} &= -\hat{\vec{M}} \cdot \hat{\vec{B}} \\ &= \frac{\hbar}{2}\gamma_S \left(B_\perp \left(\hat{a} + \hat{a}^\dagger \right) \hat{\sigma}_x + B_\parallel \hat{\sigma}_z \right). \end{aligned} \tag{1.38}$$

We consider the rotating frame of the microwave given by $V_r = \exp\left(i\omega_{\mathrm{mw}} \left(\hat{a}^\dagger \hat{a} + \frac{\hat{\sigma}_z}{2} \right) t \right)$ and define the electron spin resonance frequency $\omega_{0S} = \gamma_S B_\parallel$. The resulting Hamiltonian components read:

$$\begin{aligned} \tilde{H}_{MW}/\hbar &= H_{MW}/\hbar, \\ \tilde{H}_{e-B}/\hbar &= \frac{1}{2}\gamma_S B_\perp \left(\hat{a} e^{-i\omega_{\mathrm{mw}} t} + \hat{a}^\dagger e^{+i\omega_{\mathrm{mw}} t} \right) \cdot \left(\hat{\sigma}_+ e^{+i\omega_{\mathrm{mw}} t} + \hat{\sigma}_- e^{-i\omega_{\mathrm{mw}} t} \right) + \frac{1}{2}\omega_{0S} \hat{\sigma}_z, \\ -iV_r \dot{V}_r^\dagger &= -\omega_{\mathrm{mw}} \frac{\hat{\sigma}_z}{2} - \omega_{\mathrm{mw}} \hat{a}^\dagger \hat{a}, \end{aligned} \tag{1.39}$$

[1] A full derivation of the quantised electromagnetic fields is given in reference [61].

where $\hat{\sigma}_\pm = \frac{1}{2}(\hat{\sigma}_x \pm i\hat{\sigma}_y)$ are the ladder operators. The full Hamiltonian in the rotating frame becomes

$$\begin{aligned}\tilde{H}/\hbar = \omega_{\mathrm{mw}}\hat{a}^\dagger\hat{a} - \omega_{\mathrm{mw}}\hat{a}^\dagger\hat{a} + \frac{1}{2}\omega_{0S}\hat{\sigma}_z - \frac{1}{2}\omega_{\mathrm{mw}}\hat{\sigma}_z \\ + \frac{1}{2}\gamma_S B_\perp\Big(\hat{a}\Big(\hat{\sigma}_+ e^{-i(\omega_{\mathrm{mw}}-\omega_{\mathrm{mw}})t} + \hat{\sigma}_- e^{-i(\omega_{\mathrm{mw}}+\omega_{\mathrm{mw}})t}\Big) + \\ \hat{a}^\dagger\Big(\hat{\sigma}_+ e^{+i(\omega_{\mathrm{mw}}+\omega_{\mathrm{mw}})t} + \hat{\sigma}_- e^{+i(\omega_{\mathrm{mw}}-\omega_{\mathrm{mw}})t}\Big)\Big).\end{aligned} \tag{1.40}$$

We now apply the rotating wave approximation (RWA), i.e. assume that terms with frequency $\omega = 2\omega_{\mathrm{mw}}$ are oscillating much more quickly than everything else and will average out [39]. After dropping these counter rotating terms, we get

$$\tilde{H}/\hbar = \frac{\gamma_S B_\perp}{2}\left(\hat{a}\hat{\sigma}_+ + \hat{a}^\dagger\hat{\sigma}_-\right) + \frac{1}{2}(\omega_{0S} - \omega_{\mathrm{mw}})\hat{\sigma}_z. \tag{1.41}$$

By introducing the detuning $\Delta = \omega_{0S} - \omega_{\mathrm{mw}}$ and the amplitude $\Omega = \gamma_S B_\perp$, we arrive at the familiar form of the Jaynes-Cummings model

$$\tilde{H}/\hbar = \frac{\Omega}{2}\left(\hat{a}\hat{\sigma}_+ + \hat{a}^\dagger\hat{\sigma}_-\right) + \Delta\frac{\hat{\sigma}_z}{2}. \tag{1.42}$$

By transforming back into the lab frame using $V_r^\dagger$, we get

$$H/\hbar = \omega_{\mathrm{mw}}\hat{a}^\dagger\hat{a} + \omega_{0S}\frac{\hat{\sigma}_z}{2} + \frac{\Omega}{2}\left(\hat{a}\hat{\sigma}_+ + \hat{a}^\dagger\hat{\sigma}_-\right). \tag{1.43}$$

1.1.2.2 Including the Drive

Next we consider the electron spin to be inside a resonator. The MW field is coupled to an external drive which acts like a strongly excited coherent state with a slowly varying envelope $\beta(t)$. As a result, the field of the drive can be treated as a classical component in the Hamiltonian drive term H_d.

$$H_d/\hbar \approx \left(\hat{a} + \hat{a}^\dagger\right)\cdot\left(\beta(t)e^{+i\omega_{\mathrm{d}}t} + \beta^*(t)e^{-i\omega_{\mathrm{d}}t}\right). \tag{1.44}$$

If we consider the rotating frame of the drive i.e. $V_d = \exp\left(i\omega_\mathrm{d}\left(\hat{a}^\dagger\hat{a} + \frac{\hat{\sigma}_z}{2}\right)t\right)$, we can make the same case as before for another RWA.

$$\begin{aligned}\tilde{H}_d/\hbar &= \left(\hat{a}e^{-i\omega_\mathrm{d}t} + \hat{a}^\dagger e^{+i\omega_\mathrm{d}t}\right)\cdot\left(\beta(t)e^{+i\omega_\mathrm{d}t} + \beta^*(t)e^{-i\omega_\mathrm{d}t}\right)\\ &= \hat{a}\left(\beta^*(t) + \beta(t)e^{-2i\omega_\mathrm{d}t}\right) + \hat{a}^\dagger\left(\beta^*(t)e^{+2i\omega_\mathrm{d}t} + \beta(t)\right)\\ &\approx \hat{a}\beta^*(t) + \hat{a}^\dagger\beta(t),\\ -iV_d\dot{V}_d^\dagger &= -\omega_\mathrm{d}\hat{a}^\dagger\hat{a} - \omega_\mathrm{d}\frac{\hat{\sigma}_z}{2}.\end{aligned} \tag{1.45}$$

Defining the cavity detuning $\Delta_\mathrm{mw} = \omega_\mathrm{mw} - \omega_\mathrm{d}$ and the detuning from the electron spin's resonant frequency $\Delta_\mathrm{es} = \omega_{0S} - \omega_\mathrm{d}$, the full Hamiltonian (dropping the tilde) in the drive's rotating frame then reads

$$H/\hbar = \Delta_\mathrm{mw}\hat{a}^\dagger\hat{a} + \Delta_\mathrm{es}\frac{\hat{\sigma}_z}{2} + \frac{\Omega}{2}\left(\hat{a}\hat{\sigma}_+ + \hat{a}^\dagger\hat{\sigma}_-\right) + \hat{a}\beta^*(t) + \hat{a}^\dagger\beta(t). \tag{1.46}$$

Please note that the term multiplied by $\Omega/2$ stays the same in this frame, which is why we have not shown the explicit transformation. This Hamiltonian now corresponds to the full electron and cavity model shown in Fig. 1.3.

1.1.2.3 Connecting the Rabi Frequency and the Drive

To investigate the effect of the drive on the electron spin's Rabi frequency, we first assume, that the field inside the cavity can be described by a coherent bosonic mode of amplitude $\alpha(t) = \langle\hat{a}\rangle(t)$. In principle, we could now apply a mean field approximation. However, first, we need to established the connection between the field inside the cavity and the drive. Hence, we only shift into the reference frame centred on the field amplitude i.e. displace the system by $-\alpha(t)$. This frame is defined by the displacement operator $\hat{D}(-\alpha) = \exp\left(-\left(\alpha(t)\hat{a}^\dagger - \alpha^*(t)\hat{a}\right)\right)$. Please note that the hatless D refers to $\hat{D}(-\alpha)$ from now on for legibility.
The following relations are useful to reproduce the algebra below:

$$\begin{aligned}\hat{D}^\dagger(-\alpha) &= \hat{D}(\alpha),\\ D\hat{a}^\dagger\hat{a}D^\dagger &= \hat{a}^\dagger\hat{a} + \hat{a}^\dagger\alpha(t) + \hat{a}\alpha^*(t) + |\alpha(t)|^2,\\ D\hat{a}D^\dagger &= \hat{a} + \alpha(t),\\ D\hat{a}^\dagger D^\dagger &= \hat{a}^\dagger + \alpha^*(t).\end{aligned} \tag{1.47}$$

The transformed Hamiltonian is given by

$$\begin{aligned} H_\alpha/\hbar =& DHD^\dagger/\hbar - iD\dot{D}^\dagger \\ =& \Delta_{\mathrm{mw}}\left(\hat{a}^\dagger\hat{a} + \alpha(t)\hat{a}^\dagger + \alpha^*(t)\hat{a} + |\alpha(t)|^2\right) \\ &+ \frac{\Omega}{2}\left((\hat{a}+\alpha(t))\hat{\sigma}_+ + (\hat{a}^\dagger+\alpha^*(t))\hat{\sigma}_-\right) \\ &+ \beta^*(t)(\hat{a}+\alpha(t)) + \beta(t)(\hat{a}^\dagger+\alpha^*(t)) + \Delta_{\mathrm{es}}\frac{\hat{\sigma}_z}{2} \\ &- i(\dot{\alpha}(t)\hat{a}^\dagger - \dot{\alpha}^*(t)\hat{a}). \end{aligned} \tag{1.48}$$

Rearranging the terms shows that the original Hamiltonian is maintained but some additional terms are introduced:

$$\begin{aligned} H_\alpha/\hbar =& \Delta_{\mathrm{mw}}\hat{a}^\dagger\hat{a} + \frac{\Omega}{2}\left(\hat{a}\hat{\sigma}_+ + \hat{a}^\dagger\hat{\sigma}_-\right) + \Delta_{\mathrm{es}}\frac{\hat{\sigma}_z}{2} \\ &+ \hat{a}\left(\Delta_{\mathrm{mw}}\alpha^*(t) + \beta^*(t) + i\dot{\alpha}^*(t)\right) + \hat{a}^\dagger\left(\Delta_{\mathrm{mw}}\alpha(t) + \beta(t) - i\dot{\alpha}(t)\right) \\ &+ \frac{\Omega}{2}\left(\alpha(t)\hat{\sigma}_+ + \alpha^*(t)\hat{\sigma}_-\right) \\ &+ \Delta_{\mathrm{mw}}|\alpha(t)|^2 + \beta^*(t)\alpha(t) + \beta\alpha^*(t). \end{aligned} \tag{1.49}$$

The first line includes terms from the Hamiltonian's original form in Eq. (1.46). The second line represents the influence of the drive and detuning on the MW field. The third line gives the mean field contribution of the MW field to the electron spin dynamics. The last line, however, only contains terms which result in a global phase and disappear during normalisation. Hence, they will be dropped in the next step.

To connect the field amplitude $\alpha(t)$ to the drive $\beta(t)$, we introduce the quantum-Langevin equation [49]. It represents the expectation value of the field $\alpha(t)$, showing that it behaves like a simple harmonic oscillator $\alpha(t)$ which is damped and driven by the coupling to another harmonic oscillator with amplitude $\beta(t)$. The coupling is characterised by the loss rate γ and detuning Δ_{mw}. A full quantum-mechanical derivation starting from the Heisenberg picture (see Eq. (1.25)) can be found in Chapter 11 of reference [48] or in Chapter 10 of reference [47][2]. The quantum-Langevin equation is given by

$$\Delta_{\mathrm{mw}}\alpha(t) + \beta(t) - i\dot{\alpha}(t) = i\gamma\alpha(t). \tag{1.50}$$

[2]Please note that the drive is defined differently here but the principles are the same.

The terms in line two of Eq. (1.49) partially cancel according to Eq. (1.50) and the Hamiltonian becomes

$$\begin{aligned} H_\alpha/\hbar = \Delta_{\mathrm{mw}}\hat{a}^\dagger\hat{a} + \frac{\Omega}{2}(\hat{a}\hat{\sigma}_+ + \hat{a}^\dagger\hat{\sigma}_-) + \Delta_{\mathrm{es}}\frac{\hat{\sigma}_z}{2} \\ + \frac{\Omega}{2}\left(\alpha(t)\hat{\sigma}_+ + \alpha^*(t)\hat{\sigma}_-\right) + i\gamma(\alpha(t)\hat{a}^\dagger - \alpha^*(t)\hat{a}). \end{aligned} \tag{1.51}$$

The second term shows how the energy of the system changes depending on the coupling to the resonator $\Omega/2$ for the few photon regime. However, we will now assume that the field inside the cavity is strong enough to be treated classically. First, we transform back into the drive frame using $D^\dagger$, then the operator $\hat{a}$ is replaced with its expectation value $\hat{a} \to \langle\hat{a}\rangle + (\hat{a} - \langle\hat{a}\rangle) = \alpha + \delta\alpha \approx \alpha$. As a result, all terms that only include creation and annihilation operators of the MW field turn into energy offsets, leaving only

$$H/\hbar = \frac{\Omega}{2}\left(\alpha(t)\hat{\sigma}_+ + \alpha^*(t)\hat{\sigma}_-\right) + \Delta_{\mathrm{es}}\frac{\hat{\sigma}_z}{2}. \tag{1.52}$$

Delaying the mean field approximation until now allowed us to established the connection to the quantum-Langevin equation (Eq. (1.50)) and maintain the information about the coupling between the drive and the field.

The goal of the next steps is to find an expression for the Rabi frequency components along the x- and y-direction $\vec{\Omega} = (\Omega_x, \Omega_y)^\intercal$ dependent on $\alpha(t)$. We replace $\alpha(t)$ with $\alpha(t) = \mathrm{Re}[\alpha] + i\,\mathrm{Im}[\alpha]$ and substitute the ladder operators $\hat{\sigma}_\pm$ with their definition in terms of Pauli matrices, i.e. $\hat{\sigma}_\pm = \frac{1}{2}(\hat{\sigma}_x \pm i\hat{\sigma}_y)$. The Hamiltonian becomes

$$\begin{aligned} H/\hbar &= \frac{\Omega}{2}\Big(\mathrm{Re}[\alpha]\hat{\sigma}_x - \mathrm{Im}[\alpha]\hat{\sigma}_y\Big) + \Delta_{\mathrm{es}}\frac{\hat{\sigma}_z}{2} \\ &= \frac{\Omega_x}{2}\hat{\sigma}_x + \frac{\Omega_y}{2}\hat{\sigma}_y + \frac{\Delta_{\mathrm{es}}}{2}\hat{\sigma}_z, \end{aligned} \tag{1.53}$$

clearly showing the directional Rabi frequency is given by $(\Omega_x, \Omega_y)^\intercal = \Omega(\mathrm{Re}[\alpha], -\mathrm{Im}[\alpha])^\intercal$. To find its dependence on the drive, we rearrange Eq. (1.50) for $\dot{\alpha}(t)$ obtaining

$$\dot{\alpha}(t) = -\gamma\left(\frac{i\beta(t)}{\gamma} + \alpha(t)\right) - i\Delta_{\mathrm{mw}}\alpha(t). \tag{1.54}$$

This form is split into a system of two equations, considering the real and imaginary part:

$$\begin{aligned} \mathrm{Re}[\dot{\alpha}] = \frac{d\,\mathrm{Re}[\alpha]}{dt} &= \gamma\left(\frac{\mathrm{Im}[\beta]}{\gamma} - \mathrm{Re}[\alpha]\right) + \Delta_{\mathrm{mw}}\,\mathrm{Im}[\alpha], \\ -\mathrm{Im}[\dot{\alpha}] = -\frac{d\,\mathrm{Im}[\alpha]}{dt} &= \gamma\left(\frac{\mathrm{Re}[\beta]}{\gamma} + \mathrm{Im}[\alpha]\right) + \Delta_{\mathrm{mw}}\,\mathrm{Re}[\alpha]. \end{aligned} \tag{1.55}$$

Multiplying the above by the Rabi frequency and rewriting the drive as $\Omega\beta/\gamma = d\exp(i\phi) = d(\cos\phi + i\sin\phi)$, this becomes

$$\begin{aligned} \dot{\Omega}_x &= \gamma(d\sin\phi - \Omega_x) - \Delta_{\mathrm{mw}}\Omega_y, \\ \dot{\Omega}_y &= \gamma(d\cos\phi - \Omega_y) + \Delta_{\mathrm{mw}}\Omega_x. \end{aligned} \tag{1.56}$$

This system of equations represents a more practical form of Eq. (1.50). It shows how the rescaled drive d with phase ϕ influences the Rabi frequency and how the x- and y-directions become coupled in the presence of a drive detuning Δ_{mw}. In combination with Eq. (1.53) these equations provide a concise description of the system.

1.1.2.4 Coupling to Nuclear Spins

Nuclear spins interact with the magnetic field through their magnetic moment $\hat{\vec{M}}_I$ as described in Section 1.1.2.1. For a spin-half nuclear spin, the magnetic moment is given by

$$\hat{\vec{M}}_I = -\frac{\hbar}{2}\gamma_I\hat{\vec{I}}, \tag{1.57}$$

where $\hat{\vec{I}}$ is the usual set of Pauli operators[3] and γ_I the nuclear gyromagnetic ratio. As the gyromagnetic ratio of the nuclear spin is a factor thousand smaller than that of an electron spin, the coupling between the microwave field and the nucleus is negligible, leaving

$$H_I/\hbar = \frac{\omega_L}{2}\hat{I}_z + \hat{\vec{\sigma}}\mathcal{A}\hat{\vec{I}}, \tag{1.58}$$

where $\omega_L = \gamma_I B_{\|}$ is the nuclear Larmor frequency. The second term represents the hyperfine coupling [62] caused by the interaction of the electron spin's magnetic moment with the magnetic field of the nuclear spin. $\mathcal{A}$ is the rank 2 hyperfine tensor. It can be calculated using the dipolar interaction and hence depends on the magnetic moments of electron spin and nucleus, and their respective position in the crystal. The hyperfine coupling could also be

[3] To describe a nuclear spin with a different spin quantum number, $\hbar\hat{\vec{I}}/2$ should be replaced with the respective spin operator.

affected by the Fermi contact interaction, but this effect is negligible in the cases discussed in this thesis [63].
As the nucleus rotates around $B_{||}$ much more slowly than the electron spin, one can drop the hyperfine components perpendicular to the electron spin's axis as they will average out. This assumption is known as the "secular" approximation [64] and explained in Section 1.1.1.1. The updated Hamiltonian for the nucleus reads

$$H_I/\hbar \approx \frac{\omega_L}{2}\hat{I}_z + \hat{\sigma}_z\left(A_{zx}\hat{I}_x + A_{zy}\hat{I}_y + A_{zz}\hat{I}_z\right). \tag{1.59}$$

Assuming the interaction between nuclei is negligible and they are of the same species, this can be expanded to N_n nuclei:

$$H_I^n/\hbar = \frac{\omega_L}{2}\sum_i^{N_n}\hat{I}_z^i + \hat{\sigma}_z\sum_i^{N_n}\left(A_{zx}^i\hat{I}_x^i + A_{zy}^i\hat{I}_y^i + A_{zz}^i\hat{I}_z^i\right), \tag{1.60}$$

where the index i represents the different nuclei.
In the rotating frame of the drive all nuclear terms stay the same. Hence we can combine H_I^n with Eq. (1.53) to give the full system Hamiltonian:

$$H/\hbar = \frac{\Omega_x}{2}\hat{\sigma}_x + \frac{\Omega_y}{2}\hat{\sigma}_y + \frac{\Delta_{\text{es}}}{2}\hat{\sigma}_z + \frac{\omega_L}{2}\sum_i^{N_n}\hat{I}_z^i + \hat{\sigma}_z\sum_i^{N_n}\left(A_{zx}^i\hat{I}_x^i + A_{zy}^i\hat{I}_y^i + A_{zz}^i\hat{I}_z^i\right). \tag{1.61}$$

1.2 Atomic Condensates

1.2.1 Introduction

> We can cool down [atoms] and when we reach the point where the de Broglie waves overlap, [...] they become a kind of quantum soup of wave packets.
>
> *Wolfgang Ketterle*

Wolfgang Ketterle described Bose Einstein Condensates (BECs) as a quantum soup to his beginners class at MIT. To complete this image it should be noted that BECs are a state of matter that is usually associated with a large number of indistinguishable bosons which are trapped and cooled down far enough for all of them to occupy the same state. So it is really more of a quantum gazpacho.

1.2.2 Standard Approach to BEC Simulation

1.2.2.1 Setup

To understand the dynamics of a BEC we start with the basic inputs of the Schrödinger equation: The Hamiltonian H_{BEC} and the many-body wavefunction Ψ.
The Hamiltonian needs to characterise each boson's kinetic and potential energy, as well as the interaction between them.

$$H_{\mathrm{BEC}} = \sum_{i=1}^{N} \left(\underbrace{-\frac{\hbar^2}{2m}\frac{\partial^2}{\partial \mathbf{r}_i^2}}_{\text{kinetic}} + \underbrace{V(\mathbf{r}_i)}_{\text{potential}} \right) + \sum_{i<j} \underbrace{\lambda\delta(\mathbf{r}_i - \mathbf{r}_j)}_{\text{interaction}}. \tag{1.62}$$

The total atom number is given by N and m is the mass of a single particle. The first term of the Hamiltonian describes the kinetic energy of the i^{th} boson, where $\mathbf{r}_i$ gives its position. $V(\mathbf{r})$ is the potential[4] usually formed by an electromagnetic trap. The last term represents the inter particle interaction, where λ is the average energy exchanged during a scattering event between two bosons.
In this Hamiltonian some approximations have been made: First, only two-particle interactions are considered as it is unlikely that more than two scatter at a time. This assumption is true for dilute gasses. Second, instead of considering every single scattering event, an average potential λ is applied. This corresponds to a mean field approximation which is valid as long as the inter particle distance is much larger than the scattering length.
The many-body wavefunction of a BEC can be described as a product of single-particle states, also called the mean-field approach,

$$\Psi(\mathbf{r}_1, \mathbf{r}_2, \ldots, \mathbf{r}_N) = \prod_{i=1}^{N} \psi_0(\mathbf{r}_i). \tag{1.63}$$

This is valid for BECs as all atoms are indistinguishable and occupy the same single-particle state $\psi_0(\mathbf{r})$ by definition.

1.2.2.2 Gross-Pitaevskii Equation

With the above assumptions, it is possible to derive an equation that guides the dynamics of the many-body wavefunction. As many explanations of that derivation exist, we will only outline the results here [65, 66]. The many-body Schrödinger equation is the Euler-Lagrange

[4] Not to be confused with the frame transformation operator V.

equation of the many-body action functional [67]. The action functional can be constructed from the Hamiltonian in Eq. (1.62). Using the variational principle to minimise it, then leads to a solution for the mean field wavefunction $\psi(\mathbf{r}) = \sqrt{N}\psi_0(\mathbf{r})$, namely the time-dependent Gross-Pitaevskii Equation (GPE):

$$i\hbar\frac{\partial\psi(\mathbf{r})}{\partial t} = \left(-\frac{\hbar^2}{2m}\nabla^2 + V(\mathbf{r}) + \lambda|\psi(\mathbf{r})|^2\right)\psi(\mathbf{r}). \tag{1.64}$$

Unfortunately, there are limits to the applicability of the GPE in the modelling of many-body dynamics. One limit comes up when some particles occupy a state different from ψ_0. This circumstance can be taken into account by considering more than one single-particle basis function. These basis functions ψ_i are called **orbitals**, similar to the atomic orbitals described in quantum chemistry. When some population N_f of a condensate occupies different orbitals than the other $N - N_f$ atoms, the condensate is called **fragmented**[5] [68].
An example, illustrating the GPE's limitations is the transition between superfluid and Mott insulator [34] shown in Fig. 1.4. A superfluid can be represented with the GPE as all particles are in the same single-particle state, equally occupying all lattice sites. In a Mott insulator, however, all particles are localised, hence they all occupy their own single-particle state and the condensate is maximally fragmented. In the following we discuss how to model such fragmented states.

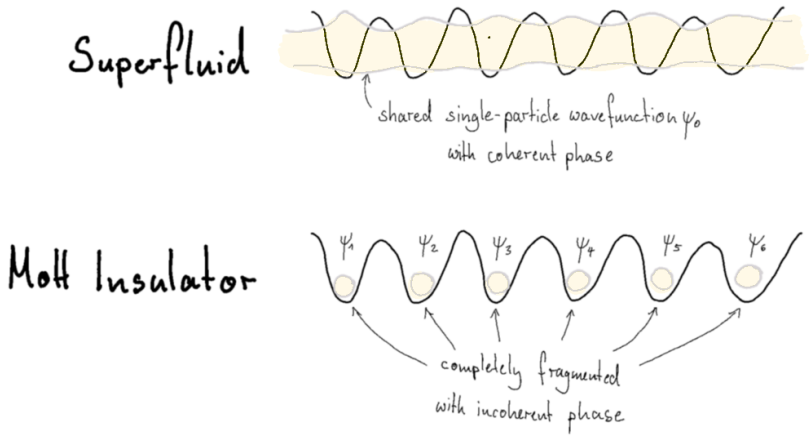

Fig. 1.4 Superfluid vs Mott insulator. The superfluid is defined by the atoms occupying the same single-particle wavefunction with a coherent phase, while the atoms in the Mott insulator all occupy different single-particle states.

[5]Throughout this text, we refer to condensates without fragmentation, i.e. where all population in a single state, as a BEC. The term "condensate" is also used for fragmented atom clouds. This definition is specified in reference [68].

1.2.3 Multi-Configurational Time-Dependent Hartree Approach for Bosons

The Multi-Configurational Time-Dependent Hartree approach for Bosons (MCTDHB) is a many-body model relying on state representation via a linear combination of time-dependent single-particle states [46, 69]. The approach has been successfully used to investigate condensates that cannot be described by one single-particle state such as fragmented condensates which are capable of producing squeezing [70, 71].
Let us consider an example with two well-defined initial orbitals to understand the method behind it. For the sake of the example they are considered to be static for now, although in the model they are time-dependent. A well-separated double well has two almost degenerate, orthonormal single-particle ground states, the symmetric state $\psi_1 = (0,\ 1)^\intercal$ and the asymmetric state $\psi_2 = (1,\ 0)^\intercal$. They will be our orbitals, hence the **number of orbitals** is $M = 2$. Now we consider two atoms in the condensate such that the **atom number** is $N = 2$. There are three different ways in which the atoms can be distributed over the orbitals. These distributions are called the **configurations** $\vec{n}$:

$$\begin{aligned} |2,0;t\rangle &= \frac{1}{\sqrt{2}}\binom{2}{0}, \\ |0,2;t\rangle &= \frac{1}{\sqrt{2}}\binom{0}{2}, \\ |1,1;t\rangle &= \frac{1}{\sqrt{2}}\binom{1}{1}. \end{aligned} \tag{1.65}$$

In this example the first two configurations are not fragmented, while the last one is fully fragmented and could not be represented with the GPE. By making the orbitals time-dependent, the wavefunction can adapt accordingly, if the condensate moves or the potential changes. Next, to produce a linear combination of these configurations we introduce the prefactors $C_{\vec{n}}(t)$, which describe the distribution of the condensate over the configurations. Consequently, the many-body wavefunction is given by:

$$|\Psi(t)\rangle = \sum_{\vec{n}} C_{\vec{n}}(t)\left|\vec{n};t\right\rangle. \tag{1.66}$$

The above equation is valid, not only for this example but for MCTDHB in general. The Hamiltonian from Eq. (1.62) can now be used with the one-dimensional variational principle to find the dynamics of $|\Psi(t)\rangle$ [46]. Initially, the functional action is defined, with the

Lagrange multipliers μ_{kj} to ensure that the time-dependent orbitals remain orthonormal.

$$S\left[C_{\vec{n}}(t), \psi_k(\mathbf{r}, t)\right] = \int dt \left(\langle \Psi | H_{\mathrm{BEC}} - i\hbar \frac{\partial}{\partial t} | \Psi \rangle - \sum_{k,j=1}^{M} \mu_{kj}(t) \left[\left\langle \psi_k \middle| \psi_j \right\rangle - \delta_{kj} \right] \right). \tag{1.67}$$

To simplify notation, the single-particle Hamiltonian $\hat{h}$ and the pairwise interaction operator $\hat{W}$ are defined:

$$\hat{h} = -\frac{\hbar^2}{2m} \frac{\partial^2}{\partial \mathbf{r}_i^2} + V(\mathbf{r}_i), \tag{1.68}$$

$$\hat{W} = \lambda \delta(\mathbf{r}_i - \mathbf{r}_j). \tag{1.69}$$

The variation of the action with respect to $C_{\vec{n}}$ results in the equation of motion describing the evolution of the orbitals.

$$i\hbar \left| \dot{\psi}_j \right\rangle = \left(1 - \sum_{j'=1}^{M} \left| \psi_{j'} \right\rangle \left\langle \psi_{j'} \right| \right) \left(\hat{h} \left| \psi_j \right\rangle + \sum_{k,s,q,l=1}^{M} \{\rho\}^{-1}_{jk} \rho_{ksql} \hat{W}_{sl} \left| \psi_q \right\rangle \right). \tag{1.70}$$

More details of the derivation can be found in the review by Alon et al. [46]. The matrix elements of the reduced one-body density matrix ρ_{kq} are expressed as ρ. Similarly, ρ_{ksql} represent the reduced two-body density matrix elements of the condensate and $\hat{W}_{kq}$ are the local interaction potentials. Now, that we can calculate the evolution of the orbitals, we still need to describe the occupation dynamics.

The second equation of motion is derived from the variation of the action with respect to an incremental change in the orbitals:

$$i\hbar \dot{C}_{\vec{n}}(t) = \sum_{\vec{n}'} \left\langle \vec{n}, t \middle| H_{\mathrm{BEC}} \middle| \vec{n}', t \right\rangle C_{\vec{n}'}(t) \tag{1.71}$$

This equation ensures that any initially normalised state stays normalised.

The evolution of the condensate is contained in Eq. (1.70) and Eq. (1.71). Still, the structure of these differential equations means there is no straight-forward analytical solution. Hence, the numerical approach is to solve the two equations sequentially with incremental time steps. First, $C_{\vec{n}}(t)$ is propagated for one time step according to Eq. (1.71), then we let the orbitals evolve following Eq. (1.70). This process repeats itself. Different methods have been developed to minimise errors and adjust the time step accordingly [46].

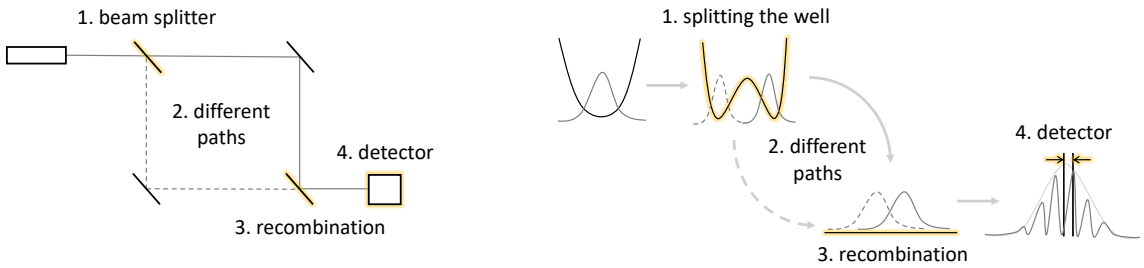

(a) Light interferometer (b) Atom interferometer

Fig. 1.5 Comparison between a light and an atom interferometer. Both including the splitting, evolution, recombination, and detection steps.

1.2.4 Atom Interferometry

For many quantum sensing applications the targeted information is encoded in a phase. With atomic condensates this can be done using the equivalent of a standard light interferometer [72]. The process is described by the following steps shown in Fig. 1.5a:

1. An incoming beam is split into two identical beams via a beam splitter.
2. The two beams travel along different paths.
3. The beams are recombined.
4. Using the interference pattern, the phase difference is detected.

After the splitting, the phase of one beam might change with respect to the other because, for example, the distance travelled was longer or it traversed a different medium. Said phase difference can be read out using the interference pattern from the detector, giving the method its name.
In atom interferometry, instead of an incoming beam, one considers a BEC in a single well potential [73, 74] shown in Fig. 1.5b. The beam splitter is then replaced by a barrier in said potential, splitting the BEC (single well) into two condensates (double well). If the condensates are decoupled, they can evolve independently to pick up a phase, dependent on environmental factors such as a magnetic field [75] or differences in the gravitational field [76]. To obtain the interference pattern, the condensates are recombined and left to evolved freely. The shift of the resulting pattern then encodes the phase difference. This difference is referred to as the relative phase.

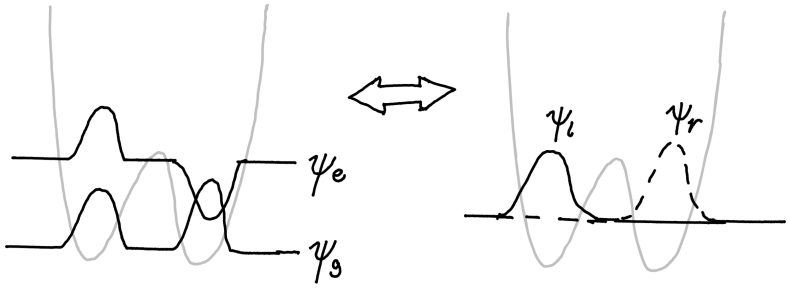

Fig. 1.6 Two-mode representation. (*left*) Ground state ψ_g and first excited state ψ_e. (*right*) Left mode ψ_ℓ and right mode ψ_r.

1.2.5 Spin Squeezing

Let us consider a condensate inside a double well with a central barrier that clearly separates the condensate into two parts [77]. The GPE of the resulting split BEC reveals that the two lowest energy levels are the almost degenerate symmetric ground state ψ_g and the anti-symmetric excited state ψ_e. By combining them, one can construct a left-localised mode ψ_ℓ and right-localised mode ψ_r, which are degenerate (see Fig. 1.6). The transformation between the two representations is given by

$$\begin{aligned} \psi_\ell &= \frac{\psi_g + \psi_e}{\sqrt{2}}, \\ \psi_r &= \frac{\psi_g - \psi_e}{\sqrt{2}}. \end{aligned} \tag{1.72}$$

If the condensate is unevenly distributed between these modes, the population oscillates between them. The frequency of that oscillation depends on the tunnel coupling J and the interaction strength λ.

Two conjugate properties connected to the left and right modes determine the sensitivity of the interferometer: The relative phase $\hat{\varphi} = \varphi_l - \varphi_r$ which is measured in the interferometer, and the half number imbalance $\hat{n} = (N_l - N_r)/2$. Their variances are connected to each other via the Heisenberg uncertainty principle:

$$\Delta\hat{\varphi}\,\Delta\hat{n} \geq \frac{1}{2}. \tag{1.73}$$

This relationship also implies the possibility of squeezing. An intuitive approach would be to squeeze with respect to the relative phase to increase the sensitivity. However, taking into account the variances' evolution reveals that the phase diffusion rate (the rate at which

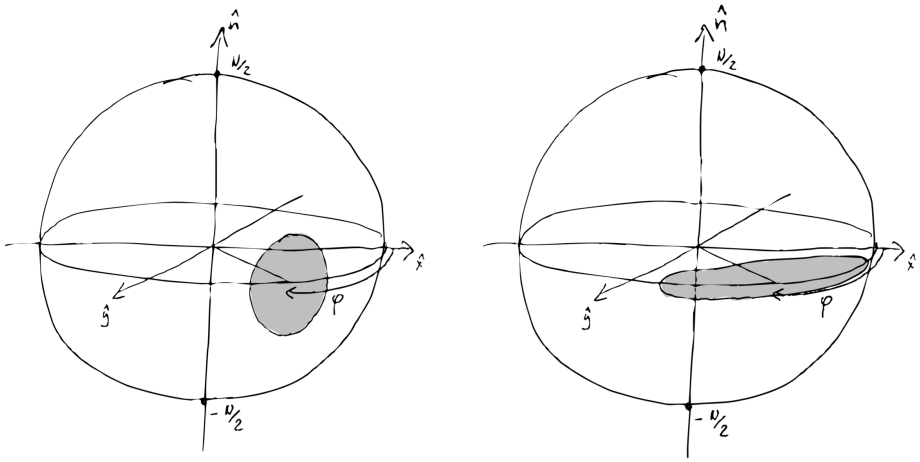

Fig. 1.7 The number and phase distribution of a condensate can be plotted on a Bloch sphere, where the z-axis corresponds to the imbalance and the angle around the z-axis to the relative phase. On the left is an exemplary distribution of a coherent state. On the right is a squeezed state. Both are displaced by a phase φ for illustrative reasons.

the phase variance broadens)[6] increases with the imbalance variance. Hence, extended measurements are actually improved by doing the opposite of phase squeezing: number squeezing [79, 80].

The term **spin** squeezing comes from the representation of these quantum properties on the Bloch sphere. In this picture $|\uparrow\rangle$ corresponds to all atoms being in ψ_ℓ and $|\downarrow\rangle$ is equivalent to a right-localised condensate, where all atoms occupy ψ_r. Consequently, the spin along z, $\hat{S}_z$, corresponds to $\hat{n}$ such that states on the equatorial plane give $\langle\hat{n}\rangle = 0$, and on the poles $\langle\hat{n}\rangle = \pm N/2$. The angle around the z-axis corresponds to $\hat{\varphi}$. Plotting the distribution of the condensate on the Bloch sphere effectively represents the squeezing as shown in Fig. 1.7.

The spin model encapsulates the condensate's collective imbalance and phase properties. The relationship between the squeezing in either direction is defined through three quantities: The phase squeezing factor ξ_φ, the number squeezing factor ξ_N (which should correctly be called half number imbalance squeezing factor, but is abbreviated in the following), and the useful squeezing factor ξ_S:

$$\xi_\varphi = \frac{\Delta\hat{\varphi}}{1/\sqrt{N}}, \tag{1.74}$$

$$\xi_N = \frac{\Delta\hat{n}}{\sqrt{N}/2}, \tag{1.75}$$

$$\xi_S = \frac{\xi_N}{\langle\widehat{\cos\varphi}\rangle}. \tag{1.76}$$

[6] A full discussion of this topic can be found in Julian Grond's PhD thesis [78] pages 46ff.

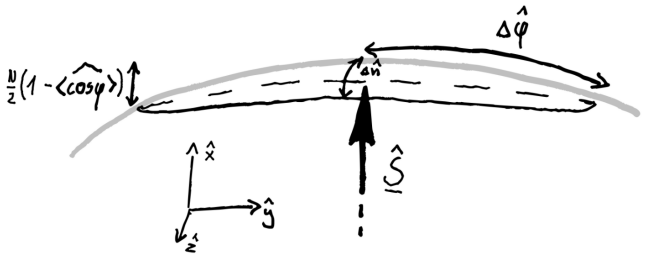

Fig. 1.8 Relationship between the length of the mean spin vector and the relative phase.

Please note that $\widehat{\cos\varphi}$ is an operator. For both, ξ_φ and ξ_N, the quantity's variance is normalised with the value of the coherent state. Hence they equal unity in the absence of squeezing and can be used to reformulate the uncertainty relations in Eq. (1.73)

$$\xi_N \xi_\varphi \geq \frac{1}{2}. \tag{1.77}$$

The form of the useful squeezing factor is less self-explanatory. In general, it is defined by the relationship between the length of the mean spin vector $\langle \hat{\underline{S}} \rangle = \frac{N}{2}\langle\widehat{\cos\varphi}\rangle$ and the smallest transverse fluctuations $\Delta\hat{n}$ shown in Fig. 1.8 [81]. The cosine term derives from the fact, that the spin commutation relations of the angular momentum (as commonly used with the Bloch sphere representation) are not directly translatable into phase and amplitude relations. Still, if the state is localised, the equivalent spin operators are given by

$$\begin{aligned} \hat{S}_x &= \frac{1}{2}\sqrt{N^2 - 4\langle\hat{n}\rangle^2}\,\widehat{\cos\varphi}, \\ \hat{S}_y &= \frac{1}{2}\sqrt{N^2 - 4\langle\hat{n}\rangle^2}\,\widehat{\sin\varphi}. \end{aligned} \tag{1.78}$$

From here, one can derive the useful squeezing factor as presented in Eq. (1.76) [77]. A coherent state corresponds to $\xi_S = 1$. The squeezing makes the interferometer more sensitive as explained under Eq. (1.73) and is deemed "useful", if $\xi_S < 1$.

1.2.6 Model

The condensate of ^{87}Rb atoms is simulated with the MCTDHB-implementation "MCTDH-X" [82–84, 69]. The system's evolution is guided by a unitless Hamiltonian $\bar{H}$ similar to Eq. (1.62) with a similarly adapted potential $\bar{V}$ and interaction strength $\bar{\lambda}$ [85]. As the computational complexity of the simulation increases with each extra dimension, the

simulations are performed in one and two dimensions using the following Hamiltonians:

$$\begin{aligned}\bar{H}_{1D} &= \frac{H_{1D}}{\hbar\omega_{\text{sys}}} = \sum_{j=1}^{N}\left[-\frac{1}{2}\frac{\partial^2}{\partial x_j^2} + \bar{V}(x_j)\right] + \sum_{j<k}^{N}\bar{\lambda}_{1D}\delta(x_j - x_k),\\ \bar{H}_{2D} &= \frac{H_{2D}}{\hbar\omega_{\text{sys}}} = \sum_{j=1}^{N}\left[-\frac{1}{2}\left(\frac{\partial^2}{\partial x_j^2} + \frac{\partial^2}{\partial z_j^2}\right) + \bar{V}(x_j, z_j)\right] + \sum_{j<k}^{N}\bar{\lambda}_{2D}\delta(x_j - x_k)\delta(z_j - z_k).\end{aligned} \tag{1.79}$$

All length scales are given in μm. The corresponding units for the propagation time becomes $\bar{t} = t/\omega_{\text{sys}} \approx t \times 1.368\,\text{ms}^{-1}$. The other parameters are defined as

$$\begin{aligned}\omega_{\text{sys}} &= \frac{\hbar}{mL^2},\\ m &= M_{\text{Rb87}} = 1.44316060 \times 10^{-25}\,\text{kg (atom mass)},\\ L &= 10^{-6}\,\text{m} = 1\,\mu\text{m (length scale)}^{7},\\ \hbar &= 1.054589 \times 10^{-34}\,\text{J s (reduced Planck constant)},\\ a_0 &= 5.291771 \times 10^{-11}\,\text{m (Bohr radius)},\\ a_s &= 100.44 \times a_0 \text{ (3D atom-atom scattering length)}.\end{aligned} \tag{1.80}$$

An exemplary potential is shown in Fig. 1.9. It produces the characteristic cigar-shaped condensate because the energy scales are of the same order of magnitude along the transverse directions x and y (kHz), while the longitudinal potential along z is much more shallow (Hz). In the experiment, the trap frequencies are measured to be

$$\begin{aligned}\omega_{\parallel} &= \omega_z \approx 2\pi\,15.0\,\text{Hz},\\ \omega_x &= 2\pi\,1.83 \times 10^3\,\text{Hz (for the single well case)},\\ \omega_y &= 2\pi\,2.58 \times 10^3\,\text{Hz},\\ \omega_{\perp} &= \sqrt{\omega_y \omega_x}.\end{aligned} \tag{1.81}$$

The corresponding oscillator lengths are given by $a_i = \sqrt{\hbar/\omega_i m}$, where $i = \{x, y, z, \parallel, \perp\}$.
To understand the relationship between the different directions we consider their respective spectra. The energy scale of the potential along y is 0.75 kHz larger than that along x. As a result the spacing between the eigenmodes is largest in the y-direction, i.e. $\Delta E_y > \Delta E_x \gg \Delta E_z$. In the single well, the condensate is assumed to be in the ground state so none of the higher modes play a role. However, during the splitting the added energy leads to the occupation of higher modes. In the double well, the eigenmodes along x move closer together with

[7] Please note that in this section, we make no use of Lindblad operators and L always refers to scalars.

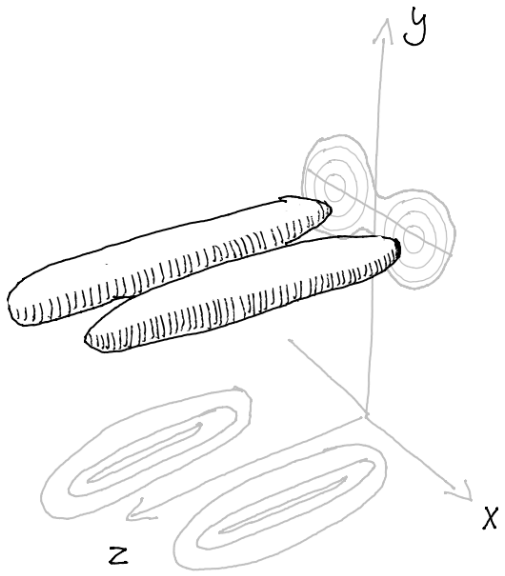

Fig. 1.9 Illustration of the condensate and potential. In the x-direction the potential is given by a double well, along z and y it corresponds to a harmonic well with an additional shift of the x-component along z. The resulting condensate has the shape of two cigars.

respect to the y-modes. As a result we can assume that the energy levels along y are well-separated and the condensate stays in the corresponding ground state. This type of approximation is common for cigar-shaped condensates [86] and has been validated in different experiments [77, 87] similar to the one considered here.

In contrast, the modes in the z-direction are tightly packed. However, as the energy difference between them is very small, the transition time-scales are large compared to the evolution time we consider in this work. Consequently, the mean-field condensate wavefunction is expected to be separable into $\psi(\mathbf{r}) = \psi_\perp(x,y)\psi_z(z)$ and stay in the ground state along z. The dynamics during the splitting are more complex. As the two lowest x-modes of the double well become degenerate, there are crossings between the z- and x-modes. These dynamics will be explored further in Section 3.3.

We consider a harmonic potential in z- and y-directions and an adaptable profile, $V_{\mathrm{RF}}(x;\kappa)$,

going from a single to a double well in x-direction:

$$\begin{aligned}
\hbar\omega_{\mathrm{sys}}\bar{V}(x,y,z;\kappa) &= V_{\mathrm{RF}}(x;\kappa) + \frac{1}{2}\omega_y^2 y^2 m + \frac{1}{2}\omega_z^2 (z-\chi x)^2 m, \\
\hbar\omega_{\mathrm{sys}}\bar{V}(x,z) &= V_{\mathrm{RF}}(x;\kappa) + \frac{1}{2}\omega_z^2 (z-\chi x)^2 m, \\
\hbar\omega_{\mathrm{sys}}\bar{V}(x) &= V_{\mathrm{RF}}(x;\kappa), \\
&\text{with } \chi = \frac{\delta_z}{\delta_x}.
\end{aligned} \tag{1.82}$$

The factor χ is a correction to account for a shift of the trap minima by δ_z, when the two wells are separated by δ_x. An estimate from the experimental data suggests a maximum shift of $\chi = 5\,\mu\mathrm{m}/2\,\mu\mathrm{m}$. $V_{\mathrm{RF}}(x;\kappa)$ corresponds to the experimental potential shown in Fig. 1.10. The parameter κ stands for the voltage applied across the wires generating the trap. A single well is described by $\kappa = 0.3$, while higher values create a double well. The potential is calculated by fitting the electric potential of the wires with a sixth order polynomial[8] (valid for $0.3 \leq \kappa \leq 0.7$):

$$\begin{aligned}
V_{\mathrm{RF}}(x;\kappa) =& 2\pi\hbar \times 10^3 \Big(f_0(\kappa) + f_1(\kappa)x + f_2(\kappa)x^2 + f_3(\kappa)x^3 \\
&+ f_4(\kappa)x^4 + f_5(\kappa)x^5 + f_6(\kappa)x^6 \Big) \text{ [in J]} \\
&\text{with} \\
f_0(\kappa) =& -190 + 3980\kappa - 29710\kappa^2 + 101460\kappa^3 \\
&- 168920\kappa^4 + 137700\kappa^5 - 44170\kappa^6 \\
f_1(\kappa) =& 0 \\
f_2(\kappa) =& 88.7 - 402.5\kappa + 422.5\kappa^2 + 872.0\kappa^3 \\
&- 3093.6\kappa^4 + 3224.8\kappa^5 - 1203.1\kappa^6 \\
f_3(\kappa) =& 0 \\
f_4(\kappa) =& -9.8 + 209.2\kappa - 690.2\kappa^2 + 1090.8\kappa^3 \\
&- 958.3\kappa^4 + 514.3\kappa^5 - 139.1\kappa^6 \\
f_5(\kappa) =& 0 \\
f_6(\kappa) =& 0.9877 - 31.6373\kappa + 139.5386\kappa^2 - 333.6785\kappa^3 \\
&+ 512.4129\kappa^4 - 457.9392\kappa^5 + 171.6\kappa^6
\end{aligned} \tag{1.83}$$

While the potential along x changes dynamically, it is static and harmonic along y. Assuming

[8] The fit was kindly provided by TianTian Zhang.

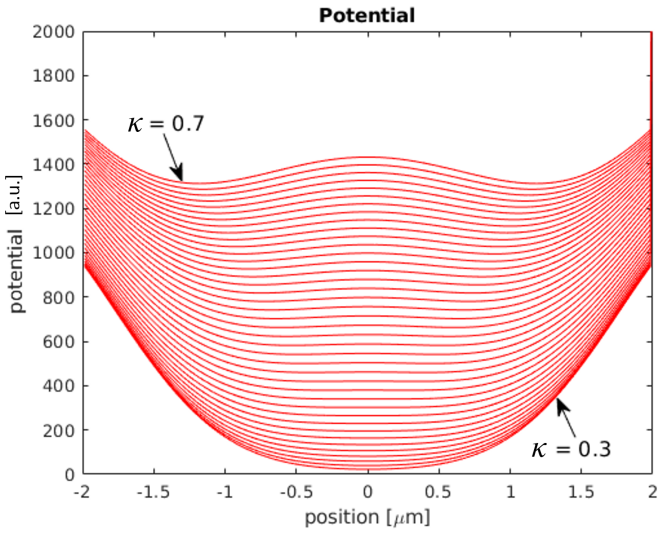

Fig. 1.10 The transverse potential created by the RF wires in the experiment with factors from $\kappa = 0.3$ up to $\kappa = 0.7$.

that the condensate stays in the ground state along y, the transverse mean-field condensate wavefunction becomes separable, such that $\psi_\perp(x,y) = \psi_x(x)\psi_y(y)$. Each component is normalised to unity. The ground state along y is considered to be in the single-particle ground state

$$\psi_y(y) = \frac{1}{\sqrt{a_y \pi^{1/2}}} e^{-y^2/2a_y^2}. \tag{1.84}$$

As the condensate along y is static and decoupled, the y-potential only affects the overall condensate by changing the interaction strength via the average density. To model the dynamics along x an z, the y-direction is integrated out giving the new 2D interaction strength

$$\begin{aligned} \bar{\lambda}_{2D} &= I_y \lambda_{3D} \frac{1}{\hbar \omega_{\text{sys}} L^2} = 2\sqrt{2\pi}\frac{a_s}{a_y}, \text{ where} \\ \lambda_{3D} &= \frac{4\pi\hbar^2 a_s}{m}, \\ I_y &= \int_{-\infty}^{\infty} |\psi_y(y)|^4 dy = \frac{1}{a_y\sqrt{2\pi}}. \end{aligned} \tag{1.85}$$

Similarly, the 1D interaction strength is obtained by integrating over z

$$\begin{aligned} \bar{\lambda}_{1D} &= I_y I_z \lambda_{3D} \frac{1}{\hbar \omega_{\text{sys}} L}, \text{ where} \\ I_z &= \int_{-\infty}^{\infty} |\psi_z(z)|^4 dz = \int_{-\infty}^{\infty} \left| \frac{n_{1D}(z)}{N} \right|^2 dz. \end{aligned} \tag{1.86}$$

$n_{1D}(z) = N|\psi_z(z)|^2$ describes the one-dimensional atomic number density, where $\psi(z)$ is the longitudinal condensate wavefunction normalised to unity.
As described above, the connection between the x- and z-direction is more complex. If they were perfectly decoupled, the condensate would be in the "1D Thomas Fermi regime" and we could repeat the same mean-field approach as for y. This is only applicable, if the spacing between the transverse energy levels is too large to overcome and hence it is transversely frozen. The regime in which the directions cannot be separated is called the "3D Thomas Fermi regime". The fact that our condensate is located in between is taken into account via a cross-over method [88], which is more accurate than the mean-field but still allows to reduce the dimensionality of the problem [86, 89]. Such methods have been shown to agree well with 3D simulations [90]. In the presented approach the density is considered to be locally in equilibrium. The energy is minimised to find the shape of the longitudinal profile considering a Gaussian ansatz. The resulting integral I_z is dependent on the factor[9] α, which is determined by the ODE below:

$$\begin{aligned} I_z &= \frac{L_c\alpha^2(21+9\alpha+\alpha^2)}{315a_s^2N^2}, \\ \alpha^3(\alpha+5)^2 &= \left(15N\frac{a_\perp a_s}{a_\parallel^2}\right)^2, \end{aligned} \tag{1.87}$$

where $L_c = a_\parallel^2\sqrt{\alpha}/a_\perp$ is the condensate length. By combining the above equations, the full 1D interaction strength is given by

$$\bar{\lambda}_{1D} = 2\sqrt{2\pi}\frac{L_cL}{a_sa_y}\frac{\alpha^2}{315N^2}(\alpha^2+9\alpha+21). \tag{1.88}$$

It should be noted that the different assumptions made above lead to the 1D interaction strength being dependent on the atom number, while the 2D interaction is not. For an atom number $N = 1500$ their values are different by two orders of magnitude:

$$\begin{aligned} \bar{\lambda}_{1D} &= 2.85808\times10^{-3}, \\ \bar{\lambda}_{2D} &= 0.137446. \end{aligned} \tag{1.89}$$

[9] not to be confused with the cavity field $\alpha(t)$ from Section 1.1

1.2.7 Data Analysis

1.2.7.1 The Single Shot Method

To calculate the number and phase squeezing we use the so-called single shot method [91]. It relies on taking snapshots of the atoms and results in data of a similar form as the experimental output. Producing snapshots requires the full many-body probability density $p(\mathbf{r}_1,\ldots,\mathbf{r}_N) = |\Psi(\mathbf{r}_1,\ldots,\mathbf{r}_N)|^2$ of the system. Unfortunately, the functional form of the full many-body wavefunction $\Psi(\mathbf{r}_1,\ldots\mathbf{r}_N)$ is not available to us. However, the probability density can be represented as a product of conditional probabilities

$$p(\mathbf{r}_1,\ldots,\mathbf{r}_N) = p(\mathbf{r}_1)\,p(\mathbf{r}_2|\mathbf{r}_1)\times\cdots\times p(\mathbf{r}_N|\mathbf{r}_{N-1},\ldots,\mathbf{r}_1). \tag{1.90}$$

Here, $p(\mathbf{r}_1|\mathbf{r}_2)$ is the conditional probability of finding an atom at position $\mathbf{r}_2$ after the previous one was found at $\mathbf{r}_1$. This representation allows us to consider one atom after the other. We sequentially select a random position from a probability distribution starting from the density. Then, one atom at the selected position is removed from the probability distribution, the result is used in the next step until all N atoms have been extracted.
The output of each single shot is used to calculate the number imbalance.[10] Equivalently, we use momentum space single shots to find the relative phase distribution.
The single shots are calculated with the analysis tools provided by MCTDH-X. An example of a single shot image in 2D is shown in Fig. 1.11.

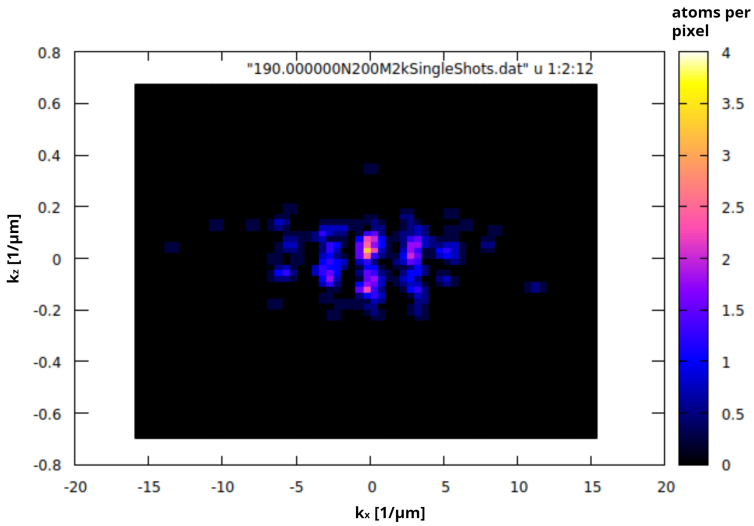

Fig. 1.11 Exemplary single shot image in momentum space in two dimensions with $N = 200$.

[10] The squeezing of the number imbalance could alternatively be calculated directly from the MCTDHB-produced density matrix as shown in the Appendix of reference [70]. However, this technique does not provide the phase squeezing of the system and is only applicable in 1D.

1.2.7.2 Fitting Procedure

The number imbalance can be easily calculated by counting the atoms on the left or the right side from the centre for each of the K single shots. The difference between the number of atoms on the left, $N_{L,i}$, and the number of atoms on the right, $N_{R,i}$, gives the half number imbalance $n_i = (N_{L,i} - N_{R,i})/2$ for the i^{th} shot. A histogram of this imbalance reveals a distribution around μ_n with standard deviation Δn. An example can be seen in Fig. 1.12e.

$$\mu_n = \frac{1}{K}\sum_{i=1}^{K} n_i \tag{1.91}$$

$$\Delta n = \sqrt{\frac{1}{K}\sum_{i=1}^{K} (n_i - \mu_n)^2} \tag{1.92}$$

To obtain the standard deviation of the relative phase $\Delta\varphi$, the single shots are drawn from the momentum space wavefunction. The contrast of each image is limited by the number of atoms and the average of the images might, by definition, not enhance the signal. To overcome these difficulties, we have concatenated different fitting steps. A version of the code provided by the author of this thesis is published as `rel_phase_package.py` in the UNIQORN repository: A. U. J. Lode, P. Molignini, R. Lin, M. Büttner, P. Rembold, C. Lévêque, M. C. Tsatsos, and L. Papariello, *UNIQORN: Universal Neural network Interface for Quantum Observable Readout from N-body wavefunctions*, `https://gitlab.com/auj.lode/UNIQORN.git` (2020) [7]. The repository contains a software for the readout of observables from single shot images using machine learning [92]. In this thesis, we analyse both 1D and 2D images. In the latter case, the single shots are integrated over the longitudinal direction before the analysis. The phase of each single shot image is determined following these steps:

1. The minimum requirement to obtain an interference pattern is that the position space density contains more than one peak and a sufficient dip in between. If this condition is not met, the phase variance calculation is aborted.

2. The mean of all single shots is used to find the average momentum space distribution.

3. The average distribution is Fourier transformed to extract the peak frequency ω_α. This gives a good estimate, if the phase distribution is narrow. However, for strongly number squeezed condensates, the average distribution is a Gaussian.

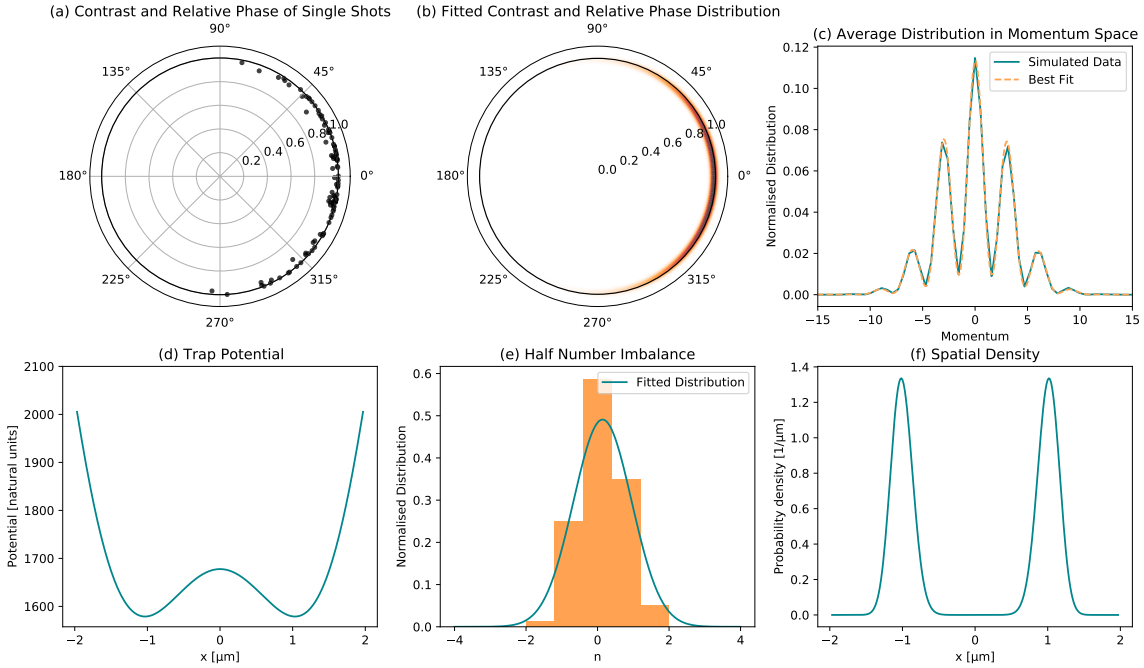

Fig. 1.12 Single shot measurements ($K = 100$) of the ground state of a condensate with $N = 1500$ atoms simulated with $M = 2$ orbitals. (a) Single shots represented in phase space where the angle corresponds to the relative phase and the radius to the contrast. (b) Fitted distribution of the single shots, defined by $\varphi = -0.0558 \pm 0.6120$ and $C = 0.99 \pm 0.01$ resulting in $\xi_\varphi = 23.701$. (c) Fitted average distribution in momentum space. (d) Transverse trap potential with RF amplitude $\kappa = 0.62$. (e) Normalised histogram of the half number imbalance with $n = 0.2800 \pm 1.6253$ resulting in $\xi_N = 0.04197$ and $\xi_S = 0.05069$. (f) Spatial probability density of the condensate.

4. The average distribution is fitted to a Gaussian $G_{\text{fit}}(k_x; A_\alpha, w_\alpha)$ to find the amplitude A_α and spread w_α:

$$G_{\text{fit}}(k_x; A, w) = A e^{-k_x^2 w}. \tag{1.93}$$

5. The average distribution is fitted to the full model $F_{\text{fit}}(k_x; A_\beta, w_\beta, C_\beta, \omega_\beta, \varphi_\beta)$. As initial guess values we use $(A_\alpha, w_\alpha, 0.9, \omega_\alpha, 0.0)$ to find the fit parameters $(A_\beta, w_\beta, C_\beta, \omega_\beta, \varphi_\beta)$. C_β is the average's contrast and φ_β its phase.

$$F_{\text{fit}}(k_x; A, w, C, \omega, \varphi) = \underbrace{A e^{-k_x^2 w}}_{\text{envelope}} \left[1 + \underbrace{C \cos(\omega k_x + \varphi)}_{\text{interference}} \right], \tag{1.94}$$

where the first term takes care of the envelope of the momentum space distribution, while the cosine term describes the interference pattern [93]. The outcome of such a fit

is shown in Fig. 1.12c. The average distribution has a low contrast if the condensate is strongly squeezed or if the fringe pattern is not straight, i.e. $\chi \gg 0$ in Eq. (1.82).

6. The fit quality is estimated using the R^2-measure. If the fit of $F_{\text{fit}}(k_x; A_\beta, w_\beta, C_\beta, \omega_\beta, \varphi_\beta)$ is better than the fit of $G_{\text{fit}}(k_x; A_\alpha, w_\alpha)$ and $C_\beta \geq 0.2$, we define $(A_\gamma, w_\gamma, C_\gamma, \omega_\gamma, \varphi_\gamma) = (A_\beta, w_\beta, C_\beta, \omega_\beta, \varphi_\beta)$ for future fits. Otherwise, the last two steps are repeated with a number of random single shots instead of the average distribution. If none of them have a contrast above 0.8, the evaluation of the phase variance is aborted. This might be the case, if the longitudinal coherence is insufficient or the number of atoms is too low. If they do have sufficient contrast, their fit values are averaged to produce $(A_\gamma, w_\gamma, C_\gamma, \omega_\gamma, \varphi_\gamma) = (A_{\text{av}}, w_{\text{av}}, C_{\text{av}}, \omega_{\text{av}}, \varphi_{\text{av}})$.

7. Each single shot is fitted to $F_{\text{fit}}(k_x; A_\gamma, w_\gamma, C_i, \omega_\gamma, \varphi_i)$, with fit parameters (C_i, φ_i) and initial guesses $(C_\gamma, \varphi_\gamma)$. To minimise the effect of the boundaries, we assume a phase distribution around φ_γ and set the limits for the fits to $[\varphi_\gamma - \pi, \varphi_\gamma + \pi]$. An example is shown in Fig. 1.12a.

8. The circular mean and standard deviation of the phase distribution are calculated [94]. As the distribution wraps around, its variance should be infinite for a perfectly uniform distribution and otherwise approximate the local normal distribution. This cannot be calculated in the same way as the variance of the number distribution as it would be naturally limited by the circle's circumference of 2π. To characterise the distribution we first calculate a unit vector $z_i = e^{i\varphi_i}$ for each single shot and then average them to get the sample moment m_φ:

$$m_\varphi = \frac{1}{K} \sum_{i=1}^{K} z_i. \tag{1.95}$$

The length of the sample moment corresponds to the spread of the distribution, i.e., if $1 - |m_\varphi| = 0$ it is strongly localised and if $1 - |m_\varphi| = 1$ it is uniform. $1 - |m_\varphi|$ is also called the circular variance. However, it is not suitable for our purposes as it does not describe the approximate normal distribution. Hence, we use the circular standard distribution given by

$$\Delta\varphi = \sqrt{-2 \ln |m_\varphi|}. \tag{1.96}$$

The mean of the distribution is given by the direction of the sample moment,

$$\mu_\varphi = \arg(m_\varphi). \tag{1.97}$$

9. The mean and standard deviation of the contrast are calculated to provide a full description of the distribution. They are given by

$$\mu_C = \frac{1}{K}\sum_{i=1}^{K} C_i, \tag{1.98}$$

$$\Delta C = \sqrt{\frac{1}{K}\sum_{i=1}^{K}(C_i - \mu_C)^2}. \tag{1.99}$$

In the end, the fitting procedure provides an estimate for the distribution of the relative phase shown in Fig. 1.12b similar to the one commonly produced with experimental data. Consequently, it enables us to get a good estimate of the useful squeezing of the condensate.

Chapter 2

Quantum Optimal Control

2.1 Introduction

> A problem well stated is a problem half solved.
>
> *John Dewey*

Almost any skill can be acquired with enough practice, including the control of quantum systems. However, practice is expensive in terms of person-hours. Repeatedly testing out different strategies to make the hardware comply with the goal simply takes very long, if done by a human. Here, optimal control comes into play. It automates the testing procedure by employing search algorithms that scout the possible solutions efficiently. There are many different such strategies, and they have found even more applications. Some only require minimal information about the system, while others are based on detailed models, still others take a reinforcement learning approach borrowed from machine learning. This section will introduce the theory behind optimal control and discuss a novel technique designed for frequency-sensitive systems.

2.2 Optimal Control Theory

This section is reproduced from P. Rembold, N. Oshnik, M. M. Müller, T. Calarco, S. Montangero, and E. Neu, *Introduction to Quantum Optimal Control for Quantum Sensing with Nitrogen-Vacancy Centers in Diamond*, AVS Quantum Science 2, 024701 (2020) with permission of AIP publishing and all co-authors. The author of this thesis was the first author responsible for the content of Section III (Optimal Control Theory) and Appendix B (The

Rotating Wave Approximation) as well as parts of Sections IV (QOC for NV Centers) and V (Conclusion). She was furthermore involved in the planning an discussion of the general contents. To ensure the flow of this manuscript, only section III is reprinted here:

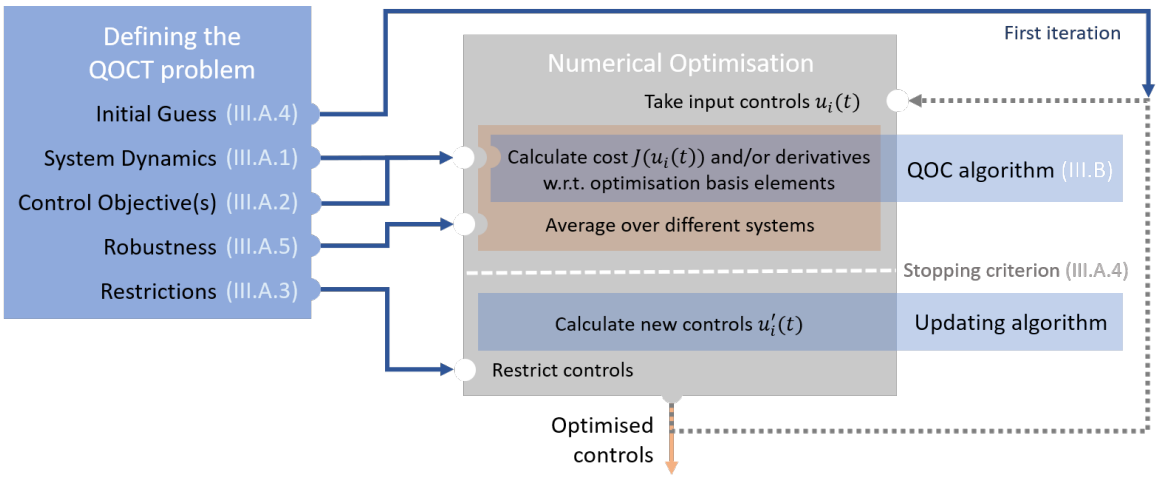

Fig. 2.1 Schematic drawing of a generic QOC optimisation. The box on the left contains the elements that define a basic QOC problem with blue solid arrows connecting them to the algorithm. The grey box at the centre illustrates the optimisation algorithm itself, with the dotted grey arrow indicating its iterative nature. The cost function J is calculated from the controls $u_i(t)$ and used to update the controls. In parenthesis the relevant sections in the review paper are indicated where applicable.

Without the ability to precisely manipulate quantum systems, researching their properties and applying them for quantum technologies is almost impossible. Quantum Optimal Control (QOC) theory [95, 18] improves the shape of dynamical controls (typically electromagnetic field pulses) to achieve a certain goal to maximum precision. The section starts with the details of defining a QOC problem in section 2.2.1 followed by a description of different numerical optimisation tools in section 2.2.2 and concluded by a brief discussion of the limits of QOC (section 2.2.3). The first part is structured according to the schematic in Fig. 2.1.
In the field of Nuclear Magnetic Resonance (NMR), pulse shaping is used since the 1980s[96] and many of the arguments for pulse shape optimisation[19] equally apply to NV centers, which we will focus on. In many cases, the time scales defining the decay of NV centers are large compared to the control time. In that case, it is sufficient to study closed system dynamics. Indeed, specific open system techniques such as population suppression and the exploitation of useful dissipation processes are often not applicable to the problems considered in this review [17]. Hence, we limit ourselves to a closed system description.

2.2.1 Defining a Control Problem

The principles of QOC theory derive from early extremisation problems such as Johann Bernoulli's brachistochrone curve problem [97]. Similarly, QOC problems are formulated through a system of equations, which broadly defines three things: First, the **system dynamics**, i.e. the theoretically obtained description reflecting the system's behaviour, for example given by the Hamiltonian. Alternatively, this first equation might be replaced by a description through the experiment itself. Second and third, the **control objectives** and **control space restrictions**. The objectives on the one hand set the goal of the optimisation, like e.g. high fidelity for the transfer to a target state. The control space restrictions on the other hand limit the resources that may be used to reach the desired goal. Together, the three aspects are combined into a so-called control landscape. Each set of controls will result in a different value of the "cost function" J, a measure for how close the system is to reaching the objective. In case of a minimisation (and throughout this review we will always assume minimisations, unless stated otherwise), each valley corresponds to a locally optimal combination of controls. The goal of the optimisation can now be easily defined as reaching the lowest point in the landscape.
We will now discuss in more detail these three ingredients of QOC problems as well as the initial guess, stopping criteria and robustness.

2.2.1.1 System Dynamics

One way to characterise the evolution of a closed quantum system with time dependent controls is through Schr "o dinger's equation. The system Hamiltonian is usually split into two parts; the drift Hamiltonian $\hat{H}^d$, which is constant and cannot be manipulated, and the control Hamiltonians $\hat{H}_i^c$ which are multiplied with time-dependent coefficients $u_i(t)$ called "control pulses". The full Hamiltonian then reads

$$\hat{H} = \hat{H}^d + \sum_i u_i(t)\hat{H}_i^c. \tag{2.1}$$

Please note that system dynamics for control problems may also be defined through Lindblad-operators and even for non-Markovian dynamics (for a review on open systems QOC see Koch[17]).

Drift and Control Hamiltonian

As an example, let us consider a NV center, approximated as a qubit with the ground state $|0\rangle$ and excited state $|1\rangle$. In this simple consideration the goal will be to create a high-fidelity $\frac{\pi}{2}_x$-rotation similar to the system in Frank et al. [26].
A static magnetic field $B_\parallel$ is applied in z-direction (the quantisation-/NV-axis) and a circularly polarised microwave field $\vec{B}_\perp$ with an amplitude $B_\perp(t)$, frequency ω_{mw} and phase φ is applied orthogonal to $B_\parallel$. Let us define the gyromagnetic ratio of the NV center as γ_{nv}. The rotating frame of $\vec{B}_\perp$ then gives the Hamiltonian

$$\begin{aligned}\hat{H}_{\mathrm{RWA}}/\hbar &= \Delta\hat{\boldsymbol{s}}_Z + \Omega(t)\left(\hat{\boldsymbol{s}}_X\cos\varphi(t) + \hat{\boldsymbol{s}}_Y\sin\varphi(t)\right)\\ &= \Delta\hat{\boldsymbol{s}}_Z + u_1(t)\hat{\boldsymbol{s}}_X + u_2(t)\hat{\boldsymbol{s}}_Y,\end{aligned} \tag{2.2}$$

where $\Delta = \omega_{nv} - \omega_{mw}$ is the detuning, $\omega_{nv} = B_\parallel\gamma_{nv}$ the NV's resonant frequency, $\Omega(t) = B_\perp\gamma_{nv}$ is the Rabi frequency and $\hat{\vec{\boldsymbol{s}}}$ are the spin operators in the $|0\rangle, |1\rangle$ basis. A derivation of this Hamiltonian can be found in Appendix [B of the original publication]. We can easily identify the drift Hamiltonian $\hat{H}^d = \Delta\hat{\boldsymbol{s}}_Z$. Let us assume, that both the Rabi frequency $\Omega(t)$ and the phase of the magnetic field $\varphi(t)$ can be manipulated dynamically. The control Hamiltonians may then be identified as $\hat{H}_1^c = \hat{\boldsymbol{s}}_X$ and $\hat{H}_2^c = \hat{\boldsymbol{s}}_Y$ and the control pulses as $u_1(t) = \Omega(t)\cos\varphi(t)$ and $u_2(t) = \Omega(t)\sin\varphi(t)$.

Once the system has evolved, it is time to test whether the goals have been reached by checking the control objectives.
It should be noted at this point that the rotating wave approximation, as presented in Appendix B of the original publication, is widely used to simplify the NV center's Hamiltonian. While it is useful, when the Rabi frequency is much lower than the NV center's resonant frequency, it can have a detrimental effect on a simulation's accuracy, if the Rabi frequency is of a similar scale as the qubit transition. In fact, Scheuer et al. [98] have shown how the inaccurate use of the RWA can affect the outcomes of optimal control procedures designed for NV centers.

2.2.1.2 Control Objective(s)

The cost function (or figure of merit) J defines what is minimised in any QOC problem. This way it describes the goal of the optimisation (terminal cost) and optionally the control limits through penalty-terms (running costs). The terminal costs are determined at the final time of the system's evolution. They quantify for instance the distance between the final state and the desired goal state in the relevant Hilbert space. The running costs are usually related to the restrictions on the control pulses, for example the limited power of a microwave source.

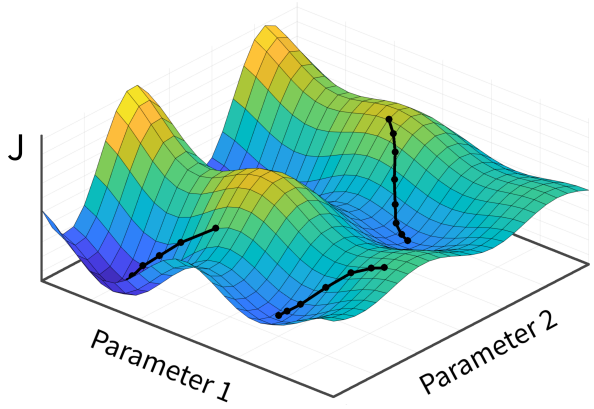

Fig. 2.2 Example of a QOC landscape. Considering two control parameters, we may represent the cost function J as a surface dependent on the set of controls. The minima correspond to locally optimal control coordinates. Each black path represents a local optimisation starting from a different initial guess.

In this review, the cost function is defined to be zero, when all objectives are met and to be greater than zero, when they are not met. Note that the running costs have a similar role as the control space restrictions that will be discussed in section 2.2.1.3.
In the following, we will briefly describe some of the most relevant cost functions found in relation to NV centers in the literature. For more examples of NV center applications, please refer to sections II an IV of the original publication for examples specifically combining them with QOC.

- **State to state transfer** (terminal cost)
  State to state transfer is the most common optimisation objective and has been used in many papers [25, 99, 26, 100]. The infidelity is a measure for the distance between two states $|\phi_t\rangle$ and $|\phi(T)\rangle$: If they are equal, it gives zero, if they are orthogonal, it has a value of one. The infidelity can be used directly to define the cost function J_{state}

$$J_{\text{state}} = 1 - |\langle\phi_t|\phi(T)\rangle|^2, \tag{2.3}$$

  describing the distance between $|\phi(T)\rangle$, the final state of the system at time T, and $|\phi_t\rangle$, the target state. An alternative way to formulate the transfer is fixing the global phase using $J_{\text{state}} = 1 - Re\{\langle\phi(T)|\phi_t\rangle\}$.

- **Unitary gate optimisation** (terminal cost)
  To measure the distance between the unitary $U(T)$ produced by the controls and the

target gate U_t, we define the cost function

$$\begin{aligned} J_{\text{gate}} &= 1 - \frac{1}{N_0^2}\left|\text{Tr}\Big(U_t^\dagger U(T)\Big)\right|^2 \\ &= 1 - \frac{1}{N_0^2}\left|\sum_{i=1}^{N_0}\langle\zeta_i|\, U_t^\dagger\, |\phi_i(T)\rangle\right|^2 . \end{aligned} \tag{2.4}$$

In the second line, the gate fidelity is defined through the N_0 basis states $|\zeta_i\rangle$ of the initial system and their propagated version $|\phi_i(T)\rangle = U(T)|\zeta_i\rangle$. Similarly to J_{state}, we can also define a global phase dependent version of this cost function, $J_{\text{gate}} = 1 - \frac{1}{N_0}\,\text{Re}\{\text{Tr}(U_t^\dagger U(T))\}$. Examples for its application can be found in references [101–104].

- **Sensitivity** (terminal cost)
  In contrast to the previous examples, the sensitivity does not directly contain information about the system. Instead, it quantifies the amount of information about a parameter θ (e.g. the magnetic field) that may be derived from a set of measurements. The sensitivity may be defined as the variance $(\Delta\theta)^2$ of the parameter estimate θ_0 obtained from N_M measurements. Each measurement produces the expectation value of some positive-operator-values measure (POVM)[1] Θ. The probability to measure $\theta(|\phi\rangle) = x$ probing a wavefunction $|\phi\rangle$ is then given by the expectation value $p(x|\theta) = \langle\phi|\,\Theta\,|\phi\rangle = \text{Tr}(\rho\Theta)$, with $\rho = |\phi\rangle\langle\phi|$.
  The cost function should, however, not contain information about the outcome of the measurement, but rather about its precision. The lower bound of $\Delta\theta$ is given by the Cramér-Rao bound

$$(\Delta\theta)^2 \geq \frac{1}{N_M F(\theta_0)}, \tag{2.5}$$

  a value which is inversely proportional to the Fisher information $F(\theta)$, calculated by

$$\begin{aligned} F(\theta) &= \int dx \frac{1}{p(x|\theta)}\left(\frac{\partial p(x|\theta)}{\partial\theta}\right)^2 \\ &= \sum_i^{N_x} \frac{1}{p(x_i|\theta)}\left(\frac{\partial p(x_i|\theta)}{\partial\theta}\right)^2, \end{aligned} \tag{2.6}$$

  where the second line is specifically related to a discrete number of possible measurement outcomes N_x.

[1] A POVM is defined by a set of Hermitian operators which produce a positively-valued expectation values with a normalised probability distribution [39].

One may interpret the Fisher information as the curvature of the logarithmic probability distribution: If it is completely flat, hence giving no information, $F(\theta_0) = 0$, if it is strongly peaked, indicating a clear parameter estimate, $F(\theta_0) \gg 0$.
The corresponding cost function may be defined as

$$J_{\text{Fisher}} = \frac{1}{N_M F(\theta)}. \tag{2.7}$$

Reviews introducing Fisher information in the context of quantum sensing and metrology were written by Degen et al. [105] and Pezze et al. [72]. The original paper relating Fisher information and quantum mechanics was published in 1994 by Braunstein and Caves [106]. Applications of Fisher information as a part of optimal control can be found in references [107, 108].

- **Limited power** (running cost)
  The power of a control pulse is typically calculated as $P_i = \int_0^T |u_i(t)|^2 dt$. To limit P_i to a reasonable range $P_i \in [0, P_{\text{lim}}]$ a penalty term can be introduced which adds a high cost to J, if a certain limit is crossed.

$$J_{\text{power}} = \kappa(P_i) = \kappa\left(\int_0^T |u_i(t)|^2 dt\right). \tag{2.8}$$

  The function $\kappa(P_i)$ should give very little to no penalty, if the power is within the acceptable range $\kappa(P_i \ll P_{\text{lim}}) \to 0$ and a high penalty, if it is out of range $\kappa(P_i \gg P_{\text{lim}}) \to \infty$. These criteria can be satisfied by a wide variety of functions and it depends on the chosen system. Examples can be found in a number of references [23, 19, 109, 110].

- **Limited bandwidth** (running cost)
  There is a number of ways to limit the bandwidth of the controls. One solution is to gently punish any quickly oscillating solutions through

$$J_{\text{bandw}} = \epsilon \int_0^T \left(\frac{\partial u(t)}{\partial t}\right)^2 dt, \tag{2.9}$$

  where ϵ is some small factor [111]. It should be noted that this expression, does not give strict bounds in terms of bandwidth. An alternative, stricter approach is to punish fast oscillations, only if they lie outside a pre-defined filter function as described by Sch "afer et al. [112] and Kosloff's group [113, 20]. A completely different approach is to restrict the basis of the control pulses. This is possible with certain algorithms of

the (d)CRAB family including GROUP, and GOAT and will be further discussed in section 2.2.2.

There are many more possible terminal costs, each describing a different control problem including partial state transfer, taking into account the full density function, maximising entanglement [1], or adjusting a certain observable [114]. Similarly, equally many different running costs exist e.g. to avoid populating fast decaying states [115].

Gate Optimisation

In the experiment by Frank et al. [26] the control objective was to optimise a unitary defined as the Hadamard gate

$$U_t = \frac{1}{\sqrt{2}}\begin{bmatrix} 1 & -i \\ -i & 1 \end{bmatrix}.$$

Hence the cost function may be defined as

$$J = J_{\text{gate}} = 1 - \frac{1}{4}\left|\text{Tr}\left(U_t^\dagger U(T)\right)\right|^2. \tag{2.10}$$

We can see that this is a good cost function as it is minimal when $U(T) = U_t$ at the final time T (up to a global phase). If we were to also include a bandwidth limitation on the two control pulses $u_1(t)$ and $u_2(t)$, we may simply sum up different cost terms. The resulting cost function, where ϵ_i are some small factors, would be

$$\begin{aligned} J =& J_{\text{gate}} + J_{\text{bandw}} = 1 - \frac{1}{4}\left|\text{Tr}\left(U_t^\dagger U(T)\right)\right|^2 \\ &+ \epsilon_1 \int_0^T \left(\frac{\partial u_1(t)}{\partial t}\right)^2 dt + \epsilon_2 \int_0^T \left(\frac{\partial u_2(t)}{\partial t}\right)^2 dt. \end{aligned} \tag{2.11}$$

Running costs favour acceptable types of controls, as opposed to physically impossible ones, but if stricter limits are required, control space restrictions might be the more suitable mean of limitation.

2.2.1.3 Control Space Restrictions

While the running costs (see section 2.2.1.2) can only passively punish controls which lie outside the achievable frame, control space restrictions actively change the controls to only allow what is experimentally achievable. One might imagine them as a horizontal squeezing and stretching of the control landscape or as the introduction of hard walls (see Fig. 2.2),

opposed to a vertical distortion induced by running costs.

Restricting the Control Amplitude

As an example, let us consider the amplitude of a control pulse $u_i(t)$ that should be restricted to $u_i^{\max}$. The pulse could be cut off at the beginning of each iteration according to

$$\tilde{u}_i(t) = \begin{cases} u_i(t), & \text{if } -u_i^{\max} < u_i(t) < u_i^{\max} \\ u_i^{\max}, & \text{if } u_i(t) \geq u_i^{\max} \\ -u_i^{\max}, & \text{if } u_i(t) \leq -u_i^{\max}. \end{cases}$$

This form ensures maximum exploitation of the amplitude space but is not differentiable, hence it requires that the control pulse is cut off during an extra step (Fig. 2.1) before the cost function and/or gradient is evaluated [116].
An alternative approach is mapping the control pulse to a restricted subspace using a continuous function. For example by replacing it with $\tilde{u}_i(t) = u_i^{\max} \sin(u_i(t))$ [117].
Another common example for the application of mapping are shape functions. They restrict the overall shape of the pulse, which is useful, if e.g. the experiment requires a smoothly rising and falling control pulse with $\Gamma(0) = \Gamma(T) = 0$, such that $u_i'(t) = \Gamma(t)u_i(t)$.

2.2.1.4 Initial Guess and Stopping Criterion

Numerical optimal control techniques are based on iterative algorithms, which require a starting point (called "initial guess") and a clearly defined situation to stop at i.e. the stopping criterion. The optimisation will in most cases find the the closest local minimum to the initial guess (see examples in Fig. 2.2). Accordingly, it is often helpful to try a number of initial guesses to find which one is closest to the global minimum.
The stopping criterion is simpler to define: It might be based on the maximum number of iterations (limited computation time or experimental run time), a measure for convergence or the clear definition of a goal.

2.2.1.5 Robustness

Usually, there is some discrepancy between the theoretical model and the experiment. In an optimisation, this can be taken into account to ensure that the optimised pulses will work in the presence of such a discrepancy by averaging over cost functions for slightly different systems. Let us consider each system being described by the Hamiltonian $\hat{H}_i$, then by taking

into account N_{rob} different versions, the cost function becomes

$$J_{\text{robust}} = \frac{1}{N_{\text{rob}}} \sum_{i=1}^{N_{\text{rob}}} J(H_i). \tag{2.12}$$

Robustness Against Detuning

The resonance line of the NV center has a finite width and can be described by the normalised distribution $f(\omega)$. Off-center NV centers can however still be described with the Hamiltonian $\hat{H}$ in Eq. (2.2) by adjusting the static magnetic field $B_{\parallel}$ and hence the detuning Δ. One may average the cost over N_{det} different detunings Δ_i to get a robust cost function

$$J = \frac{1}{N_{\text{det}}} \sum_{i=1}^{N_{\text{det}}} J(\hat{H}(\Delta_i)) f(B_{\parallel}\gamma_{nv} - \Delta_i). \tag{2.13}$$

We can see that this cost function will only reach zero, if all $J(\hat{H}(\Delta_i))$ are zero, ensuring robustness against the detuning. By including the probability distribution $f(B_{\parallel}\gamma_{nv})$, we ensure that the optimisation favours solutions centered on the average detuning.
Due to field inhomogeneities in $B_{\perp}$, the Rabi frequency can also have a finite distribution when considering an ensemble of NV centers. In many optimisations, both detuning and Rabi errors are accounted for simultaneously [118, 109].

2.2.2 Numerical QOC Algorithms

Once the problem has been defined, an algorithm is required to systematically test possible solutions minimising the cost [18]. In this review, we will only describe **numerical** optimisation algorithms as they have produced promising results and a variety of packages exist to implement them (see section 2.2.2.5 for more details).
There are, however, alternative strategies, such as geometrical optimal control [119, 120] (GOC) and shortcuts to adiabaticity [121, 122] (STA). They usually rely on a deeper analytical analysis of the control problem and hence access a smaller solution space than QOC, but can nevertheless be effective. One example is the direct application of Pontryagin's minimum principle (PMP) which falls under the category of GOC. It has been shown to provide time optimal evolution for NV centers [123, 60]. Similarly, STA has been used to implement specific gates on NV centers [124] and protect them from decoherence [125].
Section 2.2.1 started by mentioning the brachistochrone problem, whose solution is usually obtained via an analytical variational approach. In the case of quantum mechanical problems however, one would produce a set of nonlinear equations which, in most cases, cannot be

solved analytically. Instead, a variational approach combined with numerical solving was introduced by Konnov and Krotov [126], and Sklarz and Tannor [127] and further adapted by Ohtsuki et al. [128]. Since then, different attempts have been made to numerically solve this class of problems.
In general, two families of QOC algorithms can be identified: Gradient-free [129] and gradient-based [19]. Gradient-based algorithms determine the derivatives of the cost function with respect to the control pulses to find an improved solution. These methods are usually efficient as they make use of all the available information. Gradient-free methods on the other hand can be applied directly to experiments or to complicated problems, where the gradients are not straightforwardly calculated. In this review, the direct experimental implementation is referred to as closed-loop, while a purely simulation based optimisation is called open-loop. We will start by looking at the working principle of gradient-based optimisation algorithms, before exploring their gradient-free counterparts.

2.2.2.1 Gradient-based Optimisation

To understand how gradient-based algorithms work, let us first consider the effect of a small change Δu in some control $u(t)$ on the cost function $J(u(t))$ (see section 2.2.1.2). If the change Δu is small enough, we can approximate

$$J(u(t)+\Delta u) \approx J(u(t)) + \Delta u \frac{\partial J}{\partial u(t)}. \tag{2.14}$$

We can now deduce the properties Δu should have to decrease J. Indeed it enables us to make small changes and update $u(t)$ iteratively. Consider $\Delta u = -\epsilon \frac{\partial J}{\partial u(t)}$, where ϵ is a small positive factor. In this case, the new cost function becomes

$$\begin{aligned} J(u(t)+\Delta u) &\approx J(u(t)) - \epsilon \left(\frac{\partial J}{\partial u(t)}\right)^2 \\ &< J(u(t)) \end{aligned} \tag{2.15}$$

which is smaller than the previous value, implying an optimisation.
In order to avoid functional derivatives and iteratively improve the cost, the control function $u(t)$ needs to be split up into time independent control parameters $u^{(k)}$. According to the simple updating algorithm above, the new control parameters $u^{(k)\prime}$ become

$$u^{(k)\prime} = u^{(k)} - \epsilon \frac{\partial J}{\partial u^{(k)}}. \tag{2.16}$$

More advanced updating algorithms promise faster convergence. Eq. (2.14) could for example be extended to second-order [126, 130]. A popular method approximating the second-order term from the first-order term is the L-BFGS (limited-memory Broyden-Fletcher-Goldfarb-Shanno) quasi-Newton method algorithm [131, 132].
In the following, we describe the working principles of the GRadient Ascent Pulse Engineering (GRAPE) algorithm as an example for the whole class of algorithms. It was originally designed for Nuclear Magnetic Resonance (NMR) [19] but has since found various applications with NV centers. For another comprehensive explanation, we refer to Saywell et al. [133].

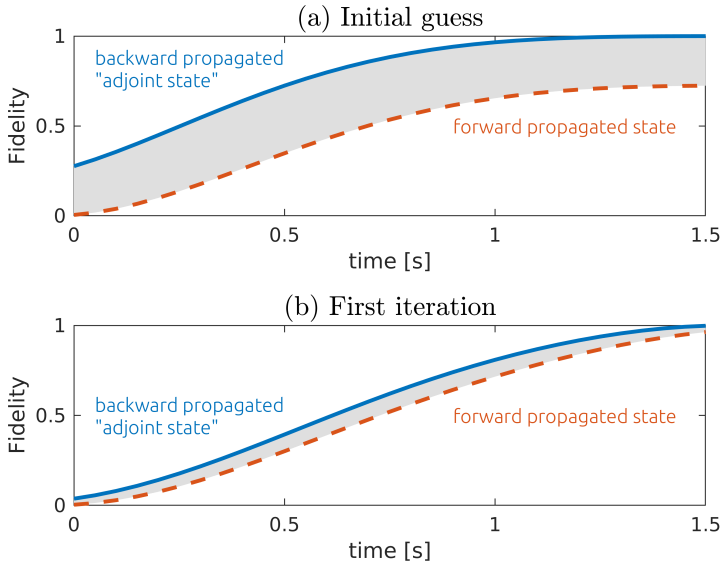

Fig. 2.3 The principle of GRAPE optimisation. A state $|\phi(t)\rangle$ was propagated for a time $T = 1.5$s according to the Hamiltonian in Eq. (2.2). The fidelity $|\langle\phi(t)|\phi_t\rangle|^2$ is plotted as a function of time. The upper panel (a) shows the fidelities resulting from the initial guess for the control pulse of a quantum process. The large grey area indicates that the forward propagated state (dashed orange) and the adjoint state (solid blue) do not match, i.e. the target state is not reached. By calculating the derivatives w.r.t. the different time slices, an updated control pulse was found using GRAPE producing the lower panel (b) with a clearly improved fidelity.

GRAPE Optimisation of a State Transfer

We start by defining an exemplary cost function J, where $J = 0$ implies the target state ϕ_t is reached at a time T (also see section 2.2.1.2):

$$\begin{aligned} J = J_{\text{state}} &= 1 - |\langle \phi_t | \phi(T) \rangle|^2 \\ &= 1 - |\langle \phi_t | U(T) | \phi_0 \rangle|^2, \\ \text{where } U(T) &= \hat{T} \exp\left(\int_0^T -\frac{i}{\hbar} \hat{H}(t) dt \right), \end{aligned} \tag{2.17}$$

The initial state is defined as $|\phi(0)\rangle = |\phi_0\rangle$ and $\hat{T}$ is the time ordering operator.
In order to take the derivatives of J, we choose the piece-wise constant control basis, chopping up the control pulses into N small slices $u_i^{(k)}$ of width Δt. This gives a new way to formulate the propagator $U(T)$:

$$U(T) = \hat{T} \prod_k \exp\left(-\frac{i\Delta t}{\hbar} (\hat{H}^d + \sum_i u_i^{(k)} \hat{H}_i^c) \right) = \hat{T} \prod_k U^{(k)} \tag{2.18}$$

It should be noted that this basis is not the only possible choice but intrinsic to GRAPE (as well as to other gradient based algorithms like Krotov [134]). We can now reformulate the cost function as

$$J = 1 - |\langle \phi_t | U^{(N)} U^{(N-1)} \dots U^{(1)} U^{(0)} | \phi_0 \rangle|^2. \tag{2.19}$$

We start by calculating the derivatives of $\langle \phi_t | \hat{T} \prod_k U^{(k)} | \phi_0 \rangle$ w.r.t. the control parameters.

$$\frac{\partial}{\partial u_i^{(k)}} \langle \phi_t | U^{(N)} U^{(N-1)} \quad \dots \quad U^{(k)} \quad \dots \quad U^{(1)} U^{(0)} | \phi_0 \rangle \tag{2.20}$$

$$= \underbrace{\langle \phi_t | U^{(N)} U^{(N-1)} \dots U^{(k+1)}}_{\langle \xi^{(k)} |} \frac{\partial U^{(k)}}{\partial u_i^{(k)}} \underbrace{U^{(k-1)} \dots U^{(1)} U^{(0)} | \phi_0 \rangle}_{|\phi^{(k)}\rangle} \tag{2.21}$$

$$\begin{aligned} &= \left\langle \xi^{(k)} \right| \frac{\partial U^{(k)}}{\partial u_i^{(k)}} \left| \phi^{(k)} \right\rangle, \\ \frac{\partial J}{\partial u_i^{(k)}} &= -2\text{Re} \left\{ \left\langle \xi^{(k)} \right| \frac{\partial U^{(k)}}{\partial u_i^{(k)}} \left| \phi^{(k)} \right\rangle \langle \phi_0 | U^\dagger(T) | \phi_t \rangle \right\}. \end{aligned} \tag{2.22}$$

We have defined the forward propagated state $\left|\phi^{(k)}\right\rangle$ and the backward propagated state $\left\langle \xi^{(k)}\right|$, which is usually referred to as the adjoint state.[a] They can both be easily

calculated by solving Schrödinger's equation. A graphical representation is given in Fig. 2.3. We applied the chain rule to find the gradient of J. In the case that the control pulses are mapped to a restricted subspace (see section 2.2.1.3), the chain rule can be used again.
The last thing left to evaluate are the following directional derivatives:

$$\frac{\partial U^{(k)}}{\partial u_i^{(k)}} = \frac{\partial}{\partial u_i^{(k)}} \left[\exp\left(-\frac{i\Delta t}{\hbar} \left(\hat{H}^d + \sum_i u_i^{(k)} \hat{H}_i^c \right) \right) \right]. \tag{2.23}$$

[a] Due to an error in the published version, Eq. (2.22) has been corrected in this thesis.

All in all, any gradient-based optimisation algorithm relies on calculating the first derivative of the cost function with respect to the control parameters. On top of this specific example of GRAPE, we list below the most commonly used gradient-based QOC algorithms and their natural features (for an illustration of the terms "sequential" and "concurrent" see Fig. 2.4):

- GRAPE [19, 132]
  GRadient Ascent Pulse Engineering concurrently optimises in the piece-wise constant basis.

- Krotov [134, 126, 130, 135, 104, 127]
  Krotov's method sequentially optimises one control parameter after the other. It also relies on the piece-wise constant basis.

- GROUP [136]
  GRadient Optimisation Using Parametrisation is based on GRAPE combined with the chain rule and optimises concurrently. Its chopped basis is flexible (also see "CRAB" in section 2.2.2.3) but relies on an initial piece-wise constant basis.

- GOAT [117]
  Gradient Optimisation of Analytic conTrols is based on a system of equations of motion obtained by differentiating the full propagator with respect to the control parameters. The parameters are optimised concurrently and its chopped basis is flexible (also see "CRAB" in section 2.2.2.3).

2.2.2.2 Gradient-free Optimisation

In an experiment, the gradients described above cannot be calculated analytically. Certain finite-difference methods help to find them regardless [137–139]. However, if the control

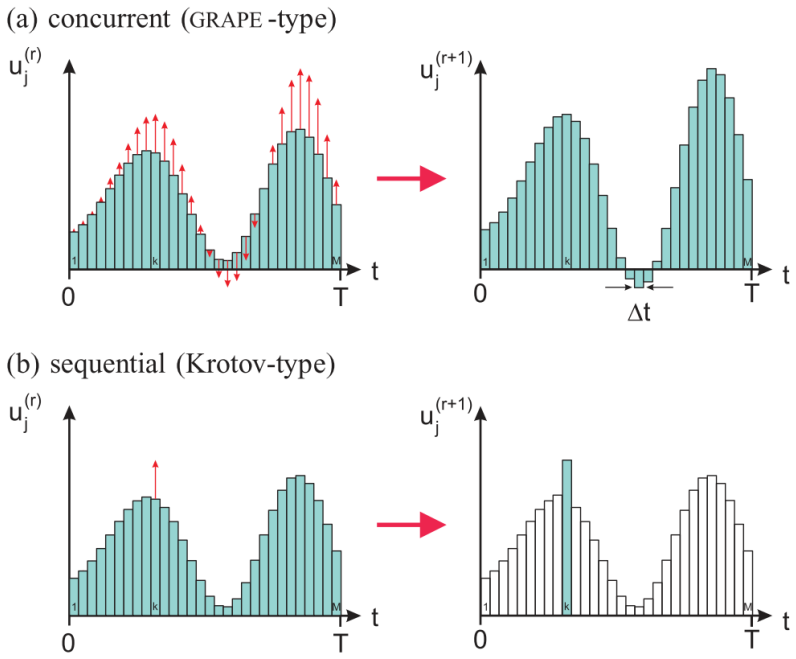

Fig. 2.4 The difference between concurrent (a) and sequential (b) QOC algorithms is illustrated. For concurrent algorithms, the update is calculated at once for the entire time grid. For sequential algorithms, the pulse's basis components i.e. time slices are updated sequentially, meaning that in each iteration the forward propagated state is calculated with the latest version of the pulse. Reprinted figure with permission from [22]. Copyright 2018 by the American Physical Society.

landscape is not smooth this method might prove inefficient or very costly in terms of measurements. This is where gradient-free optimisation algorithms shine. Even for certain open-loop optimisations they can offer an alternative, when their gradient-based counterparts fail: If e.g. the dynamics of a system are significantly more complicated than described in section 2.2.2.1, the gradient of the cost function might be hard or impossible to find analytically. One example for such a case is the CRAB algorithm, described below, which was initially introduced to optimise many-body problems using tensor networks to simulate the time dynamics [129].

The first step then is to choose an optimisation basis. In the following, we will focus on the CRAB algorithm (see section 2.2.2.3) and consider the basis of trigonometric functions but it should be noted that we could also use Slepians, Chebyshev polynomials or indeed piece-wise constant elements. Broadly following Caneva et al. [23] the expanded control

pulses each take the form

$$u^n = \sum_{\ell=1}^{N_{\text{be}}} [A_\ell^n \sin(\omega_\ell t) + B_\ell^n \cos(\omega_\ell t)]. \tag{2.24}$$

Each pulse is composed of a sum of N_{be} basis elements. Each basis element is defined by a frequency ω_ℓ and the control parameters $[A_\ell^n, B_\ell^n]$. The index n stands for the iteration number.
If the number of available basis elements is restricted (i.e. only a certain region of frequency space is accessible), this is called a chopped basis (CB). Especially in the case of bandwidth limitations, only optimising in the accessible restricted control space can be a powerful tool to avoid introducing distorting penalty terms (see section 2.2.1.2). Decreasing the number of parameters, also shrinks the size of the search space, potentially making the optimisation a lot more efficient.

2.2.2.3 CRAB

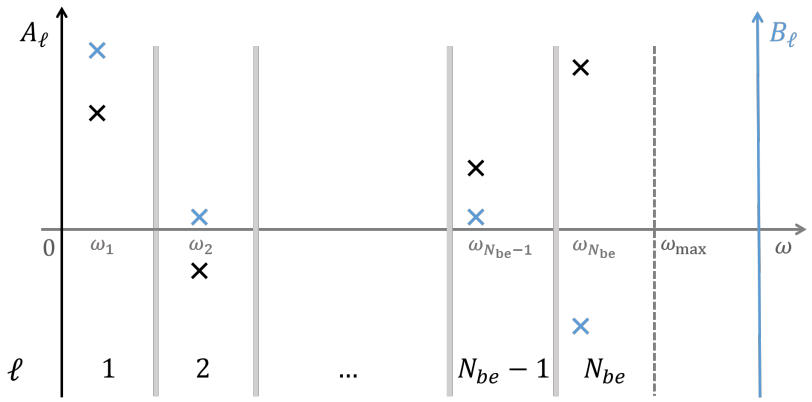

Fig. 2.5 Illustration of the chopped random basis. A frequency space is segmented into N_{be} parts. In each part ℓ, a frequency ω_ℓ is randomly selected according to Eq. (2.25). Two corresponding parameters, A_ℓ and B_ℓ, are optimised. They are defined as in Eq. (2.24) and represented in this plot by black and blue crosses.

The Chopped RAndom Basis algorithm (CRAB) [23, 129] is defined by the optimisation of a random choice of basis elements taken from a truncated function space. Intuitively, one might instead chose the basis elements to coincide with the principal harmonics of the pulse. However, Caneva et al. [23] showed that randomness can be surprisingly effective, especially if the energy scales of the system are not fully known. Indeed, a larger function space is covered, if multiple optimisations are done with different randomised bases. The elements

that make up the basis of our example in Eq. (2.24) are defined by the frequencies ω_ℓ and are illustrated in Fig. 2.5. These frequencies are chosen according to

$$\omega_\ell = \frac{\omega_{\max}}{N_{\text{be}}}\left(\ell + r_\ell - \frac{1}{2}\right), \tag{2.25}$$

where $\omega_{\max}$ is the maximum admissible frequency and $\ell = \{1, 2, ..., N_{\text{be}}\}$ is an index which selects the chunk of the frequency space that ω_ℓ is chosen from. Let us further choose the random numbers r_ℓ from an interval $[-0.5, 0.5]$. Then the bandwidth of the control pulses is automatically limited to $[0, \omega_{\max}]$, where a typical choice is $\omega_{\max} = 2\pi N_{\text{be}}/T$ (T refers to the length of the pulse). By changing the $\omega_{\max}$, we can change the bandwidth. Moreover, we can see that the available frequency space has been split into N_{be} regions permitting the optimisation to make use of the entire space. It also conditions the optimisation problem to have clearly distinct control parameters. It should be noted that the number of basis elements should be dependent on the number of degrees of freedom inherent to the system [140, 141, 128, 142].
During the optimisation the $2N_{\text{be}}$-dimensional landscape will be followed using any updating algorithm (it could even be gradient-based as in GOAT and GROUP). The most common choice is the gradient-free Nelder-Mead algorithm [143] (hence the description of this algorithm under gradient-free algorithms) but others such as CMA-ES [144], genetic algorithms or reinforcement learning are possible.

2.2.2.4 dCRAB

In the basic version of CRAB, the basis elements are fixed and the local control landscape is explored for all N_{be} frequencies simultaneously. This leads to a restriction in the number of frequencies that can efficiently be optimised. Using the dressed Chopped RAndom Basis algorithm (dCRAB), much fewer basis elements with $\omega_{d,\ell}$ need to be optimised at a time ($N_{\text{be}}(\text{dCRAB}) < N_{\text{be}}(\text{CRAB})$). Instead, when one CRAB routine converges, we move on to $\omega_{d+1,\ell}$. This enables the method to include an arbitrarily large number of bases and to derive the solutions without – whenever no other constraints are present – being trapped by local optima. The extra iterations changing up the basis after each CRAB-run are called superiterations and the index d refers to the d^{th} superiteration. Their effect is illustrated in Fig. 2.6. If their number is fixed to N_{SI}, the full description of the pulse can be summed up at the end of the optimisation u^{opt}, with all optimised parameters $A^{\text{opt}}_{d,\ell}, B^{\text{opt}}_{d,\ell}$ as

$$u^{\text{opt}} = \sum_{d=1}^{N_{\text{SI}}} \sum_{\ell=1}^{N_{\text{be}}} [A^{\text{opt}}_{d,\ell} \sin(\omega_{d,\ell} t) + B^{\text{opt}}_{d,\ell} \cos(\omega_{d,\ell} t)]. \tag{2.26}$$

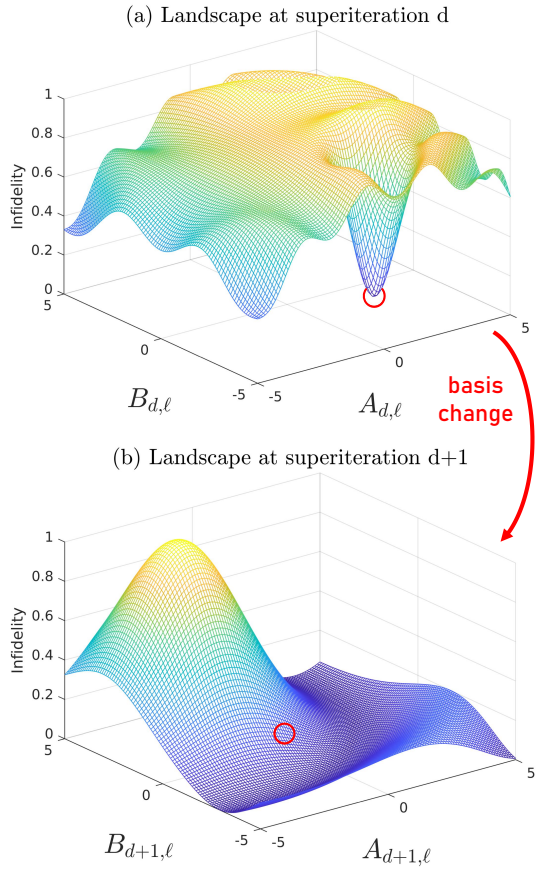

Fig. 2.6 By changing the basis of the optimisation from (a) to (b) the landscape is transformed. The prior minimum (red circle), is relocated, making it possible to escape local minima and reduce the convergence time.

In each superiteration only the parameters with corresponding index d are optimised. By repeatedly changing the basis, dCRAB does not get caught in local minima for most control problems and thus allows to retain this advantageous property of unconstrained control algorithms in a parametrised (e.g. bandwidth limited) setting. Rach et al. [140] explored the improvement from CRAB to dCRAB in detail considering the random Ising model. They found that convergence may be achieved by taking enough parameters to fix the degrees of freedom present in the optimisation problem. The underlying algorithm used for both CRAB and dCRAB performed best for a basis with 10-20 parameters. This allowed dCRAB to outperform CRAB as it requires less optimisation parameters per optimisation (i.e. superiteration).

All in all, dCRAB, promises faster convergence with respect to CRAB as fewer parameters are optimised in parallel and instead, new basis elements are chosen sequentially. An example

Table 2.1 Quantum Optimal Control Packages. In this table four widely-used Optimal Control software packages are presented which implement some of the previously described algorithms. Note that the list is not exhaustive.

Name	QOC Algorithm	Gradient required	Access	Specialty
RedCRAB[abc] [6, 5]	dCRAB	no	on request	allows connection directly to experiment
DYNAMO[a] [22]	GRAPE, Krotov	yes	github	many pre-programmed optimisation options
QuTiP[b] [145, 146]	GRAPE, CRAB	yes, no	pip, conda, etc.	all-round quantum simulation
Krotov Package[b] [147]	Krotov	yes	pip, conda, etc.	Connects to QuTip, many pre-programmed optimisation options

Environment:
[a] MATLAB
[b] python
[c] command line

for its experimental application to NV centers, among others, can be found in the work of Frank et al. [26] where a Hadamard gate was optimised.

2.2.2.5 Optimal Control Packages

In the past years, a number of QOC algorithms were implemented in ready-to-use software packages. In this section, we present four of these packages that we deem to be closest to applications with NV centers. An overview over some of their distinguishing features is given in Table 2.1. Nevertheless, more solutions exist.

RedCRAB [6, 5] is a python based programme, aiming to remotely optimise any experiment or simulation with gradient-free methods. It can be linked to the experiment setup via MATLAB, python, terminal or simple file transfer and is hence very versatile. RedCRAB makes use of the dCRAB alogithm and provides pulse updates. As it does not require any knowledge about the quantum system itself, it is compatible even with more complicated many-body systems and tensor-network simulations. RedCRAB is available from the authors on request.

DYNAMO [22] was originally developed as a GRAPE (and Krotov) implementation in

MATLAB. It allows the user to choose their own Hamiltonian and dissipator terms as well as one of the available figures of merit. Hence, it combines simulation and optimisation for certain problems dealing with small quantum systems. It allows for the optimisation of robust pulses and includes a large number of examples. The full version is available on github.
QuTiP [145, 146] is an open source python library for simulating quantum systems. One of its features is a quantum optimal control implementation. As such it offers limited optimisation techniques with GRAPE and CRAB. Conveniently, the optimisation settings are defined with the usual QuTiP structure. The library is available for example via pip or conda.[2]
The Krotov package [147] is an open source python library built on top of QuTiP. As such it offers optimisation via Krotov's method. It includes an extended range of settings in comparison to QuTiP's own QOC implementation. The library is available for example via pip and conda.
Other QOC packages include Spinach [148] and SIMPSON [31], which focus on NMR applications, as well as QEngine [136, 149] which includes a GROUP implementation designed especially for ultra-cold atom physics. GRAPE was also recently implemented in the GRAPE-Tensorflow python package [150], using methods known from machine learning to calculate the gradients.

2.2.3 Limits of Control: Controllability, and the Quantum and Information Speed Limits[3]

Whether or not a QOC problem is (approximately) solvable, is not always simple to answer. However, by examining a number of characteristics of the Hamiltonian, some general predictions can be made.
First of all, one may ask whether the control objective is in principle reachable. This can be addressed by examining the controllability of the system [151]. The drift and control Hamiltonians define a certain state (and also gate) space that is reachable. A system is called controllable when all states (gates) in the Hilbert space are accessible in finite time. It has been shown that, if the rank of the dynamical Lie algebra generated by the different terms of the Hamiltonian corresponds to the rank of the control space (and fulfills certain symmetry criteria), the system is fully controllable. Alternatively, the question of state-controllability can be examined via a geometric approach based on graph theory, which can be more convenient to check, especially for larger systems [152]. For more information on controllability, please refer to the following books [151, 153]. For open quantum systems,

[2] Popular python package managers
[3] The title has been changed with respect to the publication to better reflect the content of the subsection.

the deleterious effect of the environment usually can not be completely canceled and only a subset of the whole set of states (gates) can be reached [17].
If the controllability criteria are fulfilled, the question remains whether the controls are complex and energetic enough to navigate the Hilbert space to the specified target. In general, the quantum speed limit (QSL), i.e. the smallest possible control time needed for a system to reach its target, is influenced by two factors. First, the dynamical equation determines how fast the system may change. This is usually quantified by the so-called Schatten p-norm of the dynamical operator (see reference [154] for details). Second, the exact distance between the initial system to the objective needs to be taken into account.

Quantum Speed Limit

The minimum time it takes to evolve a system into a target state is mostly dependent on two things: The Hamiltonian $\hat{H}$ and the distance between the initial and the target state $\langle\phi_0|\phi_t\rangle$. For a time-independent Hamiltonian, we obtain the Bhattacharyya-bound [155, 156]:

$$T_{\mathrm{QSL}} \geq \Delta E^{-1} \arccos|\langle\phi_0|\phi_t\rangle| \tag{2.27}$$

This time T_{QSL} is called the quantum speed limit (QSL). It can be interpreted as follows: If the Hamiltonian has a high energy variance calculated on the initial state $\Delta E = \sqrt{\langle\phi_0|\hat{H}^2|\phi_0\rangle - \langle\phi_0|\hat{H}|\phi_0\rangle^2}$, then any other state is reached more quickly. It might be more intuitive to consider the case that ϕ_0 is an eigenstate of $\hat{H}$, hence it will never change and as $\Delta E = 0$, the speed limit will go towards infinity. The distance to the target state finally determines the exact time scale.

For a more general and complete picture of the QSL the reader is advised to refer to the following references [156, 154].
Similarly to the QSL, the information speed limit (ISL) can also restrict the minimum length of the control pulse. Behind this is the idea that the information encoded in the control pulse has to be sufficient to steer the system to the target. For example, in the noiseless case the degrees of freedom in the control (the number of independent frequencies in a bandwidth-limited control field or the number of kicks in a bang-bang control [157]) should at least reflect the dimension of the system [141]. Note that in the presence of noise in the system or in the controls, more degrees of freedom are required to transmit the same amount of information.

2.3 The Sigmoid Basis

The subsequent section is in preparation for publication [158].

2.3.1 Introduction

Finding an optimal pulse for a concrete application starts by imposing restrictions on the pulse $u(t)$ that are given by a corresponding experiment or the state of the art. Typically, one can identify three major types:

R.1 Restriction in time (finite length): $u(t) = 0$, if $0 \geq t$ or $t \geq T$

R.2 Restriction in amplitude (finite strength): $|u(t)| \geq A_{\max}$

R.3 Restriction of the rise time (finite gradient): $u'(t) \leq G_{\max}$
or restriction of the spectrum (finite bandwidth envelope): $\mathcal{F}[u(t)] = Y(\omega) \leq Y_{\max}(\omega)$

Several strategies have been developed to impose these conditions, some of which are described in Section 2.2.1.3. For the Fourier basis, these restrictions are vital as, by nature, it produces infinitely long pulses which are limited only in bandwidth. By clipping them in either amplitude or time, they also lose their strict bandwidth properties. Shrinking the pulse to fit inside the limits or applying a scaling function represent other solutions. Unfortunately, they restrict access to maximum amplitude values (e.g. producing a square pulse is very complex using only trigonometric elements). All in all, the example of the Fourier basis shows two things: First, imposing restrictions also leads to a new set of basis properties. Second, both the basis and the type of restrictions influence which shapes are complex or simple to produce.
We have designed a basis that intrinsically contains the three limits described above. As a result, its properties are well-defined. Its close relationship to the piece-wise constant basis known from GRAPE [19] and Krotov [134, 126] optimisations (see Section 2.3.5.1) makes it a potential connector between gradient-based and gradient-free algorithms. The design of the basis results in amplitude-maximising shapes such as square pulses to be constructible from a low number of basis elements.

2.3.2 Definition

We consider the pulse basis elements $u_p(t)$ to be sigmoid functions. Sigmoids can in general be defined as the integral of a function with a single maximum at the centre. For the

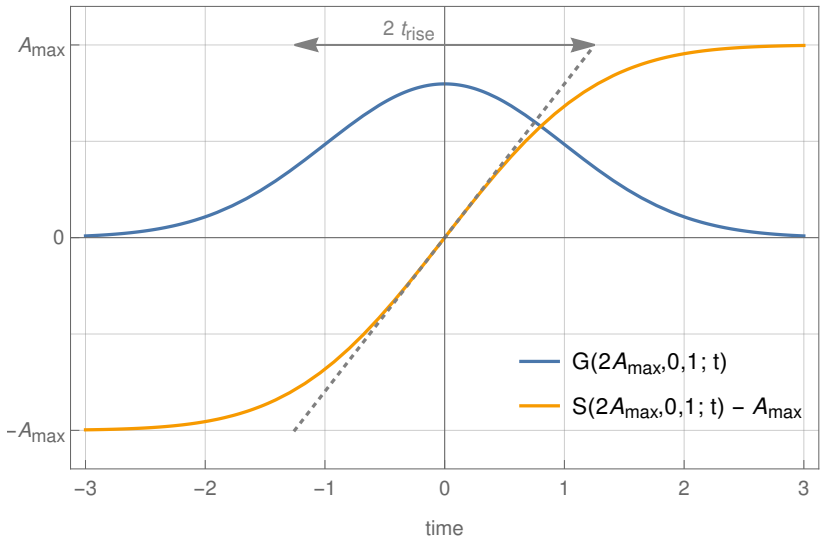

Fig. 2.7 Exemplary basis function $S(A_p,\tau_p,\sigma;t)-A_{\max}$ and its derivative $G(A_p,\tau_p,\sigma;t)$ with $A_p = 2A_{\max}$, $\tau_p = 0$, $\sigma = 1$. The dotted line represents a linear function with the maximum gradient $S'(A_p,\tau_p,\sigma;0) = G(A_p,\tau_p,\sigma;0) = A_{\max}/t_{\text{rise}}$.

sake of simplicity, we only consider the sigmoid function that is defined by the integral of the Gaussian $G(A_p,\tau_p,\sigma;\ t)$. Hence the sigmoid basis element can be defined through its derivative:

$$\begin{aligned} u'_p(t) &= \frac{A_p}{\sqrt{2\pi}\sigma} e^{-\frac{1}{2}\left(\frac{t-\tau_p}{\sigma}\right)^2} \\ &= G(A_p,\tau_p,\sigma;\ t). \end{aligned} \tag{2.28}$$

Each element is characterised by the amplitude A_p, the centre time τ_p and the width σ. Accordingly, the sigmoid function $S(A_p,\tau_p,\sigma;\ t) = \int G(A_p,\tau_p,\sigma;\ t')dt'$ resembles a smooth step function going from 0 to A_p at a time τ_p as shown in Fig. 2.7. The full basis element is defined as

$$\begin{aligned} u_p(t) &= \frac{A_p}{\sqrt{2\pi}\sigma} \int_{-\infty}^{t} e^{-\frac{1}{2}\left(\frac{t'-\tau_p}{\sigma}\right)^2} dt' \\ &= A_p \frac{1}{2}\left(1 + \operatorname{erf}\left(\frac{t-\tau_p}{\sqrt{2}\sigma}\right)\right) \\ &= S(A_p,\tau_p,\sigma;\ t), \end{aligned} \tag{2.29}$$

where $\operatorname{erf}(z)$ denotes the error function.

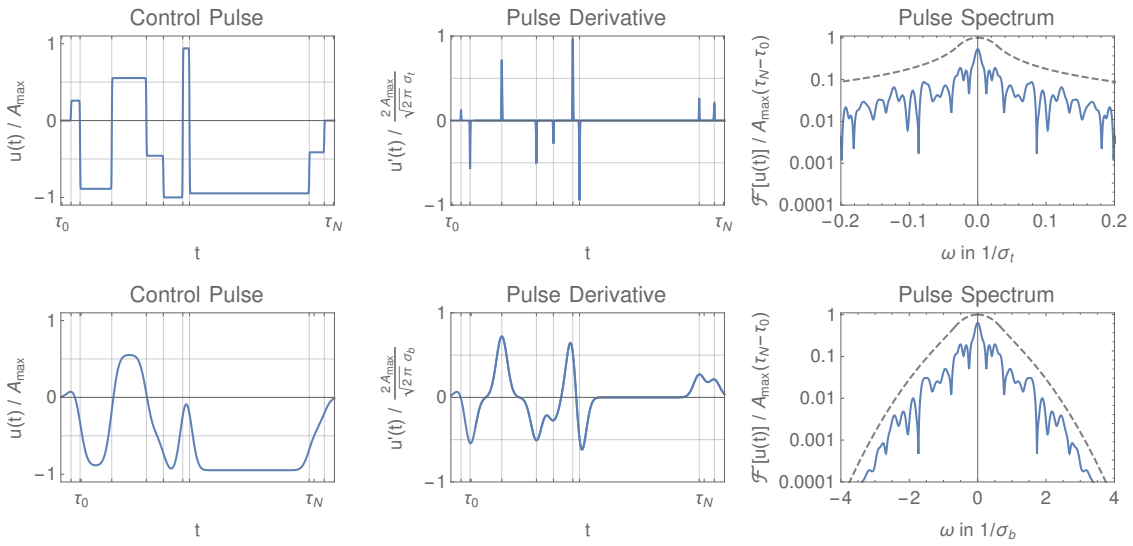

Fig. 2.8 The effect of σ. From left to right, one can see a sigmoid basis control pulse, its derivative, and its spectrum. The top row shows a pulse constructed from basis elements with $\sigma_\mathrm{t} = \frac{1}{20}\sigma_\mathrm{b}$, i.e. a much lower sigmoid width than that of the bottom row σ_b. The right collumn is plotted over the same frequency range but given in terms of the respective σ to emphasise the effect. The dashed line shows the respective bandwidth envelope (see Section 2.3.4).

2.3.3 Imposing Constraints

First, let us consider how to enforce the restriction of the rise time R.3 via the choice of σ. To restrict the maximum derivative to that of a linear rise of length t_rise from 0 to A_max one simply needs to choose

$$\sigma \geq \sqrt{\frac{2}{\pi}}\, t_\mathrm{rise}. \tag{2.30}$$

The result of this constraint is a maximum derivative of $G_\mathrm{max} = \frac{A_\mathrm{max}}{t_\mathrm{rise}}$ shown in Fig. 2.7. Its connection to the bandwidth envelope can be seen in Fig. 2.8. Each control pulse is composed of N basis elements[4], each with two variable parameters, A_p and τ_p. In the following, it is assumed that they are ordered in time, i.e. $\tau_0 \leq \tau_1 \leq ... \leq \tau_N$. We can show that, by automatically adapting the parameters according to a set of rules, one can satisfy the other two limits, R.1 and R.2 .

[4]Please note that N denotes the number of basis elements in this section, not the atom number.

To stay within the limit of pulse length T (R.1), three conditions need to be met:

$$\begin{aligned} &1.\ A_N = -\sum_{p=0}^{N-1} A_p \\ &2.\ \tau_0 \geq \sigma\sqrt{-2\ln\epsilon},\ \text{where } \epsilon \ll 1 \\ &3.\ \tau_N \leq T - \sigma\sqrt{-2\ln\epsilon} \end{aligned} \tag{2.31}$$

The first condition ensures that after N basis elements, the amplitude returns to zero. The second condition fixes the pulse amplitude to zero at $t = 0$. As Gaussians are infinite, this is never fully satisfied but approximately true, as the first derivative of the pulse will obey $\frac{|u'(0)|}{G_{\max}} \leq \epsilon$.[5] Similarly, the third condition fixes the pulse amplitude to approximately zero at $t = T$.

To constrain the control amplitude to $\pm A_{\max}$ (R.2), the time ordering is exploited, resulting in the following condition.

$$-A_{\max} \leq \sum_{p=0}^{m} A_p \leq A_{\max},\ \text{where } m \in \{0, 1, \ldots, N-1\}. \tag{2.32}$$

Starting from zero, each amplitude value A_p can be seen as a step. Thus, the sum of steps gives the current height, which should never exceed the amplitude limits $\pm A_{\max}$. A single step, however, could go from the minimum to the maximum, i.e. $|A_p| \leq 2A_{\max}$.

In conclusion, these restrictions do not change the properties of the basis as they simply set limits inside the natural basis space. This is not a given for other bases, where the constructed pulses are commonly restricted after the basis elements have been combined into a (discretised) pulse function. The advantages of the resulting pulse properties are given below.

2.3.4 Properties

The sigmoid basis is composed of spectrally narrow elements with a time-limited derivative. As a result, even under amplitude and time restrictions, its bandwidth envelope is predictable.

[5] Please note that this will limit the pulse because the pulse converges to zero beyond the limits on either side. For $\epsilon = 10^{-2}$, $|u(0)| \leq 1.2 \times 10^{-3} A_{\max}$ and $|u(T)| \leq 1.2 \times 10^{-3} A_{\max}$.

It is simple to analytically calculate the Fourier transform[6] of the derivative of the single basis element given in Eq. (2.28):

$$\mathcal{F}[u_p'(t)] = e^{-\frac{1}{2}\sigma^2\omega^2} A_p e^{i\tau_p\omega}. \tag{2.33}$$

As the Fourier transform of a sum is equivalent to the sum of Fourier transforms [159], we can write the transform for the full pulse's derivative $u'(t)$ as:

$$\mathcal{F}[u'(t)] = X(\omega) = e^{-\frac{1}{2}\sigma^2\omega^2} \sum_{p=0}^{N} A_p e^{i\tau_p\omega}. \tag{2.34}$$

The spectrum of the pulse $u(t)$ follows from the Fourier identity for integrals [159], resulting in

$$\begin{aligned} \mathcal{F}[u(t)] &= \frac{X(\omega)}{i\omega} + X(0)\delta(\omega) \\ &= \frac{1}{i\omega} e^{-\frac{1}{2}\sigma^2\omega^2} \sum_{p=0}^{N} A_p e^{i\tau_p\omega} + \delta(\omega) \underbrace{\sum_{p=0}^{N} A_p}_{\to 0}. \end{aligned} \tag{2.35}$$

The last term cancels due to R.2 implemented by the first condition in Eq. (2.31). From this expression, one can derive a bandwidth envelope for any constructible pulse, which is only dependent on σ, $A_{\max}$, τ_0, and τ_N. To do so, we consider the pulse with the highest possible integral, i.e. a square pulse with amplitude $A_{\max}$. As the integral corresponds to the zero-frequency component of the spectrum and the pulse is symmetric, we can deduce the amplitude of the bandwidth limiting envelope $Y^{\infty}_{\max}$ shown in Fig. 2.9,

$$\begin{aligned} Y^{\infty}_{\max}(\omega) &= e^{-\frac{1}{2}\sigma^2\omega^2} \lim_{\omega\to 0}\left[\frac{A_{\max}}{i\omega}(1 - e^{i(\tau_N-\tau_0)\omega})\right] \\ &= A_{\max}(\tau_N - \tau_0)\, e^{-\frac{1}{2}\sigma^2\omega^2}. \end{aligned} \tag{2.36}$$

[6] In this chapter, we use the following convention.

$$\mathcal{F}[f(t)] = \int_{-\infty}^{\infty} f(t) e^{-i\omega t} dt$$
$$\mathcal{F}^{-1}[\tilde{f}(\omega)] = \frac{1}{2\pi} \int_{-\infty}^{\infty} \tilde{f}(\omega) e^{i\omega t} dt$$

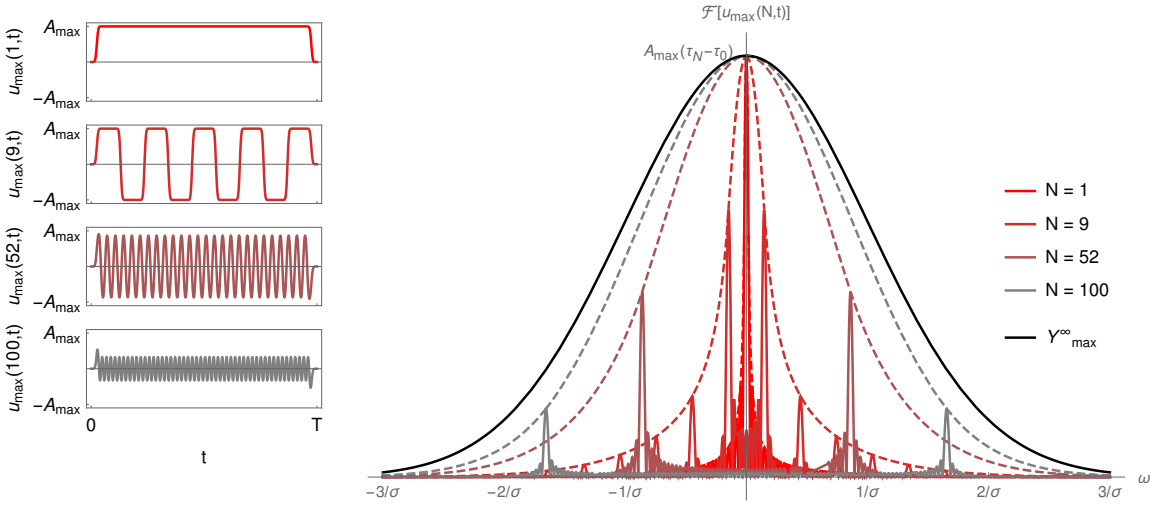

Fig. 2.9 Control pulses composed according to Eq. (2.38) and their corresponding spectra. The dashed lines represent $Y^N_{\max}$, the solid line gives $Y^{\infty}_{\max}$.

Any pulse constructed from the sigmoid basis with the constraints described in Section 2.3.3 will be spectrally limited to $Y^{\infty}_{\max}$. This relation holds for infinitely many basis elements.[7] However, we can be more specific. The limit for a pulse constructed from N basis elements is given by

$$k = \frac{(\tau_N - \tau_0)\omega}{2N}$$
$$Y^N_{\max} = Y^{\infty}_{\max} \begin{cases} -1/k & k \le -\frac{\pi}{2} \\ \sin k/k & -\frac{\pi}{2} < k < \frac{\pi}{2} \\ +1/k & k \ge \frac{\pi}{2} \end{cases}, \tag{2.37}$$

where the piece-wise part is equivalent to the envelope of the function $\mathrm{sinc}(k)$. In fact, $\mathrm{sinc}(k)$ represents the Fourier transform of a square pulse of length $(\tau_N - \tau_0)/N$. The bandwidth envelope $Y^N_{\max}$ is shown for different values of N in Fig. 2.9.

These limits can be checked empirically by assuming that the combination of basis elements with the widest spectral envelope consists of evenly spaced sigmoids. The corresponding pulse $u_{\max}(N,t)$ exhibits the strongest possible high-frequency oscillation that is producible

[7] It should be noted that simply cutting the tails of the spectral distribution would lead to an infinitely long pulse and violation of R.1.

with N basis elements. $u_{\max}(N,t)$ is described by the following conditions:

$$\begin{aligned} \tau_p &= \tau_0 + p\frac{\tau_N - \tau_0}{N} \\ A_0 &= A_{\max} \\ A_N &= A_{\max}(-1)^N \\ A_p &= 2A_{\max}(-1)^p \end{aligned} \tag{2.38}$$

Considering the pulses to be centred on zero gives the following Fourier transform.

$$\mathcal{F}[u_{\max}(N,t)] = Y^{\infty}_{\max}\,\mathrm{sinc}(k)\sum_{p=1}^{N}\mathcal{F}\left[\frac{(-1)^{p+2N}}{N}\delta\Big(t+t_p\Big)\right], \tag{2.39}$$

where $t_p = \left(p - \frac{N+1}{2}\right)\frac{\tau_N-\tau_0}{N}$ corresponds to the midpoint between the steps.
The first term of Eq. (2.39) corresponds to the Fourier transform of the error function, the second to the Fourier transform of a single square pulse and the last part depends on the exact positions of the sigmoids. The Fourier transforms of the delta functions result in oscillatory terms which are normalised to one by the factor $1/N$. As a result the last term has no effect on the envelope given by the first two terms.

2.3.5 Connection to Other Optimisation Methods

2.3.5.1 Piece-wise Constant

Many algorithms commonly apply the piece-wise constant basis. Their most prominent representatives are GRAPE [19] and Krotov's method [126, 134], both of which are gradient-based open-loop optimisation methods. Without the bandwidth-limitation, the sigmoid basis represents the same function-space as the piece-wise constant basis. Equation 2.36 shows that the bandwidth-envelope is equivalent to that of any time-limited function, if the sigmoid width $\sigma_{\mathrm{pc}} \ll 1$ creating genuine step functions. In general, all basis elements are considered to be of the same length which is taken into consideration by

$$\tau_p = \tau_0 + p\Delta\tau, \text{ where } \Delta\tau = \frac{\tau_N - \tau_0}{N}. \tag{2.40}$$

The parameter, scaling the p^{th} sigmoid basis element is given by A_p. Similarly, the k^{th} piece-wise constant element is scaled by $u^{(k)}$ in analogy to Eq. (2.22), where $u^{(0)} = u^{(N+1)} = 0$.

Assuming that $\sigma_{\text{pc}} \ll \Delta\tau$, they are connected by the following relationships:

$$\begin{aligned} A_p &= u^{(p+1)} - u^{(p)}, \\ u^{(k)} &= \sum_{p=0}^{k-1} A_p. \end{aligned} \tag{2.41}$$

The two mentioned examples of gradient-based algorithms provide methods to efficiently calculate the gradient for the piece-wise constant basis, hence we assume that $\partial J/\partial u^{(k)}$ is known. The transformation for an equivalent optimisation in the sigmoid basis then reads

$$\begin{aligned} \frac{\partial J}{\partial A_p} &= \sum_{k=1}^{N} \frac{\partial J}{\partial u^{(k)}} \frac{\partial u^{(k)}}{\partial A_p} \\ &= \sum_{k=p+1}^{N} \frac{\partial J}{\partial u^{(k)}}. \end{aligned} \tag{2.42}$$

This transformation is simple and holds for the above approximations. It could be used to reduce the number of basis elements per optimisation by selecting only a certain set of p-indices or rather distributing the cuts between piece-wise constant elements randomly. Usually, gradient-based optimisations are over-parameterised to avoid local traps. However, for computationally demanding optimisations, this might present an alternative to gradient-free or stochastic gradient approaches [160]. By starting with a small set of τ_p and adding more over a number of super iterations, the complexity of the pulse would slowly increase together with the computational cost of the gradients. For such an optimisation, the condition in Eq. (2.32) would need to be adjusted to take into account the shape of the pulse in between steps but the rest of the constraints would stay the same.

2.3.5.2 dCRAB

The dCRAB algorithm [140] is designed to overcome local minima by changing its basis after reaching convergence. The basis elements are defined by the superparameters which are replaced after each convergence through random picks from a limited (chopped) set. Commonly, these superparameters are represented by frequencies of the trigonometric elements in the Fourier basis. Here, however, they are represented by the set of centre times τ_p. The parameters, which are optimised, are the amplitudes of the respective basis elements. As the bandwidth-limiting envelope is dependent on the number of basis elements, the pulse properties evolve with each super iteration. We have included the sigmoid basis in the software suites RedCRAB [5] and QuOCS [8]. A simplified version of the sigmoid

basis is applied in the project described in Section 3.1. Here, it proves efficient in shaping the spectral properties of the optimised pulses, despite different restriction approaches, and thus enhances the sensitivity of the resulting sensing sequence. It remains to be benchmarked against other bases to test its effect on the landscape for different QOC problems.

2.3.5.3 DRAG

Derivative Removal by Adiabatic Gate (DRAG) [28] aims to create pulses which methodically avoid unwanted transitions in the quantum system at frequency Δ_0. Zeroth order DRAG pulses are described by the relationship between the in-phase I-component $I(t)$ and quadrature Q-component $Q(t)$ of the pulse. The components are orthogonal to each other and equivalent to the real and imaginary parts of the pulse $u(t) = I(t) + iQ(t)$.
First, let us consider a general pulse $f(t)$ which is limited in time i.e. $f(0) = f(T) = 0$. Its Fourier transform is given by $\mathcal{F}[f(t)] = Y(\omega)$. The Fourier identity for the first derivative of such a pulse [159] gives the following relationship.

$$\begin{aligned} \mathcal{F}[f'(t)] = X(\omega) &= -i\omega Y(\omega) \\ 0 &= Y(\omega) + i\frac{X(\omega)}{\omega}. \end{aligned} \tag{2.43}$$

To ensure that the spectrum of $u(t)$ has a node at Δ_0 (i.e. the frequency component at Δ_0 is set to zero), we define the pulse components as

$$\begin{aligned} I(t) &= f(t) \text{ and} \\ Q(t) &= -\frac{f'(t)}{\Delta_0}, \end{aligned} \tag{2.44}$$

such that its Fourier transform can be written as

$$\begin{aligned} \mathcal{F}[u(t)] &= \mathcal{F}[I(t)] + \mathcal{F}[iQ(t)] \\ &= \mathcal{F}[f(t)] - i\mathcal{F}\left[-\frac{f'(t)}{\Delta_0}\right]. \\ &= Y(\omega) + i\frac{X(\omega)}{\Delta_0}. \end{aligned} \tag{2.45}$$

Combining Eq. (2.43) and Eq. (2.45) shows that the Fourier transform is zero at $\omega = \Delta_0$. The effect of zeroth-order DRAG pulses is illustrated in Fig. 2.10.

DRAG pulses can be naturally constructed with the sigmoid basis resulting in $I(t)$ being made up of sigmoids and $Q(t)$ of Gaussians, i.e. the sigmoids' derivatives. After all, the sigmoid basis already limits the first derivative in both amplitude and time. Still, in this case

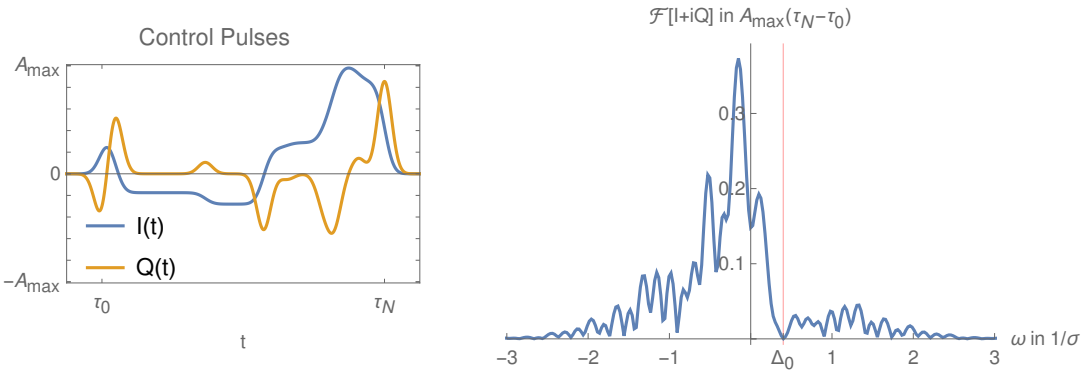

Fig. 2.10 DRAG control pulse constructed with the sigmoid basis. (*left*) I- and Q-component calculated according to Eq. (2.44) with a detuning of Δ_0. (*right*) Pulse spectrum with a distinctive node at Δ_0.[8]

the part constructed from Gaussians has to be properly amplitude-limited. The restrictions can be implemented by adjusting the amplitude limits to $B_{\max} = A_{\max}\sqrt{2\pi}\sigma\Delta_0$, if $B_{\max} > A_{\max}$. For completeness, it should be mentioned that the first order of DRAG connects the detuning of the applied control field δ to the control pulse by

$$\delta(t) = \frac{\left(\lambda_0^2 - 4\right) I^2(t)}{4\Delta_0}. \tag{2.46}$$

This relationship is derived by considering the first three levels of a driven slightly anharmonic system with only nearest level coupling [28]. λ_0 represents the relative strength of the unwanted transition with respect to the targeted transition. As the detuning is not time-limited and its amplitude-limits are usually very wide the condition in Eq. (2.46) can be added to the system without any further limitations.

2.3.6 Outlook

The sigmoid basis has some useful properties that make it worth exploring in more detail: First, the resulting pulses can be straight-forwardly restricted in time, amplitude, and rise time without leaving the sigmoid basis function space. The resulting bandwidth envelope makes its spectrum easily predictable. This provides an alternative to applying additional cost-functions or post-processing the pulses. Second, the sigmoid basis makes it simple to construct pulses with maximum amplitude without cut-offs that would induce high frequency components. Third, it can be adapted to naturally construct DRAG pulses. The resulting

[8] The first derivatives (see restriction R.3) are limited to $I'(t) \leq G_{\max} = \frac{A_{\max}}{\sqrt{2\pi}\sigma}$ and $Q'(t) \leq \frac{2\,e^{-1/2}}{\sigma\Delta_0} G_{\max}$.

optimisation always produces pulses with frequency-holes, again, without additional cost-functions. This concept of automatic DRAG-elements could also be extended to other bases. The sigmoid basis' direct connection to the piece-wise constant basis at $\sigma_{\mathrm{pc}} \ll 1$ and to CRAB-like approaches opens a route to exploring the space between traditional GRAPE/Krotov and dCRAB applications. Especially, when gradient-calculations are expensive but not impossible, the sigmoid basis might provide an efficient alternative to traditional piece-wise constant elements by gradually expanding the parameter space. Generally, many bases exist that have not been explored in detail with respect to their applicability for QOC. Three concepts that have been explored for certain examples and which show promising results are the Slepian [161], the Walsh [162], and the B-spline basis [163, 164]. We suggest benchmarking the sigmoid basis (and others) with different QOC problems to see how the resulting landscape affects convergence [165, 166]. Another approach would be characterising the complexity of known optimal pulses for specific problems with different bases. The complexity could be defined by the minimum number of basis elements required to achieve a threshold overlap between the ideal and constructed controls. The connection between a problem's complexity and the applied basis might point us towards a more efficient use of bases in QOC in general.

Chapter 3

Controlling Quantum Systems

3.1 Magnetic Field Sensing with Shallow NV Centres

3.1.1 Magnetic Field Sensing

The review paper by Degen, Reinhard, and Cappellaro [105] provides three different definitions for quantum sensing. In this section, we focus on the first and second: "Quantum sensing is typically used to describe [the u]se of [(I)] a quantum object [...] [or (II)] quantum coherence (i.e., wavelike spatial or temporal superposition states) to measure a physical quantity."

NV centres have several qualities which make them good sensors [2]. The examples in Chapter 1 illustrate most of them, so here we only give a brief summary: First, NV centres are easily initialised into the $m_s = 0$ ground state via a laser. Next, their state can be read out directly by, again, the application of a laser. To access the NV centre's superposition state and apply elaborate sensing schemes, they can be manipulated via MW fields resonant with either of the $m_s = 0 \leftrightarrow \pm 1$ transitions. Furthermore, the quantum properties of NV centres are accessible at cryogenic or room temperatures where the T_1-times typically are in the tens of milliseconds regime [50, 167]. Not only can they be used to sense magnetic fields [168, 169] but also electric fields [170, 171], temperature [172], and strain [173]. Lastly, NV centres are especially valued in the life sciences due to the bio-compatibility of their host material, diamond [50].

The fields of Nuclear Magnetic Resonance (NMR) and Electron Paramagnetic Resonance (EPR) have produced a plethora of pulsed sensing sequences [174–176]. Some of them are analogously applicable to NV centres, which have the advantage of optical readout. Likely the simplest one is the pulsed Optically Detected Magnetic Resonance (ODMR) sequence [177]. ODMR is a sensing technique, where the electronic spin state is addressed with different

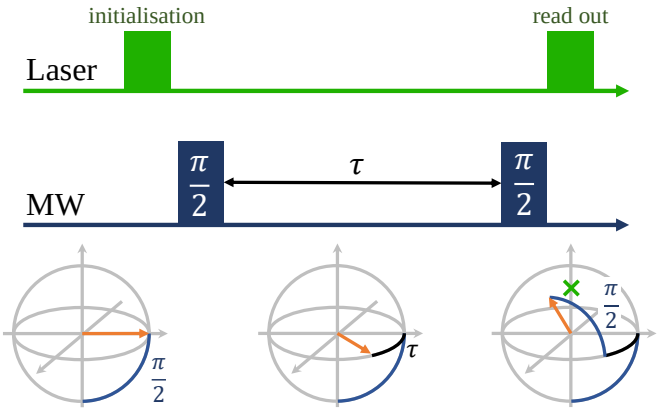

Fig. 3.1 The Ramsey protocol. The laser and MW pulses in the protocol are depicted in green and dark blue, respectively. The last row shows the evolution of the NV centre on the Bloch sphere during the first MW pulse, the free precession time, and the second MW pulse. The green cross indicates the expectation value along z, measured by the read out laser pulse.

drive frequencies, hence scanning over the detuning. When the drive is on resonance with a transition, the fluorescence rate of the NV centre drops. From the position of the resonances, one can determine the Zeeman-splitting. In contrast, the Ramsey sequence [178, 179] shown in Fig. 3.1 is the spin-equivalent of an optical interferometer. Here, the spin is first initialised by a laser pulse. Then, a $\frac{\pi}{2}$-pulse is applied to the initialised NV centre, bringing it into a superposition state. An unknown constant magnetic field along the NV's axis B_{sens} induces a phase ϕ_{ram} over the free precession time[1] τ. Another $\frac{\pi}{2}$-pulse translates the phase into a spin z component, which is read out by a second laser pulse. Typically, this measurement is carried out over a range of τ resulting in an interference pattern with a frequency ω_{ram} that is directly proportional to the amplitude of B_{sens}.

$$\begin{aligned} \omega_{\text{ram}} = \dot{\phi}_{\text{ram}} &= \frac{\partial}{\partial \tau} \left[\tau B_{\text{sens}} \gamma_{\text{nv}} \right] \\ &\sim B_{\text{sens}}, \end{aligned} \tag{3.1}$$

where γ_{nv} is the gyromagnetic ratio of the NV centre. A more detailed description of the process is given in the review by Rembold et al. [2].

[1] Please note that the free precession time τ is different from the pulse element time τ_p for the sigmoid basis.

3.1.2 Motivation

By repeating the measurement sequence at different positions with respect to a sample, one can map out the sample's magnetic field. This type of strategy finds its application in 2D material development [180, 181], the life sciences [182] and many other fields [183, 184]. For maximum resolution, the NV centre should be as close as possible to the source. The most straightforward way to achieve proximity is by placing the NV centre within a few nanometers of the diamond's surface (**shallow NVs** [185]). When the shallow NV centre sits near the tip of a diamond pillar it can be used as a **scanning probe** [169]. It should be noted, that we concentrate on setups with single NV centres, but similar approaches exist with ensembles [183, 186].
While strategies with shallow NV centres show promising results [187], they suffer from one major problem: surface-induced noise. Surface impurities and the dangling bonds of the carbon atoms at the surface cause a background field that drastically reduces the T_1-time (see Section 1.1.1.4) and gives each NV centre slightly different properties [185, 188]. The results presented hereafter improve sensing sequences for individual shallow NV centres. The presented strategy is intended as a first step toward developing robust protocols for a scanning probe setup currently being developed by the group of Elke Neu-Ruffing in Kaiserslautern. Most scanning probe setups change the position of the sample with respect to the probe, which is connected to the MW antenna [187, 181, 189].[2] Instead, the planned experimental configuration has a fully movable diamond needle while the MW antenna is static with respect to the sample. This setup allows to attach the sample directly to the antenna. As a result, the NV centre will experience different MW strengths depending on its relative position with respect to the antenna, and hence to the sample. To compensate, the MW field either needs to be homogeneous, or the MW pulses must be robust against amplitude variations. Specialised MW antennas address the first solution [190]. The second solution is approached by QOC strategies like the ones described below.

Robust Magnetometry with Single NV Centers via Two-Step Optimization

The following article is reproduced from N. Oshnik, P. Rembold, M. M. Müller, T. Calarco, S. Montangero, and E. Neu, *Robust Magnetometry with Single NV Centers via Two-Step*

[2] It should be noted that even in a setup where the probe is connected to the antenna, the distance between probe and antenna will slightly vary. The probe usually sits on the tip of an atomic force microscope [169] which oscillates and adjusts the height of the probe to keep the probe close to the sample's surface.

Optimization, in preparation for publication: arXiv:2111.12684 [quant-ph].
The author of this thesis contributed to the planning of the project and the writing of the manuscript. She was responsible for refining and extending the applied control strategies, as well as maintaining and adapting the control-software RedCRAB for this project. Additionally, she was involved in the discussion of experimental results, analysis of resulting control sequences, and the implementation of the closed-loop optimal control. She composed Figures 4 (Restriction approaches...) and 7 (Comparison between two optimized spin inversion pulses...) and parts of Figure 3 (Initialization and readout of the NV spin state...).

3.1.3 Abstract

Nitrogen-Vacancy (NV) centers in diamond are a widely-used platform in the rapidly growing field of quantum sensing. NV centers near the diamond surface are of particular interest as they can offer nanoscale resolution. However, these shallow NV centers experience considerable noise from the surface, reducing their lifetimes and consequently their sensing capabilities. This work demonstrates a two-step optimization approach to improve DC magnetometry schemes with shallow single NV centers. Both spin readout and manipulation processes are enhanced by designing laser pulses and microwave controls via closed-loop optimal control. This type of optimization inherently takes experimental limitations and unknown system parameters into consideration. In addition, the optimization objective incorporates robustness against variations of the microwave control amplitude. For the pulsed Optically Detected Magnetic Resonance (ODMR) measurements, we report sensitivities below $1\,\mu\mathrm{T\,Hz}^{-\frac{1}{2}}$ for an 83% decrease in control power, increasing the robustness by approximately one third. Furthermore, the optimized Ramsey measurements result in sensitivities below $100\,\mathrm{nT\,Hz}^{-\frac{1}{2}}$ giving a two-fold sensitivity improvement. The obtained sensing schemes are applicable for various magnetometry setups that benefit from robustness, such as ensembles of NV centers and NV-based scanning probes. The robustness does not only protect the protocol's sensitivity from drifts, but also increases the available sensing/interrogation volume.

3.1.4 Introduction

Quantum sensing with NV centers[3] have evolved into a prominent branch of quantum technologies in the last two decades [191, 37, 105, 192, 2]. NV centers serve as a multipurpose sensor for detecting magnetic [193, 168, 194, 15] and electric fields [171], tem-

[3] In this manuscript, the term NV center denotes the negatively charged state of the nitrogen-vacancy center in diamond.

perature [172, 25], and pressure [173, 195]. Additionally, NV centers find applications as quantum memories [196], quantum registers [197], and in other areas of emerging quantum technologies [2, 198, 199]. Rapid improvement in nano-fabrication methods [179, 200, 201], material science research [202, 203], as well as control methodologies [105, 2, 176, 18, 24] have led to a variety of NV-based quantum sensors with applications in the fields of life sciences [50, 204], and material studies [205]. NV centers exhibit optical spin-state polarization and spin-state dependent fluorescence [193, 191, 168]. Additionally, the NV spin-state can be manipulated with resonant microwave (MW) control fields. Various sensing protocols are available that use MW-based unitary gates under the two-level approximation [105]. However, state-of-the-art NV-based quantum sensors do not perform on par with their theoretical potential. Because of the potential applications, further improvement of NV magnetometry is a flourishing and multidisciplinary research topic [105, 192, 2]. While the NV centers particularly close to the surface may offer high nanoscale resolution [208, 185], they also exhibit especially short dephasing and decoherence times.

Likewise, limitations and errors related to the experimental setup, such as drift, finite bandwidth, and transfer functions, restrict the performance of these sensing methods. For example, to exploit the full potential of NV-based scanning probe applications, the MW antenna has to be brought close to the cantilever [169, 209, 210], which can be experimentally challenging given the microscopic scale of the scanning devices. If the distance between antenna and cantilever is larger, it reduces the contrast and hence, the sensitivity of the setup. Additionally, applications with NV-based scanning probes [211, 212] that move with respect to the antenna experience variations in control power. The power variations, in turn, lead to a correspondingly worsened sensitivity. Similarly, applications with single NV centers [213, 214] or ensembles of NV centers [215, 192, 216] in bulk diamond are subject to variation in control power depending on the distance from the MW antenna. In all these cases, robustness against control power variation can simplify the experimental procedure without the need for any modification to the setup or the control pulse itself.

One strategy to partially compensate for these limitations involves quantum optimal control (QOC) [18, 2, 24]. QOC has previously been applied to optimize MW control pulses for quantum sensing with NV centers in a variety of settings [2, 99, 98, 217, 26, 108, 218, 110, 186, 219]. Its common objective connects the diverse family of QOC algorithms: to iteratively improve a time-dependent control pulse until a given goal has been reached. Some of these algorithms rely on simulations (open-loop) to quantify the quality of the pulses. In contrast, others achieve the same via direct interaction with the experiment (closed-loop, Fig. 3.2a-c). Algorithms such as GRAPE [19, 220] (gradient ascent pulse engineering) or Krotov's method [126, 221] require the calculation of the derivative of the goal function (gradient-

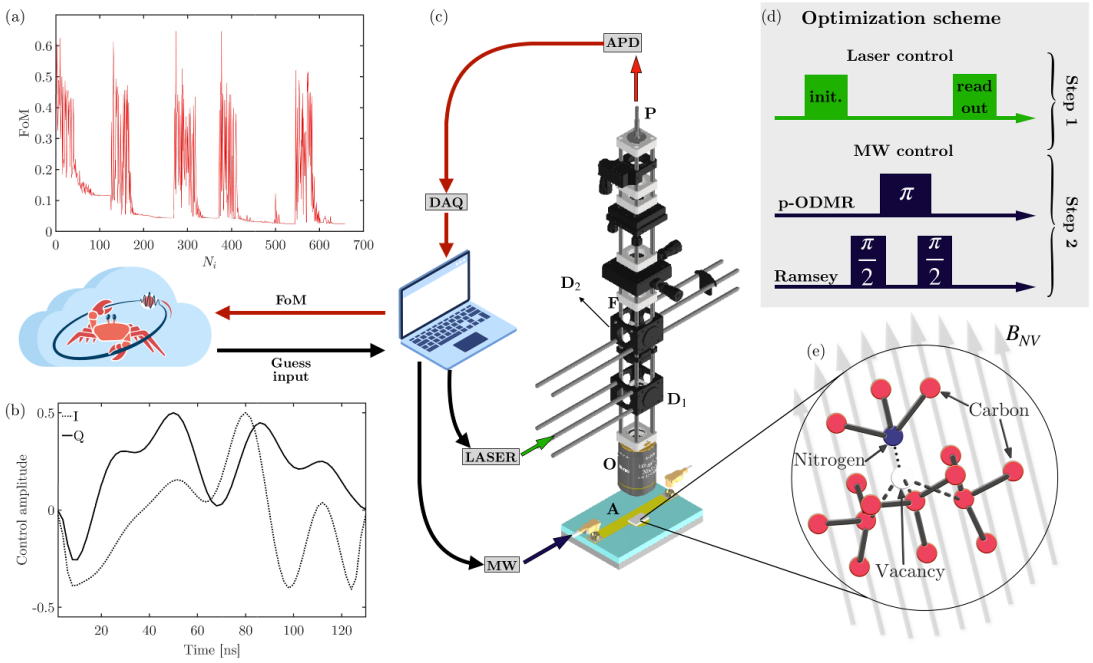

Fig. 3.2 (color online) Schematic for the closed-loop optimization with single NV centers in diamond. The optimization algorithm suggests control pulses/parameters to the setup. The resulting Figure of Merit (FoM) is calculated from the output and passed back to the optimizer. This cycle repeats until the FoM converges. (a) An exemplary plot of the convergence of the FoM with the number of algorithm iterations N_i; the algorithm suggests different controls to find the global optimal solution. (b) The in-phase and quadrature components (I and Q) of a typical guess for a MW control pulse suggested by the algorithm. (c) The confocal setup used in combination with the RedCRAB optimization program; laser (green arrow) and MW (blue arrow) pulses are used to control the NV spin state. The fluorescence (red arrow) is collected with an optical fiber, P, connected to a single photon counter (APD), logged with a data acquisition device (DAQ), and further processed on the local control system to pass the FoM to the remote optimization server. (d) The two-step optimization strategy introduced in this work. In step 1 the laser based spin state initialization and readout processes are optimized. Step 2 creates robust MW control pulses for pulsed ODMR (p-ODMR) and Ramsey sensing sequences via QOC. (e) Lattice structure of the NV center. The NV quantization axis is shown as a dotted black line. The component of the external magnetic DC field along the NV quantization axis is denoted as B_{NV} and quantified via the sensing methods. The confocal schematic in (c) is is drawn with parts adapted and modified from Ref. [206] and Ref. [207] with permission under terms of reuse. For details on the setup see appendix 3.1.11.1.

based). The dCRAB algorithm (dressed Chopped RAndom Basis) [129, 140, 24] can be implemented under a gradient-free strategy. Additionally, the functional parametrization approach of the dCRAB algorithm can be combined with gradient search methods via algorithms like GROUP [149] (gradient optimization using parametrization) or GOAT [222] (gradient optimization of analytic controls). Even with a moderate number of basis functions, the control pulse can contain enough information to steer the system [141, 223].
With the ultimate goal of enhancing the sensitivity of the main DC magnetometry methods with NV centers (section 3.1.5), this work presents a two-step strategy to exploit the full potential of feedback-based optimization algorithms and QOC [224, 26, 6, 24] in connection with shallow single NV centers in diamond ($< 10\,\text{nm}$ below the surface, Fig. 3.3a). At the first step, the optical spin initialization/readout process is optimized via a gradient-free Nelder-Mead search [143] in the parameter landscape corresponding to the properties of the experimental system and setup (section 3.1.7.1). In the second step, we utilize the gradient-free dCRAB algorithm to optimize the MW pulses for spin state manipulation. The optimization routine is implemented via the QOC software package RedCRAB (Remote dCRAB) [26, 6]. The optimized MW controls are developed for two DC magnetometry methods (section 3.1.7.2), namely the pulsed ODMR sequence [53, 172] and the Ramsey sensing protocol [168, 193]. Two optimization bases, Fourier [23] and sigmoid [158], (see appendix 3.1.11.2) are compared to assess their suitability for the involved methods. All optimizations include a Figure of Merit (FoM, see Fig. 3.2a) based on the optical readout contrast. To include robustness against variation in MW drive strength, the FoMs are adapted to scan over control amplitudes ranging from 100% to 20% of the maximum. Finally, the optimized pulses are assessed for their enhancement of the average sensitivity and robustness (section 3.1.8).

3.1.5 DC Magnetometry Methods

The transitions in the energy level structure of the NV center strongly influence its sensitivity towards external magnetic fields (more details in section 3.1.7.1). The optical ground state forms a spin one triplet system, with a Zero-Field Splitting (ZFS) of $\approx 2.871\,\text{GHz}$. In the presence of an external magnetic field along the NV center's axis (B_{NV}), Zeeman splitting lifts the degeneracy between the $m_s = \pm 1$ states. This splitting provides a direct way to quantify B_{NV}. A pseudo two-level system can be constructed from the $m_s = 0$ and one of the $m_s = \pm 1$ states. The two-level approximation forms the basis for various magnetometry techniques with NV centers [191, 193, 15, 200].
The most straightforward procedure to detect DC magnetic fields is called continuous wave optically detected magnetic resonance (cw-ODMR) [53, 225]. The method involves

continuous polarization of the NV spin state with a green laser, while MW pulses with different drive frequencies ω_{mw} are applied sequentially to locate the resonance peaks. The splitting between the resonance peaks is proportional to B_{NV}. Cw-ODMR measurements are less demanding in terms of practical resources and complexity than pulsed measurement schemes, as they do not require pulsed controls. However, by nature, continuous-wave measurements have a lower spin readout fidelity and suffer from optical and MW power broadening [53].

The dephasing time T_2^* sets a limit to the achievable sensitivities with different DC magnetometry methods (see appendix 3.1.11.3, Eq. (3.24)). Short laser and MW pulses help to overcome the power broadening effect [53] and attain better sensitivities. Pulsed ODMR involves pulsed optical excitations and spin state transfer using MW π-pulses. For shallow NV centers, the spin states decay quickly. Hence, pulsed ODMR experiments with short, high power control pulses can be advantageous. The short control pulses inherently result in faster measurements, which lead to an improvement in the overall sensitivity (see appendix 3.1.11.3). The pulsed ODMR method also offers enhanced readout contrast, which further improves the sensitivity. Note that the sensitivity is defined as the least detectable magnetic field within a measurement time of one second [105, 226].

In general, the cw- and pulsed ODMR methods do not exploit the quantum property of spin superposition, which provides a way to make the measurements more sensitive [105]. Conversely, the double-pulse-based Ramsey sequence does utilize spin superposition states for sensing. It also has the advantage of avoiding the power broadening effects [227]. The Ramsey method consists of two $\frac{\pi}{2}$-pulses, with free precession time τ in between. The optically initialized NV spin state is transferred into a superposition state by the first of the two $\frac{\pi}{2}$-pulses. This superposition state interacts with the external magnetic field for the time τ, thus accumulating a phase. Eventually, the second $\frac{\pi}{2}$-pulse converts the accumulated phase into an optically measurable population difference. In contrast to the ODMR-based frequency-sweep methods, the Ramsey sensing protocol is performed at a fixed ω_{mw}. In addition, τ can be varied to measure minimal fluctuations in external magnetic fields [105]. In general, the Ramsey method can be used to sense any magnetic fields that change slowly enough, i.e., with frequencies less than $\frac{1}{\tau}$.

3.1.6 Sample and Experimental Setup

All experiments in this work involve an electronic-grade diamond sample (300μm ×100μm ×40μm) with implanted NV centers (Fig. 3.3).The nitrogen ion implantation was performed with a fluence of $3\times10^{11}\,\mathrm{cm}^{-2}$ at 6 keV, which results in an average depth on around 9.3 ± 3.6 nm [**?**]. The implantation was followed by annealing (850°C), which disperses the

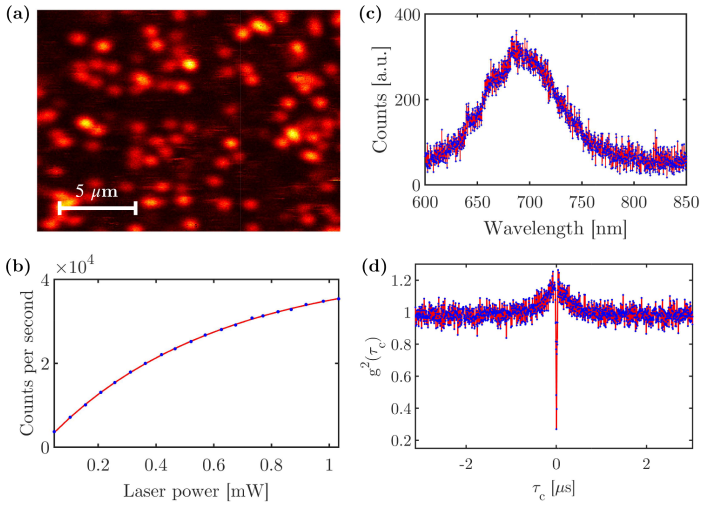

Fig. 3.3 (color online) Sample characterization; (a) Confocal scan of the diamond sample with shallow single NV centers. (b) Count rate of a single NV vs. power of the excitation laser. The saturation behavior can be studied to obtain the excitation power with the best signal-to-background ratio for the experiments. Ideally, this lies below the saturating laser power. (c) Typical emission spectra of the single NV centers in the sample. The NV charge states have different spectral signatures, the given spectrum indicates negatively charged NV state. (d) Exemplary second order correlation measurement, which is performed to identify single NV centers in the sample. τ_c is the delay time in the photon antibunching measurement with the NV ($g_2(0) \approx 0.27$).

defects, leading to a uniform NV center distribution in the sample. Afterward, a second oxidation annealing at 400°C was performed, followed by tri-acid cleaning. This process removes the top layer of the dimaond, resulting in reduced the NV density and depth. The average NV density is estimated via confocal fluorescence maps to be around $7{\times}10^7\,\mathrm{cm}^{-2}$. The value is obtained by analyzing confocal scans of the sample surface (see Fig. 3.3a).
For the experiment, the sample is mounted on an Ω-shaped strip-line MW antenna (Fig. 3.2c, A) [190]. The antenna is mounted on a piezoelectric scanner to perform multi-axial scans. The dichroic mirrors (Fig. 3.2c, D_1, and D_2) filter the excitation laser pulse and direct the fluorescence along the collection arm of the confocal setup. Additionally, a 600 nm long-pass filter (Fig. 3.2c, F) in the collection arm is used for spectral filtering. The optical initialization and readout are assisted by an objective (Fig. 3.2c, O), which delivers and collects the light to/from the in-focus diamond sample containing shallow single NV centers. Laser pulsing is achieved with a digitally modulated diode laser (modulation bandwidth: 125 MHz). The MW control pulses are generated by mixing the in-phase (I) and quadrature (Q) components (Fig. 3.2b) with a carrier signal. The resulting pulse is subsequently amplified

and delivered to the confocal setup via the strip-line antenna. For more details on the setup, see appendix 3.1.11.1.
In principle, the implementation of these magnetometry methods with NV centers is straightforward and well understood. In practice, however, various factors may affect the performance of these sensing schemes. For example, custom-built MW antennas with unknown instrument response functions are often used to deliver the control pulses. In such cases, the control pulses delivered to the NV center may slightly defer from their actual design. Additionally, for shallow NV centers it is difficult to model all surface effects with adequate precision. This lack of information a priori makes it a challenge to accurately model the system. A closed-loop optimization circumvents this issue.

3.1.7 Optimization Methods

The sensing protocols described in section 3.1.5 rely on the efficiency of two types of control: Readout/initialization via the laser and spin manipulation via the MW field. Here, two complementary optimization strategies are presented using the RedCRAB optimization suite. The first adapts the laser pulse parameters (section 3.1.7.1) and the second the MW control pulses (section 3.1.7.2). The software allows for smooth communication between the remote experimental setup and the server-based optimizer. It also incorporates additional features like amplitude limitation, bandwidth restriction, and several other parameters reflecting the accuracy and limitations of the experimental setup. Thus, the essential requirements for both optimizations are straightforwardly incorporated within RedCRAB.
In both optimization steps, we first quantify the goal with an FoM that can be measured in the experiment. Subsequently, the controllable constant parameters and time-dependent controls of the system are identified. The initialization/readout is optimized with a direct search, while the MW pulses are optimized via the dCRAB algorithm [24, 129, 140, 6].

3.1.7.1 Parameter Optimization for Spin State Initialization and Readout

Strong spin polarization and spin state dependent fluorescence are fundamental to the readout of single NV centers. These properties primarily originate from the transition rates of the spin-preserving radiative and the non-radiative decay channels between the NV energy levels (see Fig. 3.4a). The non-radiative inter-system crossing via the metastable state does not preserve the spin state [228]. Figure 3.4a shows how an NV, which is originally in $m_s = 0$ or $m_s = \pm 1$, decays via Path I or II, respectively after being excited by a green laser pulse ($\lambda = 520 - 530\,\mathrm{nm}$). The excited $m_s = 0$ state decays radiatively to the ground state, while the $m_s = \pm 1$ state might take the non-radiative route via Path II. If the laser pulse is long enough,

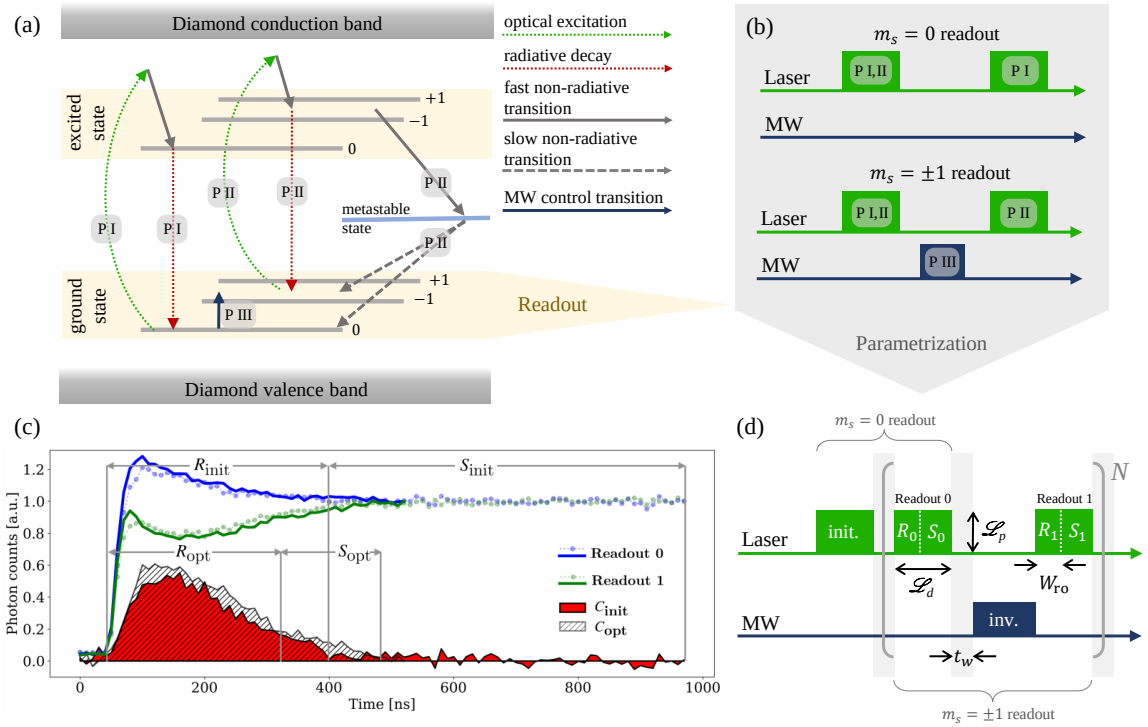

Fig. 3.4 (color online) Initialization and readout of the NV spin state. (a) The energy level structure of the NV center within the diamond bandgap. The transitions of an NV initially in the $m_s = 0$ and $m_s = \pm 1$ ground state are denoted as Path I and Path II, respectively. Note that Path II includes a decay via the metastable state, making it slower. A resonant MW pulse, may drive the $m_s = 0 \leftrightarrow \pm 1$ ground state transition (Path III). (b) Spin state readout sequences. By sweeping the MW frequency ω_{mw} this corresponds to a pulsed ODMR sequence. (c) The light curves with dots show a typical readout signal for a 1 µs laser pulse for different initial spin states (blue: $m_s = 0$, green: $m_s = \pm 1$). The solid curves indicate the optimized spin state readout (see section 3.1.7.1). The shaded areas give the readout contrast (Eq. (3.3)) obtained with the 1 µs laser pulse (C_{init}, red) and the optimized laser pulse (C_{opt}, striped). R_{opt} and S_{opt} indicate the optimized windows for the readout and saturation, respectively. (d) Parameters for the optical readout optimization. R_i and S_i correspond to the photon collection windows described in Eq. (3.6). A spin inverting rectangular MW pulse (inv.) is used for the parameter optimization. Readout 0 (1) corresponds to the readout of the $m_s = 0\,(\pm 1)$ spin states. After an initial laser pulse (init.), each measurement is repeated N times to enhance the signal-to-noise ratio.

all population ends up in the $m_S = 0$ ground state.
Figure 3.4b shows the readout procedure. To obtain a contrast, a laser pulse first initializes the system to the ground state $m_s = 0$ via Paths I and II. In the top part of Fig. 3.4b no MW is applied ($m_s = 0$ readout) and a second laser pulse leads to a decay via Path I. An intermediate MW pulse ($m_s = \pm 1$ readout) can transfer the spin state to $m_s \pm 1$ via Path III. The subsequent laser pulse induces a decay via Path II which leads to a drop in fluorescence (Fig. 3.4c) because of the decay via the long-lived metastable state. Hence, the photon count allows to differentiate the spin states during optical readout.
A simulation-based (open-loop) optimization for optical spin state initialization and readout can be done considering the NV rate equations with experimentally obtained transition rates [51]. Such methods may require specialized apparatus for optical pulse shaping [52], and in general, do not account for experimental limitations. In comparison, closed-loop parameter search offers straightforward enhancement. The photon shot noise is the primary limitation to an efficient optical readout of the NV spin state. Consequently, the statistical determination of the spin state requires an averaged readout over a large number of experimental repetitions. The spin state readout fidelity $\mathcal{F}$ for such probabilistic measurements is expressed in terms of the noise parameter σ_R [15, 229]:

$$\frac{1}{\mathcal{F}} = \sigma_R \approx \sqrt{1 + \frac{2\,(R_0 + R_1)}{(R_0 - R_1)^2}}, \tag{3.2}$$

such that $\mathcal{F} = 1$ at the spin projection noise limit of the sensitivity (see appendix 3.1.11.3). R_1 (R_0) is the total number of collected photons from the readout of the spin state initialized in $m_s = \pm 1$ ($m_s = 0$). Experimentally, the readout contrast C is given by

$$C = \frac{R_0 - R_1}{R_0 + R_1}. \tag{3.3}$$

Its relation to $\mathcal{F}$ is given in appendix 3.1.11.3. Intrinsically, the contrast depends on several system properties and experimental parameters,

$$C \equiv C[\gamma_{ij}, \mathscr{L}_p, \mathscr{L}_d, \Omega_{\max}, B_\perp, E_{xy}, T....], \tag{3.4}$$

where γ_{ij} is the transition rate between levels $i \leftrightarrow j$, $\mathscr{L}_p$ is the laser pulse intensity, $\mathscr{L}_d$ is the laser pulse duration, $\Omega_{\max}$ corresponds to the maximum amplitude of the spin inversion control pulse, $B_\perp$ and E_{xy} are off-axial magnetic and electric field components at the position of the NV center respectively, and T is the ambient temperature. In addition, several other factors, including crystal field strain and charge state stability, may affect the fluorescence of

the NV center and ultimately influence the readout contrast. The majority of the parameters in Eq. (3.4) depend on the system properties, material characteristics, and ambient conditions that are generally not fully controllable. In practice, some of the system properties can be characterized before the optimization of the readout contrast. For example, the charge state of the NV center can be determined from the emission spectrum (Fig. 3.3b). Similarly, external factors such as crystal field strain and temperature directly influence the ZFS of the NV center. In this regard, pre-characterized single NV centers (Fig. 3.3c) with ZFS ≈ 2.871 GHz, and stable photoluminescence that do not exhibit charge state related blinking allow to fully exploit the scope of laser pulse parameter optimization. Likewise, a well-aligned static magnetic field B_{NV} is a prerequisite for the optimizations performed in presence of a magnetic bias field. It is noteworthy that photons originating from NV^0 can be filtered from the readout signal (Fig. 3.2a). As a result, charge state instability leads to blinking of the NV fluorescence signal [45].

Other experimental parameters in Eq. (3.4) such as $\mathscr{L}_p$ and $\mathscr{L}_d$, directly influence the optically induced transitions, as well as the charge state stability [229, 45]. In contrast, the effect of the wait time t_w (see Fig. 3.4d) between the pulses is more indirect. Hence, it is commonly set to ca. 300 ns, which corresponds to the lifetime of the metastable state [230]. Similarly, the photon collection window W_{ro} is often calculated in advance to obtain the best SNR for every readout [37]. Consequently, Eq. (3.4) can be reduced to a simpler form based on the variables that can be controlled experimentally,

$$C \sim C[\mathscr{L}_p, \mathscr{L}_d, W_{\mathrm{ro}}, t_w, \Omega_{\mathrm{max}}]. \tag{3.5}$$

Although it is not straightforward to find an analytical form to characterize the dependence of C on these parameters, they can be directly adjusted in a closed-loop optimization on the experiment. Figure 3.4 shows the two-shot scheme for the contrast measurement used in the optimization routine. Each laser pulse (Readout 0 (1)) is divided into a spin readout window R_0 (R_1), and a spin state saturation window S_0 (S_1). Their durations are determined by the optimization parameters $\mathscr{L}_d$ and W_{ro}. A spin inversion MW pulse flips the spin state between the laser pulses. The FoM, which is minimized during the optimization, is given by

$$\mathrm{FoM}_{\mathrm{RO}} = 1 - \bar{C}\left[1 - \mathrm{var}\left(\left|\frac{S_0 - S_1}{S_0 + S_1}\right|\right)\right]. \tag{3.6}$$

Here, $\bar{C}$ is the readout contrast averaged over N experimental repetitions as shown in Fig. 3.4d. In addition to maximizing the readout contrast in the spin readout windows, $\mathrm{FoM}_{\mathrm{RO}}$ also ensures uniform spin state initialization, as the optimized value tends to minimize the variance

in the photon counts from the two spin states in the saturation windows (Fig. 3.4). The closed-loop optimization of readout parameters is generally relevant for a variety of methods, such as readout based on spin-to-charge-state conversion [229] and photoelectric readout [231], which inherently involves laser pulses. Furthermore, the optimized readout can be integrated directly with MW-free, all-optical magnetometry methods [232].

3.1.7.2 Quantum Optimal Control for Spin State Manipulation

An optimally initialized spin state and its efficient readout are two of the essential criteria for a practical quantum sensor [105]. In addition, the spin state has to be controlled accurately to implement a sensing protocol. Following parts of the text describe the optimization of MW control pulses for spin inversion and for a $\left(\frac{\pi}{2}\right)_x$-gate via the dCRAB algorithm [24, 129, 140, 6].

Before proceeding to the specifics of the optimization schemes, we discuss the dynamical equations of the system to introduce the basic concept of QOC. The system is described by a constant drift Hamiltonian H_d, and control Hamiltonians H_c^i, which are modulated by control pulses $u^i(t)$:

$$\begin{aligned} H(t) &= H_d + \sum_i H_c^i u^i(t) \\ &= \frac{\hbar}{2}\Big(\Delta\sigma_z + \sigma_x u^1(t) + \sigma_y u^2(t)\Big), \end{aligned} \tag{3.7}$$

where the complete Hamiltonian $H(t)$ is given in the rotating wave approximation (RWA) with the detuning $\Delta = \omega_{\mathrm{mw}} - \omega_{\mathrm{nv}}$, the NV's resonant frequency ω_{nv}, the Pauli matrices σ_i, and the controls $u^1(t) = \Omega(t)\cos(\phi(t))$ and $u^2(t) = \Omega(t)\sin(\phi(t))$. These controls correspond to the in-phase and quadrature components of a MW drive, with Rabi frequency $\Omega(t) \in [0, \Omega_{\mathrm{max}}]$ and phase $\phi(t)$ applied for the duration t_p.

The control objective for the MW pulses is to efficiently transfer the initial spin state $|\Psi_i\rangle$ to the final state $\left|\Psi_f\right\rangle$. Hence, the FoM is defined as the state fidelity,

$$\mathcal{F}_p = |\langle\Psi_f|U(t)|\Psi_i\rangle|^2, \tag{3.8}$$

$$\text{where } U(t) = \mathcal{T}\exp\left[-\frac{i}{\hbar}\int_0^{t_p} H(t)dt\right], \tag{3.9}$$

where $\mathcal{T}$ indicates a time-ordered exponential propagator. At this point, the FoM is a functional of the control pulses. The controls are subsequently parametrized by a set of $N_{\mathrm{set}} \times M$ basis elements $f^i(\omega_n; t)$. Each element is defined by its superparameter ω_n, which is randomly selected from $\omega_{\mathrm{min}} < \omega_n < \omega_{\mathrm{max}}$, where ω_{min} and ω_{max} are the minimum and

maximum allowed values. The number of basis functions M per superparameter depends on the basis. These superparameters can be the frequencies of a set of trigonometric functions (Fourier basis [140]; in this case ω_{min} and ω_{max} set the allowed bandwidth of the control pulse) or the offsets for a set of step functions (sigmoid basis [158]). The resulting pulses take the following form:

$$u^i(t) = u_0^i(t) + \sum_n^{N_{\text{set}}} \sum_i^M A_n f^i(\omega_n; t). \tag{3.10}$$

Here, $u_0^i(t)$ represents the initial guess for the pulse.
Following the parametrization, the goal of the QOC routine is to find the optimal values for the coefficients A_n, maximizing the FoM (Eq. (3.6)). Especially in closed-loop optimization, only a limited number of parameters can be optimized at a given time. Therefore, additional steps are required to avoid local optima. The dCRAB algorithm tackles this issue by switching the set of basis elements every time the optimization has converged under the given constraints [140]. Every new optimization (superiteration) is started with the previous optimum as an initial guess, i.e. $u_0^i(t) = u_{\text{opti}}^i(t)$.
The optimizations are performed with both, the Fourier and sigmoid basis separately. To ensure the pulse amplitude and duration are limited, i.e., that the amplitude stays within an upper and a lower limit and the pulse is zero at $t = 0$ and $t = t_p$, two different strategies are applied and illustrated in Fig. 3.5. In the cut-off approach, the pulses are cut off at $t = 0$ and the $t = t_p$ to limit the duration. Similarly, they are cut off at the top and bottom to force the amplitude limits.

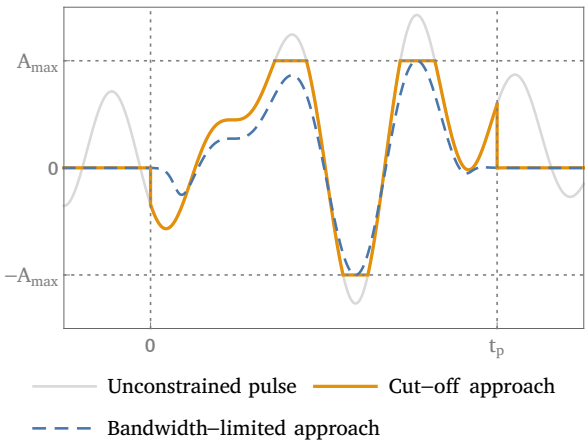

Fig. 3.5 (color online) Restriction approaches. The unconstrained pulse may either be cut off at the amplitude $\{-A_{\text{max}}, A_{\text{max}}\}$ and time $\{0, t_{\text{p}}\}$ limits ("cut-off approach") or shifted and rescaled to fit within the available window ("bandwidth-limited approach").

Instead, the bandwidth-limited approach involves re-scaling the pulse to fit within the amplitude limits, followed by multiplication with a smooth window function like a flat-top Gaussian to avoid discontinuities at initial and final time.
In the cut-off approach (see Fig. 3.5), the Fourier basis is expected to produce high-frequency components when the optimization algorithm maximizes the pulse area. Conversely, in the bandwidth-limited approach, the Fourier basis will have difficulties to significantly expand the pulse area. At the same time, the sigmoid basis has the ability to exploit the pulse area without producing high frequencies [158] when combined with the bandwidth-limited approach. The inherent smoothness offered by the sigmoid basis (see appendix 3.1.11.2) provides a particular advantage for frequency-sweep-based spectroscopic measurements, where spurious harmonics are to be avoided.
The first MW optimization presented here concerns the spin-inversion pulse in the pulsed ODMR sequence (see Fig. 3.4). The efficiency of the spin state transfer is estimated through the optical readout contrast C (Eq. (3.4)). The previously obtained parameters for the laser-based initialization/readout are used as the default for the MW control pulse optimization experiments. To achieve robustness, the control field amplitude variation is incorporated in the FoM by averaging the contrast over a range of Rabi frequencies $\Omega_{\max}$.

$$\mathrm{FoM}_{\mathrm{podmr}} = 1 - \frac{1}{N_p} \sum_{k}^{N_p} \left(\frac{R_0^k - R_1^k}{R_0^k + R_1^k} \right), \tag{3.11}$$

where N_p is the total number of sampled $\Omega_{\max}$ and R_i^k are the photon counts from the corresponding spin state collected during Readout 0 (1) (see Fig. 3.4). The goal of the optimization is to minimize $\mathrm{FoM}_{\mathrm{podmr}}$.
The Ramsey protocol does not involve spin inversion, but instead a $\left(\frac{\pi}{2}\right)_x$-gate. In the sensing procedure, this pulse plays two roles: First, it maps the spin eigenstates to a superposition state with a given phase. Second, it converts the phase back to a spin population. Gates cannot be directly quantified using the contrast. Instead, their quality is commonly quantified via gate tomography, which requires additional state preparations and related measurements. We develop a protocol to translate the $\left(\frac{\pi}{2}\right)_x$-gate's unitary properties into a readout contrast that takes the same number of measurements as the evaluation of the spin state inversion. Figure 3.6 shows the scheme connecting the pulse performance to the readout fluorescence contrast C from two spin states. Similar to the case of pulsed ODMR, the FoM is defined as

$$\mathrm{FoM}_{\mathrm{ram}} = 1 - \frac{1}{N_p} \sum_{k}^{N_p} \left(\frac{\mathcal{P}_0^k - \mathcal{P}_1^k}{\mathcal{P}_0^k + \mathcal{P}_1^k} \right), \tag{3.12}$$

where $\mathcal{P}_i^k$ is the photon count for the kth amplitude value after projection into spin state i. The photon counts $\mathcal{P}_i^k$ are related to the spin transfer to the different states using the following series of transformations,

$$U(t_p)\,\pi_x\,U(t_p) \longmapsto \mathcal{P}_0,$$
$$U(t_p)\,U(t_p) \longmapsto \mathcal{P}_1,$$

where $U(t_p)$ is the parametrized unitary operator for the optimized control pulse of duration t_p, and π_x denotes the unitary transformation for the rectangular π-pulse applied along the x-axis. The maximization of the contrast ideally corresponds to the following conditions:

$$|\langle 0|U(t_p)\,\pi_x\,U(t_p)|0\rangle|^2 = 1, \tag{3.13}$$
$$|\langle 1|U(t_p)\,U(t_p)|0\rangle|^2 = 1. \tag{3.14}$$

Here, $|0\rangle$ and $|1\rangle$ denote the two spin states of the system under the two-level approximation: $|0\rangle$ is given by the $m_s = 0$ state and $|1\rangle$ represents either $m_s = +1$ or $m_s = -1$ depending on the corresponding experiment specified in section 3.1.8. We introduce the parametrization of the unitary transformation generated by the control pulse as

$$U(t_p) = \exp\left[-i\sum_j c_j\sigma_j\right], \tag{3.15}$$

with coefficients c_j for $j = \{x,y,z\}$, and $\hat{c}_j = c_j/c$, with $c = \sqrt{c_x^2 + c_y^2 + c_z^2}$. Then, Eq. (3.14) implies

$$1 = \sin^2(2c)(\hat{c}_x^2 + \hat{c}_y^2) \tag{3.16}$$

and thus $c = \frac{1}{2}\left(\frac{\pi}{2} + k\pi\right)$, for integer k, and $c_z = 0$. Substituting this into Eq. (3.13) gives

$$1 = 4\hat{c}_x^2\sin^2 c\left[\cos^2 c + \hat{c}_z^2\sin^2 c\right] = \hat{c}_x^2, \tag{3.17}$$

finally indicating that $c_x = c = \frac{1}{2}\left(\frac{\pi}{2} + k\pi\right)$, and hence $c_y = 0$. In other words, $\mathrm{FoM}_{\mathrm{ram}}$ in Eq. (3.12) is minimized for a $\frac{\pi}{2}$ rotation around the x-axis (in the positive or negative direction):

$$U_{\mathrm{opti}}(t_p) = \exp\left[-\frac{i}{2}\left(\frac{\pi}{2} + k\pi\right)\sigma_x\right]. \tag{3.18}$$

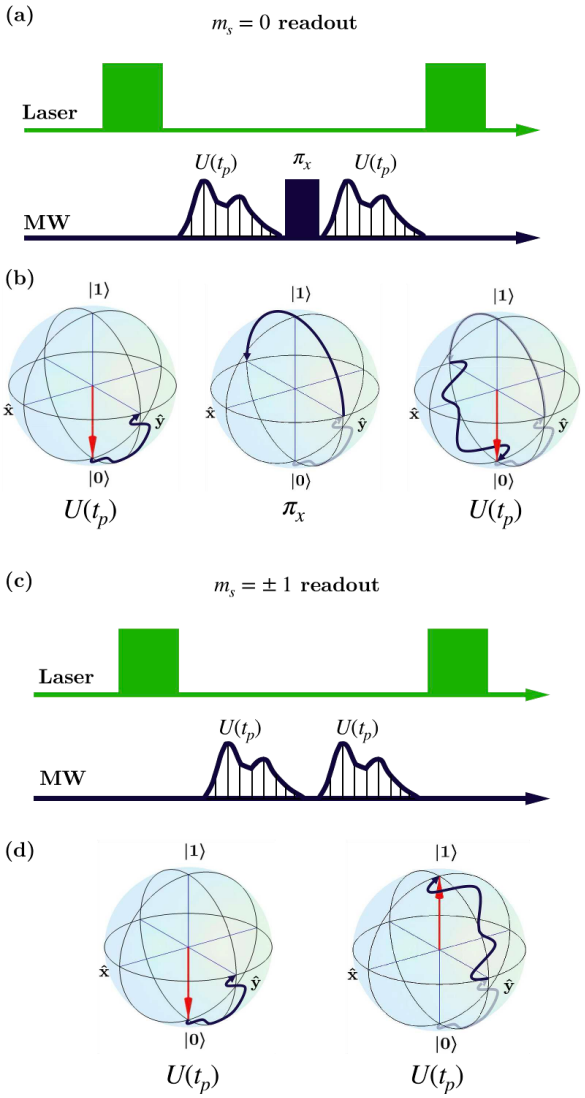

Fig. 3.6 (color online) Exemplary measurement protocol for the Ramsey sequence optimization. The spin is projected into $m_s = 0$ and $m_s = \pm 1$, similarly to the spin state measurement in Fig. 3.4b. (a) $m_s = 0$ state ($|0\rangle$) projection: A known refocusing π_x-gate (solid) is applied between two optimized pulses $U(t_p)$ (shaded). (b) Exemplary Bloch sphere representation of the process in (a). Red arrows indicate the initial and final spin state, and dark blue lines denote the path of the spin state. (c) In the absence of the intermediate π_x-pulse, the spin state is ideally transferred to the $m_s = \pm 1$ state ($|1\rangle$). (d) Exemplary Bloch sphere representation of the scheme in (c).

3.1.8 Experimental Results and Sensitivity Analysis

A straightforward way to test the general applicability of the optimization strategies discussed in the preceding section is to apply them to different single NV centers and compare the readout contrast enhancement on a case-specific basis. In addition, the average sensitivities from the experiment quantify the optimization benefits. The optimization schemes from section 3.1.7 are implemented and compared in the following section. First, we assess the improvements resulting from optimized readout (OR) (section 3.1.8.1) and the additionally optimized spin transfer pulses (section 3.1.8.2) for the pulsed ODMR method. Second, OR is applied with optimized control pulses for the Ramsey protocol, and the results are discussed in section 3.1.8.3. Finally, the robustness of the pulses is tested over a range varying from 100% to 10% of the maximum control power. This variation is artificially introduced in the experiment by changing the power at the MW source.

3.1.8.1 Initialization and Readout

Experimental restrictions are directly included in the closed-loop optimization of the initialization and readout process by limiting the optimization parameters. The bounds on the parameter set $\{\mathscr{L}_p, \mathscr{L}_d, W_{\mathrm{ro}}, t_w\}$ are given as:

$$\begin{aligned} \mathscr{L}_p &\in [2, 40] \text{ (mW)}, \\ \mathscr{L}_d &\in [300, 2000] \text{ (ns)}, \\ 0.25\,\mathscr{L}_d \leq W_{\mathrm{ro}} &\leq 0.75\,\mathscr{L}_d \text{ (ns)}, \\ \text{and } t_w &\in [0, 1000] \text{ (ns)}. \end{aligned}$$

Limits on $\mathscr{L}_p$ correspond to the available source laser power. The initial guess for the optimization is chosen to be $\{\mathscr{L}_p \leq P_{\mathrm{sat}}, 1000\,\mathrm{ns}, 450\,\mathrm{ns}, 300\,\mathrm{ns}\}$, where P_{sat} is the saturation laser power for the single emitter. In cases where the saturation limit cannot be reached with the available laser intensity, the initial guess is obtained by considering the saturation curve to identify the approximate laser intensity with the most favorable signal-to-background ratio. Some of the readout optimization results are summarized in table 3.1. As a general observation, the optimized laser pulses are shorter than the corresponding initial guesses, while the t_w values remain almost unchanged after the optimization. Moreover, reduction of the measurement time improves the overall sensitivity of the NV center (Eq. (3.25)). Figure 3.4c shows the photoluminescence behavior of one of the NV centers involved in the experiment (table 3.1, NV3). The collected signal reflects the improvement in the average readout contrast after the optimization.

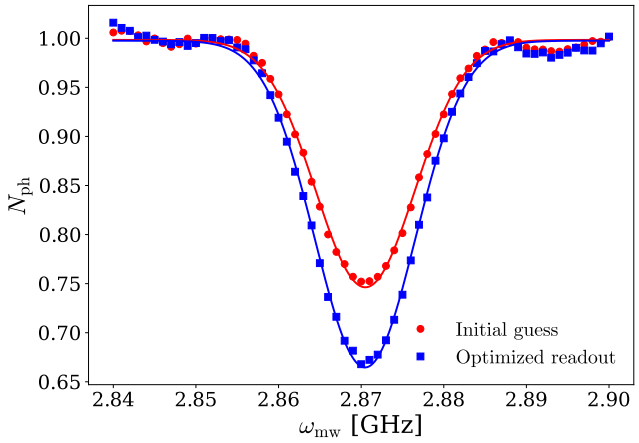

Fig. 3.7 (color online) Pulsed ODMR at ZFS with optimized parameters using a rectangular MW π-pulse of the duration of 57 ns. The experiment with optimized laser parameters exhibits an improved readout contrast $\bar{C}$ of ca. 0.33 (blue) in comparison to the initial guess with a contrast of ca. 0.25 (red).

Table 3.1 Optimized parameters for spin state readout contrast with single NV centers. Experiments with NV1 are performed at the ZFS, whereas NV2 and NV3 related experiments are performed with a bias field of 12 mT.

Identifier	$\mathscr{L}_p^{opt}$ [mW]	$\mathscr{L}_d^{opt}$ [ns]	W_{ro}^{opt} [ns]	t_w^{opt} [ns]	Ref.
NV1	21	585	260	470	Fig. 3.7
NV2	17	488	250	270	[a]Fig. 3.8
NV3	16	552	385	260	[b]Fig. 3.9, 3.10, 3.11, 3.12

[a]Pulse optimization restriction via the cut-off approach.
[b]Pulse optimization restriction via the bandwidth-limited approach.

The optimized laser parameters are tested by combining them with a standard pulsed ODMR sequence with rectangular spin inversion pulses (pulse duration of 57 ns). Their readout contrast is quantified as $\bar{C} = 1 - \min[N_{\mathrm{ph}}]$, where N_{ph} is the normalized photon count (see appendix 3.1.11.3 for details). Figure 3.7 shows a comparison between the measurement with and without optimized parameters (zero bias field, table 3.1, NV2). The optimized parameters account for a 33% improvement in peak contrast. This result can be improved even further by also optimizing the spin inversion pulses.

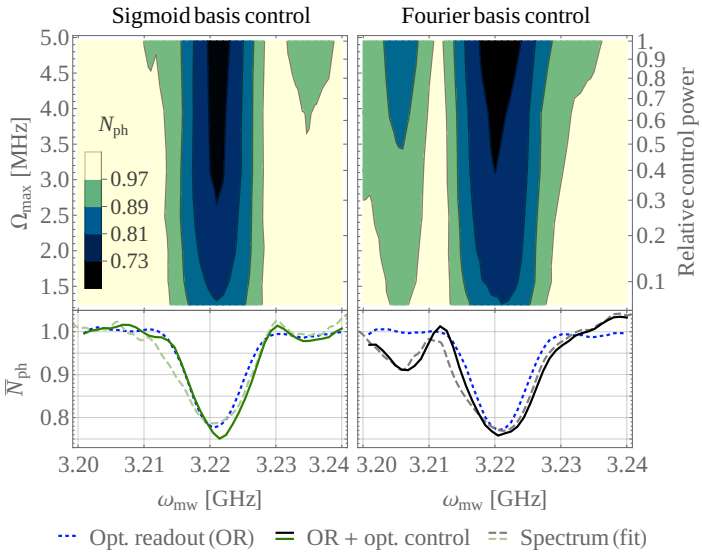

Fig. 3.8 (color online) Comparison between two optimized spin inversion pulses in presence of a bias field $B_{NV} = 12\,\text{mT}$ (table 3.1, NV2). The left (right) side shows the experimental results from a pulse optimized with the sigmoid (Fourier) basis. (*top*) Normalized counts N_{ph} over a range of Ω_{max} and drive frequencies ω_{mw}. (*bottom*) Average normalized count $\bar{N}_{ph}$ over all Ω_{max} for the optimized pulse (solid) and initial guess (blue, dotted). The spectra of the pulses (dashed) are convoluted with the NV's natural emission line and fitted to the average counts.

3.1.8.2 Pulsed ODMR Measurements with Optimized MW Pulses

The spin inversion pulse that is part of the pulsed ODMR protocol provides a target for further optimization on top of the optimized optical readout. In this regard, we investigate the additional improvement by optimizing the pulses under a bias field B_{NV} to emulate a spin resonance sensing scenario. The FoM is calculated by averaging the contrast over a set of $N_p = 5$ measurements (see Eq. (3.11)) leading to control pulses in the range of 4% - 100% of the maximum control power (or equivalently, 20% - 100% of the maximum control amplitude, Ω_{max}).

Figure 3.8 shows two maps representing the normalized count obtained with two optimized MW pulses. In this example, the laser pulses were pre-optimized according to the method described in Section 3.1.8.1, and the $m_s = 0 \leftrightarrow +1$ transition is used for the optimization as well as the assessment via pulsed ODMR. The MW pulses are optimized according to Eq. (3.11) at the center frequency of 3.22 GHz. The pulse corresponding to the left is optimized with the Fourier basis, while the right pulse is optimized with the sigmoid basis, both with a pulse duration of 200 ns. Both pulses exhibit robustness with respect to the amplitude variations, improving the contrast compared to the initial guess. However, the

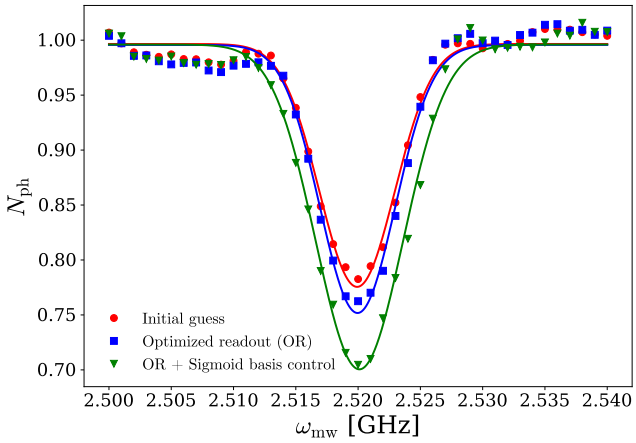

Fig. 3.9 (color online) Pulsed ODMR in presence of a bias magnetic field ($B_{\mathrm{NV}} \approx 12\,\mathrm{mT}$, NV3 from table 3.1) with optimized laser parameters and MW pulses. Following the results from Fig. 3.8 the optimization was done with the sigmoid basis, using the bandwidth-limited restriction approach. The data shows the improvement in contrast with each step of the optimization. The initial contrast for the resonance peaks is ca. 0.22 (initial guess, red), which is further improved to ca. 0.24 with optimized laser parameters (blue). The MW pulse optimized in the sigmoid basis on top improves the contrast to ca. 0.30 (green). the solid lines show the Gaussian fits for the respective data (see appendix 3.1.11.3).

sigmoid basis pulse is spectrally narrow, while the Fourier pulse has a distinct sideband. The spectral shape of the pulses can explain these features. The Fourier basis contains high-frequency elements caused by the cut-off limitation (see Fig. 3.5), which the sigmoid basis avoided. The small off-resonant area addressed by the sigmoid basis covers only a fraction of the Fourier basis' sideband and is significantly weaker. This is illustrated in the average plot at the bottom.

To test the general applicability of this method for generating bandwidth-limited control pulses, similar optimization and pulsed ODMR experiments are performed with a different NV center (table 3.1, NV3), this time using the $m_s = 0 \leftrightarrow$ -1 transition, and the bandwidth-limited approach (Fig. 3.5). The results are shown in Fig. 3.9. Here, a readout contrast of ca. 0.24 is obtained with optimized laser parameters (pulse duration of 130 ns). The sigmoid pulse (pulse duration of 200 ns) enhances the readout contrast further to ca. 0.30. Pulsed ODMR experiments with different peak control power are performed to test the robustness of the control pulse. The readout contrast and Full Width Half Maximum (FWHM) of the resonance profile are obtained by fitting the data with a Gaussian profile (see Eq. (3.26)).

Figure 3.10 shows the achievable average sensitivity η of the pulsed ODMR method. It depends on the resonance profile, its FWHM, contrast, and the measurement time involved in the experiment (see Eq. (3.25)). In addition, the spin-projection noise sets a lower limit

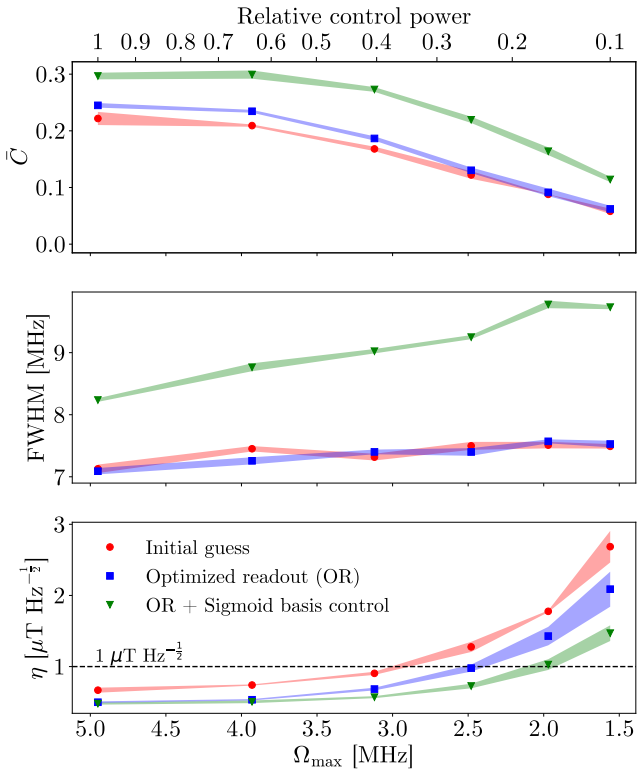

Fig. 3.10 (color online) Comparison of pulsed ODMR measurements with optimized and standard spin state inversion pulses (NV3 from table 3.1). Specifically, the robustness against amplitude variation is shown for pulses optimized in the sigmoid basis. From top to bottom, the contrast, and FWHM of the resonance peaks as well as the corresponding average sensitivity η are shown. All results are obtained with different amplitude variations. The red curves indicate the initial guess. Blue curves correspond to the experiments performed with optimized spin readout parameters. The green curves show the results for the experiments using optimized MW pulses. The dashed line in the bottom plot shows the ceiling for the η of $1\,\mu\mathrm{T}\,\mathrm{Hz}^{-\frac{1}{2}}$.

to η. The full optimization, including the laser parameters and the robust sigmoid pulse, leads to a sub-$\mu\mathrm{T}\,\mathrm{Hz}^{-\frac{1}{2}}$ average sensitivity considering up to almost 83% variation in the control power (see appendix 3.1.11.3 for details on the sensitivity calculation). Off-axial magnetic field components lead to spin-mixing, reducing the readout contrast [232]. This effect becomes apparent when comparing the contrast at ZFS (Fig. 3.7) and in presence of an external magnetic field (Fig. 3.9). The degree of spin-mixing and its effects on the transition rates cannot be straightforwardly simulated for the presented experiments. Using closed-loop optimization of the laser pulse parameters allows to nevertheless incorporate such effects into the FoM.

Up to this point, all three NV centers from table 3.1 were investigated. As the improvements

are of the same order of magnitude, only NV3 is considered in the following without loss of generality. The Ramsey sensing method, which is addressed next, fulfills a similar role to the pulsed ODMR sequence and offers better sensitivities towards external DC magnetic fields.

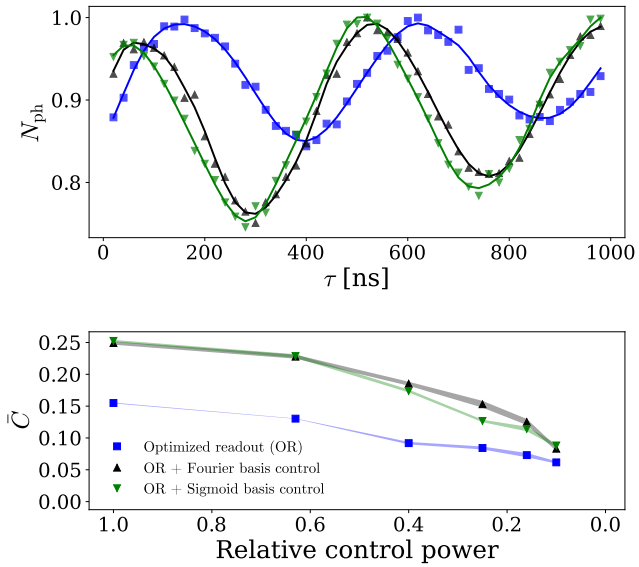

Fig. 3.11 (color online) Optimized Ramsey measurements. The top plot shows the measurements performed at peak drive power with rectangular control pulses (blue) as well as optimized pulses in the Fourier basis (black) and sigmoid basis (green). The optimized pulses exhibit almost double the contrast in comparison to the rectangular control pulse. The length of the rectangular $\frac{\pi}{2}$-pulse is determined by performing Rabi measurements, and in this case is 67 ns. The bottom plot shows the variation in readout contrast with respect to the change in relative control power of the control pulse. The performance of the robust optimized pulses surpasses the rectangular control pulse over the entire range of tested control power (90% variation).

3.1.8.3 Ramsey Measurement

The Ramsey method is a type of interference measurement for DC magnetic fields. As discussed in section 3.1.5 it consists of two $\frac{\pi}{2}$-pulses and offers a higher sensitivity in comparison to the ODMR methods. It should be noted that previous optimizations for D-Ramsey pulse sequences with NV centers were performed in an open-loop scheme using a cooperative design [25]. Our results are obtained through a closed-loop optimization and directly quantified on the setup. The $\frac{\pi}{2}$-pulses are optimized via assessment of the contrast for a range of drive amplitudes (see Eq. (3.12)) via the bandwidth-limited approach discussed in section 3.1.7.2 (see Fig. 3.5). The resulting interference fringes are shown in Fig. 3.11. This optimization is carried out in presence of a bias external magnetic field (B_{NV} = 12 mT) and on-resonance with the $m_s = 0 \leftrightarrow$ -1 transition. The fringe visibility is enhanced from

0.15 to ca. 0.24 with the Fourier basis pulse, and to ca. 0.25 with the sigmoid basis pulse using the maximum control amplitude (pulse duration of 100 ns). The fringe visibility is directly related to the readout contrast. An improvement in the readout contrast leads to a proportional improvement in the sensitivity of the sensor (see Eq. (3.27)).

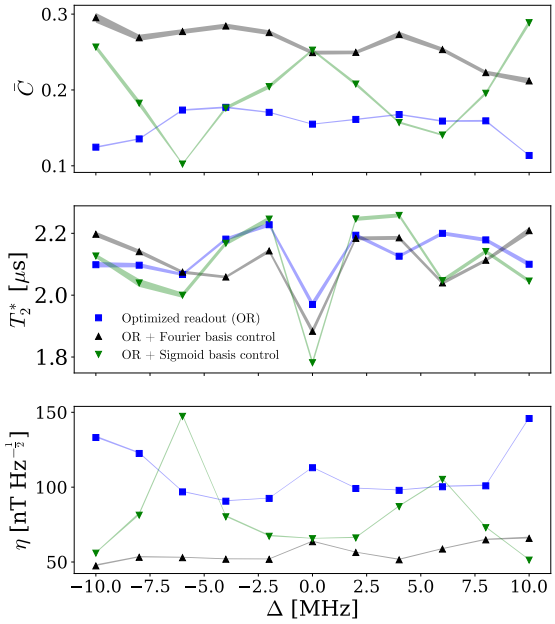

Fig. 3.12 (color online) Comparison of Ramsey sequences with standard and optimized MW $\frac{\pi}{2}$-pulses. All measurements are performed with optimized laser pulses for the readout and the optimizations were carried out with the amplitude-robust FoM from Eq. (3.12). The performance of the pulses optimized with the Fourier (black) and sigmoid (green) basis is compared to the rectangular control pulse (blue) over a range of drive detunings Δ. This range is equivalent to a variation of 0.35 mT in the external magnetic field. The upper panel shows the readout contrast $\bar{C}$. The respective T_2^* values are displayed in the middle panel. The bottom panel shows the resulting η. The sensitivity calculation is discussed in appendix 3.1.11.3.

The performance of the optimized pulses is further tested by performing Ramsey measurements with different drive frequencies in the vicinity of the spin transition frequency. These detunings correspond to a range of fields that could be measured in a sensing setup. The resulting readout signal summed over repeated iterations of the experiment is assessed for average sensitivity [15] η of the NV center. The sensitivity of the Ramsey sequence depends on the readout contrast and the dephasing time during the measurements (see appendix 3.1.11.3). Figure 3.12 shows the readout contrasts, the T_2^*-times, and the average sensitivities obtained by a series of Ramsey measurements. The Fourier pulse displays a constant readout contrast in the frequency range of ±10 MHz. This range in the frequency corresponds to around

$\pm 0.35\,\mathrm{mT}$ of variation in B_{NV}. In comparison, the sigmoid pulse shows a marginally better $\bar{C}$ around the resonance frequency but varies strongly for different detunings. The frequency components of the pulse depend on the pulse shape (see appendix 3.1.11.2). Here, the spectrum of the sigmoid pulse contains minima at a detuning of approximately $\pm 5\,\mathrm{MHz}$ (Fig. 3.12). From a control perspective, such frequency selective applications are attractive for spectral hole burning [233] and quantum logic gates for superconducting qubits [234]. The T_2^*-time is comparatively lower on resonance than off resonance for all pulses. This is due to the destructive interference of the hyperfine transition associated with the spin resonance [235]. Readout contrast enhancement inherently involves strong contributions from all the hyperfine transitions, resulting in a trade-off between $\bar{C}$ and T_2^*. The measurements with the Fourier pulse exhibit a robust η of less than $65\,\mathrm{nT\,Hz^{-\frac{1}{2}}}$. These levels of sensitivities are on par with the ones reported for single NV-based diamond scanning probes [187, 181, 189]. The method from this section could be generalized to replace the spin-refocusing π-pulse in other sensing methods. This would require applying the optimized $\frac{\pi}{2}$-pulses twice, using a strategy similar to the one discussed in section 3.1.7.2. Such refocusing pulses form the main building block for AC magnetic field sensing [2].

3.1.9 Conclusion

The optimizations in this work focused on three essential parts of quantum sensing with NV centers: optical spin state readout, population inversion, and $\frac{\pi}{2}$-pulses. All three were improved for sensing methods with single NV centers, considering control power variations of up to 90%. Such robustness enables the sensing of larger microstructures by increasing the explorable sample area and makes the pulses more robust against experimental drift over time. The resulting protocols are realized by replacing the building blocks of common laser and MW based schemes with optimized equivalents. The optimizations are based on a set of figures of merit which are directly measurable via contrast using a varying MW power. The feedback-based approach inherently takes experimental imperfections and unknown system parameters into account. Initially, we optimized the optical readout/initialization process, improving the spin readout contrast by 32% in comparison to the standard protocol. Moreover, additionally optimizing the spin inversion pulse in a pulsed ODMR protocol allowed for an overall contrast improvement by 36% leading to sub-$\mu\mathrm{T\,Hz^{-\frac{1}{2}}}$ sensitivity that is maintained over a large range of MW amplitudes. Such robust excitation pulses lead to a large interrogation volume. Especially, for ensembles of NV centers this results in improved readout counts for a larger area, and in turn, enhanced sensitivity [192]. To maintain frequency sensitivity, different optimization bases were explored. The sigmoid basis leads to spin transfer within a limited bandwidth envelope, reducing the off-resonant excitation.

Additionally, we obtained an optimized $\frac{\pi}{2}$-pulse for Ramsey measurements, enhancing the fringe contrast by 67% with respect to the square pulse with pre-optimized optical readout at maximum control power. Consequently, we obtained a two-fold enhancement in the average sensitivities, ranging below $100\,\mathrm{nT\,Hz^{-\frac{1}{2}}}$ over a set of induced bias field strengths. While we applied the optimization to shallow NV centers, the approach is straightforwardly applicable to other NV-based systems like diamond scanning probes and NV ensembles used for wide-field imaging where similar control robustness features are required.

3.1.10 Acknowledgements

We thank A. Marshall, F. Motzoi, R. Nelz, S. Z. Ahmed, T. Reisser and M. Rossignolo for their insights and suggestions. We furthermore thank T. Reisser for his assistance with the RedCRAB software suite. This work has received funding from the European Union's Horizon 2020 research and innovation program under the Marie Skłodowska-Curie grant agreement N° 765267 (QuSCo) and under the grant agreement N° 820394 (ASTERIQS).
Authors' contributions: NO and EN planned the experiments. PR, NO, and MM planned the optimization strategies and worked to facilitate the remote optimization. NO designed and performed the experiments and analyzed the data. TC, SM, EN and MM supervised the project. All the authors discussed the results and contributed to the manuscript.

3.1.11 Appendix

3.1.11.1 Experimental Setup

All the measurements were carried out on a custom-built confocal setup, with excitation wavelength of 520 nm (Swabian instruments, DL nSec, PE 520) and objective numerical aperture of 0.8 (Olympus, LMPLFLN100X). Rejection of the out-of-focus fluorescence signal was achieved by using single mode optical fibers (Thorlabs, SM450 and SM600) at the excitation and detection arm of the confocal microscope. Further, contributions from the NV^0 charge state were blocked with a spectral filter (Thorlabs, FEL0600, Longpass 600 nm) in the detection arm. Fluorescence signal from the single NVs was detected with a single photon counting module (APD, Excelitas, SPCM-AQRH-14, quantum efficiency ≈68%) and the acquired data was logged with a data acquisition card (National Instruments, PCIe-6323). Second order intensity correlation measurements were performed with a Hanbury-Brown Twiss setup attached to a time resolved counting device (PicoQuant, PicoHarp 300). The fluorescence signal was filtered and analyzed with a spectrometer (SP-2500, Princeton Instruments) to ensure the charge state stability in the diamond sample. The MW control

pulses were generated with IQ mixing with the MW signal generator source (Tektronix 4104A, IF bandwidth of 400 MHz). The in-phase and quadrature components were obtained with an arbitrary waveform generator (AWG, Tabor 1204 A, 2.3 GSa s^{-1}). Control pulses were delivered to the diamond sample with a custom-built Ω-shaped antenna [190] after amplification (ZHL-16W-43-S+, Mini-Circuits, typ. +45 dB). Channel synchronization was ensured using a sync device (Swabian Instruments, Pulse Streamer 8/2) to trigger the diode laser, AWG, MW source, APD count window and the data acquisition device. The sample along with the MW-antenna was mounted onto a piezo-scanner (Physik Instrumente (PI), P-611.3O) to perform the confocal scans and address individual NV centers. The remote connection to the optimization server was obtained via a combination of MATLAB (remote system) and Python (RedCRAB GUI) based control programs.

3.1.11.2 Random Bases for dCRAB Optimization

In the dCRAB algorithm, random bases are used whose elements can be defined through a superparameter ω which stays constant throughout the optimization. In this work, we have used two different bases, referred to as the Fourier and the sigmoid basis. They differ in their shape and properties.
The Fourier basis is most commonly used with dCRAB. It consists of $M = 2$ out of phase trigonometric elements with frequency $0 \leq \omega \leq \omega_{\max}$:

$$\begin{aligned} f^1_{\text{Fourier}}(\omega; t) &= \sin(\omega t) \\ f^2_{\text{Fourier}}(\omega; t) &= \cos(\omega t). \end{aligned} \tag{3.19}$$

The sigmoid basis [158] consists of sigmoid functions ($M = 1$) with an offset of $\epsilon\sigma \leq \omega \leq t_p - \epsilon\sigma$. ϵ represents an offset factor. The basis always includes one element at $\omega = \epsilon\sigma$ which is optimized in every superiteration to ensure the pulse length is constant (i.e. $u_i(t = 0) = u_i(t = t_p) = 0$). For the same reason, an element is added automatically with $\omega = t_p - \epsilon\sigma$ and amplitude $A = \sum_n^N A_n$.

$$f_{\text{sigmoid}}(\omega; t) = \frac{1}{\sqrt{2\pi}\sigma} \int_0^t e^{-\frac{1}{2}\left(\frac{\tau-\omega}{\sigma}\right)^2} d\tau. \tag{3.20}$$

They both have different properties. In general, the Fourier basis is bandwidth-limited through the upper limit for ω. The sigmoid basis is bandwidth-limited due to the limited rise time defined by σ. However, in both cases higher frequency terms may be introduced through cut-offs (i.e., cut-offs in the time domain or amplitude domain).
It should also be noted that the basis choice determines which shapes are complex, and which

are simple to produce. While the Fourier basis produces oscillations with few basis elements, the sigmoid basis produces approximately square pulses, without cut-offs.

3.1.11.3 Sensitivity Calculation

NV center based sensing is fundamentally limited by the spin projection limit [226]. This limit can be expressed as

$$\eta_{sp} = \frac{\hbar}{S\, g_e \mu_B} \frac{1}{\sqrt{t_m}}, \tag{3.21}$$

where, $\hbar$ is the reduced Plank's constant, g_e is the Landé factor, μ_B is the Bohr magneton, and t_m is the measurement time. In addition, optical readout processors are subjected to photon shot noise that further adheres the sensitivity. For the averaged readout process discussed in section 3.1.4, Eq. (3.2), the readout fidelity can be equivalently written as

$$\mathcal{F} = \sqrt{1 + \frac{1}{\bar{C}^2 \bar{R}}}. \tag{3.22}$$

$\bar{C}$ is the average readout contrast between the two spin states of the system and $\bar{R}$ is the average count rate. Further, an overhead cost is always involved in an experimental scenario. Really long spin initialization and readout duration deteriorates the overall sensitivity of the sensor, this can be expressed as a scaling factor for the sensitivity

$$\kappa_{exp} = \sqrt{\frac{t_m + 2 \times t_i}{t_m}}, \tag{3.23}$$

under the assumption that the initialization and readout duration are equal (t_i). Finally, for DC magnetometry methods, the dehpasing time T_2^* further limits the sensitivity, this can be expressed the decoherence function of the T_2^*-limited processes,

$$f_d = e^{\left(\frac{t_m}{T_2^*}\right)^m}, \tag{3.24}$$

where, m is the order of decoherence. For spectroscopic measurement around the NV resonance peaks, the sensitivity depends on the resonance profile itself [192]. In case of Gaussian resonance profiles for the pulsed ODMR measurements, the overall sensitivity can be computed as

$$\eta^{\mathrm{po}} = \mathscr{P} \frac{1}{\gamma_{\mathrm{nv}}} \frac{\sigma_f}{\bar{C}\sqrt{\bar{R}}} \sqrt{T_\pi + t_m}. \tag{3.25}$$

Here, f_0 is the resonance peak, σ_f is the resonance peak FWHM, $\gamma_{\mathrm{nv}} = \frac{g_e \mu_B}{\hbar}$, is the gyromagnetic ratio of the NV spin, and T_π is the pulse duration. The factor $\mathscr{P}$ relates to the

shape of the resonance, for a Gaussian profile $\mathscr{P} = \sqrt{\frac{e}{8\ln 2}}$ [53]. For shorthand notation, the measurement time is assumed to involve the overhead experimental time $t_m = t_w + 2 \times t_i$. The relevant parameters for the sensitivity calculation in section 3.1.8 were obtained by fitting the normalized count with the following function:

$$N_{\mathrm{ph}}^{\mathrm{po}}(f) = \bar{R} \times \left[1 - \bar{C} \times e^{-\frac{1}{2}\left(\frac{f-f_0}{\Delta f}\right)^2} \right], \tag{3.26}$$

where the normalized counts are calculated by dividing the data with the baseline counts (counts away from the resonance, where no spin transfer occurs). For a Gaussian profile, $\sigma_f = 2\sqrt{2\ln 2} \times \Delta f$. It is noteworthy that for pulsed ODMR measurements at low MW power, T_2^*-limit becomes relevant and has to be considered for sensitivity calculations, the reader is advised to refer to Ref. [53] for more details.
The average sensitivity for the Ramsey sequence based methods can be expressed under the T_2^*-limit as,

$$\eta^{\mathrm{Ra}} = \frac{1}{\bar{C}\gamma_{\mathrm{nv}}\tau} \exp\left[\left(\frac{\tau}{T_2^*} \right)^m \right] \sqrt{\tau + t_m}. \tag{3.27}$$

The free induction decay of the Ramsey fringes for single NV centers highlight the hyperfine structure originating from the electron-nuclear spin coupling. Likewise, the related normalized readout counts can be fitted with a sum of the three precessing hyperfine transitions,

$$N_{\mathrm{ph}}^{\mathrm{Ra}}(t) = \bar{R}\left[1 + \left(\bar{C} \times e^{-(\tau/T_2^*)^m} \sum_i^3 A_i \cos\left(2\pi\nu_i t + \phi_i\right) \right) \right], \tag{3.28}$$

where, ν_i and ϕ_i are the precession frequency and phase corresponding to the hyperfine transitions. The sensitivities in Fig. 3.12 are obtained at $\tau = 0.5 \times T_2^*$. The normalized readout count in this case is obtained by dividing the data with the $m_s = 0$ readout count.

3.1.12 Basic Scanning Probe Example

Considering the example of a simple wire antenna, we can demonstrate the increase in accessible sensing radius gained through robustness. We use the experimental details from Thiel et al. [236] to ensure a realistic model. For illustrative purposes let us assume that a sensitivity of $1\,\mu\mathrm{T\,Hz}^{-\frac{1}{2}}$ is required to resolve a sample's features.[4] To understand the area of the sample over which the sensitivity stays below this threshold we calculate the perpendicular magnetic field strength $B_\perp$ around the antenna to represent the Rabi frequency

[4] This threshold is chosen arbitrarily but lies in the ballpark of achievable sensitivities.

experienced by the NV. Any MW components parallel to the NV centre axis would induce a quickly oscillating detuning and are assumed to average out. $B_\perp$ is shown in the top plot of Fig. 3.13. The bottom plot shows the maximum sensing distance from the wire inside the $1\,\mu\mathrm{T\,Hz}^{-\frac{1}{2}}$ threshold for two pulses, one of which is optimised. We assume that the optimised pulse's robustness is given by the data from Section 3.1.3. In this theoretical example, the optimisation increases the sensing distance by 53%. However, in the experiment we used an Ω-shaped stripline antenna instead of a wire [190]. To ensure the accurate representation of the magnetic field distribution in a future scanning probe setup, the concerned antenna will have to be properly characterised. As indicated by the circles in Fig. 3.13, the model can also predict the acceptable variation in z.

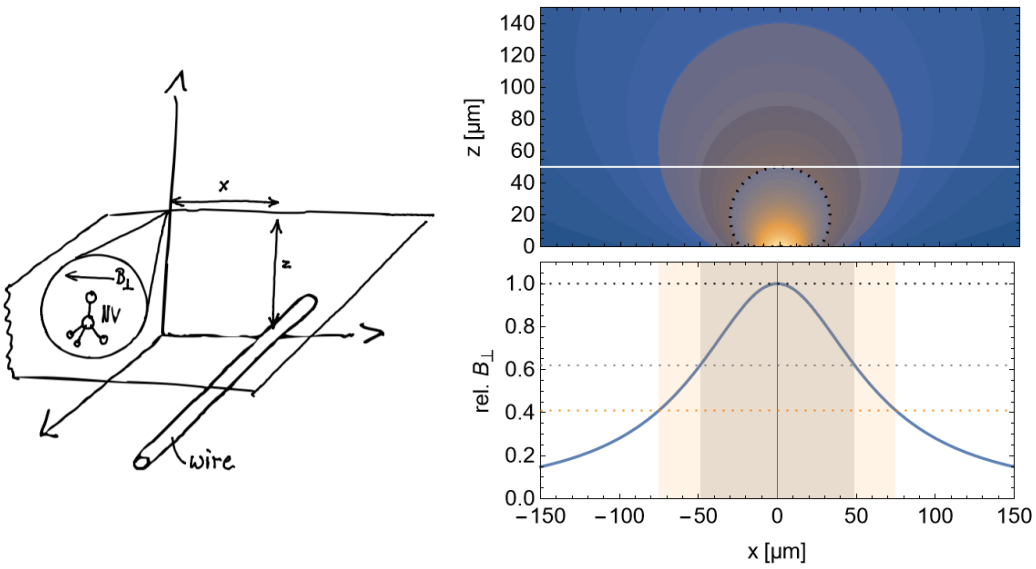

Fig. 3.13 Magnetic field around a current-carrying wire used as a MW antenna. (*left*) Schematic of the underlying sensing setup. (*top*) Strength of the orthogonal magnetic field $B_\perp$ as a function of the scanning distance x and scanning-plane-to-wire separation z. The black dotted contour outlines the maximum magnetic field strength at $z = 50\,\mu\mathrm{m}$, corresponding to the antenna setup described by Thiel et al. [236]. The scanning distance up to which an ODMR-sequence reaches a sensitivity of at least $1\,\mu\mathrm{T\,Hz}^{-\frac{1}{2}}$ depends the robustness of the corresponding MW pulse. The grey and orange areas cover the accessible area for a square and optimised pulse, respectively using the results from Section 3.1.3. (*bottom*) Relative magnetic field amplitude at a separation of $z = 50\,\mu\mathrm{m}$. The robustness is indicated by grey (square pulse) and orange (optimised pulse) areas.

3.1.13 Pulse Spectra

Measurements via ODMR rely on the external magnetic field causing (additional) Zeeman splitting and changing the resonance frequency of the NV transitions. Hence, frequency-selective pulses are important to precisely estimate the change [237, 176]. The Fourier transform of a pulse $Z(\omega) = |\mathcal{F}[I(t) + iQ(t)]|$ gives a lot of information about this selectivity and we show that it predicts the sidebands observed in Section 3.1.3. In order to mimic a realistic spectrum, we convolute the Fourier transform of the pulses with the experimentally-obtained spectrum of the NV centre $P(\omega)$ [238]. The NV spectrum consists of three Lorentzian peaks which are approximately 2.2 MHz apart due to the hyperfine splitting from the nitrogen nucleus. It is obtained by Fourier transforming a Ramsey measurement.

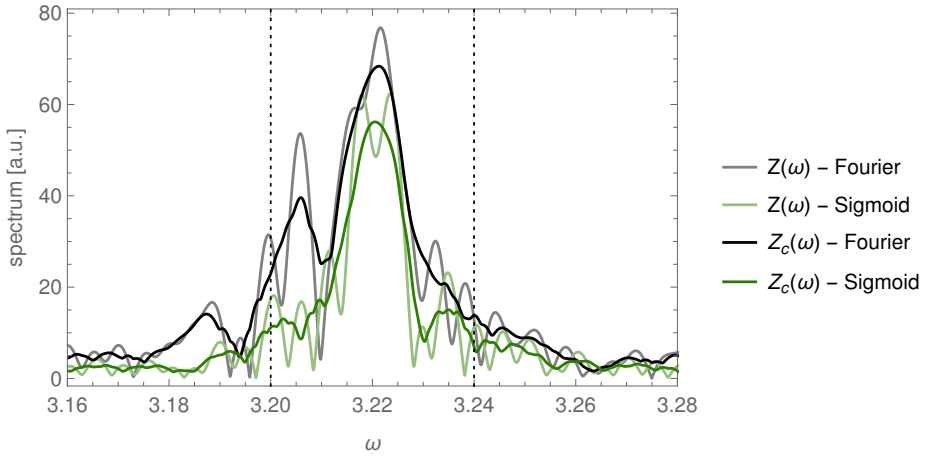

Fig. 3.14 Extended view of the pure and convoluted spectra, $Z(\omega)$ and $Z_c(\omega)$, of the optimised Fourier and sigmoid basis pulses. The lines indicate $\omega_{\text{min/max}}$ respectively and the area between them corresponds to the part of the spectra fitted in Section 3.1.3.

To produce the fitted spectrum from Section 3.1.3, the centre of the convoluted spectrum $Z_c(\omega)$ is fitted to the average fluorescence with two parameters, z_1 and z_2, giving

$$Z_{\text{fit}}(\omega) = z_1 + z_2 \underbrace{\int_{-\infty}^{\infty} Z(x) \cdot P(x-\omega)\, dx}_{Z_c(\omega)}. \tag{3.29}$$

$Z(\omega)$ and $Z_c(\omega)$ are shown in Fig. 3.14. The sigmoid and Fourier basis produce spectra with a clear amplitude difference that is not visible in the fitted version $Z_{\text{fit}}(\omega)$ from Section 3.1.3. In the fit, the amplitude difference disappears due to the normalisation of the counts. The normalisation procedure assumes that the fluorescence at $\omega_{\text{min}} = 3.20\,\text{GHz}$ and $\omega_{\text{max}} = 3.24\,\text{GHz}$ corresponds to the baseline, i.e. the fluorescence of the $m_s = 0$ state.
Still, the full theoretical spectra in Fig. 3.14 confirm that the tails of the sigmoid basis

spectrum are lower than those of the Fourier basis despite the cut-off restriction approach.[5] This trend continues outside the displayed range. Furthermore, the central peak of the sigmoid spectrum is confined to a more narrow frequency range, even though the sigmoid spectrum is scaled to the same maximum amplitude as the Fourier spectrum. It should be noted that, while the sigmoid basis still allows for the simple construction of frequency-limited, high-amplitude pulses when combined with the cut-off restriction, the frequency-limitation is not guaranteed with this approach. However, we could observe the exemplary features shown here as a general trend.

3.1.14 Outlook

In the future, it would be interesting to further investigate how combinations of different pulse bases and restrictions affect the spectrum and hence the sensitivity resulting from an optimised pulse. The frequency-selectivity is an intuitive requirement for an accurate peak to peak measurement.[6] However, to measure small changes in the magnetic field, the overall spectral shape is irrelevant, only the largest detectable slope will influence the sensitivity [53]. In future investigations, we could extend the requirements on the basis to the inherent production of pulses with a high maximum derivative at a specific frequency. This could be achieved using a strategy similar to DRAG (see Section 2.3.5.3) or by engineering an oscillatory spectrum. Similarly, the slope could be used directly as the figure of merit. Another route to improvement would be to combine our methods with the simultaneous driving of all three hyperfine couplings [219].

In summary, we have shown how the optimisation of both, laser and MW controls, can improve the sensitivity of DC magnetometry with shallow NV centres. The ODMR contrast was improved through optical optimisation, by 32%, and MW pulse shaping, by 36%. By taking into account the robustness with respect to the drive amplitude, we have furthermore extended the potential sensing volume. Additionally, the fringe contrast of Ramsey measurements was improved through pulse-shaping by 67%. The portrayed techniques are translatable to many other setups. We especially hope that they will find an application in the improvement of NV-based scanning probe microscopes.

[5] The exact effect of the tails depends on the transfer function of the experiment, which has not been considered here.

[6] The narrowness of the spectrum is reflected by assuming an approximately Gaussian spectral shape (see Section 3.1.11.3).

3.2 Hyperpolarisation of Pentacene-doped Naphthalene

3.2.1 Hyperpolarisation via the Integrated Solid Effect

The integrated solid effect (ISE) is an effective technique to transfer polarisation from one central spin to many others surrounding it [239, 63]. This type of approach is called dynamic nuclear polarisation (DNP), a form of hyperpolarisation, and has been applied in a variety of magnetic resonance settings specifically to enhance NMR signals [240, 241]. As an example, ^{13}C can be used to mark cancer cells, as it is more likely to be absorbed by them than by healthy cells. Unfortunately, the NMR contrast is extremely low at room temperature. Using hyperpolarisation enhances the contrast and consequently enables imaging the cancer cells [242]. External hyperpolarisation, as recently demonstrated by Eichhorn et al. [243] using the sequence developed in Section 3.2.3, marks a step towards the widespread application of such techniques. In the following, we will give a qualitative explanation of the ISE. Detailed derivations are available in references [244, 245].
Let us start by considering one electronic spin and one nuclear spin. The electronic spin can be addressed easily, while we have no direct control of the nuclear spin. This is due to the fact that we have no mechanism to efficiently initialise nuclear spins. In order to exploit the coupling between the spins and polarise the nucleus, we should first consider the frequencies that play a role in the system:

1. **The electronic system's resonant frequency** ω_{0S}: This frequency is defined by the strength of the applied static magnetic field.

2. **The Rabi frequency** Ω **and detuning** Δ: Transitions between the electronic energy levels are triggered by the application of a magnetic microwave field with amplitude $B_\perp$ and frequency $\omega = \omega_{0S} - \Delta$. The speed of the resulting oscillations is then given by the Rabi frequency Ω.

3. **The nucleus' resonant frequency** ω_{0I}: The static magnetic field also causes Zeeman splitting for the nucleus. Its resonant frequency is the Larmor frequency ω_{0I}.

4. **The coupling** $\vec{A}_z$: The mostly dipolar, hyperfine coupling between the electronic system and the nucleus. See Section 1.1.2.4 for more details.

In order to create polarisation, we aim to obtain a flip-flop Hamiltonian. This means that the polarisation gets transferred back and forth between the electronic system and the nucleus. The speed of these oscillations depends on the coupling $\vec{A}_z$ and power put into the system (scaling with $B_\perp^2$), while the amount of transferred polarisation is a question of

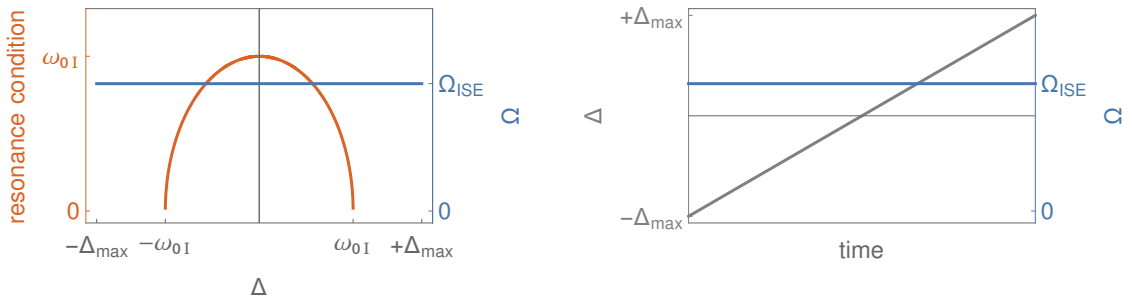

Fig. 3.15 The standard ISE sweep. (*left*) ISE sweep (blue) in comparison to the resonance condition (orange). (*right*) Characteristic linear sweep of the detuning between $\mp\Delta_{max}$ and constant Rabi frequency Ω_{ISE}.

timing. However, to achieve resonance the following condition, called the Hartmann-Hahn resonance [246], has to be met:

$$\Delta^2 + \Omega^2 = \omega_{0I}^2 \tag{3.30}$$

The resonance condition forms a half circle with radius ω_{0I}, when plotted as a function of detuning (see the left plot of Fig. 3.15). The most straightforward answer on how to reach the flip-flop Hamiltonian is to set the magnetic microwave field to almost any point on this resonance line and simply wait. Indeed, this would polarise the nucleus, but not very effectively for the following reasons:

- Not every point on the curve would be equally good. Choosing the centre, the powerful magnetic microwave pulse would rotate the electronic spin very quickly, such that the polarisation efficiency might become very sensitive to the correct timing and exact Larmor frequency. On the flipside, by choosing $\Omega = 0$ it is clear that no polarisation will be transferred either.

- We need to consider what happens when more than one nucleus and more than one electronic spin is addressed. The static magnetic field tends to not be perfectly constant across the sample (whether it is due to experimental inhomogeneity or stray magnetic fields from the environment). These inhomogeneities lead to a broadening of the linewidths. Hence, picking a point on the resonance curve tends to only polarise a fraction of the available nuclei.

Both these issues can be resolved by choosing a constant Rabi frequency Ω_{ISE} and sweeping either the detuning or the strength of the constant magnetic field. This way, even far detuned nuclei are addressed and the sweep speed can be adjusted to optimise the timing. This strategy is usually referred to as the ISE and depicted in Fig. 3.15. In practice, the sequence

is repeated many times and the electron spin is reinitialised at the start of each iteration.
In the setup considered in Section 3.2.3 the constant magnetic field cannot be changed dynamically, hence we sweep the detuning. In the experiment the sample is placed inside a cavity during the polarisation. Afterwards, it is shuttled up inside the apparatus until it reaches the NMR coils, allowing for the direct readout of the nuclear polarisation. Unfortunately, the cavity also modulates the Rabi frequency which means an external linear sweep does not translate to an ISE protocol. Counteracting this effect by compensating for the cavity leads to a very low Rabi frequency and less efficient transfer. Consequently, we use an external linear sweep as a starting point and proceed to enhance the polarisation with optimal control.

3.2.2 Pentacene-doped Naphthalene

Naphthalene consists of two benzene rings forms a crystal lattice as shown on the right in Fig. 3.16. Each naphthalene molecule hosts eight protons. These protons are the nuclear spins we plan to polarise. The electronic spin we use for hyperpolarisation is part of the energy level structure of a pentacene molecule that replaces two naphthalene molecules. Pentacene consists of five linearly-fused benzene rings and is shown in Fig. 3.17. The energy level structure of the pentacene molecule allows us to address it with a MW and initialise it with a laser, similar to the NV centre.

The hyperfine coupling $\vec{A_z^i} = \left(A^i_{xz}, A^i_{yz}, A^i_{zz}\right)^\mathsf{T}$ of the proton spins to the electronic spin is mostly given by the dipolar coupling [245] which can be calculated from each proton's position (r_i, θ_i, ϕ_i) with respect to the centre of the pentacene molecule:

$$\begin{aligned}
A^i_{xz} &= -\frac{3C_A}{r_i^3}\sin(\theta_i)\cos(\theta_i)\cos(\phi_i),\\
A^i_{yz} &= -\frac{3C_A}{r_i^3}\sin(\theta_i)\cos(\theta_i)\sin(\phi_i),\\
A^i_{zz} &= \frac{C_A}{r_i^3}\left(1-3\cos^2(\theta_i)\right),\\
A^i_{\perp} &= \sqrt{{A^i_{xz}}^2 + {A^i_{yz}}^2},
\end{aligned} \tag{3.31}$$

where $C_A = \frac{\mu_0}{4\pi}\hbar\gamma_I\gamma_S$ with the gyromagnetic ratios of the protons γ_I and the electronic spin γ_S, as well as the vacuum permeability μ_0. If we neglect the interaction between the protons, the direction of the perpendicular coupling along x or y is only dependent on the frame of reference. Hence, we are showing the absolute perpendicular coupling $A_\perp$ in Fig. 3.16. The distribution shows that the perpendicular couplings are widely distributed with the maximum at a few MHz. The parallel coupling A_{zz} has a similar distribution. When a hyperpolarisation

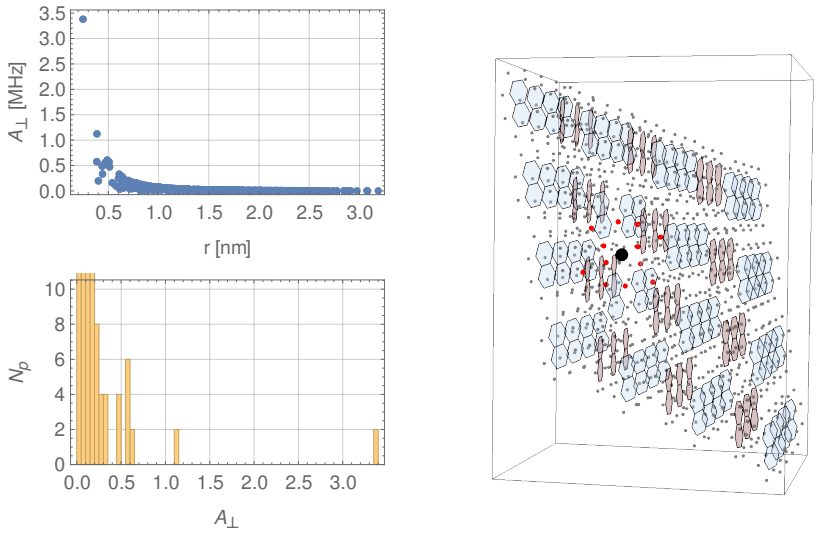

Fig. 3.16 Distribution of protons around a pentacene molecule in a naphthalene lattice. (*left*) The top plot shows the perpendicular dipolar coupling of the protons from a $3 \times 3 \times 3$ cell around a pentacene molecule dependent on their distance. The bottom plot gives the same couplings in a histogram, where N_p is the number of protons with $A_\perp$ in the corresponding bin. (*right*) Naphthalene lattice with protons as small grey dots. The centre of the pentacene molecule is represented as a large black dot with the closest twelve protons in red. The vertical axis is aligned with the pentacene molecule. A full image of the pentacene molecule is given in Section 3.2.3. The code producing these figures is derived from a version kindly provided by Tim Eichhorn [247]. The structure of the naphthalene lattice is calculated according to reference [248].

sequence is applied to the crystal, certain protons get polarised first and when the sequence is repeated the polarisation is redistributed over a further range. To take this effect into account we simulate a set of three protons with different couplings at a time and average over many sets.

Initial tests with our model showed that enhancement of the linear sweep through QOC is generally possible. To achieve the best results for the concerned setup, we apply a closed-loop optimisation to improve the polarisation.

Macroscopic Hyperpolarization Enhanced with Quantum Optimal Control

This section is reproduced from A. Marshall, T. Reisser, P. Rembold, C. Müller, J. Scheuer, M. Gierse, T. Eichhorn, J. M. Steiner, P. Hautle, T. Calarco, F. Jelezko, M. B. Plenio, S. Montangero, I. Schwartz, M. M. Müller, and P. Neumann, *Macroscopic Hyperpolarization Enhanced with Quantum Optimal Control*, in preparation for publication: arXiv:2112.15021

[quant-ph].
The author of this thesis contributed to the planning of this project, the theory and the simulations, as well as writing the manuscript. She was involved in the discussion and analysis of experimental results, as well as parts of the characterisation of the setup and the implementation of the closed-loop optimal control. She composed Figures 1b (Level scheme of pentacene and naphthalene-based protons), 2 (Implementation of a selection of polarization pulses...), 3 (Comparing the polarization build-up...), 4 (Comparison of the ISE and the optimized pulse...), and 5 (Heatmaps of the Fourier transform...).

3.2.3 Abstract

Hyperpolarization of nuclear spins enhances nuclear magnetic resonance signals, which play a key role for imaging and spectroscopy in the natural and life sciences. This signal amplification unlocks previously inaccessible techniques, such as metabolic imaging of cancer cells. In this work, electron spins from the photoexcited triplet state of pentacene-doped naphthalene crystals are used to polarize surrounding protons. As existing strategies are rendered less effective by experimental constraints, they are replaced with optimal control pulses designed with RedCRAB. In contrast to previous optimal control approaches, which consider one or two effective nuclei, this closed-loop optimization is macroscopic. A 28% improvement in signal and 15% faster polarization rate is observed. Additionally, a strategy called **A**utonomously-optimized **R**epeated L**I**near **S**w**E**ep (ARISE) is introduced to efficiently tailor existing hyperpolarization sequences in the presence of experimental uncertainty to enhance their performance. ARISE is expected to be broadly applicable in many experimental settings.

3.2.4 Introduction

Sensitive Nuclear Magnetic Resonance (NMR) spectroscopy and Magnetic Resonance Imaging (MRI) applications are a key driver in research areas from life sciences through material science to quantum computing. The feasibility and sensitivity of such experiments critically depends on the polarization of the utilized spins. Dynamic Nuclear Polarization (DNP) techniques have been shown to increase NMR signals by multiple orders of magnitude [240], enabling previously inaccessible imaging techniques [249]. DNP transfers the polarization from highly polarized electron spins to the target species of nuclear spins [250] used for NMR protocols. Electron spins are polarized, for example, by thermalization at low temperatures and high magnetic fields or by optical polarization of atoms and suitable molecules in gases, liquids, and solids [251–258, 240]. In this work, the electron spins of photoexcited

triplet states in pentacene-doped naphthalene are used as the source of polarization, and the proton spins of naphthalene as the target. This system, shown in Fig. 3.17b, exhibits unique properties. In its ground state, the electron spin is in a singlet state and therefore the host crystal is free of paramagnetic defects. Consequently, proton relaxation times of 50 hours and above have been demonstrated at 77 K and 0.5 T [259].
In its metastable triplet state, the pentacene molecule exhibits a highly polarized electron spin with favorable lifetimes. Together with surrounding nuclear spins, this forms a central spin system that resembles other well-known systems like NV centers in diamond or phosphorous in silicon. This quantum resource for DNP leads to record values of 80% proton polarization [260], which amounts to a polarized proton concentration of 50 M. Exemplary applications of these nuclear spin polarized crystals are portable neutron spin filters in neutron scattering experiments [261, 259] and polarization agents for NMR spectroscopy [243, 262].
Under typical operating conditions (e.g., high magnetic field), electron and nuclear spins are mutually off resonant, prohibiting direct polarization transfer. This is then achieved via advanced spin control methods, like DNP. Real-world experimental constraints like material quality, field inhomogeneities, and limited power and bandwidth usually impair the ideal performance of existing DNP methods. Under such constraints, the maximum achievable polarization is reduced and the time to reach a certain polarization increases.
The goal of this work is to optimize the DNP transfer process by maximizing the proton polarization. Correspondingly, a new multi-step protocol is introduced called **A**utonomously-optimized **R**epeated L**I**near **S**w**E**ep (ARISE).
In the case where the heterogeneity among spins is sufficiently small, they are all equally well controllable. As a result, techniques like nuclear orientation via electron-spin locking (NOVEL) [264, 265] can be employed to transfer polarization. As the environmental complexity and inhomogeneity increases, other techniques are needed. Transferring polarization while counteracting a broad Electron Spin Resonance (ESR) is done with the so-called "Integrated Solid Effect" (ISE) [239, 63]: After the electron spin initialization, either a linear magnetic field sweep is performed while the sample is driven by a constant microwave (MW) field $B_\perp$, or a linear MW frequency sweep is performed at a static magnetic field. The ISE method is notable for both its simplicity and robustness and has been shown to reach up to 80% total nuclear polarization in naphthalene under optimized conditions (e.g., liquid He cooling, sample quality) [260]. It has also been applied to NV centers in diamond at room temperature [266, 267, 244, 258]. While optimizing DNP sequences on a model, i.e. performing open-loop Quantum Optimal Control (QOC), is one method to recover some of their performance [268–270], another is to employ closed-loop QOC by allowing an algorithm to directly control the experiment (shown in Fig. 3.17d) [95, 18, 17, 2, 24]. The latter approach

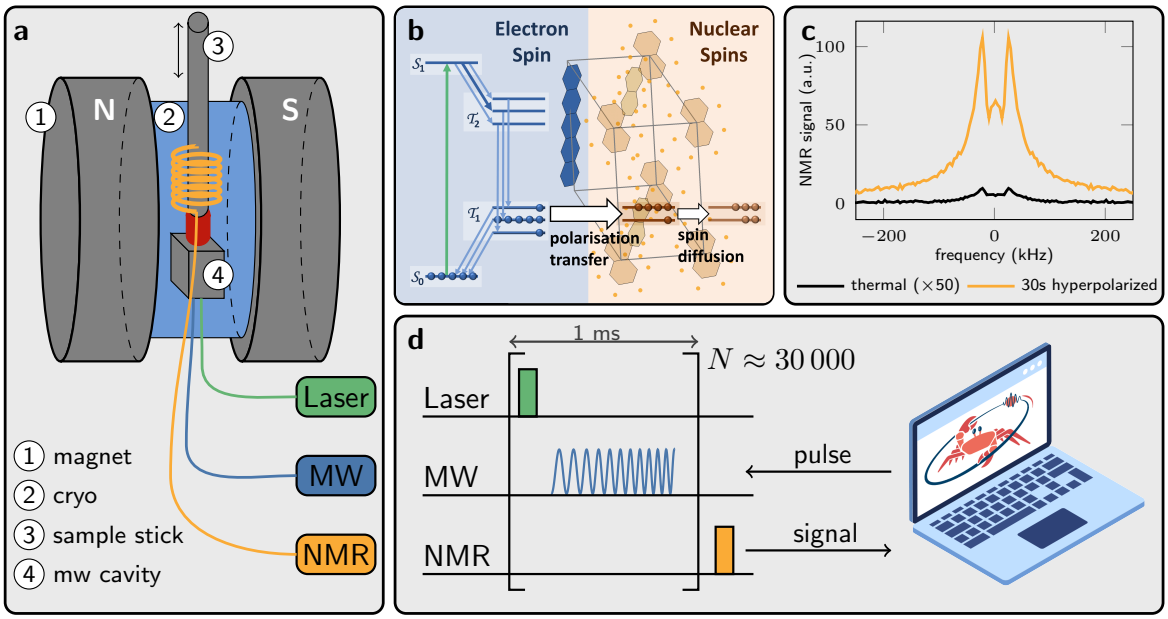

Fig. 3.17 **Experimental realization.** a) Schematic of the in-house polarizer device. The sample (red) is mounted on a sample stick, which allows moving it between a MW cavity and an NMR coil inside a magnetic field at cryogenic temperatures. b) Level scheme of pentacene (electron spin) and naphthalene-based protons (nuclear spins), including the effect of laser excitation (green) and natural decay (blue). Spin diffusion to external nuclear spins [263] is indicated. c) 30 s of hyperpolarization show a clear signal enhancement compared to a 1h thermal build-up, the thermal signal is scaled by a factor of 50 to emphasize its faint polarization peaks. d) Schematic visualization of the pulse sequence, consisting of a laser pulse for triplet state creation and a MW pulse (of variable frequency) for polarization transfer to the nuclear spins. This basic block is repeated with a repetition rate of 1 kHz (i.e. 30,000 repetitions are performed in 30 s). After the polarization, the sample is shuttled into the NMR coil, where the magnetization is measured. An integral over the detected proton polarization is passed to RedCRAB, which provides the shape of the next MW pulse.

is particularly appealing when the experimental setting is very complex or impossible to accurately model. This is the first time that closed-loop QOC has been applied to optimize DNP sequences. Due to the complex molecular environment, coupled with experimental constraints, the system's true transfer function (i.e., from optically initialized pentacene electron spins to macroscopic proton polarization throughout the naphthalene crystal) is obscured, making accurate simulation difficult. The MW DNP sequence is improved via closed-loop QOC to increase the macroscopic proton polarization.

Many advances in quantum technology were only possible due to the design of sophisticated control strategies using methods of QOC [95, 18, 17, 2, 24]. Established methods of QOC include gradient-based algorithms like GRAPE (gradient ascent pulse engineering) [271,

272], the Krotov algorithm [126, 147] or gradient-based algorithms based on automatic differentiation [273], as well as algorithms based on an expansion of the control pulse into a truncated basis like the dressed Chopped RAndom Basis (dCRAB) algorithm [129, 140, 24], typically coupled with direct search maximization algorithms. This pulse expansion ansatz can also be combined with the gradient approach [222, 161, 274]. The dCRAB algorithm is readily applicable to closed-loop control as it can be integrated directly with an experiment, allowing the user to treat the system as a black-box. For this purpose, the dCRAB algorithm was implemented in the QOC software packages Remote-dCRAB (RedCRAB) [5, 275, 26, 6] and its open-source version Quantum Optimal Control Suite (QuOCS) [276]. Recently, RedCRAB enabled automatic calibration of quantum gates [26] and robust sensing operations [3] with NV centers in diamond, optimization of BEC creation in ultracold atoms [6] and the creation of a 20-atom Schrödinger cat state with Rydberg atoms in an optical lattice [1].
In this work, the efficiency of the overall proton polarization process is increased by optimizing the DNP transfer process using closed-loop QOC. To guide the algorithm towards a solution which produces a strongly increased signal, it is helpful to provide a good initial guess. This is done through the application of the ARISE protocol introduced in this work. It provides a systematic approach to the improvement of ISE-like linear sweep DNP sequences in the presence of an unknown experimental transfer function. In Section 3.2.5 the experimental procedure is described (Section 3.2.5.1) and the polarization results and pulses are introduced (Section 3.2.5.2). In Section 3.2.6 the results are discussed and put into context. The measurement techniques are explained in more detail in Section 3.2.7.1 and a short overview of the dCRAB method is given in Section 3.2.7.2. The theoretical model that was developed and used for comparison is explained in Section 3.2.7.3.

3.2.5 Results

A pentacene-d14 naphthalene crystal is placed in a magnetic field of 230 mT at around 130 K, chosen because this is the limit of the polarizer. A $\sim$ 500 mW, 600 ns laser pulses initializes the pentacene molecules into their metastable spin-polarized triplet state $\mathcal{T}_2$ (see Fig. 3.17a) via the singlet state $\mathcal{S}_1$ from which they decay to the lower $\mathcal{T}_1$ triplet via inter-system crossing (ISC) [277]. The pulse repetition rate is fixed at 1 kHz. Depending on the occupation of the $\mathcal{T}_1$-states, the pentacene returns to its ground state $\mathcal{S}_0$ after 80-180 µs. During this intermediate time, a MW DNP sequence transfers electron spin polarization to the densely packed proximal proton spins. Strong dipolar coupling among protons distributes polarization throughout the entire crystal via spin diffusion. The macroscopic proton polarization is measured via NMR

spectroscopy after a 30 s buildup (i.e., 30,000 cycles of electron spin initialization and DNP transfer).
Starting from an external linear sweep (similar to ISE), and altering the amplitude and phase of the MW pulse via the ARISE protocol, using RedCRAB, this polarization is optimized. Closed-loop QOC implicitly accounts for all experimental conditions influencing the transfer from optically initialized pentacene spins to macroscopic polarization.
These could be, for example, the different lifetimes in the metastable state for different electron spin states or variations of the pentacence lifetimes throughout the crystal which might impact the final polarization. Another potential source of uncertainty could be the strong variation of couplings between the electron and surrounding proton spins or the distribution of polarization via spin diffusion during and after the MW DNP sequence. Fluctuations in the experimental setup might also play a role, as bandwidth limitations of microwave equipment, spatial and spectral MW field variation inside the MW resonator, and spatial variation of laser intensity can also impact the efficiency. Additionally, it is challenging to control the amplitude of the MW field while its frequency is scanned across the resonance. Black-box (closed-loop) QOC does not directly incorporate variations in these parameters, whose role in polarization transfer is not understood, but if they play a role it can be captured by such an optimization. Importantly, some of these influences are very hard to predict theoretically. The ARISE protocol results in a 26% increase in the hyperpolarized signal observed alongside a 15% higher polarization rate. As a result, the optimal sequence reaches 98% of the maximum polarization achieved with the linear external sweep in just 3.36 hours, instead of 9 hours (see Fig. 3.19). This decrease by a factor of 2.6 enables multiple follow-up experiments per day.
Additionally, by examining the shape of the optimized pulse and fitting its main features, a simplified analytical function is obtained describing the pulse (shown in Section 3.2.9, labelled “Fitted Optimal”). This retains most of the enhanced performance of the optimized sweep.

3.2.5.1 Experimental Realization

The experimental results are obtained in an in-house polarizer device, shown in Fig. 3.17a, consisting of an optically accessible MW cavity inside an electromagnet operating at fields up to 800 mT. Within the MW cavity, photo-excited triplet states are created using a 556 nm pulsed laser with a repetition rate of 1 kHz delivering 0.35 mJ optical power in a 588 ns laser pulse every 1 ms and setting the timing of experiments. With the sample positioned inside the MW cavity, the spin state is manipulated using a MW pulse in between laser pulses. Sophisticated pulse shapes can be sampled and uploaded to an Arbitrary Waveform Generator

(AWG) using the experimental control software Qudi [278]. The sample is attached to a holder that allows it to be shuttled into an NMR coil, which is located next to the MW cavity. Here, an NMR spectrometer (Magritek Kea^2) is used to read out the polarization of the proton spins using a 1Pulse measurement. This round-trip takes approximately 45 seconds from the pulse engineered by the RedCRAB software to the NMR measurement.
An optional 532 nm continuous wave laser additionally allows the readout of the pentacene's electronic spin state optically; it is not used during closed-loop optimizations, but during the pentacene spin characterization experiments. Cooling of the sample is provided by a nitrogen gas flow system, which allows precise control of the temperature from 130 K to above room temperature. The measurements are carried out at the lower limit of 130 K. A naphthalene crystal doped with pentacene grown in-house provides the electron spin system used as the polarization target.

3.2.5.2 Polarization Results

The optimization directly adjusts the pulse phase for experimental convenience, but as the detuning modulation Δ contains the same information and connects directly to the system dynamics, it is displayed in Fig. 3.18 instead. The first row of Fig. 3.18 shows the detuning modulation Δ as a function of time during the pulse. In the second row, the y-axis shows the amplitude Ω during the pulse for both the externally applied field and the internal cavity field. The Hartmann-Hahn resonance [246], shown in orange, is calculated using the time-dependent detuning assuming the target spin is a proton. In the third row of Fig. 3.18, experimental data and simulation are compared, showing how the polarization builds up during the pulse.
The first initial guess pulse is an ISE-like linear sweep whose parameters (amplitude, sweep rate and duration) had already been manually tuned on the experimental setup. This pulse serves as the benchmark against which the optimized pulses are compared both in the experiment and in the simulation. The optimization of that guess results in the pulse labelled "Optimal (Linear)" which shows a relative polarization improvement of approximately 19%. The evolution of the Figure of Merit (FoM) during the search for an optimized pulse and the comparison between the initial and the optimized version are shown in Fig. 3.20.
The "Optimal (Linear)" pulse transfers the majority of its polarization during the first 10 µs. It is notable that the detuning is oscillating during that time, and it crosses the cavity resonance several times. The algorithm slows the sweep down as the detuning approaches the resonance. Both features appear in multiple optimization outcomes. Arguably, if some electron population is left untransferred, subsequent sweeps through the resonance in both

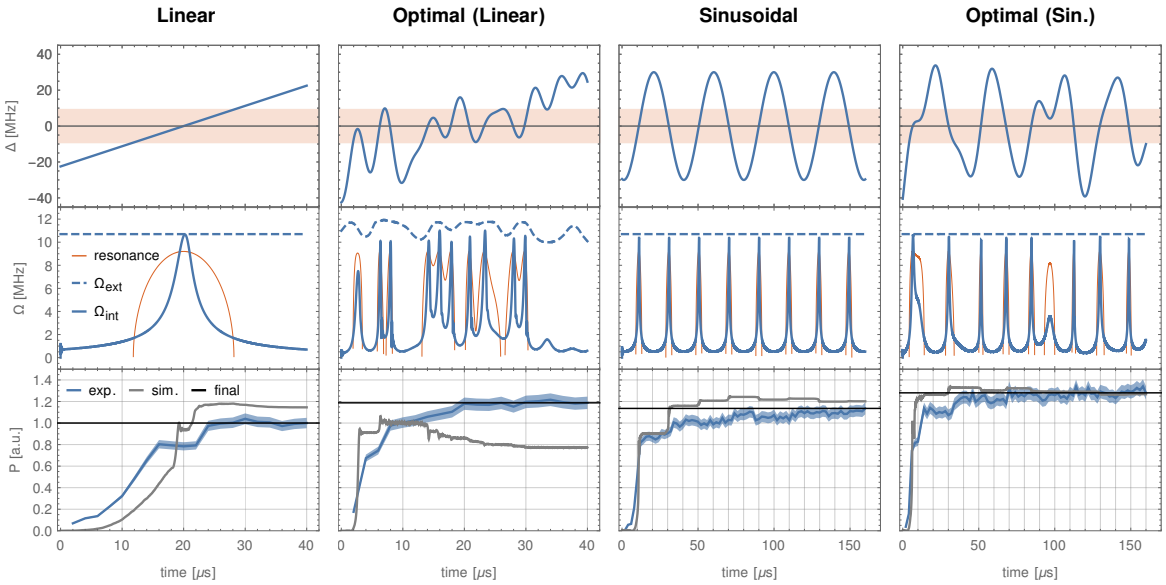

Fig. 3.18 **Implementation of a selection of polarization pulses.** From left to right, the figure presents the following MW pulse schemes on the resonator: The externally applied linear sweep, a linear sweep-based QOC-generated pulse, sinusoidal sweep of the detuning, a corresponding QOC-generated pulse. The first row gives the detuning applied by the drive with respect to time. The orange area comprises the window in which the Hartmann-Hahn resonance condition lies ($\Delta^2 = \omega_{0I}^2 - \Omega^2$). The second row shows the Rabi frequency as applied externally (dashed), the field inside the cavity (solid blue), and the resonance condition for the given detuning (thin, orange). The last row shows how the polarization builds up over the course of the pulse. Experimental values (exp.) are shown in blue, theoretical values (sim. for simulation) in gray. The solid black line indicates the final polarization.

directions (from positive to negative detuning and back) can serve as additional opportunities for the polarization of more weakly coupled nuclear spins.

After analyzing the effect of the amplitude and phase of the pulse independently (see supplementary information for more details Section 3.2.9), the MW amplitude is kept constant in later optimizations. To further explore the idea that repeated sweeps through the resonance are beneficial, pulses with phase oscillations that use a range of frequencies and pulse durations are tested, see the supplementary material Section 3.2.9 for more details. The "Sinusoidal" pulse shown in column three of Fig. 3.18 is guessed in this manner. It outperforms the linear sweep by approximately 14%.

The "Sinusoidal" protocol in Fig. 3.18 then becomes the new guess pulse for the optimal control algorithm. After adding more frequency components, RedCRAB obtains the "Optimal (Sin.)" pulse. It outperforms all other pulses in both final polarization (approximately 28%

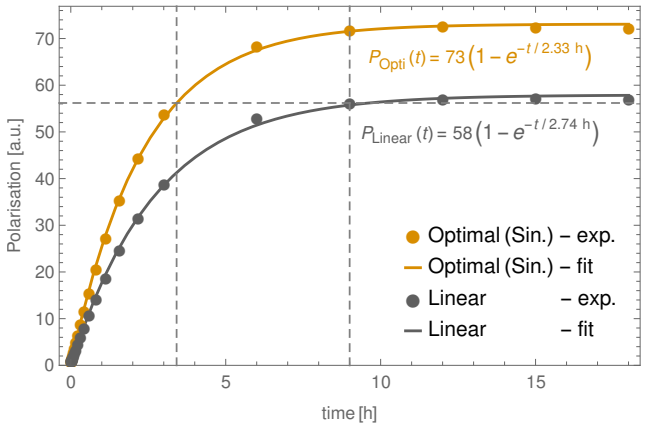

Fig. 3.19 **Long-term polarization build-up.** Comparing the polarization build-up using the optimal settings for the linear sweep and the RedCRAB optimized pulse, shown in Fig. 3.18. Using closed-loop optimal control, we reach a higher final polarization in a shorter build-up time before saturation. The vertical dashed lines mark the times at which the polarization reaches 98% of the maximum polarization of the linear sweep pulse. This level is reached in 3.35 h using the optimized pulse, in contrast to 9 h with the linear sweep. The formulas placed in the figure correspond to the exponential fits, P_{Opti} and P_{Linear}, of the polarization build-up during the optimized pulse and the linear sweep, respectively.

higher with respect to the linear sweep for the short build-up measurement) and polarization rate on our setup.

When the pulse is significantly detuned from the resonance, as in the first 5 µs, the energy gap between the spins is large and so very little polarization can be transferred. As this gap closes, the nuclei are more likely to be polarized and the pulse slows down to allow for an extended transfer period. The detuning "slow down" was recreated with an analytical polynomial function. (For details, see supplementary information in Section 3.2.9.) The resulting "Fitted Optimal" pulse largely retains the polarization capability of the optimized pulse. The comparable efficiency corroborates that the "slow down"-feature contributes to the substantial polarization build-up during the first 30 µs. This behavior is reminiscent of optimal adiabatic passages with Landau-Zener protocols and optimal controlled crossings of quantum phase transitions. Both have been investigated in different theoretical and experimental scenarios [279–283] providing a basis for further exploration.

The key result of the paper is shown in Fig. 3.19, where the RedCRAB-optimized "Optimal (Sin.)" demonstrates two clear improvements over the linear sweep. Firstly, the magnitude of polarization increases by 26% when using the optimized pulse. Secondly, the optimized pulse reaches, in only 3.35 hours, the same polarization that the linear sweep approach obtains after 9 hours of continuously repeating the protocol, making it a factor of 2.6 faster. These times correspond to ~98% of the maximum polarization of the linear sweep, which

is within the error margin of the polarization measurements. This allows for more than doubling the number of polarized crystals in a given time. Previously, crystals were left to polarize overnight to reach sufficiently high polarization. Using the optimal protocol, it is now possible, on the current experimental setup, to polarize several crystals per day. Due to its increased performance, the "Optimal (Sin.)" pulse was also applied as the hyperpolarization method of choice by Eichhorn et al. [243]. In that paper, a bulk crystal polarization of 25% is achieved using the optimized pulse.
The saturation of the polarization at this higher level is likely due to an equilibrium being reached between the polarizing sequence and the competing T_1 decay process of the nuclear spins [263]. The lifetime of the nuclear states is measured to be approximately 3-4 hours under laser illumination, considering the specific values for the magnetic field B_0 and temperature. In this case, it is limited due to the laser illumination and MW fields causing, for example, additional heating. While this is the limit for the lifetime during polarization transfer, the polarization can be stored in the sample afterwards for much longer. Lifetimes between 50 hours [243] and 800 hours [259] have been reported for similar crystals at different temperatures and magnetic fields.

3.2.5.3 ARISE

Generalizing the steps taken to achieve the results of the previous section, the **A**utonomously-optimized **R**epeated L**I**near **S**w**E**ep (ARISE) procedure is introduced. Each step provides a recipe for finding a good initial guess for the following optimization. While this should be unimportant for an infinite-dimensionally parameterized optimization without limits and infinite measurement precision, in practice those restrictions apply, leading the algorithm to local instead of global optima. Despite the dCRAB algorithm's approach allowing it to escape local minima under certain circumstances, the optimization time is also drastically reduced if the initial guess is chosen carefully [24]. The protocol consists of three steps:

1. **Tune the linear sweep.** Do a parameter search for the sweep range $\Delta_{\max}$ and duration t_{Linear} producing the most efficient polarization transfer.

2. **Construct multi-sweep.** Set up a protocol which sweeps the detuning repeatedly between $\pm\Delta_{\max}$ for N_{osc} times with a period τ. Do a parameter search for N_{osc} and τ, starting from $\tau = t_{\text{Linear}}$.

3. **Apply quantum optimal control.** Search the full function space of the detuning $\Delta(t)$ using an optimal control algorithm. The initial guess is provided by the multi-sweep protocol from the previous step.

In this work, steps one and two are accomplished through a simple parameter sweep. During the second step, the detuning is swept with the function $-\Delta_{\max}\cos(2\pi t/\tau)$, however this could be replaced by linear sweeps. As the setup requires the pulse phase $\varphi_{\text{ext}}(t)$ as an input, all detunings are translated to phase modulations (see Section 3.2.7.3). In general, experimental feedback determines the best solution for the respective step. Here, it took the form of the proton NMR signal after 30,000 repetitions of the sequence. The third step is implemented using the RedCRAB software, which suggests different shapes for the phase of the pulse (see Section 3.2.7.2).

3.2.5.4 Comparison to Simulation

As shown in Fig. 3.17b the electron spin of the pentacene molecule is excited to the $\mathcal{S}_1$ state with a short laser pulse. From there it decays to the triplet states $\mathcal{T}_2$ and subsequently $\mathcal{T}_1$ via ISC [277]. $\mathcal{T}_1$ then couples to the nuclear spins in the vicinity of the molecule. The three states of the triplet correspond to spin quantum numbers $m_s = 0$ and $m_s = \pm 1$. An external magnetic field induces a Zeeman splitting of the $m_s = \pm 1$ levels, allowing for a two-level approximation. As the pentacene is deuterated, the resonances of the pentacene's own nuclear spins are shifted far enough from the other protons in the crystal that they can be neglected. The electron spin is assumed to have its origin at the center of the pentacene molecule. To extract the parallel and perpendicular dipolar coupling to the pentacene's electron spin, 574 protons of the nearest naphthalene molecules contained in the $3\times3\times3$ unit cells around the pentacene molecule are modelled (for details, see Section 3.2.7.3).
The first column of Fig. 3.18 shows the external linear sweep approach. Here, the polarization is transferred when the system is close to the fulfillment of the Hartmann-Hahn resonance condition. The external amplitude is kept constant while the frequency is swept across the resonance, allowing for polarization transfer. During the experiment, the polarization plateaus at the center of the pulse before continuing to rise in the second half of the pulse. The simulation results contain the same features, however the plateau is shorter and the initial rise is slightly delayed compared to the experimental data. These differences might be caused by the lack of a full analytical model that extends the existing description of the cavity with distortions due to electronics and other components of the setup. It should be noted that polarization plateaus occur in the simulated results across all pulses when the detuning is above the resonance condition. The relative speed-up of the polarization transfer in the "Optimal (Linear)" pulse is visible in both the simulation, and the experiment. However, a divergence between the measurement and the simulation arises in the latter part of the pulse. This could be explained by the very fast oscillations in cavity field amplitude, which are not

captured in full detail in the simulation, due to the unknown transfer function of the setup's electronics.
The simulated polarization of both, the "Sinusoidal" and the "Optimal (Sin.)" pulse, match the experimental data closely. Again, the initial step-plateau-step shape of the "Sinusoidal" is reduced after optimization. Almost all the performance gained by optimizing the pulses arise from the behavior during the first 40-50 µs of the pulse. This is on a similar timescale as the electron's decay to the singlet state. In the simulation, the polarization of the longer pulses slowly decreases after ca. 80 µs. This was not seen in the experiment, most likely due to spin diffusion: The large amount of weakly coupled nuclear spins leads to a slow distribution of polarization away from the electron spin. Spin diffusion is expected on a timescale of ca. 100 µs according to calculations of the dipolar interaction strength between the protons [263].

3.2.6 Discussion

The use of closed-loop optimal control provides a strategy for improving hyperpolarized NMR signals in complex experimental setups despite the unknown transfer function. A concern often raised about numerically optimized sequences is that they lose generality and only apply to a specific setup or sample. This is not the case for the "Optimal (Sin.)" sequence which, due to its increased efficiency, has been successfully applied on different crystals with varying spin relaxation times across an extended period of time [243]. This is now the gold-standard pulse in the lab.
The combination of a 15% faster polarization rate and a 26% higher polarization level provides a factor of 2.6 reduction in the time taken to polarize crystals to within the margin of error of the previous method. This allows for multiple crystals to be polarized per day to be used in external hyperpolarization experiments [243]. Furthermore, these improvements lead to higher levels of polarization in a shorter time, resulting in an overall polarization within the crystal of about 25% [243]. Such strongly polarized crystals are necessary to transfer polarization to external nuclear spins. By operating under liquid Helium conditions and with improved crystal quality, even higher values are anticipated [260]. Mimicking the features of the optimized pulse by fitting an analytical function to it (as shown in the supplementary material Section 3.2.9) retains almost all the improved performance. This is a good starting point not only for future optimization, but also for further investigations of the system dynamics.
A key feature of all the sequences that outperform the linear sweep is that they repeatedly sweep through the cavity resonance. This gives the sequences an extra opportunity to transfer polarization, suggesting that the first sweep leaves some electron polarization untransferred. The simulation shows that the first sweep primarily transfers to one of the most strongly

coupled nuclear spins, while subsequent sweeps redistribute the polarization to a wider range of couplings. This type of dynamics can only be accounted for when multiple nuclear spins are considered or the optimization is done on a macroscopic system.
The ARISE protocol offers a starting point for future optimizations of DNP sequences using both open and closed-loop protocols. Inherently flexible, the protocol is easily customized to fit any number of experiment setups, including the complex molecular environment seen here.
In conclusion, the application of the ARISE protocol results in a 26% improvement of the polarization level and 15% faster polarization rate. Consequently, crystals were efficiently polarized to 25% bulk proton polarization. These crystals were then used as the polarization source for an external hyperpolarization experiment [243] which demonstrated strong transfer to external spins.

3.2.7 Materials and Methods

3.2.7.1 Measurement Technique

The crystal grown in-house is cleaved along the *ab* crystallographic plane, and it is mounted into a sample holder oriented along the *b* crystallographic axis. The sample holder is then attached to a motorized stage, enabling it to be shuttled into the MW cavity, where it is cooled to 130 K. Optically Detected Magnetic Resonance (ODMR) can be observed in pentacene-doped naphthalene crystals, where the triplet state is created using a 556 nm laser pulse. By observing the fluorescence of the crystal under constant MW illumination, while changing the magnetic field, the electron spin resonance of pentacene can be found. The high-field transition of the pentacene triplet is used for both alignment and polarization. The crystal is then aligned by monitoring the ODMR spectrum while the sample is rotated, the best alignment is found when the resonance field is maximized. Rabi oscillations are observed with a maximum Rabi frequency of 19.3 MHz, by varying the duration of a resonant MW pulse.
The experimental sequence used to hyperpolarize the sample is shown in Fig. 3.17 (d). Initially, the sample is shuttled into the MW cavity and a laser pulse is used to create a photo-excited triplet state. A pre-sampled waveform is applied, which has been suggested by the optimal control algorithm, and uploaded to the AWG. To measure the signal produced by the suggested pulse, the sample is shuttled into an NMR coil. Using a Kea NMR spectrometer, the proton polarization is then measured using a single pulse NMR experiment. Integrating over the peak of the resulting NMR spectrum provides a relative estimate of the proton polarization. The RedCRAB algorithm is fed with this integrated signal and its estimated

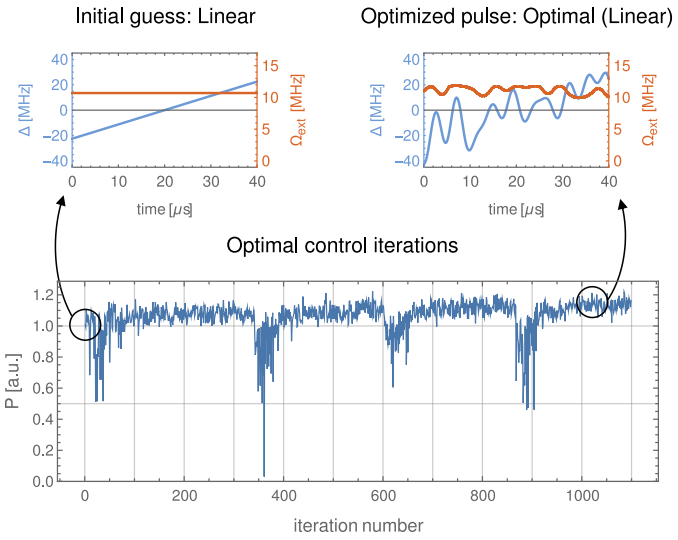

Fig. 3.20 **Optimization procedure.** Comparison between the linear sweep pulse (*top left*) and the pulse after optimization (*top right*). The MW amplitudes are shown in red and the detuning from cavity resonance in blue. The bottom graph shows the change of the FoM over different sub- and super-iterations during the optimization.

uncertainty to produce the next guess pulse. One experimental cycle lasted approximately 40 seconds, and the optimizations typically ran for 12 hours.

3.2.7.2 Optimal Control

As previously mentioned, methods based on optimal control theory aim to optimize a functional f by modifying time-dependent control functions $u_i(t)$. This functional is the FoM, it includes all the relevant information contributing to the quality of an operation. To simplify the optimization problem, the controls can be parameterized in terms of N_{be} basis functions $v_\ell(t)$ with corresponding parameters c_ℓ

$$u_i(t) = \sum_{\ell=1}^{N_{\text{be}}} c_\ell v_\ell(t)\,. \tag{3.32}$$

The FoM therefore depends on the coefficients of these basis functions

$$\text{FoM}(u_i) = f(c_\ell, v_\ell, t)\,. \tag{3.33}$$

The solution to the problem is found using an iterative optimization algorithm, which takes in the FoM for a defined set of parameters and returns a new set of parameters. Closed-loop control involves the algorithm directly interacting with the experimental setup. Hence, it

automatically takes into account real-world imperfections. Specifics of the measurement technique can be found in Section 3.2.7.1. The algorithm improves the FoM by comparing the results from different iterations. It follows the direction of improvement, while exploring the parameter landscape and exploiting its features. An optimal set of controls is eventually obtained after a number of iterations and FoM evaluations.
Limiting the size of the parameter landscape reduces the number of experimental runs and hence the total optimization time. The dCRAB algorithm [129, 140, 23, 24], in combination with the Nelder-Mead [284, 143] simplex optimization algorithm, is a good choice for this. A small parameter space is created by randomly picking a number of basis functions, optimizing them, and then switching to a new parameter space. An optimization in a single parameter space is called a super-iteration. This allows the optimization to start afresh and continue, even if it temporarily gets stuck in a local optimum.
For the parameterization the Fourier basis is chosen, which provides a simple method to restrict the bandwidth of the controls by limiting their maximum oscillation frequency component through a capping of $\omega_{d,\ell}$ in

$$u(t) = \sum_{d=1}^{N_{\mathrm{SI}}} \sum_{\ell=1}^{N_{\mathrm{be}}} [A_{d,\ell}^{\mathrm{opt}} \sin(\omega_{d,\ell} t) + B_{d,\ell}^{\mathrm{opt}} \cos(\omega_{d,\ell} t)]\,. \tag{3.34}$$

N_{be} represents the number of basis elements (i.e., the size of the parameter space in each super-iteration), while N_{SI} corresponds to the number of super-iterations. The parameter space of the optimization is spanned by $c_{d,\ell} = \{A_{d,\ell}^{\mathrm{opt}}, B_{d,\ell}^{\mathrm{opt}}\}$ while $\omega_{d,\ell}$ is randomly initialized with frequencies within a pre-defined interval for each super-iteration defining the basis functions $v_{d,\ell} = \{\sin(\omega_{d,\ell} t), \cos(\omega_{d,\ell} t)\}$. Meanwhile, the length of the pulses is kept constant. The combination of this limited search space for efficient closed-loop optimization together with the three-step ARISE protocol (see Section 3.2.5.3) enables the encoding of a sufficient amount of information in the control pulse to substantially increase its performance [285].

3.2.7.3 System Model

The model for the simulation consists of an electron spin coupled to three nuclear spins. Both the electron and nuclear spins are considered to be spin-half particles. A strong, constant magnetic field $\boldsymbol{B}_0 = B_0 \hat{z}$ is aligned along the long axis of the pentacene molecule, representing the z-axis. The total spin Hamiltonian of the electron can be written as,

$$H_{el} = \frac{\hbar}{2} \omega_{0S} \sigma_z + \frac{\hbar^2}{4} \left[D \left(\sigma_z^2 - \frac{1}{3} \boldsymbol{\sigma}(\boldsymbol{\sigma} + 1) \right) + E(\sigma_x^2 - \sigma_y^2) \right], \tag{3.35}$$

where $\boldsymbol{\sigma} = \{\sigma_x, \sigma_y, \sigma_z\}$ are the Pauli matrices σ_k. The Zeeman interaction is described by $\omega_{0S} = -\gamma_S B_0$, where γ_S is the electron spin's gyromagnetic ratio. The factors D and E correspond to the zero-field splitting [277, 286]. The exact transition frequency is determined experimentally, and the magnetic field is aligned such that the splitting is symmetric.
The driving field has a carrier frequency which is resonant with the electron spin $\omega_{\text{res}} = D - \omega_{0S}$. Its amplitude $\Omega_{\text{ext}}(t)$ and phase $\varphi_{\text{ext}}(t)$ are modulated to control the system. It is then transformed to the field inside the cavity Ω_{int} using Eq. (3.40). Coupling between the electron and nuclear spins is described by the hyperfine interaction tensor $\mathbf{A}^i$ with the nuclear spin indices $i = \{1, 2, 3\}$. A detuning Δ_{es} is introduced, describing the deviation of the field inside the cavity from the electron resonance frequency. In the rotating frame of the MW, applying the rotating wave approximation, the Hamiltonian is then given by [287]

$$H = \hbar\left(\text{Re}[\Omega_{\text{int}}(t)]S_x + \text{Im}[\Omega_{\text{int}}(t)]S_y + \Delta_{\text{es}}S_z + \omega_{\text{L}}\sum_{i=1}^{3} I_z^i + \sum_{i=1}^{3}\mathbf{S}\cdot\mathbf{A}^i\cdot\mathbf{I}^i\right), \tag{3.36}$$

where $\mathbf{S} = \{S_x, S_y, S_z\}$ with $S_k = \frac{1}{2}\sigma_k \otimes \mathbb{I} \otimes \mathbb{I} \otimes \mathbb{I}$, $(k \in \{x, y, z\})$ are the electron's spin operators. $\mathbf{I}^i$ and I_k^i are the equivalent operators for the nuclear spin with index i and Ω_{int} is the complex, time-dependent field inside the cavity $\omega_{\text{L}} \approx 9.2\,\text{MHz}$ corresponds to the Larmor frequency of the nuclei. The voltage signal, which is fed into the AWG, is given by

$$V_{\text{ext}} = V(t)\cos\left((\omega_{\text{res}} + \Delta_{\text{cs}})\,t + \varphi_{\text{ext}}(t)\right). \tag{3.37}$$

The conversion between $V(t)$ and $\Omega_{\text{ext}}(t)$ is determined directly from experimental data. The phase modulation $\varphi_{\text{ext}}(t)$ can be translated into the drive detuning $\Delta(t) = \dot{\varphi}_{\text{ext}}(t)$.
In the secular approximation [64], only the dominant coupling terms along z are kept, giving

$$\mathbf{S}\cdot\mathbf{A}^i\cdot\mathbf{I}^i \approx S_z\cdot\left(A_{zx}^i I_x^i + A_{zy}^i I_y^i + A_{zz}^i I_z^i\right). \tag{3.38}$$

They are calculated for the respective position of the nucleus in the crystal structure by considering a purely dipolar interaction [245].
The static detuning values Δ_{es} for the Hamiltonian shown in Eq. (3.36) are drawn from a normal distribution with a full width half maximum (FWHM) of 10 MHz to mimic additional frequency shifts due to magnetic field inhomogeneities and other impurities.
The system description includes the dephasing of the electron spin via a Lindblad operator $R_1 = \sqrt{\frac{\Gamma_{\text{el}}}{2}}S_z$, where Γ_{el} is the dephasing rate [43]. The only electron states that interact with surrounding nuclei are the $|0\rangle$ and $|1\rangle$ states in the $\mathcal{T}_1$ triplet (see Fig. 3.17). To account for the decay from $\mathcal{T}_1$ to $\mathcal{S}_0$, the model includes a shelf state, which does not interact with the

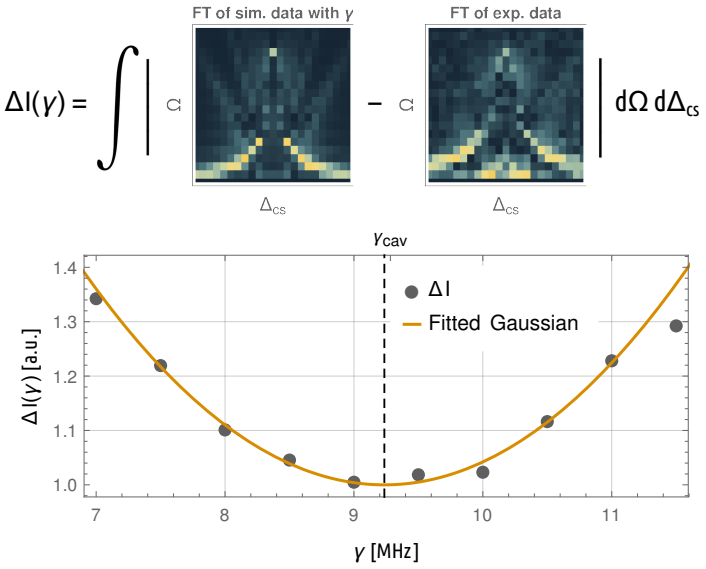

Fig. 3.21 **Characterization of the set-up via response factor γ.** The agreement between experiment and simulation, ΔI, is calculated via the Fourier transform Ω of the driven Rabi signal for varying cavity detunings (*top*). The integral indicates the overlap of measured and simulated distribution, which is shown for different values of cavity response fed to the simulation in the bottom plot. The black line indicates the minimum of the error in overlap between simulation end experiment at $\gamma_{\mathrm{cav}} = 9.24\,\mathrm{MHz}$ (*bottom*).

drive. It is only coupled via the loss rates $\Gamma_{\mathrm{loss},0}$ and $\Gamma_{\mathrm{loss},1}$ from the respective triplet states. The corresponding Lindbladians are given by $R_2 = \sqrt{\Gamma_{\mathrm{loss},0}}\,\sigma_{-,0}$ and $R_3 = \sqrt{\Gamma_{\mathrm{loss},1}}\,\sigma_{-,1}$ with $\sigma_{-,0} = |s\rangle\langle 0|$ and $\sigma_{-,1} = |s\rangle\langle 1|$.
The evolution of the density matrix is then solved using the Lindblad master equation

$$\dot{\rho} = -\frac{i}{\hbar}[H,\rho] + \sum_{j=1,2,3}\left(R_j\rho R_j^{\dagger} - \frac{1}{2}R_j^{\dagger}R_j\rho - \frac{1}{2}\rho R_j^{\dagger}R_j\right), \tag{3.39}$$

where ρ is the density matrix of the system.
The effect of the cavity on the external driving field is characterized by the cavity response factor γ_{cav} and given by the differential equation

$$\frac{\partial}{\partial t}\Omega_{\mathrm{int}}(t) = \gamma_{\mathrm{cav}}\left(\Omega_{\mathrm{ext}}(t)\cdot e^{-i\varphi_{\mathrm{ext}}(t)} - \Omega_{\mathrm{int}}(t)\right) - i\Delta_{\mathrm{cs}}\Omega_{\mathrm{int}}, \tag{3.40}$$

where Δ_{cs} describes the constant detuning of the cavity from the resonance of the electron spin transition frequency [288].

The solutions to the differential equations in Eq. (3.39) and Eq. (3.40) are calculated numerically using the DifferentialEquations.jl [289] and other Julia packages [290–304]. To obtain a realistic polarization build-up in Fig. 3.19, Eq. (3.39) is solved for and averaged over 1000 instances. For each instance, three random but distinct nuclei are picked from the 30 most strongly coupled nuclei and the detuning Δ_{es} is sampled from a Gaussian distribution. This way, mechanisms which are neglected in the common weighted sum single nucleus approximation are captured. Examples include the re-polarization of the electron spin through partially polarized nuclei or the redistribution of polarization from one nucleus to another. The mean over many runs with different coupling combinations takes into account the variety of couplings in the system with reasonable computational resources.
The cavity response γ_{cav} is determined by repeatedly applying constant external drive fields with different cavity detunings Δ_{cs}, obtaining a photon count that corresponds to the electron state. B_0 is adjusted such that the spin always stays resonant with the drive frequency. Oscillations are recorded for times up to 0.6 µs from the start of the drive pulse. The detuning is swept through a range of ±25 MHz around the resonance. The maximum of the Fourier transform of the photon count then corresponds to the Rabi frequency Ω for a detuning Δ_{cs}. The cavity dynamics are complex, leading to a response similar to the example shown at the top right of Fig. 3.21. These measurements are modeled for an electron spin inside a cavity with a response factor γ_{cav} between 5 and 14 MHz (range suggested by response time based on the measured Q factor of the resonator using a spectrum analyzer). The resulting Fourier transforms are compared to the experimental values. The comparison was done by calculating the overlap of the normalized measurement and simulation grids as shown in Fig. 3.21. The minimum of the sum of the absolute difference between each grid point of the measurement and simulation data is obtained by a Gaussian fit resulting in $\gamma_{cav} = 9.24$ MHz. The values for the decoherence rate, Γ_{el}, of the electron spin and the loss rates to the shelf state, $\Gamma_{loss,0}$ and $\Gamma_{loss,-1}$, are found by performing a Hahn echo measurement and state-dependent lifetime measurements. For the dephasing time of the electron we obtain $1/\Gamma_{el} = 10$ µs and the triplet-state decay times are measured to be $1/\Gamma_{loss,0} = 80$ µs and $1/\Gamma_{loss,-1} = 180$ µs.

3.2.8 Acknowledgements

The authors would like to acknowledge receiving funding from the European Union's Horizon 2020 research and innovation programme under the Marie Sklodowska-Curie QuSCo (N° 765267), EU Quantum Flagship projects ASTERIQS (N° 820394), PASQuANS (N° 817482) and the ERC Synergy grant HyperQ (N° 856432).

Author contributions

AM and CM performed the experiments with help of JS, and PN. TR simulated the system with support from PR, AM, and MMM. TR, PR, and MMM developed the theoretical model and facilitated access to, maintained, and tailored the closed-loop control software. AM and CM integrated and configured the control software to work with the experiment. MG grew the sample, while TE provided background on the properties and structure of pentacene-doped naphthalene. JMS and PH provided help with the implementation of the ISE-like linear sweep and advice on growing the pentacene-naphthalene crystals. The setup was characterized by AM, TR, PR, CM, and JS. The original project was planned by PN, together with SM, AM, and PR. AM, TR, PR, CM, JS, MMM, and PN discussed, and analyzed the results. PN, MMM, IS, SM, MBP, FJ, and TC supervised the project. All authors contributed to the manuscript.

Competing interests

The authors declare no competing interests.

Data availability

All data that support the plots within this paper and other findings of this study are available from the corresponding authors upon reasonable request. **Correspondence** and requests for materials should be addressed to Alastair Marshall or Thomas Reisser.

Code availability

All code that support the plots within this paper and other findings of this study are available from the corresponding authors upon reasonable request.

3.2.9 Supplementary Material

3.2.9.1 Amplitude vs. Phase Variation

To separate the respective effects of amplitude and phase modulation these two parameters are investigated independently (Fig. 3.22). We first ran the basic linear sweep and the Optimal (Linear) pulse, where we saw that the optimized pulse leads to higher polarization. To test only the optimized amplitude modulation the optimized phase is reset to the initial guess while the phase modulation was kept (Optimal amplitude + Linear phase). Similarly, to test

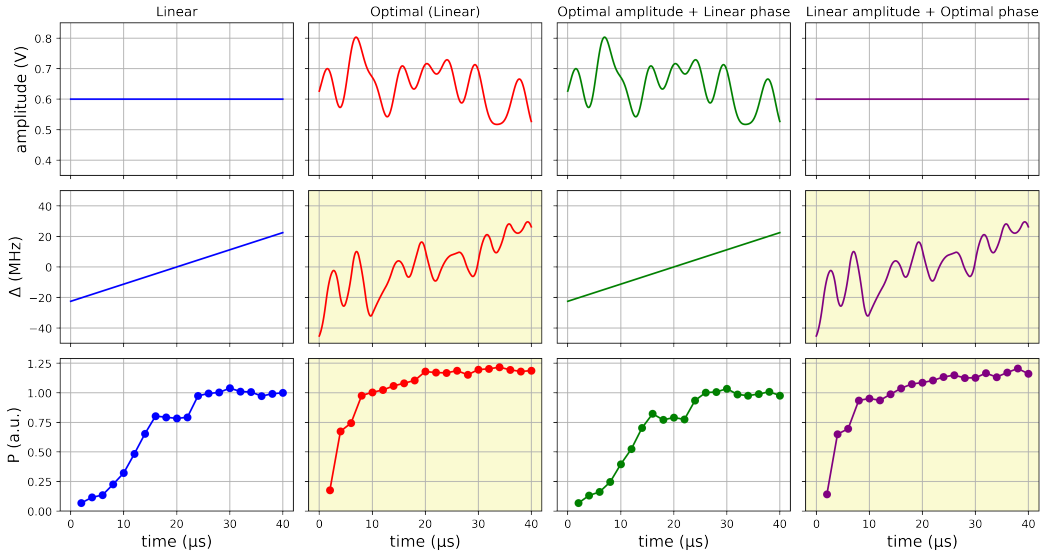

Fig. 3.22 Amplitude vs phase variations: Comparing the linear sweep (Linear) to the corresponding QOC-generated pulse (Optimal (Linear)), as well as combinations of both. In the third and fourth column the amplitude array of one is combined with the phase array of the other (Optimal amplitude + Linear phase and Linear amplitude + Optimal phase). The increase in polarization over the optimization is caused solely by the changes in phase rather than amplitude (compare highlighted plots).

the optimized phase modulation the amplitude is held constant, as in the linear sweep, and the optimized phase is applied (Linear amplitude + Optimal phase).
By comparing those four pulses it becomes clear that the amplitude modulation plays no role in the polarization transfer and only the pulses with optimally controlled phase modulation lead to enhanced polarization (highlighted in Fig. 3.22) . Testing the phase of the optimized pulses with different constant MW amplitudes shows that using a higher MW amplitude always leads to better polarization transfer (see Fig. 3.24).

3.2.9.2 Sine Oscillation Frequency Tests

Following the idea that subsequent sweeps through the resonance in alternating directions further enhance the polarization, we tried to polarize with a sinusoidal pulse. In order to find the optimal pulse, we were varying both, the frequency of the oscillation and the number of resonance passages. For better comparison we here use the lenght of a half oscillation as a parameter instead of the frequency, which means passing through the resonance once, similar to a basic ISE-like linear sweep (Fig. 3.23, upper left). The second parameter, that describes the passages through the resonance is then given by the number of half oscillations (examples given in Fig. 3.23, upper right).

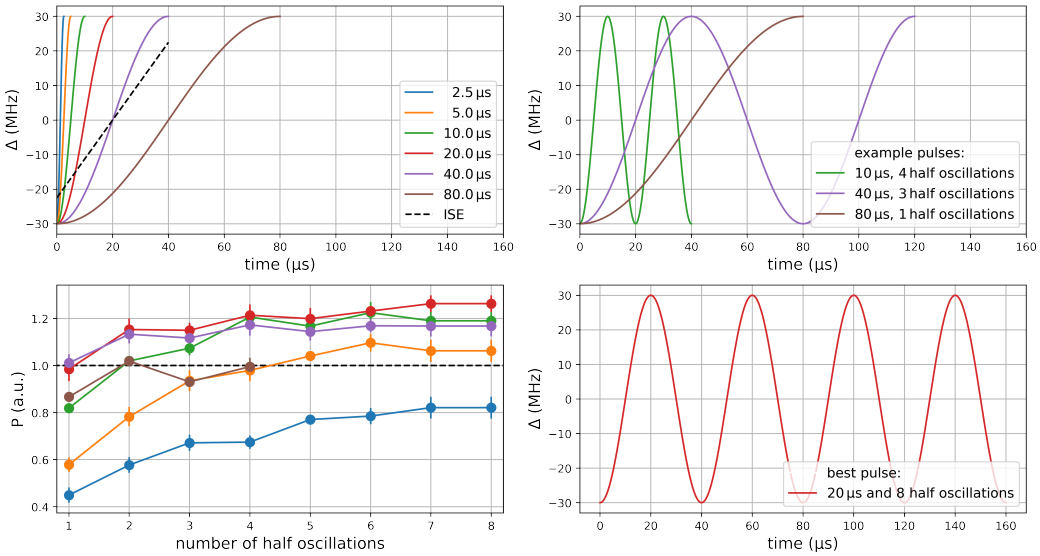

Fig. 3.23 Comparing different sinusoidal pulses. Upper left: Half oscillations width different frequencies comparable to different speeds of the ISE-like linear sequences. Upper right: Example pulses to visualize the idea of the measurement. Lower left: For all six frequencies of the first plot we measure the polarization after up to eight half oscillations and compare it to the polarization after the linear sweep (dashed line). Lower right: Sinusoidal pulse that gave the highest polarization.

In (Fig. 3.23, lower left) we compare the polarization that we got for different parameter sets (length and number of half oscillation) to the standard linear sweep (dashed line). We find that increasing the number of resonance passages leads to an increase in polarization for a lenghts. While most of the applied pulses are beating the standard linear pulse we found maximum polarization for a length of 20 µs and 8 half oscillations (Fig. 3.23, lower right). This pulse was characterized in the main text and used a a new starting point for the sinusoidal based optimal control.

3.2.9.3 Fitted Optimal Pulse

The “Fitted Optimal” pulse shown on the right-hand side in Fig. 3.24 was designed by modelling the shoulder feature of the sin.-based OC pulse resulting from closed-loop optimizations of the sinusoidally varying pulse in the detuning regime. Repeating mirrored polynomial functions emulate the slow-down of the detuning sweep around resonance. A variation of the externally applied voltage kept constant during the pulses displays an improvement of polarization transfer for higher external drive amplitude. Except for the highest driving amplitudes, at the limit of the experimental capabilities, the fitted pulse is equal or outperforms the pulse resulting from the closed-loop iterations. Therefore it serves as a

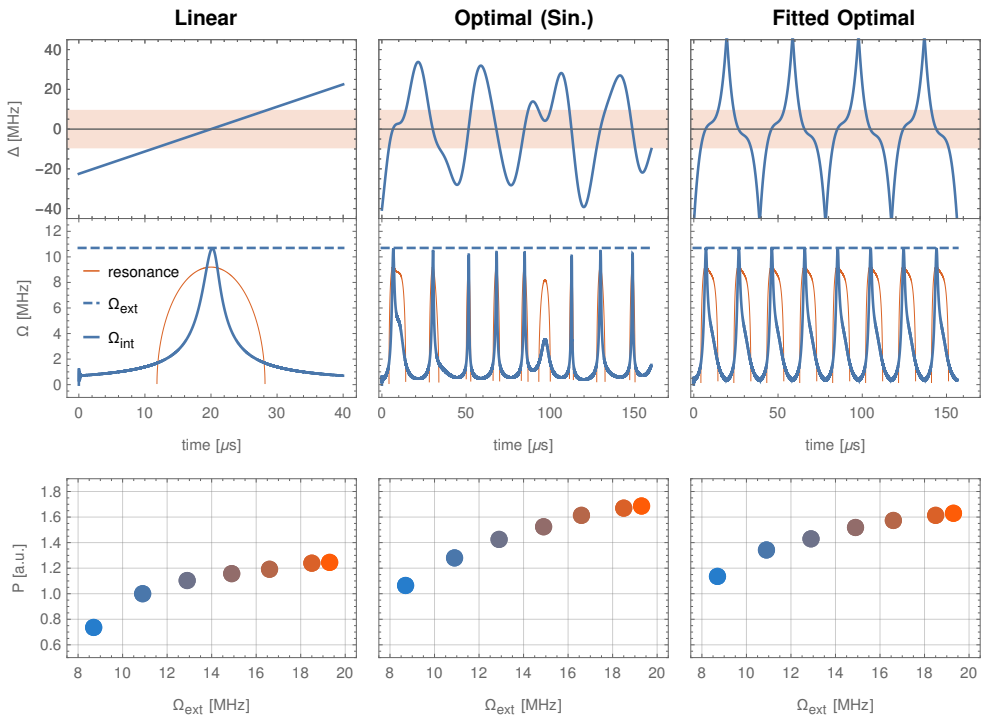

Fig. 3.24 Polarization performance of the linear sweep (Linear), the QOC-pulse generated from a sinusoidal initial guess (Optimal (Sin.)), and its fit (Fitted Optimal) for increasing constant drive amplitudes. Guided by the outcome of the optimal control algorithm the first ~ 20 µs of the optimal (sin.) pulse are re-modelled analytically by tuning polynomial functions to match the detuning's shoulder feature. Even for lower Rabi frequencies the optimized pulses outperform the initial ISE-like linear approach.

good starting point for the use in other, similar setups and further optimisations as well as theoretical and analytical transfer calculations and numerical simulations.

3.2.9.4 Naïve Sweep Corrections

While we applied a linear sweep outside the cavity, the mentioned effects lead to a non-linear sweep inside the cavity. However, the drive would be faster when passing the cavity resonance, compared to the part of the sweep where we are outside of the cavity. Measuring the cavity linewidth and Q-factor allows to calculate the expected deviation from the linear sweep. Calculating an input function with modified amplitude that takes the cavity properties into account would be the first naïve approach to overcome this issue. Trying this did however not improve our polarisation values.

3.2.9.5 Coherence Measurements

We measured the nuclear spin relaxation time T_1 and the electron spin coherence time T_2. For the nuclear spins, we measured T_1 under experimental conditions (e.g. temperature, laser illumination) and got a value of around 223 min (Fig. 3.25 left). For the T_2 coherence time of the electron spin, a standard Hahn-Echo sequence [305] was used and a value of around 9 µs was obtained. (Fig. 3.25 right).

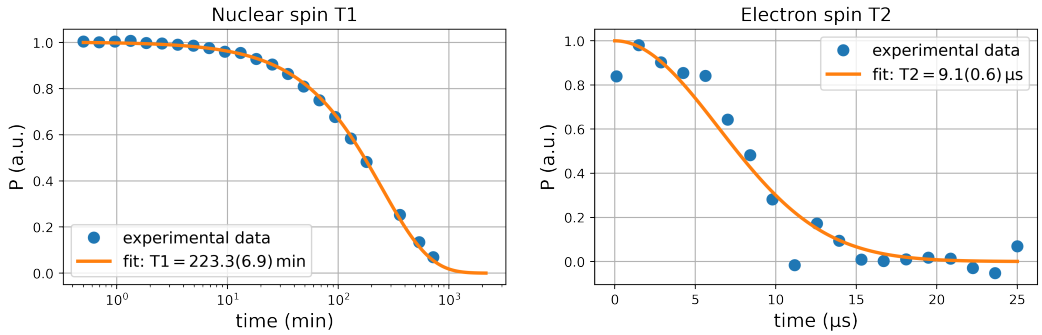

Fig. 3.25 Left: T_1 measurement of the nuclear spins under experimental conditions. Right: T_2 measurement of the electron spin via Hahn-Echo.

3.2.9.6 Polarization Build-up

We can build up polarization p in the crystal iteratively by applying the basic polarization sequence many times (see Fig. 3 in the main text). The final polarization will be given at the equilibrium of two competing effects: each time we apply the basic sequence a fraction $\alpha(1-p)$ of the remaining unpolarized nuclear spins will be polarized, where α is the polarization power of the sequence. At the same time, the polarized nuclear spins decay at a constant rate γ.

$$\frac{dp}{dt} = \alpha(1-p) - \gamma p \tag{3.41}$$

Solving leads to the equation

$$p(t) = p_{\max}\left(1 - e^{-\tilde{\gamma}t}\right), \tag{3.42}$$

where $p_{\max} = \alpha/(\gamma+\alpha)$ and the parameter $\tilde{\gamma} = \gamma + \alpha$ can be obtained from a fit to the data. We obtain $\tilde{\gamma} \approx 0.0061\,\mathrm{min}^{-1}$ and $p_{\max} \approx 14140$ a.u. from the polarization build up obtained by the linear sweep and $\tilde{\gamma} \approx 0.0071$ and $p_{\max} \approx 17850$ a.u. from the polarization build-up obtained from the optimal sequence. An additional measurement T1 measurement gives $1/\gamma \approx 223$ min (Fig. 3.25 left). This translates into estimates for the final polarization of $p_{\max} \approx 27.8 \pm 1.3\,\%$ for the linear sweep and $p_{\max} \approx 35.1 \pm 1.7\,\%$ for the optimal sequence. Note, that the true value of γ is probably slightly larger than in the T_1 measurement due to

the polarization pulse sequences. If we consider, e.g., $1/\gamma \approx 200\,\text{min}$ (or $1/\gamma \approx 180\,\text{min}$), the polarization for the optimal sequence drops to $p_{\max} \approx 26.2 \pm 3.4\,\%$ (or $p_{\max} \approx 16.5 \pm 5.2\,\%$) and similarly for the linear sweep.

3.2.9.7 Effect of the Number of Nuclei on the Model

Each electron spin is surrounded by a large number of protons forming the nuclear spin bath. As only a limited amount can be simulated at a time, sub-groups of nuclei are considered and averaged over. Fortunately, the molecular and crystallographic properties of the naphthalene-h_8 specimen doped with pentacene-d_{14} are well-known. Hence, the orthogonal (A^i_{zx}, A^i_{zy}) and parallel (A^i_{zz}) parts of the hyperfine tensor can be directly calculated [245] for the surrounding protons in the crystal. Instead of including the entire bath as a single effective nuclear spin [287], several nuclei are considered individually in the polarization dynamics. This step is necessary to reflect the effects caused by complex pulse shapes obtained by the optimization as well as the distortion by the cavity. Since the pulses cross the resonance line multiple times and are repeated successively for polarization build-up, strongly coupled nuclei are usually polarized first but can be depolarized again so that excitation is transferred to other nuclear spins. Because the electron spin is re-initialized before each pulse application, each iteration can polarize different nuclei. Up to six nuclei were considered during the initial investigation. However for the figures presented in this manuscript, the following combinations of spins was used to keep computational resources within an acceptable range: The electron spin is coupled to three nuclear spins where the hyperfine coupling values are randomly selected from the top 30 most strongly coupled protons. This simulation is repeated and average for 1000 sets using three different random nuclei in each run. This captures the dynamics of multiple protons coupling to the electron at the same time, as well as the repetition of the transfer operation in the experiment.

3.2.10 Outlook

We have shown that our model can predict the general shape of a pulse's polarisation profile. However, the final polarisation could not be extracted reliably, ruling out open loop optimisations. There are two clear ways to improve the model: First, by characterising the cavity in more detail. This could, for example, be achieved by measuring the system response function [306, 307]. Second, by including more spins in the model through advanced simulation techniques [308]. We have further shown that ARISE provides a way to find good polarisation strategies where common linear sweeps underperform. Preliminary tests indicate that a multi-sweep approach could also improve hyperpolarisation on certain

NV-based setups. A natural next step would be to apply ARISE to other setups to further explore its applicability.
In summary, this work presents the first time closed-loop QOC has been applied to hyperpolarisation. We have improved the overall polarisation by 26%, as well as the polarisation rate by 15%. Additionally, we have introduced the ARISE protocol to translate our methodology into a more general language.

3.3 Spin Squeezing with Atomic Condensates

3.3.1 Regimes of Squeezing

As described in Section 1.2.4, a condensate in a double well resembles a highly sensitive system. It is crucial for the sensing sequence that the condensates on either side start with the same phase. During the sensing period, they are then decoupled to evolve freely under the respective conditions before being recombined. Hence it is important to understand at what trap-generating voltage κ the condensates are decoupled. We can identify three regimes of coupling:

1. **The fully coherent regime:** The phase is perfectly coherent across the transverse direction of the condensate, as the tunnelling dominates over the interaction. Hence, the condensates are fully coupled.

2. **The fully incoherent regime:** The two wells are perfectly decoupled, as the interaction energy dominates over the tunnelling. The number variance is negligible.

3. **The intermediate regime:** In between is where the relationship between the number and phase distributions are sensitive, i.e. easily manipulable, and hence where the squeezing happens.

We estimate the regime through the squeezing of the ground state as shown in Fig. 3.26 for $N = 100$. In the fully coherent regime, we cannot identify any fringes as the two condensates are still connected. The fully incoherent regime, where the wells are decoupled, is marked by strong number squeezing. Additionally, the decoupling can be estimated directly by measuring the decoherence time of the phase. To do so, the barrier is ramped from a single well up to a certain κ. In the fully coherent regime, the phase variance quickly diverges, while the condensates stay coherent for an extended time in the intermediate regime.
Simulations have shown that for a higher atom number ($N = 500$) the regimes are distributed

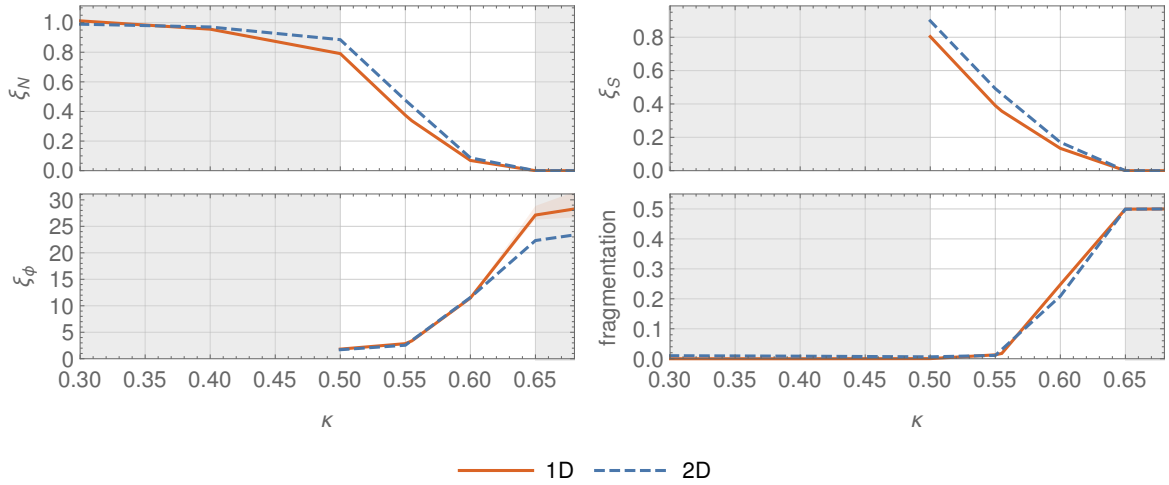

Fig. 3.26 The transitions between the regimes are shown with respect to ξ_N, ξ_φ, ξ_S, and the fragmentation for $N = 100$ and $M = 2$ in one and two dimensions. When $\kappa < 0.5$ the two wells are not separated enough to create an interference pattern, hence ξ_φ is cut off. Here, we can assume that $\xi_\varphi \approx 0$ and the condensate is in the fully coherent regime. Beyond $\kappa = 0.65$ the phase is widely distributed while the number imbalance distribution is point-like. Hence, we can identify the fully incoherent regime.

differently for one and two dimensions.[7] As the barrier is generally lower with respect to the atom number, the point of decoupling moves towards higher κ for increased N. However, in two dimensions the transitions are not as clear and the condensate does not reach complete fragmentation. Similarly, the deviations are larger for the fully coherent regime. These differences reflect that the longitudinal direction and hence two-dimensional calculations uncover details that are not accessible in one dimension.

3.3.2 Josephson Oscillations

In the experiment, the coupling between the wells is measured through the Josephson frequency ω_J, which is the frequency of oscillation between the wells in the presence of an imbalance.[8] This property can be well approximated with the GPE [311, 312], hence we only use one orbital to calculate it. The Josephson frequency represents a good point of comparison between the experiment and the simulation.

We can measure ω_J in a number of ways [310]. Here, we choose to relax the condensate into a tilted double well, before releasing it into an even well. The Josephson frequency is extracted from the evolution of the condensate's centre of mass shown in the first row of Fig. 3.27. To

[7] These calculations were done with both two and three orbitals delivering almost identical results.

[8] If the imbalance is too strong, the condensate experiences self-trapping and the oscillations are at a different frequency [309] but we keep the imbalance sufficiently small.

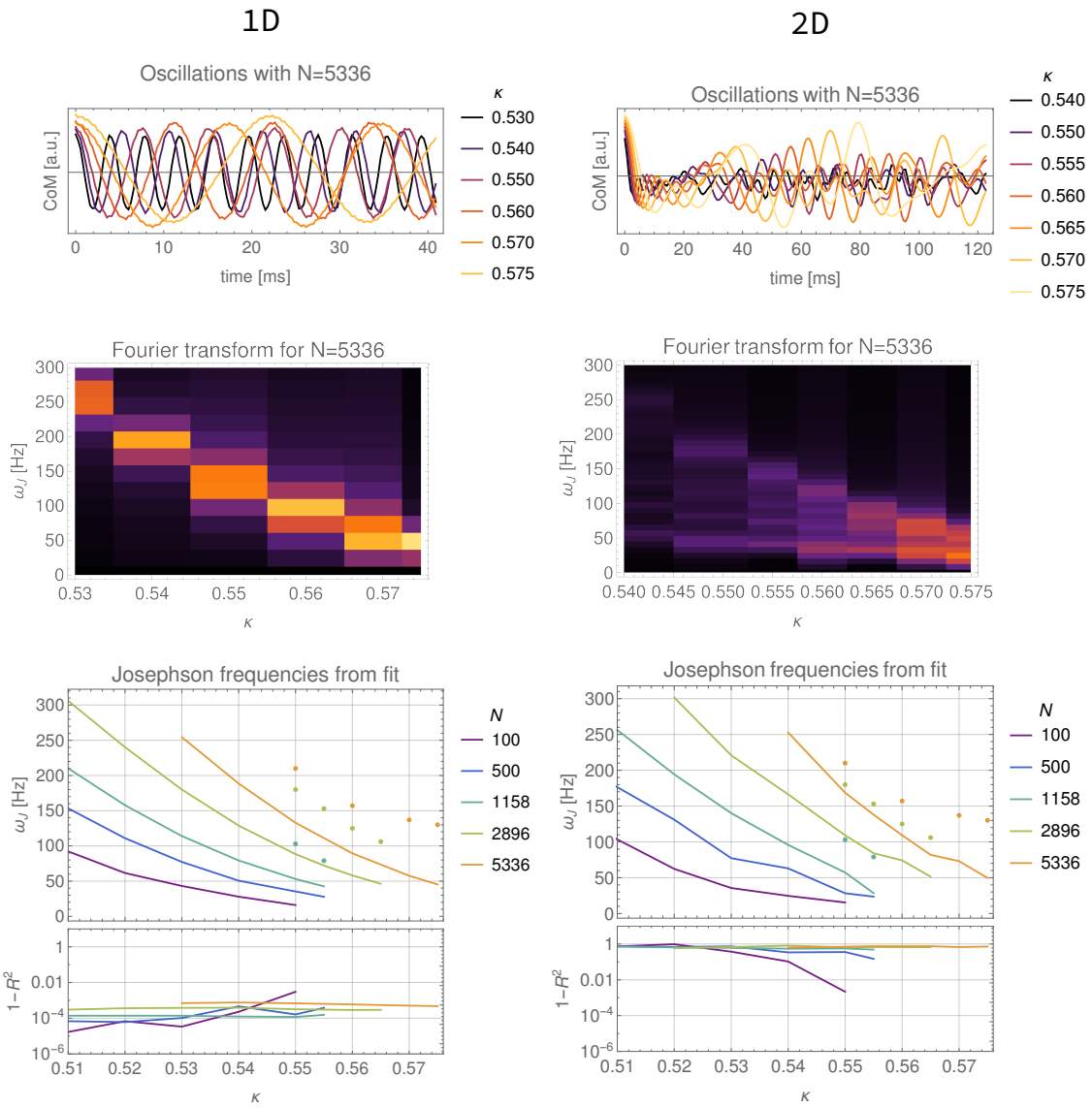

Fig. 3.27 Josephson oscillation in one and two dimensions simulated with $M = 1$. (*first row*) Exemplary Josephson oscillations for different κ and $N = 5336$. CoM stands for Centre of Mass, which oscillates about the centre of the well at zero which is indicated by a grey line.[a] (*second row*) Fourier transform of the CoM oscillations for $N = 5336$. (*third row*) Fitted Josephson frequency as a function of κ for different atom numbers. The dots represent experimental data[b], while the lines are produced by simulation. The frequency is determined by fitting the function $e_1 + e_2 \cos(2\pi\omega_J t + e_3)$ to the CoM oscillations using the position of the highest frequency peak of the Fourier transform as an initial guess for ω_J. The quality of the fit is depicted in the bottom panels such that a perfect fit would give $1 - R^2 = 0$.

[a] We have made sure that the initial imbalance does not put the condensate in the self-trapping regime [309, 310].

[b] The data was provided by TianTian Zhang.

extract ω_J we fit the function $e_1 + e_2 \cos(2\pi\omega_J t + e_3)$ to the oscillations with the initial guess $(e_1, e_2, \omega_J, e_3) = (0, n_{\max}, \omega_0, 0)$, where $n_{\max}$ represents the initial imbalance. The frequency guess ω_0 is obtained from the Fourier transform of the centre of mass motion. In one dimension, this produces very clear results, indicated by the excellent fit ($1 - R^2 \ll 1$). In two dimensions, however, it does not. As one can see in the second row of Fig. 3.27, the Fourier transform of the 2D data consists of multiple bands. We relate this behaviour to two factors: First, due to the harmonic potential along z, the number density and hence the tunnel coupling differs between the centre and the edges of the condensate, i.e. $\omega_J^{\text{centre}} > \omega_J^{\text{edge}}$ [313]. Second, the condensate is instantaneously released from the tilted well which may result in different (longitudinal) energy modes contributing to the oscillations [309]. Future calculations should include a ramp down of the tilt, to differentiate between those effects. Based on the computation in 1D and keeping these circumstances in mind, we use the higher energy peaks of the spectrum for the fit. The resulting frequencies and an estimate of the quality of the fits are shown in the last row of Fig. 3.27. The comparison to experimental data shows a noticeable offset in both cases.

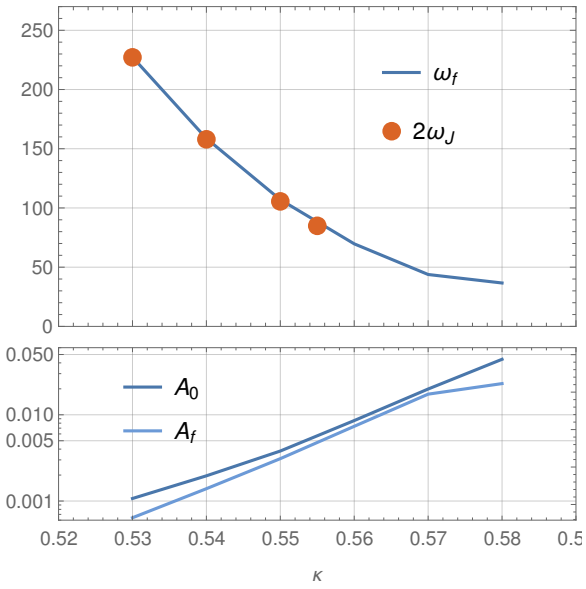

Fig. 3.28 Frequency and amplitude of the fragmentation oscillations after a 10 ms ramp to a range of κ with $N = 1158$ and $M = 2$ in 1D. The oscillations were fitted with a function $A_0 + A_f \cos\left(2\pi\omega_f t + \phi_f\right)$.

In order to match the theoretical values of ω_J at a given κ with the experiment, one could adjust the atom interaction λ. The matching is crucial as the coupling between the wells has a strong effect on the dynamics of the fragmentation. We illustrate this connection by ramping the potential up from $\kappa = 0.3$ over 10 ms. The fragmentation starts to oscillate

with a frequency $\omega_f \approx 2\omega_J$. The κ-dependent frequencies are shown in Fig. 3.28. In Section 1.2.3 we explained how squeezing can only be represented with multiple orbitals and hence requires fragmentation. Indeed, the squeezing oscillates along with the fragmentation. This phenomenon has been observed before [312] and can be explained by imagining the distribution of a squeezed state on the Bloch sphere. Josephson oscillations rotate the distribution about the x-axis. For a displaced state, it takes a full oscillation to return to its original position. For a squeezed state centred on the x-axis, however, it only takes half a rotation. These observations reinforce the statement that it is vital to match ω_J as closely as possible to accurately represent the squeezing in the experiment.

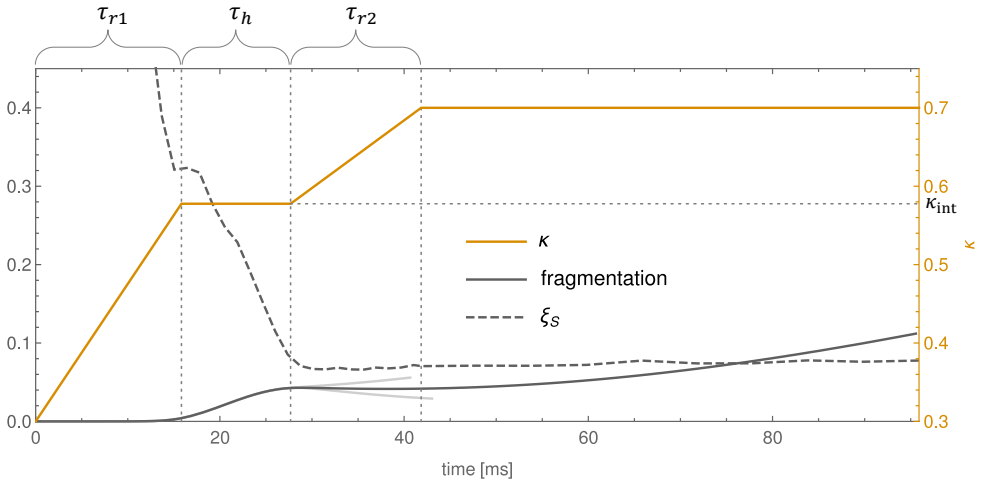

Fig. 3.29 The best double ramp from a direct search, where $N = 1500$ and $(\tau_{r1}, \tau_h, \tau_{r2}, \kappa_{\text{int}}) = (15.8255\,\text{ms}, 11.8519\,\text{ms}, 14.1745\,\text{ms}, 0.5776)$. The light grey lines indicate the fragmentation for modified τ_h.

3.3.3 1D Optimisation

Previous results from Marine Pigneur indicate improved squeezing after splitting the condensate via an easily implementable double ramp [312]. However, it was not clear, whether the squeezing could be maintained afterwards. In the double-ramp protocol, κ is linearly raised starting from 0.3, then held constant in the intermediate regime, and finally raised until the split condensate is decoupled at $\kappa = 0.7$. We define the protocol in Fig. 3.29 such that the duration of the first ramp is denoted as τ_{r1} going up to κ_{int}, and the duration of the second ramp is given by τ_{r2} going up to $\kappa = 0.7$. The duration of the holding time is given by τ_h. To apply experimentally realistic limits in the optimisation we re-parameterise the problem

giving

$$\begin{aligned} 2\,\text{ms} < \nu_1 &= \tau_{r1} + \tau_{r2} < 30\,\text{ms}, \\ 0 \leq \nu_2 &= \nu_1/\tau_{r1} \leq 1, \\ 0\,\text{ms} < \nu_3 &= \tau_h < 50\,\text{ms}, \\ 0 \leq \nu_4 &= (0.7 - 0.3)/\kappa_{\text{int}} \leq 1. \end{aligned} \tag{3.43}$$

The best ramp found during a direct search is shown together with the evolution of the squeezing and the fragmentation in Fig. 3.29. It results in a useful squeezing factor of $\xi_S \approx 0.067$ which is an improvement by a factor of four compared to a linear ramp taking the same time ($\xi_S \approx 0.280$). Moreover, holding the potential steady at $\kappa = 0.7$ for >50 ms shows that the squeezing is maintained in the split potential.

We assess the robustness of the ramp with respect to different parameters. Changes in the ramp times, τ_{r1} and τ_{r2}, have a small effect on the squeezing. Generally, the useful squeezing stays below 0.1 for ramp times $\tau_{r1/r2}$ between 8 ms and 40 ms. We observe, however, that τ_h and κ_{int} are closely coupled to each other. In Fig. 3.29 the evolution of fragmentation with a modified τ_h is indicated by grey lines forking off from the optimised fragmentation. The rising and falling fragmentation belongs to ramps with $0.9\tau_h$ and $1.1\tau_h$ respectively. As the fragmentation directly affects squeezing, this effect is mirrored in the squeezing and explored in more detail in Fig. 3.30.

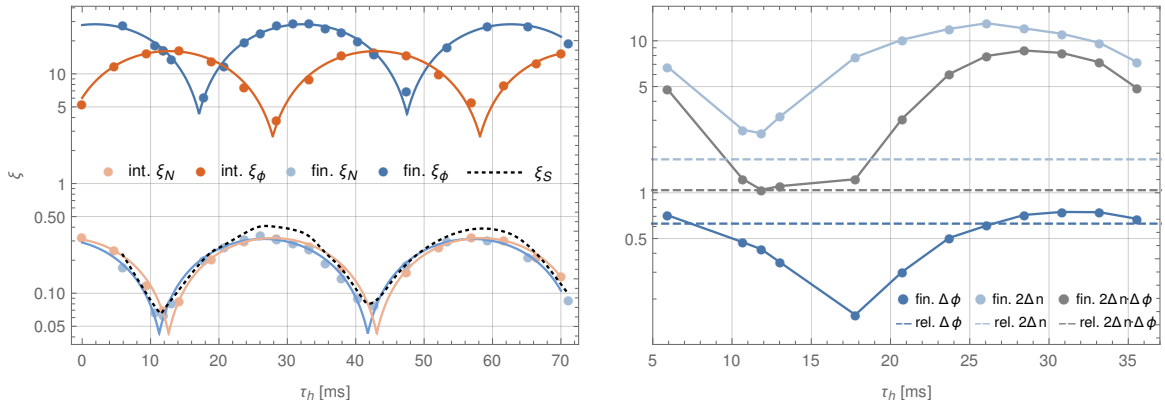

Fig. 3.30 Dependence of the squeezing on the holding time. All calculations were done with $N = 1500$ and $M = 2$. (*left*) Intermediate (orange) and final (blue) number squeezing as light dots and phase squeezing as dark dots. The final useful squeezing is indicated by a black dashed line. The intermediate squeezing is measured after $\tau_{r1} + \tau_h$ at κ_{int}, while the final squeezing is calculated after the second ramp at $\kappa = 0.7$, when the wells are fully decoupled. (*right*) The standard deviation of the relative phase and full number imbalance at the end of the ramp (fin.) and for a ground state condensate (rel.).

Figure 3.30 shows the squeezing of the imbalance and relative phase at the end of the intermediate hold time and at the end of the second ramp (final), as well as the standard deviations for the final and ground state (relaxed). The left plot shows that, while the number squeezing is almost the same at the intermediate and final time, the phase squeezing changes during the second ramp. It is raised or lowered depending on τ_h. The oscillatory behaviour of the squeezing factors is modelled by $|\cos\left(2\pi\omega_f t\right)|$. The frequency of the fragmentation oscillations is given by $\frac{\omega_f}{2} = 16.6\,\mathrm{kHz} \approx \omega_J$. The fact that the evolution of the squeezing is directly dependent on ω_J shows once again, how important the role is that the tunnel coupling plays.
The right plot of Fig. 3.30 shows the comparison between the final and relaxed values of $2\Delta n$ and $\Delta\varphi$. For the optimised holding time at 11.6 ms the squeezing hits the limit given by the Heisenberg uncertainty relation in Eq. (1.73). For longer holding times (up to ca. 18 ms) it stays close to the limit but is less squeezed. This behaviour can be explained by the shift of the final with respect to the intermediate phase squeezing displayed on the left.
In general, we see that the squeezing dynamics are highly dependent on the fragmentation and tunnel coupling. While ramp speeds have a very small influence on the squeezing dynamics, the holding time τ_h and potential κ_{int} are crucial for multi-ramp protocols. By extending these observations, it might be possible to create a simpler model to use for open-loop optimisations, especially for the 2D case, or derive good initial guess pulses for a future closed-loop optimisation.

3.3.4 Shifted Well

The longitudinal profiles of the left and right condensate are not perfectly aligned in the experiment. To reflect this fact in the model, we introduced the shift χ in Eq. (1.82). Figure 3.31a shows the transverse view of the shifted condensate which is unchanged with respect to a non-shifted one. The effect is only visible in the longitudinal view shown in Fig. 3.31b, where the centres of the left and right condensates are 6 µm apart. Please note, that the condensates are comparatively short, as they only contain 100 atoms in total. For higher atom numbers the same shift is less noticeable. A condensate with 1000 atoms, for example, is approximately twice as long. Imagining transverse slices of the potential makes it simpler to understand the consequences of the shift in momentum space. The centre slice resembles a straight double well, while the edge-slices correspond to a well tilted in either direction. As a result, the ground state's relative phase changes along the condensate as shown in Fig. 3.31c. As the relative phase is obtained by integrating the single shots of the condensate longitudinally, the contrast of each single shot is reduced. The effect on the full distribution is shown in Fig. 3.31d, where the left plot represents the ground state of a non-

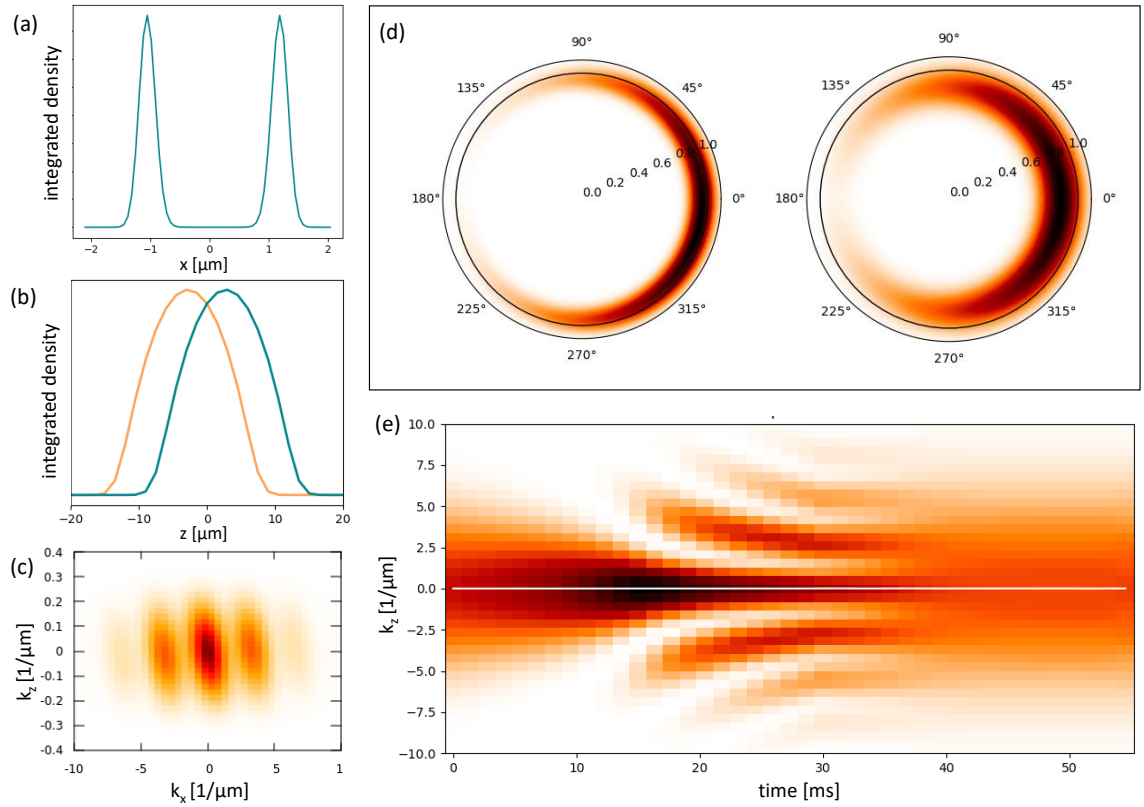

Fig. 3.31 The effect of shifted wells with $\chi = 2.5$ and $N = 100$. To understand the consequences of the shift, we first show the integrated density over the transverse (a) and longitudinal (b) direction of the condensate with $\kappa = 0.68$. (c) The momentum space density of the shifted ground state. (d) Comparison between the phase distribution of a non-shifted (*left*) and a shifted (*right*) condensate. The distribution was simulated with $\kappa = 0.60$ and $M = 2$. (e) Evolution of the integrated momentum space density of a condensate in a shifted potential. The barrier was ramped up from 0.3 to 0.68 over 50 ms and then held constant. We calculated the evolution with a single orbital.

shifted well and the right plot that of a shifted well. The evolution in a shifted potential as shown in Fig. 3.31e starts like it would in an non-shifted well as the shift has no measurable effect on the initial single well. However, it becomes stronger as the two wells move further apart, leading to higher local phase changes resulting in lower contrast. We simulated the evolution with one orbital to show that this loss of contrast is completely independent of fragmentation and squeezing. It should be noted that the contrast sees a revival at a later time.

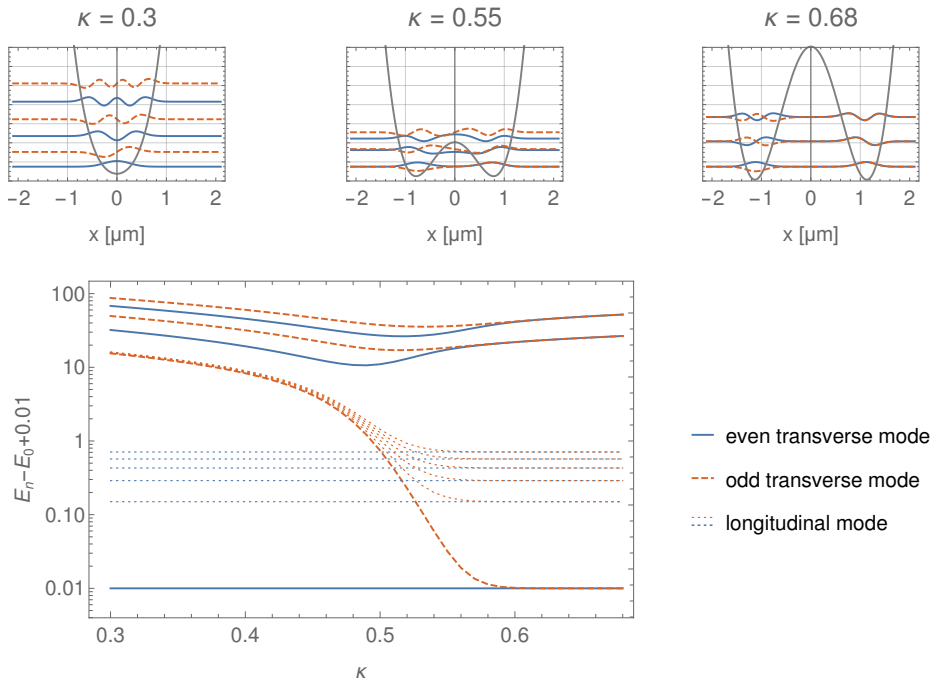

Fig. 3.32 Eigenmodes in two dimensions. The top row shows the transverse potential and the first six eigenmodes of a single atom according to the Schrödinger equation with an offset corresponding to their eigenenergies. Please note that the amplitude of the modes is slightly exaggerated to provide a clearer picture. The thick lines in the main plot give the eigenenergies of the first six transverse modes. The dotted lines represent the corresponding longitudinal modes. For the sake of clarity only the first six longitudinal modes are plotted per transverse mode.

3.3.5 1D vs 2D

Two-dimensional simulations provide more degrees of freedom. Figure 3.32 shows the transverse and longitudinal eigenstates, which we call modes, going from a single to a double well. The lowest energy levels in the 2D single well are given by the combination of the transverse ground state and longitudinal modes. Raising the barrier leads to the transverse first excited state to become degenerate with the transverse ground state. During this transition, the longitudinal and transverse modes cross. As a result, the 2D double well behaves similarly to the 1D double well, but the transition looks very different. In two dimensions the first orbitals of low-κ states are all transversely symmetric (even), due to the small energy gaps between the longitudinal eigenmodes. Squeezing cannot be captured without transverse anti-symmetry (odd modes). Hence, we need to take into account many more orbitals.

Previous work by Bhowmik et al. [71] has shown that for a condensate with $N = 10$ atoms, six

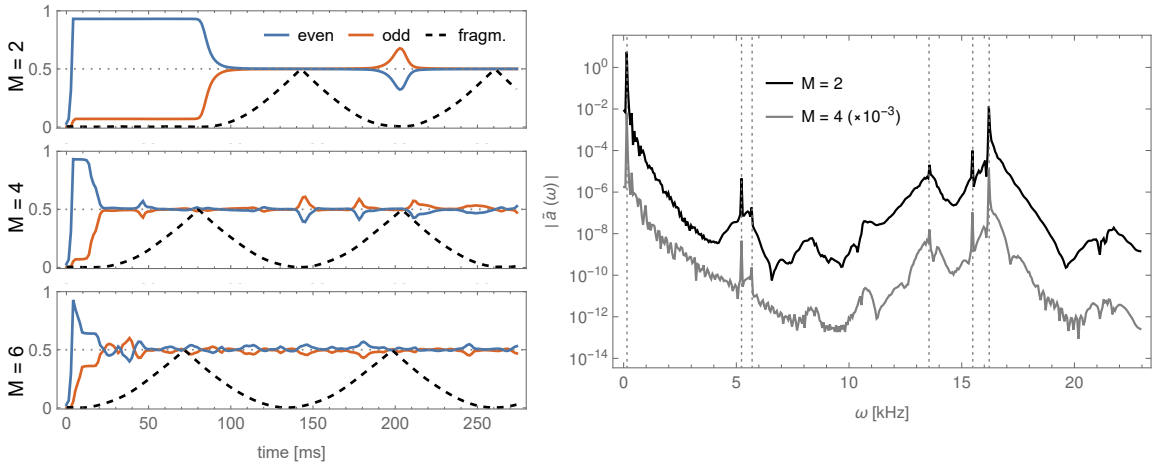

Fig. 3.33 Contributions of different modes during and after a 5 ms ramp from $\kappa = 0.3$ to $\kappa = 0.6$ with $N = 2$. (*left*) Normalised composition of the natural orbitals from the first 200 modes of the $\kappa = 0.6$ potential. As the single well's modes are complex to represent in the double well basis, the graph does not capture the composition at $t = 0$. (*right*) Spectra after the ramp with different orbital numbers calculated from the autocorrelation function according to reference [314]. The data in this figure was kindly provided by Camille Lévêque.

to ten orbitals are required to accurately capture the dynamics. The specific number depends on the initial state. Considering that they kept the potential constant and their atom number is drastically smaller, it is difficult to compare to our model. On the one hand, higher atom numbers usually lead to better agreement with the GPE (i.e. fewer orbitals are required). On the other hand, the dynamics are very different as the type of evolution as shown in Fig. 3.31e is influenced by more factors than the ones provided by Bhowmik et al. Moreover, one might argue that, in order to capture the squeezing behaviour, we do not have to represent the full two-dimensional dynamics but only the fragmentation into transversely odd and even basis states.

We have analysed the composition of the orbitals of two atoms after a simple ramp of duration $\tau_r = 5$ ms to understand the connection between orbital symmetry and fragmentation. To do so, the natural orbitals[9] are projected onto the first 200 modes of the final potential ($\kappa = 0.6$) at each time step. The left side of Fig. 3.33 shows that the orbitals are almost exclusively composed of even modes for the first 70 ms with $M = 2$. Once this changes, the condensate starts to fragment. For $M > 2$, the fragmentation happens earlier indicating convergence at a higher orbital number. While this type of analysis is very time consuming for more atoms, we have observed a similar behaviour of the fragmentation for $N = 20, 50, 100$. Here, the fragmentation also rises from 0 to 0.5 with occasional revivals. Moreover, these features are

[9]The natural orbitals are the diagonalised form of the orbitals, i.e. they are the eigenvectors of the density matrix.

also shifted to earlier times with increased M and the rise in fragmentation occurs after one of the orbitals acquires a strong transversely anti-symmetric component.
Another type of analysis reveals the spectrum of the condensate after the ramp. It is obtained by Fourier transforming the autocorrelation function $a(t) = \langle\psi(\tau_r)|\psi(t-\tau_r)\rangle$ [314]. The right part of Fig. 3.33 shows the spectra of two atoms simulated with two and four orbitals. The modes are indicated by the peaks marked with dotted lines. Both simulations produce the same occupation of modes which is given by the amplitudes of the peaks. The same holds for calculations with three and five orbitals not shown in this plot. The leftmost peak is actually a double peak of the almost degenerate transverse ground states. Most of the population resides in those two states. The rightmost and second highest peak belongs to the transverse first excited state, while the peaks in between are highly excited longitudinal modes. It should be noted, that their occupation is very low. The fact that the spectra are so similar shows that the addition of orbitals does not lead to a higher number of modes being simulated. This opens up the question of whether the dimensionality of the problem truly exceeds the representation with few orbitals or whether the basis of the representation simply does not fit. Other indicators supporting the latter hypothesis is that the longitudinal modes are barely populated and that one-dimensional simulations with two orbitals result in similar dynamics to two-dimensional simulations with many orbitals.
A potential way to simplify the two-dimensional method while representing the squeezing dynamics is to impose an anti-symmetry condition on the transverse part of the second orbital.[10] As the single well ground state exhibits next to no fragmentation this condition is expected to have no effect on it, especially for high atom numbers. It would, however, provide a basis for representing squeezing in high-κ potentials with few orbitals and in two dimensions.

3.3.6 Conclusion

We have examined the behaviour of a condensate in a potential derived from experimental conditions to study squeezing. During our investigation, we explored the boundaries of our main method of simulation, MCTDHB. We calculated the squeezing from single shots (see Section 1.2.7.1) which allowed us insight, not only into the number but also into the phase squeezing. We have shown that improvements are achievable with a simple optimisation using a one-dimensional model. Next, we presented the connection between tunnel coupling and squeezing dynamics. The strong effect of small changes indicates that matching model and experiment is very important for a meaningful representation. Several matching indicators

[10] The symmetry of the orbitals is preserved, if the occupation of odd orbitals is always kept even [315, 70].

were identified such as the Josephson frequency ω_J and the shift χ. Finally, we showed the limits of few-orbital calculations in two dimensions and discussed a possible route for further theoretical investigation.

3.4 Schrödinger Cat States with Rydberg Atoms

Rydberg atoms are an incredibly versatile platform [316]. They are formed when an atom is excited such that the inner electrons shield the outermost electron from the nucleus' electric field resulting in a structure similar to a hydrogen atom [317]. As a consequence of this specific excitation, Rydberg atoms have some unique properties such as a strong response to electromagnetic fields and long decay times. These properties allow us to manipulate them and their interaction, hence they find applications in many fields such as quantum sensing [318], quantum computing [319], and quantum simulation [320]. To fully exploit their quantum nature it once again comes down to state engineering. In this section, we will present the goal of an optimisation which resulted in the following publication and involved the author of this thesis: A. Omran, H. Levine, A. Keesling, G. Semeghini, T. T. Wang, S. Ebadi, H. Bernien, A. S. Zibrov, H. Pichler, S. Choi, J. Cui, M. Rossignolo, P. Rembold, S. Montangero, T. Calarco, M. Endres, M. Greiner, V. Vuletić, M. D. Lukin, *Generation and manipulation of Schrödinger cat states in Rydberg atom arrays*, Science, 365 (6453), 570–574 (2019) [1]. She was part of providing and maintaining the optimal control software that enabled the necessary enhancements to build a 20 qubit Schrödinger cat state. At the time of publication, this was the largest such cat state ever created.

3.4.1 Greenberger-Horne-Zeilinger states

The Greenberger-Horne-Zeilinger (GHZ) state is a genuinely entangled multipartite Schrödinger-cat state, where each subsystem is in a superposition of orthogonal states [321]. It is created from two states $|A_N\rangle$ and $|\bar{A}_N\rangle$. One example for an N-dimensional GHZ state is the following:

$$|\mathrm{GHZ}_N\rangle = \frac{1}{\sqrt{2}}(|0101\cdots\rangle + |1010\cdots\rangle). \tag{3.44}$$

In this case $|A_N\rangle$ and $|\bar{A}_N\rangle$ correspond to $|0101\cdots\rangle$ and $|1010\cdots\rangle$, respectively. Without requiring full information about the system, GHZ states can be characterised through only two diagonal terms ($p_{|A_N\rangle}$, $p_{|\bar{A}_N\rangle}$) and two off-diagonal terms (c_N, c_N^*) of the density matrix ρ. The diagonal terms represent the probability to be in a certain state $|\phi\rangle$ and are given by $p_{|\phi\rangle} = \langle\phi|\rho|\phi\rangle$, while the off-diagonal terms distinguish the cat-state from a statistical mixture

and are given by $c_N = \langle A_N|\rho|\bar{A}_N\rangle$. Together, they form the GHZ-fidelity $\mathcal{F}_{\text{GHZ}}$:

$$\mathcal{F}_{\text{GHZ}} = \langle \text{GHZ}_N|\rho|\text{GHZ}_N\rangle = \frac{1}{2}\left(p_{|A_N\rangle} + p_{|\bar{A}_N\rangle} + c_N + c_N^*\right). \tag{3.45}$$

Quantifying entanglement is generally a complicated task. However, for these states, the GHZ-fidelity is enough to determine whether a system is in a genuine N-particle entangled state: It has been shown that, as long as $\mathcal{F}_{\text{GHZ}} > 0.5$, the state can be transformed into a perfect cat-state [322]. This type of transformation is called entanglement purification and only consists of local operations and classical communication, which means that operations are only performed on parts of the system (locally) and then communicated classically to possibly trigger other local operations [323].
GHZ states do not provide any squeezing and yet they can improve sensitivity through their quantum properties [105, 72]. While N repeated measurements of a single system (or N uncorrelated systems) enhance the measurement by N times, the signal will be subject to shot noise N times more often. Shot noise refers to the variance in the signal that stems from the quantised nature of the photons counted during the measurement. However, with a GHZ state of N atoms, the signal is enhanced by a factor of N but only read out on a single atom. The resulting sensitivity is called the Heisenberg limit. Here, the shot noise stays the same, while the sensitivity is increased. It is clear that GHZ states consequently form an important part of quantum sensing [72], but they also find applications in quantum computing [324], as they are scalable and entanglement is key to many protocols.

3.4.2 Hamiltonian Design

The system is composed of a one-dimensional array of N atoms (^{87}Rb) which are trapped via optical tweezers. They are expected to behave like qubits, defined by the ground state $|0\rangle$ and the excited Ryberg state $|1\rangle$. When the tweezers are switched off the system corresponds to the Hamiltonian H_{ryd}, illustrated in Fig. 3.34A and defined as:

$$H_{\text{ryd}}/\hbar = \frac{\Omega(t)}{2}\sum_{i=1}^{N}\hat{\sigma}_x^i - \sum_{i=1}^{N}(\Delta(t) + \delta_i)\hat{n}_i + \sum_{i<j}\frac{V}{|i-j|^6}\hat{n}_i\hat{n}_j. \tag{3.46}$$

The Rydberg laser enables the transition between the ground and Rydberg state via two-photon coupling. The strength of this coupling is given by the Rabi frequency $\Omega(t)$. The lasers' detuning $\Delta(t)$ determines how many Rydberg states are in the multi-particle ground state. For large negative values, the amount is zero, while large positive values maximise it. δ_i represents the static detuning for a specific site i. It is introduced to represent the edge lasers

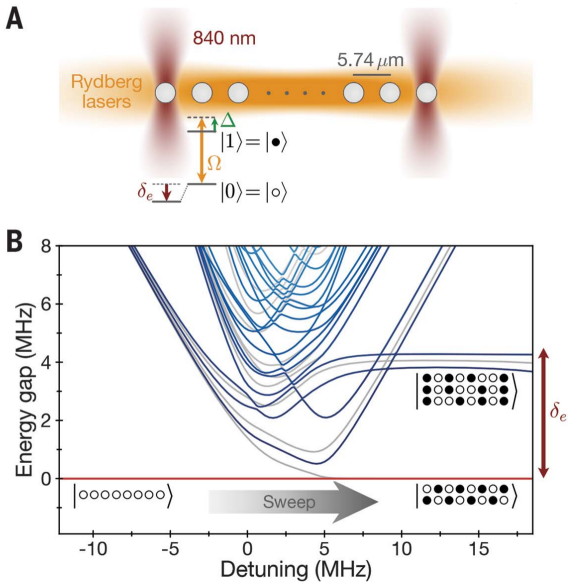

Fig. 3.34 Representation of the Rydberg atom array. (A) Schematic of the line of Rydberg atoms. Rydberg lasers are applied with an amplitude proportional to $\Omega(t)$, and detuning $\Delta(t)$, as well as edge lasers with detuning δ_e. The inset level diagram represents the states of a single atom. (B) Energy level diagram for $N = 8$ atoms depending on the detuning $\Delta(t)$. This figure was originally published as part of Fig. 1 in reference [1].

which result in an effective detuning for the outermost atoms. As shown in Fig. 3.34B, they ensure that the multi-particle ground states for an even number of atoms are well-separated from the states with two edge-excitations (faux ground states). The Rydberg blockade V corresponds to the strong distance-dependent van der Waals coupling between neighbouring atoms. As a result, there are no two adjacent atoms in the Rydberg state in the multi-particle ground state. $\hat{n}_i$ is the operator representing the number of Rydberg excitations on site i. Ultimately, H_{ryd} is designed to create a GHZ-state as in Eq. (3.44).
Fig. 3.34B shows an adiabatic route to obtaining the GHZ state. First, the detuning is strongly negative and all atoms are prepared in the ground state, then the detuning is swept until it is strongly positive. However, to stay adiabatic, the sweep needs to be slow enough not to trigger excitations. Unfortunately, this is not possible while staying inside the decoherence time of the system. To circumvent this speed restriction we applied QOC.

3.4.3 Optimisation

The optimisation is performed via open-loop on a model which exactly solves the Schrödinger equation. The GHZ-fidelity is used as the FoM, while the dynamical control pulses are represented by the detuning $\Delta(t)$ and amplitude $\Omega(t)$. Previously, the potential of this optimisation

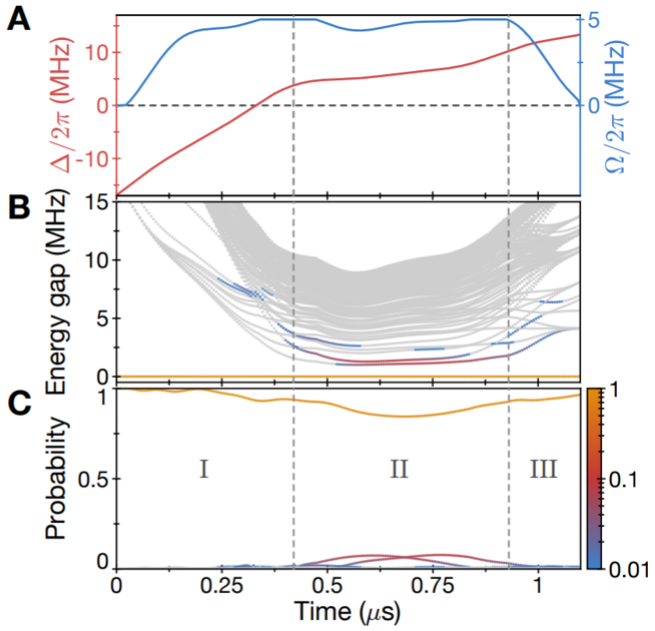

Fig. 3.35 Optimised ramp for a 20 atom GHZ state. (A) The optimised pulses for the amplitude Ω and the detuning Δ of the Rydberg lasers. It is clear, that the slope of the detuning correlates with the gap between the multi-particle ground and first excited state. However, the panels below show, that this is not an adiabatic control. (B) The energy of the lowest 100 energy levels relative to the ground state over the course of the pulse. (C) The population of the energy levels. The population during the steep ramp-up of the detuning (I) is mostly in the ground state. During the slow ramp in the middle (II), the population gets transferred to two of the excited states, before being transferred back before and during the last stage (III). The fact that the population does not remain in the ground state over the entire pulse, illustrates the diabaticity of the control sequence. This figure is reprinted from Fig. S4 of reference [1].

were explored with a tensor-network simulation [325]. The amplitude limitations are implemented using a cut-off restriction. To ensure that the amplitude is zero at the initial and final time, a shape function is used. The result of the optimisation can be seen in Fig. 3.35. The optimised pulse clearly slows down at the centre, where the spectrum around the ground state gets crowded. Still, some population is transferred to excited states confirming the diabaticity of the protocol. The population is subsequently transferred back. To understand the gain through the optimal control protocol, it is compared with an optimised adiabatic sequence in Fig. 3.36. The optimised adiabatic protocol is constructed to minimise the probability of exciting a diabatic transition. The sweep speed of the detuning and the amplitude are adjusted accordingly. The result shows some improvement with respect to the linear ramp but cannot compete with the optimal control pulse. Intrinsically, it is slower which would

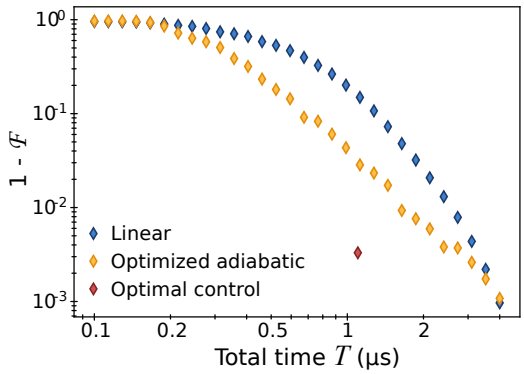

Fig. 3.36 The GHZ-infidelity is shown as a function of the pulse length T for $N = 12$. A linear sweep of the detuning (blue) requires the longest time to produce sufficiently low infidelity. The optimised adiabatic scheme (yellow) produces better results for shorter times. In red, one can see the results from a QOC, i.e. diabatic, pulse with a total sweep time of T =1.1 µs. This simulation shows that the optimised control pulses outperform both, the linear and the optimised adiabatic control sequences. This figure is reprinted from Fig. S3 of reference [1].

cause the system in the experiment to decohere before the sequence is fully executed.

The first step to calculate the GHZ-fidelity from the experiment is measuring the state fidelities, $p_{|A_N\rangle}$, $p_{|\bar{A}_N\rangle}$. To do so, the trapping laser is switched on after the protocol. It recaptured the atoms in the ground state, which can then be detected, and repels the atoms in the Rydberg state. The off-diagonal terms are determined by applying a local light shift to every second atom. This causes the GHZ states to develop a phase between $|A_N\rangle$ and $\left|\bar{A}_N\right\rangle$. The lights are applied for different durations resulting in oscillations that can be transformed into a measurable observable (the parity). The oscillation contrast is then used to infer the lower limit of the off-diagonal elements, c_N and c_N^*. Finally, the GHZ-fidelity is found to be $\mathcal{F}_{\mathrm{GHZ}} \geq 0.542(18) > 0.5$.

3.4.4 Derived Results

The constructed GHZ-state is subsequently transformed into a Bell-state of the edge-atoms. First, the two atoms of interest are shifted from the resonance of the others, then the rest is disentangled through a reverse detuning sweep resulting in the Bell state

$$\left|\Phi^+\right\rangle = \frac{|00\rangle + |11\rangle}{\sqrt{2}}. \tag{3.47}$$

This protocol is performed with eight atoms. Generally, a Bell state between distant atoms has many applications, for example, in quantum teleportation [326] as well as quantum cryprography [327].
After QOC had provided a way to prepare GHZ and Bell states, our collaborators continued to use our tool and showed the implementation of a three-atom CCZ gate using RedCRAB [328]. It was one of the building blocks used to build a Toffoli-gate; a three-qubit gate where two qubits simultaneously restrain a third qubit. Such gates are important for quantum error correction and form a step into the direction of a neutral atom quantum computer [329].

Conclusion

As quantum technologies evolve, so do the tools which explore and unlock their potential. Quantum Optimal Control (QOC) produces tailored control strategies to improve quantum technological applications. Our results showcase sensing-focused enhancements of quantum processes enabled through QOC. We pushed quantum hardware to its limits on various platforms: We amplified the sensitivity of single shallow nitrogen-vacancy (NV) centres, which are promising high-resolution quantum magnetometers. The subsequent optimisation with pentacene-doped naphthalene showed how an ensemble of spins in a complex setup can effectively polarise a bulk crystal. Exploring the creation of number-squeezing with ultracold atoms provided us with a deeper understanding of the considered atom interferometry experiment. Lastly, QOC enabled the production of a record-breaking Schrödinger cat state with Rydberg atoms in an optical lattice.

Two of the presented projects exploit the connection between electron spins and magnetic fields. While one turned NV centres close to the diamond surface into robust quantum sensors, the other used pentacene molecules buried throughout a naphthalene crystal as polarising agents.

We approached the closed-loop optimisation of shallow-NV sensing through the basic building blocks of the underlying sensing sequences. The contrast improvements, ranging from 32% to 67% dependent on the method, led to better sensitivities for each addressed NV centre [3]. By focusing on the robustness of the pulses, we increased the potential sensing volume for future applications on scanning probes. To take these considerations one step further, the optimisation should be done directly on a scanning probe setup taking into account the specific magnetic field distribution of the microwave antenna. In our experiment, one targeted sensing protocol required pulses with more frequency-selective properties than the other. Consequently, we introduced a new basis, i.e. the sigmoid basis, that could implement these constraints automatically. In the future, we plan further investigations of the convergence properties and restrictions attached to the sigmoid basis in particular and a wider variety of basis functions in general. While there are effort to change this, QOC bases are commonly chosen according to the default of the applied algorithm. When the problem is

over-parametrised, it becomes clear that any complete basis equally covers the full function space [330]. However, a different basis, i.e. type of parametrisation, will naturally change the landscape and possibly the landscape properties [165]. An investigation into the convergence behaviour of optimisations with alternative bases might guide the way towards more efficient QOC strategies.

The hyperpolarisation setup had many unknowns and some particular features that limited the efficiency of our standard single-sweep polarisation method, namely the integrated solid effect. Subsequently, the closed-loop optimised pulses not only increased the overall polarisation by almost one third, but also sped it up by 15% [4]. We generalised our findings by introducing the ARISE strategy to efficiently tailor and enhance hyperpolarisation sequences in the face of experimental uncertainty. ARISE is a multi-sweep strategy that allows an increased polarisation transfer. Our model showed that ARISE redistributes the polarisation between protons with different couplings, which could hint at the reason of its success. To further explore the effectiveness of ARISE, one has to better understand the influence of the setup on the pulse shapes. An in-depth characterisation of the cavity [306, 307] might be able to mitigate the discrepancies between model and measurement. A natural next step would be to apply ARISE to other systems to further explore its applicability both in theory and experiment.

Atomic states come in many shapes and sizes. The platforms presented in this thesis include an atomic condensate consisting of possibly thousands of atoms as well as twenty Rydberg atoms trapped in an optical lattice and entangled with a laser.

Squeezed states in atomic condensates harness the quantum properties to improve the sensitivity of atom interferometry measurements. After considering several criteria to model the experiment, we showed the potential of optimal control by enhancing the squeezing by a factor of four with an easily implementable pulse scheme. However, our results highlight the importance of a detailed model and further investigations of appropriate, spatially two-dimensional simulation techniques. The improvements we made in matching model and setup, take us a step closer to representative open-loop optimisations of the system.

There are different definitions for quantum sensing, one of which includes explicitly non-local interactions [105]. The Schrödinger cat state carries exactly those properties. With 20 Rydberg atoms we created the most extensive cat state to the date of its publication [1]. The increased amount of atoms also made its simulation a lot more complex, which is why the RedCRAB software package was needed to provide a suitable gradient-free approach for its optimisation. The resulting cat state does not only provide the basis for quantum-computational applications, but also for sensors. This project showed how QOC could decrease the preparation time by more than 50%, beating decoherence and thus enabling the

state preparation. The responsible experimental group continued by optimising multi-qubit gates with the same method [328], offering a glimpse of the possibilities that might lie in the future.

Throughout these projects, we upgraded and improved the software suite RedCRAB. It became clear that an intuitive and versatile interface is crucial to accommodate a swift connection to experimental components. Accordingly, RedCRAB was turned into a convenient tool with an easily accessible user interface and various features specifically designed to simplify its integration with experiments. A new open-source version named QuOCS [276] is currently under development, with a more flexible code structure. Among other features, it includes a direct interface to specialised experimental software, i.e. Qudi [278], and gradient-based methods. The experiences with closed-loop QOC problems have shown the importance of shared terminology and understanding of effects outside of the usual theoretical considerations. While we cannot incorporate these lessons directly into the software, they have shaped our approach toward such projects.

Each optimisation tells a different story when the figure of merit converges. Over many applications, we have developed an intuition to adapt the hyperparameters, i.e. the general optimisation settings, accordingly. Let us consider an example: Choosing the initial step size too small results in intermediate convergence to saddlepoints. When the step size is too large, the convergence becomes unnecessarily slow. This process of adapting hyperparameters could be automated [331] and extended to select the best search algorithm. Moreover, it would allow us to extract information about the size of landscape features and the robustness of optimised pulses with respect to the parameterisation. Could the analysis of convergence data provide an opportunity to estimate the efficiency of different bases with respect to a QOC problem? The elements of every basis possess an inherent set of properties. To give an example, Fourier components are bandwidth-limited, while piece-wise constant elements have limited temporal resolution. If the basis is complete, these properties are not reconstructable from the composed pulse as the number of elements goes towards infinity. However, incomplete bases with tailored properties can help to restrict the function space to what is experimentally feasible or specifically desired. We could use this fact to encode analytical conditions, like DRAG [28] or pulse criteria for dynamical decoupling [332], into a basis that always stays in the selected function space.

In summary, this thesis involved theoretical studies of various quantum platforms. By improving existing gradient-free QOC methods, we have reached four very distinct goals all promising to advance sensing; sensitivity, hyperpolarisation, number squeezing, and entangled state preparation. The wide scope of these enhancements shows how QOC can speed up the quantum revolution.

References

[1] A. Omran, H. Levine, A. Keesling, G. Semeghini, T. T. Wang, S. Ebadi, H. Bernien, A. S. Zibrov, H. Pichler, S. Choi, J. Cui, M. Rossignolo, P. Rembold, S. Montangero, T. Calarco, M. Endres, M. Greiner, V. Vuletić, and M. D. Lukin, "Generation and manipulation of Schrödinger cat states in Rydberg atom arrays," *Science*, vol. 365, no. 6453, pp. 570–574, 2019.

[2] P. Rembold, N. Oshnik, M. M. Müller, S. Montangero, T. Calarco, and E. Neu, "Introduction to quantum optimal control for quantum sensing with nitrogen-vacancy centers in diamond," *AVS Quantum Science*, vol. 2, no. 2, p. 024701, 2020.

[3] N. Oshnik, P. Rembold, T. Calarco, S. Montangero, E. Neu, and M. M. Müller, "Robust magnetometry with single nv centers via two-step optimization." arXiv:2111.12684 [quant-ph], 2021.

[4] A. Marshall, T. Reisser, P. Rembold, C. Müller, J. Scheuer, M. Gierse, T. Eichhorn, J. M. Steiner, P. Hautle, T. Calarco, F. Jelezko, M. B. Plenio, S. Montangero, I. Schwartz, M. M. Müller, and P. Neumann, "Macroscopic hyperpolarization enhanced with quantum optimal control." arXiv:2112.15021 [quant-ph], 2021.

[5] J. Zoller, *Optimal Quantum Engineering*. PhD thesis, Faculty of Natural Sciences, University of Ulm, 2018.

[6] R. Heck, O. Vuculescu, J. J. Sørensen, J. Zoller, M. G. Andreasen, M. G. Bason, P. Ejlertsen, O. Elíasson, P. Haikka, J. S. Laustsen, L. L. Nielsen, A. Mao, R. Müller, M. Napolitano, M. K. Pedersen, A. R. Thorsen, C. Bergenholtz, T. Calarco, S. Montangero, and J. F. Sherson, "Remote optimization of an ultracold atoms experiment by experts and citizen scientists," *Proceedings of the National Academy of Sciences of the United States of America*, vol. 115, pp. E11231–E11237, Nov 2018.

[7] A. U. J. Lode, P. Molignini, R. Lin, M. Büttner, P. Rembold, C. Lévêque, M. C. Tsatsos, and L. Papariello, "UNIQORN: Universal Neural network Interface for Quantum Observable Readout from N-body wavefunctions." *GitLab*, https://gitlab.com/auj.lode/UNIQORN.git, 2020.

[8] M. Rossignolo, A. Marshall, T. Reisser, P. Rembold, A. Pagano, P. Vetter, R. Said, M. Müller, T. Calarco, S. Montangero, and F. Jelezko, "QuOCS: Quantum Optimal Control Suite." *GitHub*, https://github.com/Quantum-OCS/QuOCS, 2021.

[9] P. Rembold, "A Tale of Claw Machines and Quantum Mechanics." *QuSCo Blog*, Oct 2019.

[10] A. Kosloff, "Diamond and boxing gloves: an introduction to quantum sensing and quantum control." *YouTube*, Oct 2021.

[11] J. Preskill, "Quantum Computing in the NISQ era and beyond," *Quantum*, vol. 2, p. 79, Aug 2018.

[12] R. McKinlay, "Technology: Use or lose our navigation skills," *Nature*, vol. 531, pp. 573–575, Mar 2016.

[13] P. Wallden and E. Kashefi, "Cyber security in the quantum era," *Communications of the ACM*, vol. 62, no. 4, pp. 120–120, 2019.

[14] P. Neumann, I. Jakobi, F. Dolde, C. Burk, R. Reuter, G. Waldherr, J. Honert, T. Wolf, A. Brunner, J. H. Shim, D. Suter, H. Sumiya, J. Isoya, and J. Wrachtrup, "High-Precision Nanoscale Temperature Sensing Using Single Defects in Diamond," *Nano Letters*, vol. 13, pp. 2738–2742, Jun 2013.

[15] J. M. Taylor, P. Cappellaro, L. Childress, L. Jiang, D. Budker, P. R. Hemmer, A. Yacoby, R. Walsworth, and M. D. Lukin, "High-sensitivity diamond magnetometer with nanoscale resolution," *Nature Physics*, vol. 4, pp. 810–816, Oct 2008.

[16] F. Baumgärtner, R. J. Sewell, S. Eriksson, I. Llorente-Garcia, J. Dingjan, J. P. Cotter, and E. A. Hinds, "Measuring Energy Differences by BEC Interferometry on a Chip," *Physical Review Letters*, vol. 105, p. 243003, Dec 2010.

[17] C. P. Koch, "Controlling open quantum systems: tools, achievements, and limitations," *Journal of Physics: Condensed Matter*, vol. 28, p. 213001, May 2016.

[18] S. J. Glaser, U. Boscain, T. Calarco, C. P. Koch, W. Köckenberger, R. Kosloff, I. Kuprov, B. Luy, S. Schirmer, T. Schulte-Herbrüggen, D. Sugny, and F. K. Wilhelm, "Training Schrödinger's cat: Quantum optimal control: Strategic report on current status, visions and goals for research in Europe," *European Physical Journal D*, vol. 69, no. 12, 2015.

[19] N. Khaneja, T. Reiss, C. Kehlet, T. Schulte-Herbrüggen, and S. J. Glaser, "Optimal control of coupled spin dynamics: Design of NMR pulse sequences by gradient ascent algorithms," *Journal of Magnetic Resonance*, vol. 172, pp. 296–305, Feb 2005.

[20] J. Werschnik and E. K. Gross, "Quantum optimal control theory," *Journal of Physics B: Atomic, Molecular and Optical Physics*, vol. 40, Sep 2007.

[21] J.-F. Mennemann, D. Matthes, R. m Weishäupl, and T. Langen, "Optimal control of Bose–Einstein condensates in three dimensions," *New Journal of Physics*, vol. 17, p. 113027, 11 2015.

[22] S. Machnes, U. Sander, S. J. Glaser, P. Defouquì, A. Gruslys, S. Schirmer, T. Schulte-Herbrüggen, P. de Fouquières, A. Gruslys, S. Schirmer, and T. Schulte-Herbrüggen, "Comparing, optimizing, and benchmarking quantum-control algorithms in a unifying programming framework," *Physical Review A*, vol. 84, p. 22305, 2011.

[23] T. Caneva, T. Calarco, and S. Montangero, "Chopped random-basis quantum optimization," *Physical Review A*, vol. 84, no. 2, p. 22326, 2011.

[24] M. M. Müller, R. S. Said, F. Jelezko, T. Calarco, and S. Montangero, "One decade of quantum optimal control in the chopped random basis." arXiv:2104.07687 [quant-ph], 2021.

[25] P. Konzelmann, T. Rendler, V. Bergholm, A. Zappe, V. Pfannenstill, M. Garsi, F. Ziem, M. Niethammer, M. Widmann, S. Y. Lee, P. Neumann, and J. Wrachtrup, "Robust and efficient quantum optimal control of spin probes in a complex (biological) environment. Towards sensing of fast temperature fluctuations," *New Journal of Physics*, vol. 20, no. 12, 2018.

[26] F. Frank, T. Unden, J. Zoller, R. S. Said, T. Calarco, S. Montangero, B. Naydenov, and F. Jelezko, "Autonomous calibration of single spin qubit operations," *npj Quantum Information*, vol. 3, p. 48, Dec 2017.

[27] F. Dolde, V. Bergholm, Y. Wang, I. Jakobi, B. Naydenov, S. Pezzagna, J. Meijer, F. Jelezko, P. Neumann, T. Schulte-Herbrüggen, J. Biamonte, and J. Wrachtrup, "High-fidelity spin entanglement using optimal control," *Nature Communications*, vol. 5, 2014.

[28] F. Motzoi, J. M. Gambetta, P. Rebentrost, and F. K. Wilhelm, "Simple pulses for elimination of leakage in weakly nonlinear qubits," *Physical Review Letters*, vol. 103, p. 110501, Sep 2009.

[29] J. Kelly, R. Barends, B. Campbell, Y. Chen, Z. Chen, B. Chiaro, A. Dunsworth, A. G. Fowler, I.-C. Hoi, E. Jeffrey, A. Megrant, J. Mutus, C. Neill, P. J. J. O'Malley, C. Quintana, P. Roushan, D. Sank, A. Vainsencher, J. Wenner, T. C. White, A. N. Cleland, and J. M. Martinis, "Optimal quantum control using randomized benchmarking," *Physical Review Letters*, vol. 112, p. 240504, Jun 2014.

[30] M. Werninghaus, D. J. Egger, F. Roy, S. Machnes, F. K. Wilhelm, and S. Filipp, "Leakage reduction in fast superconducting qubit gates via optimal control," *npj Quantum Information*, vol. 7, p. 14, Jan 2021.

[31] Z. Tošner, T. Vosegaard, C. Kehlet, N. Khaneja, S. J. Glaser, and N. C. Nielsen, "Optimal control in NMR spectroscopy: Numerical implementation in SIMPSON," *Journal of Magnetic Resonance*, vol. 197, no. 2, pp. 120–134, 2009.

[32] N. Timoney, V. Elman, S. Glaser, C. Weiss, M. Johanning, W. Neuhauser, and C. Wunderlich, "Error-resistant single-qubit gates with trapped ions," *Physical Review A*, vol. 77, p. 052334, May 2008.

[33] P. Cerfontaine, T. Botzem, J. Ritzmann, S. S. Humpohl, A. Ludwig, D. Schuh, D. Bougeard, A. D. Wieck, and H. Bluhm, "Closed-loop control of a GaAs-based singlet-triplet spin qubit with 99.5% gate fidelity and low leakage," *Nature Communications*, vol. 11, p. 4144, Aug 2020.

[34] S. Rosi, A. Bernard, N. Fabbri, L. Fallani, C. Fort, M. Inguscio, T. Calarco, and S. Montangero, "Fast closed-loop optimal control of ultracold atoms in an optical lattice," *Physical Review A*, vol. 88, p. 021601, Aug 2013.

[35] W. Heisenberg, *Encounters with Einstein: And Other Essays on People, Places, and Particles*. Princeton Science Library, Princeton University Press, 1989.

[36] J. Wrachtrup, C. Von Borczyskowski, J. Bernard, M. Orritt, and R. Brown, "Optical detection of magnetic resonance in a single molecule," *Nature*, vol. 363, no. 6426, pp. 244–245, 1993.

[37] M. W. Doherty, N. B. Manson, P. Delaney, F. Jelezko, J. Wrachtrup, and L. C. Hollenberg, "The nitrogen-vacancy colour centre in diamond," *Physics Reports*, vol. 528, no. 1, pp. 1–45, 2013.

[38] E. Schrödinger, "An undulatory theory of the mechanics of atoms and molecules," *Physical Review*, vol. 28, pp. 1049–1070, Dec 1926.

[39] M. A. Nielsen and I. L. Chuang, *Quantum Computation and Quantum Information*. Cambridge University Press, 2000.

[40] A. M. Stoneham, *Theory of defects in solids : electronic structure of defects in insulators and semiconductors*. Clarendon Press, 2001.

[41] J. Olšina and T. Mančal, "Role of markov and secular approximations in ultra-fast excited state dynamics of molecular aggregates," *WDS'10 Proceedings of Contributed Papers, Part III*, pp. 13–18, 2010.

[42] M. Maggiore, *A Modern Introduction to Quantum Field Theory*. EBSCO ebook academic collection, Oxford University Press, 2005.

[43] F. Marquardt and A. Püttmann, "Dissipation and decoherence in quantum systems," *Langeoog Workshop of the SFB/TR "Symmetries and Universality in Mesoscopic Systems"*, 2007. arXiv:0809.4403 [quant-ph].

[44] A. Norambuena, E. Muñoz, H. T. Dinani, A. Jarmola, P. Maletinsky, D. Budker, and J. R. Maze, "Spin-lattice relaxation of individual solid-state spins," *Physical Review B*, vol. 97, p. 094304, Mar 2018.

[45] N. Aslam, G. Waldherr, P. Neumann, F. Jelezko, and J. Wrachtrup, "Photo-induced ionization dynamics of the nitrogen vacancy defect in diamond investigated by single-shot charge state detection," *New Journal of Physics*, vol. 15, p. 013064, Jan 2013.

[46] O. E. Alon, A. I. Streltsov, and L. S. Cederbaum, "Multiconfigurational time-dependent Hartree method for bosons: Many-body dynamics of bosonic systems," *Physical Review A*, vol. 77, no. 033613, pp. 1–14, 2008.

[47] O. Benson, "System Reservoir Interactions," in *Quantum Optics (Lecture Notes)*, ch. 10, Humboldt-Universität zu Berlin, 2009.

[48] D. Walls and G. Milburn, *Quantum Optics*. SpringerLink: Springer e-Books, Springer Berlin Heidelberg, 2008.

[49] G. W. Ford, J. T. Lewis, and R. F. O'Connell, "Quantum langevin equation," *Physical Review A*, vol. 37, pp. 4419–4428, Jun 1988.

[50] R. Schirhagl, K. Chang, M. Loretz, and C. L. Degen, "Nitrogen-vacancy centers in diamond: Nanoscale sensors for physics and biology," *Annual Review of Physical Chemistry*, vol. 65, pp. 83–105, Apr 2014.

[51] L. Robledo, H. Bernien, T. van der Sar, and R. Hanson, "Spin dynamics in the optical cycle of single nitrogen-vacancy centres in diamond," *New Journal of Physics*, vol. 13, p. 025013, Feb 2011.

[52] T. Liu, J. Zhang, H. Yuan, L. Xu, G. Bian, P. Fan, M. Li, Y. Liu, S. Xia, C. Xu, and X. Xiao, "A pulsed time-varying method for improving the spin readout efficiency of nitrogen vacancy centers," *Journal of Physics D: Applied Physics*, vol. 54, p. 395002, 7 2021.

[53] A. Dréau, M. Lesik, L. Rondin, P. Spinicelli, O. Arcizet, J.-F. Roch, and V. Jacques, "Avoiding power broadening in optically detected magnetic resonance of single nv defects for enhanced dc magnetic field sensitivity," *Physical Review B*, vol. 84, p. 195204, Nov 2011.

[54] K. Jensen, V. M. Acosta, A. Jarmola, and D. Budker, "Light narrowing of magnetic resonances in ensembles of nitrogen-vacancy centers in diamond," *Physical Review B*, vol. 87, p. 014115, Jan 2013.

[55] K. Kraus, A. Bohm, J. Dollard, and W. Wootters, "States, effects, and operations: fundamental notions of quantum theory," in *Mathematical Physics (Lecture Notes)*, University of Texas at Austin, 1983.

[56] J. Preskill, "Quantum information," in *Ph219/CS219 (Lecture Notes)*, ch. 3, California Institute of Technology, 2018.

[57] T. Unden, P. Balasubramanian, D. Louzon, Y. Vinkler, M. B. Plenio, M. Markham, D. Twitchen, A. Stacey, I. Lovchinsky, A. O. Sushkov, M. D. Lukin, A. Retzker, B. Naydenov, L. P. McGuinness, and F. Jelezko, "Quantum Metrology Enhanced by Repetitive Quantum Error Correction," *Physical Review Letters*, vol. 116, p. 230502, Jun 2016.

[58] L. S. Bishop, *Circuit Quantum Electrodynamics*. PhD thesis, Yale University, 2010.

[59] B. Julsgaard, C. Grezes, P. Bertet, and K. Mølmer, "Quantum memory for microwave photons in an inhomogeneously broadened spin ensemble," *Physical Review Letters*, vol. 110, p. 250503, Jun 2013.

[60] Q. Ansel, S. Probst, P. Bertet, S. J. Glaser, and D. Sugny, "Optimal control of an inhomogeneous spin ensemble coupled to a cavity," *Physical Review A*, vol. 98, no. 2, pp. 1–10, 2018.

[61] C. Nietner, *Quantum Phase Transition of Light in the Jaynes-Cummings Lattice*. Diploma thesis, Freie Universität Berlin, 2010.

[62] P. M. Schosseler, *Electron paramagnetic resonance study of the copper(II) complexation with carbonate ligands in aqueous solution and at calcium carbonate surfaces*. PhD thesis, ETH Zürich, 1998. Ch: Hyperfine Interaction.

[63] A. Henstra, T.-S. Lin, J. Schmidt, and W. Wenckebach, "High dynamic nuclear polarization at room temperature," *Chemical Physics Letters*, vol. 165, no. 1, pp. 6–10, 1990.

[64] T. Can, Q. Ni, and R. Griffin, "Mechanisms of dynamic nuclear polarization in insulating solids," *Journal of Magnetic Resonance*, vol. 253, pp. 23–35, 2015.

[65] L. P. L. P. Pitaevskii and S. Stringari, *Bose-Einstein condensation and superfluidity*. Oxford University Press, 2016.

[66] C. J. Pethick and H. Smith, *Bose–Einstein Condensation in Dilute Gases*. Cambridge University Press, 2001.

[67] L. Salasnich, *Quantum Physics of Light and Matter*. Springer International Publishing, 2014.

[68] E. J. Mueller, T.-L. Ho, M. Ueda, and G. Baym, "Fragmentation of Bose-Einstein condensates," *Physical Review A*, vol. 74, p. 033612, Sep 2006.

[69] A. U. Lode, C. Lévêque, L. B. Madsen, A. I. Streltsov, and O. E. Alon, "Colloquium: Multiconfigurational time-dependent hartree approaches for indistinguishable particles," *Reviews of Modern Physics*, vol. 92, 2020.

[70] J. Grond, G. von Winckel, J. Schmiedmayer, and U. Hohenester, "Optimal control of number squeezing in trapped Bose-Einstein condensates," *Physical Review A*, vol. 80, no. 5, pp. 1–15, 2009.

[71] A. Bhowmik, S. K. Haldar, and O. E. Alon, "Impact of the transverse direction on the many-body tunneling dynamics in a two-dimensional bosonic josephson junction," *Scientific Reports 2020 10:1*, vol. 10, pp. 1–18, 12 2020.

[72] L. Pezzè, A. Smerzi, M. K. Oberthaler, R. Schmied, and P. Treutlein, "Quantum metrology with nonclassical states of atomic ensembles," *Reviews of Modern Physics*, vol. 90, no. 3, 2018.

[73] C. Adams, M. Sigel, and J. Mlynek, "Atom optics," *Physics Reports*, vol. 240, p. 143–210, 05 1994.

[74] A. D. Cronin, J. Schmiedmayer, and D. E. Pritchard, "Optics and interferometry with atoms and molecules," *Reviews of Modern Physics*, vol. 81, pp. 1051–1129, Jul 2009.

[75] Y.-J. Wang, D. Z. Anderson, V. M. Bright, E. A. Cornell, Q. Diot, T. Kishimoto, M. Prentiss, R. A. Saravanan, S. R. Segal, and S. Wu, "Atom Michelson Interferometer on a Chip Using a Bose-Einstein Condensate," *Physical Review Letters*, vol. 94, p. 090405, Mar 2005.

[76] B. P. Anderson and M. A. Kasevich, "Macroscopic quantum interference from atomic tunnel arrays," *Science*, vol. 282, no. 5394, pp. 1686–1689, 1998.

[77] T. Berrada, *Mach-Zehnder interferometry with interacting Bose-Einstein condensates in a double-well potential*. PhD thesis, Technischen Universität Wien, Fakultät für Physik, 2014.

[78] Julian Grond, *Optimal quantum control of trapped Bose-Einstein condensates*. PhD thesis, Karl-Franzens-Universität Graz, Naturwissenschaftliche Fakultät, 2010.

[79] Y. Castin and J. Dalibard, "Relative phase of two bose-einstein condensates," *Physical Review A*, vol. 55, p. 4330, 6 1997.

[80] M. Kitagawa and M. Ueda, "Squeezed spin states," *Physical Review A*, vol. 47, p. 5138, 6 1993.

[81] D. J. Wineland, J. J. Bollinger, W. M. Itano, and D. J. Heinzen, "Squeezed atomic states and projection noise in spectroscopy," *Physical Review A*, vol. 50, p. 67, 7 1994.

[82] E. Fasshauer and A. U. J. Lode, "Multiconfigurational time-dependent hartree method for fermions: Implementation, exactness, and few-fermion tunneling to open space," *Physical Review A*, vol. 93, p. 033635, Mar 2016.

[83] R. Lin, P. Molignini, L. Papariello, M. C. Tsatsos, C. Lévêque, S. E. Weiner, E. Fasshauer, R. Chitra, and A. U. Lode, "MCTDH-X: The multiconfigurational time-dependent Hartree method for indistinguishable particles software," *Quantum Science and Technology*, vol. 5, p. 24004, Mar 2020.

[84] A. U. J. Lode, "Multiconfigurational time-dependent hartree method for bosons with internal degrees of freedom: Theory and composite fragmentation of multicomponent bose-einstein condensates," *Physical Review A*, vol. 93, p. 063601, Jun 2016.

[85] A. U. Lode, A. I. Streltsov, K. Sakmann, O. E. Alon, and L. S. Cederbaum, "How an interacting many-body system tunnels through a potential barrier to open space," *Proceedings of the National Academy of Sciences*, vol. 109, no. 34, pp. 13521–13525, 2012.

[86] L. Salasnich, A. Parola, and L. Reatto, "Effective wave equations for the dynamics of cigar-shaped and disk-shaped bose condensates," *Physical Review A*, vol. 65, p. 6, 2002.

[87] Sandrine van Frank, *Coherent control over the motional states of a Bose-Einstein condensate and applications*. PhD thesis, Technischen Universität Wien, Fakultät für Physik, 2015.

[88] F. Gerbier, "Quasi-1D Bose-Einstein condensates in the dimensional crossover regime," *Europhysics Letters*, vol. 66, no. 6, pp. 771–777, 2004.

[89] T. Yang, A. J. Henning, and K. A. Benedict, "Bogoliubov excitation spectrum of an elongated condensate throughout a transition from quasi-one-dimensional to three-dimensional," *Journal of Physics B: Atomic, Molecular and Optical Physics*, vol. 47, 2 2014.

[90] L. Salasnich, "Generalized nonpolynomial schrödinger equations for matter waves under anisotropic transverse confinement," *Journal of Physics A: Mathematical and Theoretical*, vol. 42, p. 335205, Jul 2009.

[91] K. Sakmann and M. Kasevich, "Single-shot simulations of dynamic quantum many-body systems," *Nature Physics*, vol. 12, no. 5, pp. 451–455, 2016.

[92] A. U. J. Lode, R. Lin, M. Büttner, L. Papariello, C. Lévêque, R. Chitra, M. C. Tsatsos, D. Jaksch, and P. Molignini, "Optimized observable readout from single-shot images of ultracold atoms via machine learning," *Physical Review A*, vol. 104, p. L041301, Oct 2021.

[93] M. Bonneau, W. J. Munro, K. Nemoto, and J. Schmiedmayer, "Characterizing twin-particle entanglement in double-well potentials," *Physical Review A*, vol. 98, no. 3, pp. 1–9, 2018.

[94] N. I. Fisher, *Statistical Analysis of Circular Data*. Cambridge University Press, 1993.

[95] C. Brif, R. Chakrabarti, and H. Rabitz, "Control of quantum phenomena: past, present and future," *New Journal of Physics*, vol. 12, p. 075008, Jul 2010.

[96] S. McDonald and W. S. Warren, "Uses of shaped pulses in NMR: A primer," *Concepts in Magnetic Resonance*, vol. 3, no. 2, pp. 55–81, 1991.

[97] P. Costabel (eds.), J. Peiffer (eds.), and J. I. Bernoulli, *Der Briefwechsel von Johann I Bernoulli. Band 2 : Der Briefwechsel mit Pierre Varignon*. Birkhäuser Basel, 1988.

[98] J. Scheuer, X. Kong, R. S. Said, J. Chen, A. Kurz, L. Marseglia, J. Du, P. R. Hemmer, S. Montangero, T. Calarco, B. Naydenov, and F. Jelezko, "Precise qubit control beyond the rotating wave approximation," *New Journal of Physics*, vol. 16, 2014.

[99] T. Häberle, D. Schmid-Lorch, K. Karrai, F. Reinhard, and J. Wrachtrup, "High-dynamic-range imaging of nanoscale magnetic fields using optimal control of a single qubit," *Physical Review Letters*, vol. 111, p. 170801, Oct 2013.

[100] K. Tsurumoto, R. Kuroiwa, H. Kano, Y. Sekiguchi, and H. Kosaka, "Quantum teleportation-based state transfer of photon polarization into a carbon spin in diamond," *Communications Physics*, vol. 2, pp. 1–6, Dec 2019.

[101] R. S. Said and J. Twamley, "Robust control of entanglement in a nitrogen-vacancy center coupled to a C 13 nuclear spin in diamond," *Physical Review A*, vol. 80, p. 032303, Sep 2009.

[102] S. Montangero, T. Calarco, and R. Fazio, "Robust Optimal Quantum Gates for Josephson Charge Qubits," *Physical Review Letters*, vol. 99, p. 170501, Oct 2007.

[103] M. H. Goerz, G. Gualdi, D. M. Reich, C. P. Koch, F. Motzoi, K. B. Whaley, J. Vala, M. M. Müller, S. Montangero, and T. Calarco, "Optimizing for an arbitrary perfect entangler. ii. application," *Physical Review A*, vol. 91, p. 062307, Jun 2015.

[104] J. P. Palao and R. Kosloff, "Optimal control theory for unitary transformations," *Physical Review A*, vol. 68, no. 6, p. 13, 2003.

[105] C. L. Degen, F. Reinhard, and P. Cappellaro, "Quantum sensing," *Reviews of Modern Physics*, vol. 89, no. 3, pp. 1–39, 2017.

[106] S. L. Braunstein and C. M. Caves, "Statistical distance and the geometry of quantum states," *Physical Review Letters*, vol. 72, no. 22, pp. 3439–3443, 1994.

[107] M. M. Müller, S. Gherardini, and F. Caruso, "Noise-robust quantum sensing via optimal multi-probe spectroscopy," *Scientific Reports*, vol. 8, no. 1, p. 14278, 2018.

[108] F. Poggiali, P. Cappellaro, and N. Fabbri, "Optimal Control for One-Qubit Quantum Sensing," *Physical Review X*, vol. 8, Jun 2018.

[109] K. Kobzar, T. E. Skinner, N. Khaneja, S. J. Glaser, and B. Luy, "Exploring the limits of broadband excitation and inversion: II. Rf-power optimized pulses," *Journal of Magnetic Resonance*, vol. 194, no. 1, pp. 58–66, 2008.

[110] T. Nöbauer, A. Angerer, B. Bartels, M. Trupke, S. Rotter, J. Schmiedmayer, F. Mintert, and J. Majer, "Smooth Optimal Quantum Control for Robust Solid-State Spin Magnetometry," *Physical Review Letters*, vol. 115, p. 190801, Nov 2015.

[111] D. L. Goodwin, *Advanced Optimal Control Methods for Spin Systems*. PhD thesis, University of Southampton, 2018.

[112] I. Schaefer and R. Kosloff, "Optimization of high-order harmonic generation by optimal control theory: Ascending a functional landscape in extreme conditions," *Physical Review A*, vol. 101, p. 023407, Feb 2020.

[113] S. Pezeshki, M. Schreiber, and U. Kleinekathöfer, "Shaping femtosecond coherent anti-Stokes Raman spectra using optimal control theory," *Physical Chemistry Chemical Physics*, vol. 10, no. 15, pp. 2058–2066, 2008.

[114] G. Riviello, R.-B. Wu, Q. Sun, and H. Rabitz, "Searching for an optimal control in the presence of saddles on the quantum-mechanical observable landscape," *Physical Review A*, vol. 95, p. 63418, 2017.

[115] J. P. Palao, R. Kosloff, and C. P. Koch, "Protecting coherence in optimal control theory: State-dependent constraint approach," *Physical Review A*, vol. 77, no. 6, 2008.

[116] T. E. Skinner, T. O. Reiss, B. Luy, N. Khaneja, and S. J. Glaser, "Reducing the duration of broadband excitation pulses using optimal control with limited rf amplitude," *Journal of Magnetic Resonance*, vol. 167, no. 1, pp. 68 – 74, 2004.

[117] S. Machnes, E. Assémat, D. Tannor, and F. K. Wilhelm, "Tunable, Flexible, and Efficient Optimization of Control Pulses for Practical Qubits," *Physical Review Letters*, vol. 120, no. 15, p. 150401, 2018.

[118] K. Kobzar, S. Ehni, T. E. Skinner, S. J. Glaser, and B. Luy, "Exploring the limits of broadband 90° and 180° universal rotation pulses," *Journal of Magnetic Resonance*, vol. 225, pp. 142–160, 2012.

[119] B. Bonnard and M. Chyba, *Singular trajectories and their role in control theory*. Springer, 2003.

[120] U. Boscain and B. Piccoli, *Optimal syntheses for control systems on 2-D manifolds*. Springer, 2004.

[121] D. Guéry-Odelin, A. Ruschhaupt, A. Kiely, E. Torrontegui, S. Martínez-Garaot, and J. G. Muga, "Shortcuts to adiabaticity: Concepts, methods, and applications," *Rev. Mod. Phys.*, vol. 91, p. 045001, Oct 2019.

[122] E. Torrontegui, S. Ibáñez, S. Martínez-Garaot, M. Modugno, A. del Campo, D. Guéry-Odelin, A. Ruschhaupt, X. Chen, and J. G. Muga, "Shortcuts to Adiabaticity," in *Advances in Atomic, Molecular and Optical Physics*, vol. 62, pp. 117–169, Elsevier, 2013.

[123] C. Avinadav, R. Fischer, P. London, and D. Gershoni, "Time-optimal universal control of two-level systems under strong driving," *Physical Review B*, vol. 89, no. 24, pp. 1–7, 2014.

[124] F. Kleißler, A. Lazariev, and S. Arroyo-Camejo, "Universal, high-fidelity quantum gates based on superadiabatic, geometric phases on a solid-state spin-qubit at room temperature," *npj Quantum Information*, vol. 4, pp. 1–6, Dec 2018.

[125] J. Kölbl, A. Barfuss, M. S. Kasperczyk, L. Thiel, A. A. Clerk, H. Ribeiro, and P. Maletinsky, "Initialization of Single Spin Dressed States using Shortcuts to Adiabaticity," *Physical Review Letters*, vol. 122, p. 090502, Mar 2019.

[126] A. I. Konnov and V. F. Krotov, "On global methods for the successive improvement of control processes," *Avtomatika i Telemekhanika*, vol. 60, no. 10, pp. 77–88, 1999.

[127] S. E. Sklarz and D. J. Tannor, "Loading a Bose-Einstein condensate onto an optical lattice: An application of optimal control theory to the nonlinear Schrödinger equation," *Physical Review A*, vol. 66, no. 5, p. 9, 2002.

[128] Y. Ohtsuki, G. Turinici, and H. Rabitz, "Generalized monotonically convergent algorithms for solving quantum optimal control problems," *Journal of Chemical Physics*, vol. 120, no. 12, pp. 5509–5517, 2004.

[129] P. Doria, T. Calarco, and S. Montangero, "Optimal Control Technique for Many-Body Quantum Dynamics," *Physical Review Letters*, vol. 106, p. 190501, May 2011.

[130] D. M. Reich, M. Ndong, and C. P. Koch, "Monotonically convergent optimization in quantum control using Krotovs method," *Journal of Chemical Physics*, vol. 136, no. 10, p. 104103, 2012.

[131] J. Nocedal and S. Wright, *Numerical optimization*. Springer Science & Business Media, 2006.

[132] P. de Fouquieres, S. Schirmer, S. Glaser, and I. Kuprov, "Second order gradient ascent pulse engineering," *Journal of Magnetic Resonance*, vol. 212, pp. 412–417, Oct 2011.

[133] J. C. Saywell, I. Kuprov, D. Goodwin, M. Carey, and T. Freegarde, "Optimal control of mirror pulses for cold-atom interferometry," *Physical Review A*, 2019.

[134] V. F. Krotov and A. B. Kurzhanski, *Global Methods in Optimal Control Theory*, pp. 74–121. Boston, MA: Birkhäuser Boston, 1993.

[135] R. Eitan, M. Mundt, and D. J. Tannor, "Optimal control with accelerated convergence: Combining the Krotov and quasi-Newton methods," *Physical Review A*, vol. 83, p. 53426, 2011.

[136] J. J. W. H. Sørensen, M. O. Aranburu, T. Heinzel, and J. F. Sherson, "Quantum optimal control in a chopped basis: Applications in control of Bose-Einstein condensates," *Physical Review A*, vol. 98, p. 022119, Aug 2018.

[137] G. Feng, F. H. Cho, H. Katiyar, J. Li, D. Lu, J. Baugh, and R. Laflamme, "Gradient-based closed-loop quantum optimal control in a solid-state two-qubit system," *Physical Review A*, vol. 98, no. 5, pp. 1–11, 2018.

[138] C. Ferrie and O. Moussa, "Robust and efficient in situ quantum control," *Physical Review A*, vol. 91, no. 5, p. 52306, 2015.

[139] Q. Sun, I. Pelczer, G. Riviello, R.-B. Wu, and H. Rabitz, "Experimental exploration over a quantum control landscape through nuclear magnetic resonance," *Physical Review A*, vol. 89, p. 033413, Mar 2014.

[140] N. Rach, M. M. Müller, T. Calarco, and S. Montangero, "Dressing the chopped-random-basis optimization: A bandwidth-limited access to the trap-free landscape," *Physical Review A*, vol. 92, p. 62343, 2015.

[141] S. Lloyd and S. Montangero, "Information theoretical analysis of quantum optimal control," *Physical Review Letters*, vol. 113, pp. 1–5, 1 2014.

[142] K. W. Moore and H. Rabitz, "Exploring constrained quantum control landscapes," *Journal of Chemical Physics*, vol. 137, Oct 2012.

[143] J. A. Nelder and R. Mead, "A Simplex Method for Function Minimization," *The Computer Journal*, vol. 7, pp. 308–313, 01 1965.

[144] H.-G. Beyer and H.-P. Schwefel, "Evolution strategies – A comprehensive introduction," *Natural Computing*, vol. 1, no. 1, pp. 3–52, 2002.

[145] J. Johansson, P. Nation, and F. Nori, "Qutip 2: A python framework for the dynamics of open quantum systems," *Computer Physics Communications*, vol. 184, no. 4, pp. 1234 – 1240, 2013.

[146] J. Johansson, P. Nation, and F. Nori, "Qutip: An open-source python framework for the dynamics of open quantum systems," *Computer Physics Communications*, vol. 183, no. 8, pp. 1760 – 1772, 2012.

[147] M. H. Goerz, D. Basilewitsch, F. Gago-Encinas, M. G. Krauss, K. P. Horn, D. M. Reich, and C. P. Koch, "Krotov: A Python implementation of Krotov's method for quantum optimal control," *SciPost Physics*, vol. 7, p. 80, 2019.

[148] H. J. Hogben, M. Krzystyniak, G. T. Charnock, P. J. Hore, and I. Kuprov, "Spinach - A software library for simulation of spin dynamics in large spin systems," *Journal of Magnetic Resonance*, vol. 208, pp. 179–194, Feb 2011.

[149] J. Sørensen, J. Jensen, T. Heinzel, and J. Sherson, "Qengine: A c++ library for quantum optimal control of ultracold atoms," *Computer Physics Communications*, vol. 243, pp. 135 – 150, 2019.

[150] N. Leung, M. Abdelhafez, J. Koch, and D. Schuster, "Speedup for quantum optimal control from automatic differentiation based on graphics processing units," *Physical Review A*, vol. 95, p. 042318, Apr 2017.

[151] Domenico D'Alessandro, *Introduction to Quantum Control and Dynamics*. Chapman and Hall/CRC, 2007.

[152] G. Turinici and H. Rabitz, "Wavefunction controllability for finite-dimensional bilinear quantum systems," *Journal of Physics A: Mathematical and General*, vol. 36, p. 2565, 2003.

[153] Velimir Jurdjevic, *Geometric control theory*. Cambridge University Press, 1996.

[154] S. Deffner and S. Campbell, "Quantum speed limits: from heisenberg's uncertainty principle to optimal quantum control," *Journal of Physics A: Mathematical and Theoretical*, vol. 50, p. 453001, Oct 2017.

[155] K. Bhattacharyya, "Quantum decay and the Mandelstam-Tamm-energy inequality," *Journal of Physics A: Mathematical and General*, vol. 16, no. 13, pp. 2993–2996, 1983.

[156] T. Caneva, M. Murphy, T. Calarco, R. Fazio, S. Montangero, V. Giovannetti, and G. E. Santoro, "Optimal control at the quantum speed limit," *Physical Review Letters*, vol. 103, no. 24, pp. 1–4, 2009.

[157] L. Viola and S. Lloyd, "Dynamical suppression of decoherence in two-state quantum systems," *Physical Review A*, vol. 58, no. 4, pp. 2733–2744, 1998.

[158] P. Rembold, M. Müller, T. Calarco, and S. Montangero *Manuscript in preparation*, 2022.

[159] A. Oppenheim, "Fourier transform properties," in *RES.6-007 Signals and Systems*, ch. 9, Cambridge MA: Massachusetts Institute of Technology, 2011. MIT OpenCourseWare.

[160] Z. Leng, P. Mundada, S. Ghadimi, and A. Houck, "Robust and efficient algorithms for high-dimensional black-box quantum optimization." arXiv:1910.03591 [quant-phys], 2019.

[161] D. Lucarelli, "Quantum optimal control via gradient ascent in function space and the time-bandwidth quantum speed limit," *Physical Review A*, vol. 97, p. 062346, Jun 2018.

[162] H. Ball and M. J. Biercuk, "Walsh-synthesized noise filters for quantum logic," *EPJ Quantum Technology*, vol. 2, p. 11, 12 2015.

[163] S. Günther, N. A. Petersson, and J. L. DuBois, "Quantum optimal control for pure-state preparation using one initial state," *AVS Quantum Science*, vol. 3, no. 4, p. 043801, 2021.

[164] N. A. Petersson, F. M. Garcia, A. E. Copeland, Y. L. Rydin, and J. L. DuBois, "Discrete adjoints for accurate numerical optimization with application to quantum control." arXiv:2001.01013 [quant-ph], 2020.

[165] M. Dalgaard, F. Motzoi, and J. Sherson, "Predicting quantum dynamical cost landscapes with deep learning," *Physical Review A*, vol. 105, p. 012402, Jan 2022.

[166] J. H. M. Jensen, F. S. Møller, J. J. Sørensen, and J. F. Sherson, "Achieving fast high-fidelity optimal control of many-body quantum dynamics," *Physical Review A*, vol. 104, p. 052210, Nov 2021.

[167] T. de Guillebon, B. Vindolet, J.-F. Roch, V. Jacques, and L. Rondin, "Temperature dependence of the longitudinal spin relaxation time T_1 of single nitrogen-vacancy centers in nanodiamonds," *Physical Review B*, vol. 102, p. 165427, Oct 2020.

[168] G. Balasubramanian, I. Y. Chan, R. Kolesov, M. Al-Hmoud, J. Tisler, C. Shin, C. Kim, A. Wojcik, P. R. Hemmer, A. Krueger, T. Hanke, A. Leitenstorfer, R. Bratschitsch, F. Jelezko, and J. Wrachtrup, "Nanoscale imaging magnetometry with diamond spins under ambient conditions," *Nature*, vol. 455, pp. 648–651, Oct 2008.

[169] P. Maletinsky, S. Hong, M. S. Grinolds, B. Hausmann, M. D. Lukin, R. L. Walsworth, M. Loncar, and A. Yacoby, "A robust scanning diamond sensor for nanoscale imaging with single nitrogen-vacancy centres," *Nature Nanotechnology*, vol. 7, no. 5, 2012.

[170] E. Van Oort and M. Glasbeek, "Electric-field-induced modulation of spin echoes of N-V centers in diamond," *Chemical Physics Letters*, vol. 168, pp. 529–532, May 1990.

[171] F. Dolde, H. Fedder, M. W. Doherty, T. Nöbauer, F. Rempp, G. Balasubramanian, T. Wolf, F. Reinhard, L. C. L. Hollenberg, F. Jelezko, and J. Wrachtrup, "Electric-field sensing using single diamond spins," *Nature Physics*, vol. 7, pp. 459–463, Jun 2011.

[172] V. M. Acosta, E. Bauch, M. P. Ledbetter, A. Waxman, L.-S. Bouchard, and D. Budker, "Temperature dependence of the nitrogen-vacancy magnetic resonance in diamond," *Physical Review Letters*, vol. 104, p. 070801, Feb 2010.

[173] M. W. Doherty, V. V. Struzhkin, D. A. Simpson, L. P. McGuinness, Y. Meng, A. Stacey, T. J. Karle, R. J. Hemley, N. B. Manson, L. C. Hollenberg, and S. Prawer, "Electronic properties and metrology applications of the diamond nv center under pressure," *Physical Review Letters*, vol. 112, p. 047601, Jan 2014.

[174] R. Benn and H. Günther, "Modern Pulse Methods in High-Resolution NMR Spectroscopy," *Angewandte Chemie International Edition in English*, vol. 22, pp. 350–380, 5 1983.

[175] T. Prisner, M. Rohrer, and F. MacMillan, "Pulsed EPR Spectroscopy: Biological Applications," *Annual Review of Physical Chemistry*, vol. 52, no. 1, pp. 279–313, 2001. PMID: 11326067.

[176] L. M. K. Vandersypen and I. L. Chuang, "NMR techniques for quantum control and computation," *Reviews of Modern Physics*, vol. 76, pp. 1037–1069, Jan 2005.

[177] A. Gruber, A. Dräbenstedt, C. Tietz, L. Fleury, J. Wrachtrup, and C. v. Borczyskowski, "Scanning confocal optical microscopy and magnetic resonance on single defect centers," *Science*, vol. 276, no. 5321, pp. 2012–2014, 1997.

[178] N. F. Ramsey, "A molecular beam resonance method with separated oscillating fields," *Physical Review*, vol. 78, pp. 695–699, Jun 1950.

[179] G. Balasubramanian, P. Neumann, D. Twitchen, M. Markham, R. Kolesov, N. Mizuochi, J. Isoya, J. Achard, J. Beck, J. Tissler, V. Jacques, P. R. Hemmer, F. Jelezko, and J. Wrachtrup, "Ultralong spin coherence time in isotopically engineered diamond," *Nature Materials*, vol. 8, no. 5, pp. 383–387, 2009.

[180] E. Marchiori, L. Ceccarelli, N. Rossi, L. Lorenzelli, C. L. Degen, and M. Poggio, "Nanoscale magnetic field imaging for 2d materials," *Nature Reviews Physics 2021*, pp. 1–12, 10 2021.

[181] Q.-C. Sun, T. Song, E. Anderson, A. Brunner, J. Förster, T. Shalomayeva, T. Taniguchi, K. Watanabe, J. Gräfe, R. Stöhr, X. Xu, and J. Wrachtrup, "Magnetic domains and domain wall pinning in atomically thin crbr3 revealed by nanoscale imaging," *Nature Communications*, vol. 12, p. 1989, Mar 2021.

[182] A. Boretti and S. Castelletto, "Nanometric resolution magnetic resonance imaging methods for mapping functional activity in neuronal networks," *MethodsX*, vol. 3, pp. 297–306, 2016.

[183] E. Bernardi, R. Nelz, S. Sonusen, and E. Neu, "Nanoscale sensing using point defects in single-crystal diamond: Recent progress on nitrogen vacancy center-based sensors," *Crystals*, vol. 7, p. 124, 4 2017.

[184] F. Casola, T. van der Sar, and A. Yacoby, "Probing condensed matter physics with magnetometry based on nitrogen-vacancy centres in diamond," *Nature Reviews Materials*, vol. 3, p. 17088, 01 2018.

[185] Y. Romach, C. Müller, T. Unden, L. J. Rogers, T. Isoda, K. M. Itoh, M. Markham, A. Stacey, J. Meijer, S. Pezzagna, B. Naydenov, L. P. McGuinness, N. Bar-Gill, and F. Jelezko, "Spectroscopy of surface-induced noise using shallow spins in diamond," *Physical Review Letters*, vol. 114, p. 017601, Jan 2015.

[186] F. Ziem, M. Garsi, H. Fedder, and J. Wrachtrup, "Quantitative nanoscale mri with a wide field of view," *Scientific Reports*, vol. 9, p. 12166, Aug 2019.

[187] M. Radtke, E. Bernardi, A. Slablab, R. Nelz, and E. Neu, "Nanoscale sensing based on nitrogen vacancy centers in single crystal diamond and nanodiamonds: achievements and challenges," *Nano Futures*, vol. 3, p. 042004, Dec 2019.

[188] B. K. Ofori-Okai, S. Pezzagna, K. Chang, M. Loretz, R. Schirhagl, Y. Tao, B. A. Moores, K. Groot-Berning, J. Meijer, and C. L. Degen, "Spin properties of very shallow nitrogen vacancy defects in diamond," *Physical Review B*, vol. 86, p. 081406, Aug 2012.

[189] M. S. Grinolds, S. Hong, P. Maletinsky, L. Luan, M. D. Lukin, R. L. Walsworth, and A. Yacoby, "Nanoscale magnetic imaging of a single electron spin under ambient conditions," *Nature Physics*, vol. 9, no. 4, 2013.

[190] O. R. Opaluch, N. Oshnik, R. Nelz, and E. Neu, "Optimized planar microwave antenna for nitrogen vacancy center based sensing applications," *Nanomaterials*, vol. 11, no. 8, 2021.

[191] F. Jelezko and J. Wrachtrup, "Single defect centres in diamond: A review," *physica status solidi (a)*, vol. 203, pp. 3207–3225, Oct 2006.

[192] J. F. Barry, J. M. Schloss, E. Bauch, M. J. Turner, C. A. Hart, L. M. Pham, and R. L. Walsworth, "Sensitivity optimization for nv-diamond magnetometry," *Reviews of Modern Physics*, vol. 92, p. 015004, Mar 2020.

[193] L. Childress, J. M. Taylor, A. S. Sørensen, and M. D. Lukin, "Fault-tolerant quantum communication based on solid-state photon emitters," *Physical Review Letters*, vol. 96, no. 7, 2006.

[194] J. R. Maze, P. L. Stanwix, J. S. Hodges, S. Hong, J. M. Taylor, P. Cappellaro, L. Jiang, M. V. G. Dutt, E. Togan, A. S. Zibrov, A. Yacoby, R. L. Walsworth, and M. D. Lukin, "Nanoscale magnetic sensing with an individual electronic spin in diamond," *Nature*, vol. 455, pp. 644–647, Oct 2008.

[195] M. Lesik, T. Plisson, L. Toraille, J. Renaud, F. Occelli, M. Schmidt, O. Salord, A. Delobbe, T. Debuisschert, L. Rondin, P. Loubeyre, and J.-F. Roch, "Magnetic measurements on micrometer-sized samples under high pressure using designed NV centers," *Science*, vol. 366, no. 6471, pp. 1359–1362, 2019.

[196] G. D. Fuchs, G. Burkard, P. V. Klimov, and D. D. Awschalom, "A quantum memory intrinsic to single nitrogen-vacancy centres in diamond," *Nature Physics*, vol. 7, pp. 789–793, Oct 2011.

[197] C. E. Bradley, J. Randall, M. H. Abobeih, R. C. Berrevoets, M. J. Degen, M. A. Bakker, M. Markham, D. J. Twitchen, and T. H. Taminiau, "A Ten-Qubit Solid-State Spin Register with Quantum Memory up to One Minute," *Physical Review X*, vol. 9, p. 031045, Sep 2019.

[198] Y. Wang, F. Dolde, J. Biamonte, R. Babbush, V. Bergholm, S. Yang, I. Jakobi, P. Neumann, A. Aspuru-Guzik, J. D. Whitfield, and J. Wrachtrup, "Quantum Simulation of Helium Hydride Cation in a Solid-State Spin Register," *ACS Nano*, vol. 9, pp. 7769–7774, Aug 2015.

[199] M. P. Ledbetter, K. Jensen, R. Fischer, A. Jarmola, and D. Budker, "Gyroscopes based on nitrogen-vacancy centers in diamond," *Physical Review A*, vol. 86, p. 052116, Nov 2012.

[200] C. L. Degen, "Scanning magnetic field microscope with a diamond single-spin sensor," *Applied Physics Letters*, vol. 92, p. 243111, Jun 2008.

[201] D. Bluvstein, Z. Zhang, and A. C. B. Jayich, "Identifying and mitigating charge instabilities in shallow diamond nitrogen-vacancy centers," *Physical Review Letters*, vol. 122, p. 076101, Feb 2019.

[202] C. Osterkamp, M. Mangold, J. Lang, P. Balasubramanian, T. Teraji, B. Naydenov, and F. Jelezko, "Engineering preferentially-aligned nitrogen-vacancy centre ensembles in CVD grown diamond," *Scientific Reports*, vol. 9, pp. 1–7, Dec 2019.

[203] M. Schreck, S. Gsell, R. Brescia, and M. Fischer, "Ion bombardment induced buried lateral growth: The key mechanism for the synthesis of single crystal diamond wafers," *Scientific Reports*, vol. 7, pp. 1–8, Mar 2017.

[204] N. Mohan, C.-S. Chen, H.-H. Hsieh, Y.-C. Wu, and H.-C. Chang, "In vivo imaging and toxicity assessments of fluorescent nanodiamonds in caenorhabditis elegans," *Nano Letters*, vol. 10, no. 9, pp. 3692–3699, 2010.

[205] R. Nelz, M. Radtke, A. Slablab, Z.-Q. Xu, M. Kianinia, C. Li, C. Bradac, I. Aharonovich, and E. Neu, "Near-field energy transfer between a luminescent 2d material and color centers in diamond," *Advanced Quantum Technologies*, vol. 3, no. 2, p. 1900088, 2020.

[206] Thorlabs, "Parts: C6w, cp08/m, cp02t/m, ersca, er1, cp90f," 2021. https://www.thorlabs.com Accessed on: 30.11.2020.

[207] GrabCAD, "Coaxial connector design by avitek, coaxial cable design by steven minichiello, and objective design by thorfynn." https://grabcad.com Accessed on: 07.06.2021.

[208] B. K. Ofori-Okai, S. Pezzagna, K. Chang, M. Loretz, R. Schirhagl, Y. Tao, B. A. Moores, K. Groot-Berning, J. Meijer, and C. L. Degen, "Spin properties of very shallow nitrogen vacancy defects in diamond," *Physical Review B*, vol. 86, p. 081406, Aug 2012.

[209] P. Appel, E. Neu, M. Ganzhorn, A. Barfuss, M. Batzer, M. Gratz, A. Tschöpe, and P. Maletinsky, "Fabrication of all diamond scanning probes for nanoscale magnetometry," *Review of Scientific Instruments*, vol. 87, no. 6, p. 063703, 2016.

[210] T. X. Zhou, R. J. Stöhr, and A. Yacoby, "Scanning diamond nv center probes compatible with conventional afm technology," *Applied Physics Letters*, vol. 111, no. 16, p. 163106, 2017.

[211] A. W. Schell, P. Engel, J. F. M. Werra, C. Wolff, K. Busch, and O. Benson, "Scanning single quantum emitter fluorescence lifetime imaging: Quantitative analysis of the local density of photonic states," *Nano Letters*, vol. 14, no. 5, pp. 2623–2627, 2014.

[212] A. Ariyaratne, D. Bluvstein, B. A. Myers, and A. C. B. Jayich, "Nanoscale electrical conductivity imaging using a nitrogen-vacancy center in diamond," *Nature Communications*, vol. 9, 2018.

[213] I. Lovchinsky, A. O. Sushkov, E. Urbach, N. P. de Leon, S. Choi, K. D. Greve, R. Evans, R. Gertner, E. Bersin, C. Müller, L. McGuinness, F. Jelezko, R. L. Walsworth, H. Park, and M. D. Lukin, "Nuclear magnetic resonance detection and spectroscopy of single proteins using quantum logic," *Science*, vol. 351, no. 6275, pp. 836–841, 2016.

[214] C. Bonato, M. S. Blok, H. T. Dinani, D. W. Berry, M. L. Markham, D. J. Twitchen, and R. Hanson, "Optimized quantum sensing with a single electron spin using real-time adaptive measurements," *Nature Nanotechnology*, vol. 11, no. 3, pp. 836–841, 2016.

[215] M. Chipaux, A. Tallaire, J. Achard, S. Pezzagna, J. Meijer, V. Jacques, J.-F. Roch, and T. Debuisschert, "Magnetic imaging with an ensemble of nitrogen-vacancy centers in diamond," *The European Physical Journal D*, vol. 69, p. 166, July 2015.

[216] Y. Schlussel, T. Lenz, D. Rohner, Y. Bar-Haim, L. Bougas, D. Groswasser, M. Kieschnick, E. Rozenberg, L. Thiel, A. Waxman, J. Meijer, P. Maletinsky, D. Budker, and R. Folman, "Wide-field imaging of superconductor vortices with electron spins in diamond," *Physical Review Applied*, vol. 10, p. 034032, Sep 2018.

[217] S. Hernández-Gómez and N. Fabbri, "Quantum control for nanoscale spectroscopy with diamond nitrogen-vacancy centers: A short review," *Frontiers in Physics*, vol. 8, p. 652, 2021.

[218] M. M. Müller, S. Gherardini, and F. Caruso, "Noise-robust quantum sensing via optimal multi-probe spectroscopy," *Scientific Reports*, vol. 8, no. 1, p. 14278, 2018.

[219] A. F. L. Poulsen, J. D. Clement, J. L. Webb, R. H. Jensen, K. Berg-Sørensen, A. Huck, and U. L. Andersen, "Optimal control of a nitrogen-vacancy spin ensemble in diamond for sensing in the pulsed domain." arXiv:2101.10049 [quant-ph], 2021.

[220] S. Machnes, U. Sander, S. J. Glaser, P. Defouquì, A. Gruslys, S. Schirmer, T. Schulte-Herbrüggen, P. de Fouquières, A. Gruslys, S. Schirmer, and T. Schulte-Herbrüggen, "Comparing, optimizing, and benchmarking quantum-control algorithms in a unifying programming framework," *Physical Review A*, vol. 84, p. 22305, 2011.

[221] M. H. Goerz, D. Basilewitsch, F. Gago-Encinas, M. G. Krauss, K. P. Horn, D. M. Reich, and C. P. Koch, "Krotov: A Python implementation of Krotov's method for quantum optimal control," *SciPost Physics*, vol. 7, p. 80, 2019.

[222] S. Machnes, E. Assémat, D. Tannor, and F. K. Wilhelm, "Tunable, Flexible, and Efficient Optimization of Control Pulses for Practical Qubits," *Physical Review Letters*, vol. 120, no. 15, p. 150401, 2018.

[223] M. M. Müller, S. Gherardini, T. Calarco, S. Montangero, and F. Caruso, "Information theoretical limits for quantum optimal control solutions: Error scaling of noisy channels," 2020.

[224] L. M. Rios and N. V. Sahinidis, "Derivative-free optimization: a review of algorithms and comparison of software implementations," *Journal of Global Optimization*, vol. 56, pp. 1247–1293, Jul 2013.

[225] V. M. Acosta, E. Bauch, M. P. Ledbetter, C. Santori, K.-M. C. Fu, P. E. Barclay, R. G. Beausoleil, H. Linget, J. F. Roch, F. Treussart, S. Chemerisov, W. Gawlik, and D. Budker, "Diamonds with a high density of nitrogen-vacancy centers for magnetometry applications," *Physical Review B*, vol. 80, p. 115202, Sep 2009.

[226] D. Budker and M. G. Kozlov, "Sensing: Equation one." arXiv:2011.11043 [quant-ph], 2020.

[227] D. Budker, D. Kimball, and D. DeMille, *Atomic physics: An exploration through problems and solutions*. Oxford, New York: Oxford University Press, second edition ed., July 2008.

[228] S. Choi, M. Jain, and S. G. Louie, "Mechanism for optical initialization of spin in nv-center in diamond," *Physical Review B*, vol. 86, p. 041202, Jul 2012.

[229] B. J. Shields, Q. P. Unterreithmeier, N. P. de Leon, H. Park, and M. D. Lukin, "Efficient readout of a single spin state in diamond via spin-to-charge conversion," *Physical Review Letters*, vol. 114, p. 136402, Mar 2015.

[230] T. Rendler, *Fluorescent nanodiamonds as a sensor and life science probe*. PhD thesis, Faculty of Mathematics and Physics, University of Stuttgart, Apr. 2018.

[231] E. Bourgeois, A. Jarmola, P. Siyushev, M. Gulka, J. Hruby, F. Jelezko, D. Budker, and M. Nesladek, "Photoelectric detection of electron spin resonance of nitrogen-vacancy centres in diamond," *Nature Communications*, vol. 6, p. 8577, Oct. 2015.

[232] J.-P. Tetienne, L. Rondin, P. Spinicelli, M. Chipaux, T. Debuisschert, J.-F. Roch, and V. Jacques, "Magnetic-field-dependent photodynamics of single NV defects in diamond: an application to qualitative all-optical magnetic imaging," *New Journal of Physics*, vol. 14, p. 103033, Oct 2012.

[233] C. J. Foot, *Atomic Physics*. Oxford Master Series in Physics, Oxford, New York: Oxford University Press, Feb. 2005.

[234] L. S. Theis, F. Motzoi, S. Machnes, and F. K. Wilhelm, "Counteracting systems of diabaticities using DRAG controls: The status after 10 years," *Europhysics Letters*, vol. 123, p. 60001, Oct 2018.

[235] T. D. Ladd, F. Jelezko, R. Laflamme, Y. Nakamura, C. Monroe, and J. L. O'Brien, "Quantum computers," *Nature*, vol. 464, pp. 45–53, Mar 2010.

[236] L. Thiel, D. Rohner, M. Ganzhorn, P. Appel, E. Neu, R. Kleiner, D. Koelle, and P. Maletinsky, "Quantitative nanoscale vortex imaging using a cryogenic quantum magnetometer," *Nature Nanotechnology*, vol. 11, 2016.

[237] Y.-C. Chang, J. Xing, F.-H. Zhang, G.-Q. Liu, Q.-Q. Jiang, W.-X. Li, C.-Z. Gu, G.-L. Long, and X.-Y. Pan, "Band-selective shaped pulse for high fidelity quantum control in diamond," *Applied Physics Letters*, vol. 104, no. 26, p. 262403, 2014.

[238] L. T. Hall, P. Kehayias, D. A. Simpson, A. Jarmola, A. Stacey, D. Budker, and L. C. Hollenberg, "Detection of nanoscale electron spin resonance spectra demonstrated using nitrogen-vacancy centre probes in diamond," *Nature communications*, vol. 7, 1 2016.

[239] A. Henstra, P. Dirksen, and W. Wenckebach, "Enhanced dynamic nuclear polarization by the integrated solid effect," *Physics Letters A*, vol. 134, no. 2, pp. 134–136, 1988.

[240] J. H. Ardenkjaer-Larsen, B. Fridlund, A. Gram, G. Hansson, L. Hansson, M. H. Lerche, R. Servin, M. Thaning, and K. Golman, "Increase in signal-to-noise of >10,000 times in liquid-state NMR," *Proceedings of the National Academy of Sciences*, vol. 100, pp. 10158–10163, 2003.

[241] D. B. Bucher, D. R. Glenn, H. Park, M. D. Lukin, and R. L. Walsworth, "Hyperpolarization-Enhanced NMR Spectroscopy with Femtomole Sensitivity Using Quantum Defects in Diamond," *Physical Review X*, vol. 10, p. 021053, Jun 2020.

[242] Z. J. Wang, M. A. Ohliger, P. E. Z. Larson, J. W. Gordon, R. A. Bok, J. Slater, J. E. Villanueva-Meyer, C. P. Hess, J. Kurhanewicz, and D. B. Vigneron, "Hyperpolarized 13C MRI: State of the Art and Future Directions," *Radiology*, vol. 291, no. 2, pp. 273–284, 2019.

[243] T. R. Eichhorn, A. J. Parker, F. Josten, C. Müller, J. Scheuer, J. M. Steiner, M. Gierse, J. Handwerker, M. Keim, S. Lucas, M. U. Qureshi, A. Marshall, A. Salhov, Y. Quan, J. Binder, K. Jahnke, P. Neumann, S. Knecht, J. W. Blanchard, M. B. Plenio, F. Jelezko, L. Emsley, C. C. Vassiliou, P. Hautle, and I. Schwartz, "Hyperpolarized solution-state NMR spectroscopy with optically polarized crystals." arXiv:2108.06147 [physics.chem-ph], 2021.

[244] Q. Chen, I. Schwarz, F. Jelezko, A. Retzker, and M. B. Plenio, "Optical hyperpolarization of 13 C nuclear spins in nanodiamond ensembles," *Physical Review B*, vol. 92, p. 184420, 2015.

[245] A. Henstra, *The Integrated Solid Effect*. PhD thesis, Rijksuniversiteit te Leiden, 1990.

[246] S. R. Hartmann and E. L. Hahn, "Nuclear Double Resonance in the Rotating Frame," *Physical Review*, vol. 128, pp. 2042–2053, 1962.

[247] T. R. Eichhorn, *Dynamic Nuclear Polarization with Paramagnetic Centers Created by Photo-Excitation*. PhD thesis, École Polytechnique Fédérale de Lausanne, 2013.

[248] D. W. J. Cruickshank, "A detailed refinement of the crystal and molecular structure of naphthalene," *Acta Crystallographica*, vol. 10, pp. 504–508, Aug 1957.

[249] Z. J. Wang, M. A. Ohliger, P. E. Z. Larson, J. W. Gordon, R. A. Bok, J. Slater, J. E. Villanueva-Meyer, C. P. Hess, J. Kurhanewicz, and D. B. Vigneron, "Hyperpolarized 13C MRI: State of the Art and Future Directions," *Radiology*, vol. 291, no. 2, pp. 273–284, 2019.

[250] K. Tateishi, M. Negoro, S. Nishida, A. Kagawa, Y. Morita, and M. Kitagawa, "Room temperature hyperpolarization of nuclear spins in bulk," *Proceedings of the National Academy of Sciences*, vol. 111, no. 21, pp. 7527–7530, 2014.

[251] D. M. Lilburn, G. E. Pavlovskaya, and T. Meersmann, "Perspectives of hyperpolarized noble gas MRI beyond 3He," *Journal of magnetic resonance*, vol. 229, pp. 173–186, 2013.

[252] M. Albert, G. Cates, B. Driehuys, W. Happer, B. Saam, C. Springer Jr, and A. Wishnia, "Biological magnetic resonance imaging using laser-polarized 129Xe," *Nature*, vol. 370, no. 6486, p. 199, 1994.

[253] M. Auzinsh and R. Ferber, *Optical Polarization of Molecules*. Cambridge University Press, 2005.

[254] T. E. Lee, S. Gopalakrishnan, and M. D. Lukin, "Unconventional Magnetism via Optical Pumping of Interacting Spin Systems," *Physical Review Letters*, vol. 110, p. 257204, Jun 2013.

[255] G. Liu, S.-H. Liou, N. Enkin, I. Tkach, and M. Bennati, "Photo-induced radical polarization and liquid-state dynamic nuclear polarization using fullerene nitroxide derivatives," *Physical Chemistry Chemical Physics*, vol. 19, pp. 31823–31829, Dec. 2017.

[256] J. P. King, K. Jeong, C. C. Vassiliou, C. S. Shin, R. H. Page, C. E. Avalos, H.-J. Wang, and A. Pines, "Room-temperature in situ nuclear spin hyperpolarization from optically pumped nitrogen vacancy centres in diamond," *Nature Communications*, vol. 6, p. 8965, Dec. 2015.

[257] P. London, J. Scheuer, J.-M. Cai, I. Schwarz, A. Retzker, M. B. Plenio, M. Katagiri, T. Teraji, S. Koizumi, J. Isoya, R. Fischer, L. P. McGuinness, B. Naydenov, and F. Jelezko, "Detecting and Polarizing Nuclear Spins with Double Resonance on a Single Electron Spin," *Physical Review Letters*, vol. 111, p. 067601, 2013.

[258] J. Scheuer, I. Schwartz, Q. Chen, D. Schulze-Sünninghausen, P. Carl, P. Höfer, A. Retzker, H. Sumiya, J. Isoya, B. Luy, MartinBPlenio, B. Naydenov, and F. Jelezko, "Optically induced dynamic nuclear spin polarisation in diamond," *New Journal of Physics*, vol. 18, no. 013040, 2016.

[259] Y. Quan, B. van den Brandt, J. Kohlbrecher, W. Wenckebach, and P. Hautle, "A transportable neutron spin filter," *Nuclear Instruments and Methods in Physics Research Section A: Accelerators, Spectrometers, Detectors and Associated Equipment*, vol. 921, pp. 22–26, 2019.

[260] Y. Quan, N. Nekitic, B. van den Brandt, and P. Hautle, "A novel broad-band neutron spin filter based on dynamically polarized protons using photo-excited triplet states," *EPJ Web of Conferences*, vol. 219, p. 10006, 2019.

[261] Y. Quan, B. van den Brandt, J. Kohlbrecher, and P. Hautle, "Polarization analysis in small-angle neutron scattering with a transportable neutron spin filter based on polarized protons," *Journal of Physics: Conference Series*, vol. 1316, p. 012010, Oct 2019.

[262] H. Kouno, Y. Kawashima, K. Tateishi, T. Uesaka, N. Kimizuka, and N. Yanai, "Nonpentacene Polarizing Agents with Improved Air Stability for Triplet Dynamic Nuclear Polarization at Room Temperature," *The Journal of Physical Chemistry Letters*, vol. 10, pp. 2208–2213, May 2019.

[263] A. C. Pinon, J. Schlagnitweit, P. Berruyer, A. J. Rossini, M. Lelli, E. Socie, M. Tang, T. Pham, A. Lesage, S. Schantz, and L. Emsley, "Measuring Nano- to Microstructures from Relayed Dynamic Nuclear Polarization NMR," *The Journal of Physical Chemistry C*, vol. 121, pp. 15993–16005, Jul 2017.

[264] A. Henstra, P. Dirksen, J. Schmidt, and W. Wenckebach, "Nuclear spin orientation via electron spin locking (NOVEL)," *Journal of Magnetic Resonance (1969)*, vol. 77, no. 2, pp. 389–393, 1988.

[265] H. Brunner, R. H. Fritsch, and K. H. Hausser, "Notizen: Cross Polarization in Electron Nuclear Double Resonance by Satisfying the Hartmann-Hahn Condition," *Zeitschrift für Naturforschung A*, vol. 42, no. 12, pp. 1456–1457, 1987.

[266] K. Miyanishi, T. F. Segawa, K. Takeda, I. Ohki, S. Onoda, T. Ohshima, H. Abe, H. Takashima, S. Takeuchi, A. I. Shames, K. Morita, Y. Wang, F. T.-K. So, D. Terada, R. Igarashi, A. Kagawa, M. Kitagawa, N. Mizuochi, M. Shirakawa, and M. Negoro, "Room-temperature hyperpolarization of polycrystalline samples with optically polarized triplet electrons: pentacene or nitrogen-vacancy center in diamond?," *Magnetic Resonance*, vol. 2, no. 1, pp. 33–48, 2021.

[267] I. Schwartz, J. Scheuer, B. Tratzmiller, S. Müller, Q. Chen, I. Dhand, Z. Y. Wang, C. Müller, B. Naydenov, F. Jelezko, and M. B. Plenio, "Robust optical polarization of nuclear spin baths using Hamiltonian engineering of nitrogen-vacancy center quantum dynamics," *Science Advances*, vol. 4, Aug 2018.

[268] H. Yuan, R. Zeier, N. Pomplun, S. J. Glaser, and N. Khaneja, "Time-optimal polarization transfer from an electron spin to a nuclear spin," *Physical Review A*, vol. 92, p. 053414, Nov 2015.

[269] N. Pomplun, B. Heitmann, N. Khaneja, and S. J. Glaser, "Optimization of electron–nuclear polarization transfer," *Applied Magnetic Resonance*, vol. 34, pp. 331–346, Aug 2008.

[270] N. Pomplun and S. J. Glaser, "Exploring the limits of electron-nuclear polarization transfer efficiency in three-spin systems," *Physical Chemistry Chemical Physics*, vol. 12, pp. 5791–5798, 5 2010.

[271] N. Khaneja, T. Reiss, C. Kehlet, T. Schulte-Herbrüggen, and S. J. Glaser, "Optimal control of coupled spin dynamics: design of NMR pulse sequences by gradient ascent algorithms," *Journal of Magnetic Resonance*, vol. 172, no. 2, pp. 296–305, 2005.

[272] S. Machnes, U. Sander, S. J. Glaser, P. de Fouquières, A. Gruslys, S. Schirmer, and T. Schulte-Herbrüggen, "Comparing, optimizing, and benchmarking quantum-control algorithms in a unifying programming framework," *Physical Review A*, vol. 84, p. 022305, Aug 2011.

[273] N. Leung, M. Abdelhafez, J. Koch, and D. Schuster, "Speedup for quantum optimal control from automatic differentiation based on graphics processing units," *Physical Review A*, vol. 95, p. 042318, Apr 2017.

[274] J. J. W. H. Sørensen, M. O. Aranburu, T. Heinzel, and J. F. Sherson, "Quantum optimal control in a chopped basis: Applications in control of Bose-Einstein condensates," *Physical Review A*, vol. 98, p. 022119, Aug 2018.

[275] F. Hoeb, F. Angaroni, J. Zoller, T. Calarco, G. Strini, S. Montangero, and G. Benenti, "Amplification of the parametric dynamical Casimir effect via optimal control," *Physical Review A*, vol. 96, p. 033851, Sep 2017.

[276] M. Rossignolo, A. Marshall, T. Reisser, P. Vetter, P. Rembold, A. Pagano, R. Said, M. Müller, T. Calarco, S. Montangero, and F. Jelezko, "QuOCS: A Quantum Optimal Control Suite," *in preparation*, 2022.

[277] T. Eichhorn, B. van den Brandt, P. Hautle, A. Henstra, and W. T. Wenckebach, "Dynamic nuclear polarisation via the integrated solid effect II: experiments on naphthalene-h8 doped with pentacene-d14," *Molecular Physics*, vol. 112, no. 13, pp. 1773–1782, 2014.

[278] J. M. Binder, A. Stark, N. Tomek, J. Scheuer, F. Frank, K. D. Jahnke, C. Müller, S. Schmitt, M. H. Metsch, T. Unden, T. Gehring, A. Huck, U. L. Andersen, L. J. Rogers, and F. Jelezko, "Qudi: a modular python suite for experiment control and data processing," *SoftwareX*, vol. 6, pp. 85–90, 2017.

[279] D. Stefanatos and E. Paspalakis, "Speeding up adiabatic passage with an optimal modified roland–cerf protocol," *Journal of Physics A: Mathematical and Theoretical*, vol. 53, p. 115304, Feb 2020.

[280] J. Roland and N. J. Cerf, "Quantum search by local adiabatic evolution," *Physical Review A*, vol. 65, p. 042308, Mar 2002.

[281] T. Caneva, T. Calarco, R. Fazio, G. E. Santoro, and S. Montangero, "Speeding up critical system dynamics through optimized evolution," *Physical Review A*, vol. 84, p. 012312, Jul 2011.

[282] S. van Frank, M. Bonneau, J. Schmiedmayer, S. Hild, C. Gross, M. Cheneau, I. Bloch, T. Pichler, A. Negretti, T. Calarco, and S. Montangero, "Optimal control of complex atomic quantum systems," *Scientific Reports*, vol. 6, p. 34187, Oct 2016.

[283] N. Malossi, M. G. Bason, M. Viteau, E. Arimondo, R. Mannella, O. Morsch, and D. Ciampini, "Quantum driving protocols for a two-level system: From generalized landau-zener sweeps to transitionless control," *Physical Review A*, vol. 87, p. 012116, Jan 2013.

[284] F. Gao and L. Han, "Implementing the Nelder-Mead simplex algorithm with adaptive parameters," *Computational Optimization and Applications*, vol. 51, pp. 259–277, Jan 2012.

[285] S. Lloyd and S. Montangero, "Information theoretical analysis of quantum optimal control," *Physical Review Letters*, vol. 113, p. 010502, Jul 2014.

[286] A. Van Strien and J. Schmidt, "An EPR study of the triplet state of pentacene by electron spin-echo techniques and laser flash excitation," *Chemical Physics Letters*, vol. 70, no. 3, pp. 513–517, 1980.

[287] A. Henstra and W. Wenckebach, "Dynamic nuclear polarisation via the integrated solid effect I: theory," *Molecular Physics*, vol. 112, no. 13, pp. 1761–1772, 2014.

[288] B. Julsgaard, C. Grezes, P. Bertet, and K. Mølmer, "Quantum Memory for Microwave Photons in an Inhomogeneously Broadened Spin Ensemble," *Physical Review Letters*, vol. 110, p. 250503, Jun 2013.

[289] C. Rackauckas and Q. Nie, "DifferentialEquations.jl – A Performant and Feature-Rich Ecosystem for Solving Differential Equations in Julia," *The Journal of Open Research Software*, vol. 5, no. 1, 2017.

[290] T. Besard, C. Foket, and B. De Sutter, "Effective extensible programming: Unleashing julia on gpus," *IEEE Transactions on Parallel and Distributed Systems*, vol. 30, no. 4, pp. 827–841, 2019.

[291] T. Besard, V. Churavy, A. Edelman, and B. D. Sutter, "Rapid software prototyping for heterogeneous and distributed platforms," *Advances in Engineering Software*, vol. 132, pp. 29–46, 2019.

[292] J. F. Seth Bromberger and contributors, "JuliaGraphs/LightGraphs.jl: an optimized graphs package for the Julia programming language." *GitHub*, https://github.com/sbromberger/LightGraphs.jl, 2017.

[293] J. Chen, J. Revels, and A. Edelman, "Robust benchmarking in noisy environments," in *HPEC'16 Proceedings of the Twentieth IEEE High Performance Extreme Computing Conference*, (Waltham, Massachusetts, USA), IEEE, September13—15 2016.

[294] M. Besançon and other contributors, "VertexSafeGraphs.jl." *GitHub*, https://github.com/matbesancon/VertexSafeGraphs.jl, 5 2019.

[295] P. K. Mogensen and A. N. Riseth, "Optim: A mathematical optimization package for Julia," *Journal of Open Source Software*, vol. 3, no. 24, p. 615, 2018.

[296] C. Rackauckas and Q. Nie, "Adaptive methods for stochastic differential equations via natural embeddings and rejection sampling with memory," *Discrete and continuous dynamical systems. Series B*, vol. 22, no. 7, p. 2731, 2017.

[297] T. Besard, C. Foket, and B. De Sutter, "Effective Extensible Programming: Unleashing Julia on GPUs," *IEEE Transactions on Parallel and Distributed Systems*, vol. 30, no. 4, pp. 827–841, 2019.

[298] Y. Ma, S. Gowda, R. Anantharaman, C. Laughman, V. Shah, and C. Rackauckas, "ModelingToolkit: A Composable Graph Transformation System For Equation-Based Modeling." arXiv:2103.05244 [cs.MS], 2021.

[299] C. Fieker, W. Hart, T. Hofmann, and F. Johansson, "Nemo/Hecke: Computer Algebra and Number Theory Packages for the Julia Programming Language," in *Proceedings of the 2017 ACM on International Symposium on Symbolic and Algebraic Computation*, ISSAC '17, (New York, NY, USA), pp. 157–164, ACM, 2017.

[300] S. G. Johnson, "QuadGK.jl: Gauss–Kronrod integration in Julia." *GitHub*, https://github.com/JuliaMath/QuadGK.jl, 2016.

[301] M. Innes, "Don't Unroll Adjoint: Differentiating SSA-Form Programs." arXiv:1810.07951 [cs.PL], 2018.

[302] M. Udell, K. Mohan, D. Zeng, J. Hong, S. Diamond, and S. Boyd, "Convex optimization in Julia," in *Proceedings of the 1st First Workshop for High Performance Technical Computing in Dynamic Languages*, pp. 18–28, IEEE Press, 2014.

[303] B. Legat, O. Dowson, J. D. Garcia, and M. Lubin, "MathOptInterface: A Data Structure for Mathematical Optimization Problems," *INFORMS Journal on Computing*, vol. 0, no. 0, pp. 0–0, 2021.

[304] M. Frigo and S. G. Johnson, "The Design and Implementation of FFTW3," *Proceedings of the IEEE*, vol. 93, no. 2, pp. 216–231, 2005.

[305] E. L. Hahn, "Spin Echoes," *Physical Review*, vol. 80, pp. 580–594, Nov 1950.

[306] D. D. Rife and J. Vanderkooy, "Transfer-function measurement with maximum-length sequences," *Journal of the Audio Engineering Society*, vol. 37, pp. 419–444, Jun 1989.

[307] P. E. Spindler, *Electron Paramagnetic Resonance with Shaped Microwave Pulses*. PhD thesis, Johann-Wolfgang Goethe-Universität, 2014.

[308] A. Karabanov, A. V. D. Drift, L. J. Edwards, I. Kuprov, and W. Köckenberger, "Quantum mechanical simulation of solid effect dynamic nuclear polarisation using krylov–bogolyubov time averaging and a restricted state-space," *Physical Chemistry Chemical Physics*, vol. 14, pp. 2658–2668, 2 2012.

[309] J. Gillet, M. A. Garcia-March, T. Busch, and F. Sols, "Tunneling, self-trapping, and manipulation of higher modes of a bose-einstein condensate in a double well," *Physical Review A*, vol. 89, 2 2014.

[310] R. Gati and M. K. Oberthaler, "A bosonic josephson junction," *Journal of Physics B: Atomic, Molecular and Optical Physics*, vol. 40, pp. 61–89, 2007.

[311] K. Sakmann, A. I. Streltsov, O. E. Alon, and L. S. Cederbaum, "Exact quantum dynamics of a bosonic josephson junction," *Physical Review Letters*, vol. 103, p. 220601, 11 2009.

[312] M. Pigneur, *Relaxation to a Phase-locked Equilibrium State in a One-dimensional Bosonic Josephson Junction*. PhD thesis, Technischen Universität Wien, Fakultät für Physik, 2019.

[313] J.-F. Mennemann, I. E. Mazets, M. Pigneur, H. P. Stimming, N. J. Mauser, J. Schmiedmayer, and S. Erne, "Relaxation in an extended bosonic josephson junction," *Physical Review Research*, vol. 3, p. 023197, 6 2021.

[314] C. Lévêque and L. B. Madsen, "Excitation spectra of systems of indistinguishable particles by the autocorrelation function technique: Circumventing the exponential scaling for bosons," *The Journal of Chemical Physics*, vol. 150, p. 194105, 5 2019.

[315] Private communication with Camille Lévêque.

[316] J. Lim, H.-G. Lee, and J. Ahn, "Review of Cold Rydberg Atoms and Their Applications," *Journal of the Korean Physical Society*, vol. 63, pp. 867–876, 2013.

[317] F. B. D. R F Stebbings, *Rydberg states of atoms and molecules*. Cambridge University Press, 1983.

[318] M. T. Simons, A. B. Artusio-Glimpse, A. K. Robinson, N. Prajapati, and C. L. Holloway, "Rydberg atom-based sensors for radio-frequency electric field metrology, sensing, and communications," *Measurement: Sensors*, vol. 18, p. 100273, 2021.

[319] X. Wu, X. Liang, Y. Tian, F. Yang, C. Chen, Y.-C. Liu, M. K. Tey, and L. You, "A concise review of Rydberg atom based quantum computation and quantum simulation," *Chinese Physics B*, vol. 30, p. 020305, Feb 2021.

[320] S. Ebadi, T. T. Wang, H. Levine, A. Keesling, G. Semeghini, A. Omran, D. Bluvstein, R. Samajdar, H. Pichler, W. W. Ho, S. Choi, S. Sachdev, M. Greiner, V. Vuletić, and M. D. Lukin, "Quantum phases of matter on a 256-atom programmable quantum simulator," *Nature*, vol. 595, pp. 227–232, Jul 2021.

[321] D. M. Greenberger, M. A. Horne, A. Zeilinger, and M. Kafatos, *Going Beyond Bell's Theorem*, pp. 69–72. Dordrecht: Springer Netherlands, 1989.

[322] C. H. Bennett, H. J. Bernstein, S. Popescu, and B. Schumacher, "Concentrating partial entanglement by local operations," *Physical Review A*, vol. 53, pp. 2046–2052, Apr 1996.

[323] D. Leibfried, E. Knill, S. Seidelin, J. Britton, R. B. Blakestad, J. Chiaverini, D. B. Hume, W. M. Itano, J. D. Jost, C. Langer, R. Ozeri, R. Reichle, and D. J. Wineland, "Creation of a six-atom 'schrödinger cat' state," *Nature*, vol. 438, pp. 639–642, Dec 2005.

[324] D. Cruz, R. Fournier, F. Gremion, A. Jeannerot, K. Komagata, T. Tosic, J. Thiesbrummel, C. L. Chan, N. Macris, M.-A. Dupertuis, and C. Javerzac-Galy, "Efficient quantum algorithms for ghz and w states, and implementation on the ibm quantum computer," *Advanced Quantum Technology*, vol. 2, 2019.

[325] J. Cui, R. van Bijnen, T. Pohl, S. Montangero, and T. Calarco, "Optimal control of Rydberg lattice gases," *Quantum Science and Technology*, vol. 2, p. 035006, Aug 2017.

[326] J. Preskill, "Quantum information and computation," in *Ph219/CS219 (Lecture Notes)*, ch. 4, California Institute of Technology, 2001.

[327] A. K. Ekert, "Quantum cryptography based on bell's theorem," *Physical Review Letters*, vol. 67, pp. 661–663, Aug 1991.

[328] H. Levine, A. Keesling, G. Semeghini, A. Omran, T. T. Wang, S. Ebadi, H. Bernien, M. Greiner, V. Vuletić, H. Pichler, and M. D. Lukin, "Parallel implementation of high-fidelity multiqubit gates with neutral atoms," *Physical Review Letters*, vol. 123, p. 170503, Oct 2019.

[329] M. Saffman, "Quantum computing with atomic qubits and Rydberg interactions: progress and challenges," *Journal of Physics B: Atomic, Molecular and Optical Physics*, vol. 49, p. 202001, Oct 2016.

[330] X. Ge, R. Wu, and H. Rabitz, "Optimization landscape of quantum control systems," *Complex System Modeling and Simulation*, vol. 1, pp. 77–90, 7 2021.

[331] T. M. Hospedales, A. Antoniou, P. Micaelli, and A. J. Storkey, "Meta-learning in neural networks: A survey," *IEEE Transactions on Pattern Analysis and Machine Intelligence*, pp. 1–1, 2021.

[332] J. Choi, H. Zhou, H. S. Knowles, R. Landig, S. Choi, and M. D. Lukin, "Robust dynamic hamiltonian engineering of many-body spin systems," *Physical Review X*, vol. 10, p. 031002, Jul 2020.

Declaration & License

Hiermit versichere ich an Eides statt, dass ich die vorliegende Dissertation selbstständig und ohne die Benutzung anderer als der angegebenen Hilfsmittel und Literatur angefertigt habe. Alle Stellen, die wörtlich oder sinngemäß aus veröffentlichten und nicht veröffentlichten Werken dem Wortlaut oder dem Sinn nach entnommen wurden, sind als solche kenntlich gemacht. Ich versichere an Eides statt, dass diese Dissertation noch keiner anderen Fakultät oder Universität zur Prüfung vorgelegen hat; dass sie - abgesehen von unten angegebenen Teilpublikationen und eingebundenen Artikeln und Manuskripten - noch nicht veröffentlicht worden ist sowie, dass ich eine Veröffentlichung der Dissertation vor Abschluss der Promotion nicht ohne Genehmigung des Promotionsausschusses vornehmen werde. Die Bestimmungen dieser Ordnung sind mir bekannt. Darüber hinaus erkläre ich hiermit, dass ich die Ordnung zur Sicherung guter wissenschaftlicher Praxis und zum Umgang mit wissenschaftlichem Fehlverhalten der Universität zu Köln gelesen und sie bei der Durchführung der Dissertation zugrundeliegenden Arbeiten und der schriftlich verfassten Dissertation beachtet habe und verpflichte mich hiermit, die dort genannten Vorgaben bei allen wissenschaftlichen Tätigkeiten zu beachten und umzusetzen. Ich versichere, dass die eingereichte elektronische Fassung der eingereichten Druckfassung vollständig entspricht.

- "Introduction to Quantum Optimal Control for Quantum Sensing with Nitrogen-Vacancy Centers in Diamond", Rembold et al., *AVS Quantum Science 2, 024701* (2020)
- "Robust Magnetometry with Single NV Centers via Two-Step Optimization", Oshnik et al., arXiv:2111.12684 [quant-ph] (2021)
- "Macroscopic Hyperpolarization Enhanced with Quantum Optimal Control", Marshall et al., arXiv:2112.15021 [quant-ph] (2021)

Phila Rembold
14 February 2022

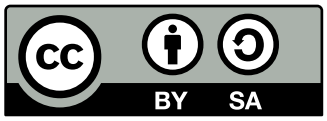

Acknowledgements

I am grateful to Simone Montangero and Tommaso Calarco for providing me with the opportunity to work on such a wide variety of projects and supporting me throughout this challenge. Similarly, Matthias M. Müller has been part of many discussions, helping me to focus my work and sharing his experience.
I would like to thank my fellow PhD students Thomas Reisser, Alastair Marshall, Marco Rossignolo, and Nimba Oshnik for the many fruitful discussions and mutual support. Furthermore, I am grateful for the QuSCo project and its organisers for providing a nurturing network and the majority of the funding that enabled this work. Concerning the sigmoid basis, I would like to thank Matthias M. Müller and Robert Zeier for their comments. I would further like to acknowledge everyone involved in the project on atomic condensates: TianTian Zhang, who did all the experimental work and was part of every project discussion, Camille Lévêque and Axel Lode, who provided support on MCTDH-X, helped to guide the project, and analyse the results, Jörg Schmiedmeyer who supervised the experimental part, as well as Marie Bonneau and Ioannis Brouzos who helped to get the project off the ground. Furthermore, I would like to thank Camille Lévêque for his support and for always being available to answer my questions.
My experience was also shaped by the people who provided me with bits of advice and kind words along the way, including Phillipp Neumann, Ressa Said, Daniel Jaschke, Felix Motzoi, Richard Nelz, Jian Cui, and Elke Neu-Ruffing as well as my groups in Padua and in Jülich.
Finally, I would like to thank my family, especially my mother, and my boyfriend, Linus, for their patience and continuous support. This thesis would not have been possible without them and my friends, who were there for me throughout the COVID-19 pandemic.